University of Leoben

Dissertation

Fracture behavior of tungsten based materials

Dipl.-Ing. Stefan Wurster

Leoben, July 2011

This work, supported by the European Communities under the Contract of Association between EURATOM and the ÖAW, was carried out within the framework of the European Fusion Development Agreement (EFDA). The views and opinions expressed herein do not necessarily reflect those of the European Commission.

The financial support of the Commission for the Coordination of Nuclear Fusion Research in Austria (KKKÖ) is acknowledged.

University of Leoben
Franz Josef Straße 18
8700 Leoben
Austria

Erich Schmid Institute of Materials Science
Austrian Academy of Sciences
Jahnstraße 12
8700 Leoben
Austria

Affidavit

I declare in lieu of oath, that I wrote this thesis and performed the associated research myself, using only literature cited in this volume.

Leoben, 11th of July 2011

… but the sun is eclipsed by the moon

Pink Floyd, Eclipse

Für Gerlinde

Danksagung

Allen Personen, die mir während der letzten Jahre geholfen haben, möchte ich an dieser Stelle ein „Dankeschön!“ aussprechen.

Größten Dank schulde ich Prof. Dr. Reinhard Pippan für seine Unterstützung während der letzten Jahre. Es waren vor allem seine Ideen, sein unerschütterlicher Optimismus, seine stets offene Tür und seine unerschöpflichen Antworten auf viele Fragen, die weiter halfen wenn es mal nicht so klappte.

Sämtliche Mitarbeiter des Erich Schmid Institutes mit Prof. Dr. Gerhard Dehm an der Spitze haben sehr viel zum Gelingen dieser Arbeit beigetragen.

Besonders hervorheben möchte ich das stets hilfsbereite Team der Werkstätte: Franz Hubner, Günter Aschauer und Christian Scheiner. Ein herzliches Dankeschön an Traude Haberz, Gabi Moser und Silke Modritsch, den Damen der Metallographie für die unermüdliche Probenpräparation. Bei Peter Kutleša möchte ich mich für die Arbeit an der HPT-Anlage und für die Versuche Wolfram klein zu bekommen bedanken. Mit technischen Problemen unterschiedlichster Art konnte ich stets zu Herwig Felber gehen – er wusste eine Lösung. Vielen Dank! Marianne Fliesser und Doris Schrutt sind unersetzlich, wenn es darum geht Administratives und Organisatorisches zu erledigen.

Dr. Christian Motz war eine große Hilfe, wenn es darum ging Versuche an kleinsten Proben durchzuführen und zu verstehen; ich möchte mich für die vielen großen und kleinen Hilfestellungen bedanken.

Dr. Lorenz Romaner und Dr. Hong Li lieferten auf einer anderen, experimentell kaum zugänglichen Ebene interessante Einsichten in das Material. Vielen Dank für die angenehme Zusammenarbeit.

Bei Dr. Andreas Hoffmann und Dr. Wolfram Knabl möchte mich ich für die Unterstützung, die sie mir in vielen Punkten zu Teil haben lassen, bedanken.

Mag. Monika Fischer und Mag. Anna Kantner danke ich für die administrative Abwicklung des Projektes.

Furthermore, I would like to thank Prof. Dr. Monika Jenko for the opportunity to perform the ion slicing sample preparation at the Institute of Metals and Technology and B.Sc. Miroslav Pečar for the realization of this preparation. Gerald Pintsuk bin ich für viele aufschlussreiche Diskussionen

dankbar. Ein großes Dankeschön an Jeong-Ha You, Juan Du und Johann Riesch für die interessante Zusammenarbeit.

Sehr wichtige Wegbegleiter während der letzten Jahre waren meine Mit-Dissertanten, Post-Docs, Diplomanden, studentische Mitarbeiter und Freunde am ESI. Allen voran Kurt Matoy, der mich dankenswerterweise nach Leoben gelotst hat. Mir konnte kaum etwas Besseres passieren. Bernd Gludovatz hat mir mit seiner unnachahmlichen Art die Stunden im Büro verschönert; Bernhard Völker hat diesen Part nahtlos übernommen. Bei Christian Rehrl möchte ich mich für die Einführung in die Welt des A220 und die Rehrl'schen Weckerl bedanken. Bei Wolfgang Schiller und Thomas Leitner bedanke ich mich für die großartige Hilfe bei Probenpräparation und Experimenten – ihr wart beide fabelhaft. Viel Glück für eure Zukunft. Allen, auch jenen die ich nun nicht namentlich genannt habe, möchte ich für das angenehme Arbeitsklima während der letzten Jahre und die nicht notwendigerweise fachspezifischen Diskussionen bei einigen Tassen Kaffee danken.

Zuletzt möchte ich mich bei den wichtigsten Personen bedanken. Ohne meiner Familie, insbesondere meiner Eltern, Josefine und Walter, und Dir, Gerlinde, wäre all das nie möglich gewesen.

Kurzfassung

Wolfram und auf Wolfram basierende Werkstoffe sollen in neuralgischen Bereichen von Kernfusionsreaktoren eingesetzt werden. Einer der Nachteile, den man aufgrund dieser Werkstoffwahl zu berücksichtigen hat, ist die Sprödigkeit des Materials bei „tiefen“ Temperaturen, unterhalb von einigen hundert Grad Celsius. Eine Verschiebung des spröd-duktil Übergangs zu tieferen Temperaturen und eine generelle Erhöhung der Zähigkeit würden maßgeblich zu einem erfolgreichen Einsatz dieser Werkstoffe in Fusionsreaktoren beitragen. Dafür ist es aber notwendig, jene Mechanismen zu kennen und zu verstehen, die das Verformungs- und vor allem das Bruchverhalten bestimmen.

Eine Steigerung der Bruchzähigkeit wurde durch das Hinzulegieren von Rhenium und durch mikrostrukturelle Veränderungen erzielt. Da Rhenium, das bisher einzig bekannte Legierungselement, welches eine maßgebliche Duktilitäts- und Zähigkeitssteigerung hervorruft, sehr selten und teuer ist, scheint bis jetzt die gezielte Veränderung der Mikrostruktur der einzig gangbare Weg zu sein, bruchzähes Material in entsprechender Menge herzustellen. Im Falle der vorliegenden Arbeit wurde zur Herstellung und Verformung unterschiedlicher, auf Wolfram basierender Materialien die Methode der Hochverformung eingesetzt. Durch Bruchversuche an ultrafeinkörnigen Verbundwerkstoffen bestehend aus Wolfram-Vanadium und Wolfram-Tantal wurde die Erhöhung der Bruchzähigkeit in zwei von drei Testrichtungen nachgewiesen. Eine “allseitige” Erhöhung der Bruchzähigkeit scheint durch mikrostrukturelles Design nicht oder nur in relativ geringen Maße möglich zu sein.

Um nun die Einflüsse einzelner Gefügebestandteile, wie Korngrenzen, Poren und Ausscheidungen, auf das Bruchverhalten im Detail und gesondert voneinander untersuchen zu können, wurden Bruchexperimente an mikrometergroßer Proben – vor allem gekerbten Biegebalken – weiterentwickelt. Ein „Ionen-Slicer“, normalerweise verwendet um Proben für die Transmissionselektronenmikroskopie zu präparieren, stellt hierbei einen wichtigen Zwischenschritt dar, um die Herstellungszeit der Proben mittels fokussiertem Gallium-Ionen Strahl zu minimieren. Um einerseits die während des Bruches ablaufenden Prozesse zu identifizieren und zu verstehen und andererseits die durch die veränderte Probengeometrie notwendigen Adaptionen der Auswertungen der Experimente zu erarbeiten, wurde einkristallines Wolfram in sprödester Orientierung als Modellmaterial gewählt. Linear elastische Bruchmechanik ist wegen der großen plastischen Zone in Relation zur sehr kleinen Probengröße nicht anwendbar, elastisch-plastische Bruchmechanik wurde daher herangezogen. Dadurch konnte die Bruchzähigkeit von einkristallinem Wolfram mittels Proben von einigen Mikrometern Größe bestimmt und eine experimentelle Basis für das bessere Verständnis des Rissfortschrittes in Wolfram geschaffen werden.

Abstract

Tungsten and tungsten-based materials will be used in neuralgic sections of fusion reactors. A disadvantage of this choice of the material that has to be considered is the brittleness at “low” temperatures, below a few hundred centigrade. Both, a decrease of the brittle-to-ductile transition temperature and an increase of materials’ toughness at low temperatures will contribute to the successful application of tungsten for fusion applications. Hence, it is necessary to comprehensively understand the mechanisms governing the deformation of tungsten, in particular the fracture behavior.

An increase in fracture toughness was observed when alloying tungsten with rhenium and through microstructural modification of tungsten-based materials. Rhenium is a rare element and it is the only element known to markedly increase the ductility and fracture toughness of tungsten. Specific microstructure design is then the best route to produce large batches of “tough” tungsten. For the work presented in this thesis, severe plastic deformation was used for production and deformation of tungsten based materials. Fracture experiments using ultra-fine grained composites of tungsten-vanadium and tungsten-tantalum show an increase in fracture toughness in two out of three possible testing directions. An increase in fracture toughness for all testing directions seems difficult, maybe even impossible, to realize by microstructural design.

To better understand the separate influences of certain microstructural constituents such as grain boundaries, pores and precipitations on the fracture behavior, fracture experiments using micrometer-sized samples – notched bending beams – were developed and improved. A so-called “ion slicer”, typically used for transmission electron microscopy sample production, was used to improve the final sample production with a focused ion beam workstation. In order to identify and better understand the fracture processes and to develop the analysis of the micrometer–scaled experiments, single crystalline tungsten was chosen as a model material. Linear elastic fracture mechanics is not applicable due to the large plastic zone in relation to the small sample size; elastic – plastic fracture mechanics has to be used. In doing so, the fracture toughness of single crystalline tungsten was determined. Furthermore, an experimental basis was set in order to better understand crack propagation in tungsten.

Content

Motivation and Aim of the Work

In a recent *Scientific American* article [ScA10], the editors collected several reports and rated them according to their likelihood that the described events will occur. The development of a practical fusion reactor was amongst them, rated to be “very unlikely”, being the only one in this category. Other events, such as the discovery of extra dimensions at the Large Hadron Collider (LHC), room temperature superconductors and sighting of extraterrestrial intelligence were deemed more likely. Well … Let’s see.

The possibility of fusing atoms is nothing new, not to the universe for billions of years and not to human technology for several decades. There already exist experimental fusion facilities which demonstrate the general possibility of technical realization of fusion on earth. However, there persists the problem of upscaling this process for commercial power generation. As it is impossible to construct a huge windmill which stands in the North Sea based on a wooden pinwheel the same is valid for the process towards large first generation fusion reactors. Design has not to be modified but to be changed completely. From the point of view of a materials scientist, wood has to be replaced by concrete and steel in this childish example. For fusion technology this means that other solutions for structural and plasma facing materials have to be found. Low Z-materials, e.g. beryllium or carbon, might have been interesting for small units, which were immanently necessary to understand the fusion process, but when increasing the power output, hence facilities’ energy content, high-melting tungsten might be more appropriate.

Worldwide research directs towards solving the problem to find the right material in its right configuration for the right place within the fusion reactor. Japan, South Korea, China, India, Russia, the United States of America and the European Union are jointly constructing the International Thermonuclear Experimental Reactor (ITER). The part in which our scientific group has been involved for the last couple of years deals with the investigation of tungsten and tungsten-based materials for structural and armor materials [Riet11b]. A necessity, especially for tungsten to be used as a structural material, is to find toughening mechanisms, i.e. to make tungsten less prone to fracture. Several measures were taken: rhenium, an alloying element being known to ductilize tungsten, was investigated in order to better understand this fact and to get an idea where to possibly find other alloying elements having the same effect.

As already determined in previous work, the microstructure of tungsten and tungsten-based materials has a pronounced influence on mechanical properties, including fracture properties. Consequently, the idea evolved to produce tungsten-based composites from powder using severe plastic deformation by high pressure torsion. The very fine grained material was supposed to have advantageous fracture properties and furthermore – by alloying e.g. vanadium to tungsten – it

should be possible to adjust important thermo-mechanical parameters such as the coefficient of thermal expansion, which is crucial when joining tungsten to steel.

A problem that evolves when operating a fusion power plant is irradiation of the materials enclosing the plasma. Alpha particle and neutron radiation introduce defects and alter the behavior of materials not necessarily enhancing the mechanical properties. A part of this work will review the increased irradiation resistance of nanocrystalline and ultra-fine grained material. Linked with the topic of irradiated materials is the subject of small-scaled fracture experiments. Irradiation of materials in order to simulate a fusion-reactor-like environment is a time- and money-consuming experiment. A facility that accurately simulates the neutron spectrum of the next large-scaled fusion facility does not even exist yet. In case it will in the future, irradiated material will be, nevertheless, highly restricted in volume. Hence, it is reasonable to investigate whether it is possible to downsize fracture experiments to the micrometer regime, as it was already done for a variety of other experiments such as bending, compression and tensile testing. Probing small volumes of materials, which are preferably of high ductility, makes it necessary to examine how to introduce elastic-plastic fracture mechanics to experiments in the micrometer regime. The production and testing of small samples will be outlined in the last part of this thesis.

Coming back to the first paragraph, to the author's point of view the realization of the International Thermonuclear Experimental Reactor (ITER) seems to be feasible, as the operational demands are gradually increasing from existing fusion facilities. Going ahead to larger first generation nuclear power plants, which are supposed to operate all day long and for years, even decades, will be a tough challenge.

1. Introduction

1.1. Nuclear Fusion

> *"While it is unfortunately true that theorists have not told the experimentalists how to build a thermonuclear machine, it is also true that we have been looking hard for many years for a fundamental reason why a plasma fusion reactor should be impossible and we have not found any such reason."* Marshall Nicholas Rosenbluth at the IAEA Conference on Plasma Physics and Controlled Nuclear Fusion at Salzburg, Austria, September 1961 [IAE62]

Nuclear fusion would be the most yielding source of energy when asking for the amount which could be released from a certain quantity of material. As the worldwide need for energy is far from declining, this is an interesting fact. Yet, there exists no machine taking advantage from nuclear fusion in a way that a surplus of energy could be fed into the power grid. Difficulties in designing and constructing first generation fusion power plants or even smaller scaled predecessors to these plants, may lead to the longest time span between the emergence of a principle idea and the completion of industrial facilities.

ITER, the International Thermonuclear Experimental Reactor [ITE11] (iter, lat. for "the way"), is at present the most important long-term project to narrow the gap between currently existing experimental nuclear fusion devices and power plants. At the moment, the construction at Cadarache (Arrondisement Aix-en-Provence, France) is ongoing. The goal for ITER's energy gain factor Q is set to ≥10, which means that the fusion power output of the tokamak[1] is ten times the auxiliary power fed into the plasma. In previous experimental efforts, more energy was used to drive the fusion process than energy could be obtained. 500 MW is the fusion power output of ITER during a burn length of about 7 min, given in the final design report [FDR01]. Hence, 50 MW of auxiliary power have to be injected. Scientific and engineering goals of this international project are to combine different fusion technologies and components for a future fusion reactor, especially to demonstrate the practicability of tritium breeding. The completion of the succeeding DEMO-project (DEMOnstration Power Plant) [Mai08], the first fusion power plant, would finally show the feasibility of fusion power as a long-term source of energy.

In the core of our sun, most of the energy is released via the proton-proton reaction due to the mass defect. Hydrogen cores fuse to form heavier cores. The technical realization of fusion is based, however, on combining deuterium and tritium particles [Reb05], which are the heavy hydrogen isotopes:

[1] TOroidalnaya KAmera, MAgnitaya Katushka (rus.: toroidal chamber, magentic coil) [Cam05]

$$ {}^{2}_{1}D + {}^{3}_{1}T \rightarrow {}^{4}_{2}He(3.5MeV) + {}^{1}_{0}n(14.1MeV) \quad (1) $$

Both particles, deuterium (D) and tritium (T), have to be at high speed, temperature respectively, to overcome the electrostatic repulsion of the positively charged nuclei, hence the fuel is present in the state of ionized plasma. The ratio of energy of heavy alpha particles and light particles is due to the conservation of momentum. In general, it is possible to heat the plasma by ohmic heating, injection of fast neutral particles, compressing the plasma by confining the magnetic field lines or by electromagnetic waves. High temperatures are necessary but not sufficient; furthermore, the product of plasma density and time of confinement has to reach certain critical values (Lawson criterion). The kinetic energy of the two particles on the right side of Equation (1) will be transformed into heat by stopping these particles in the surrounding matter. When taking one mol of deuterium and tritium each – being about 5 g in total – the energy output on the right side of Equation (1) would be enough to heat about 40,000 t of water from 14.5 °C to 15.5 °C. Just imagine how warm an Olympic swimming pool gets with the heat from 5 g of burned coal or oil. To operate a fusion power plant with an electric power output of 1 GW for 1 year, only about 110 kg of deuterium and 380 kg of lithium, for tritium breeding, would have to be used [Reb05]. Materials on the left side of Equation (1) are not directly available, but deuterium can be found in water, tritium – the very rare and expensive radioactive hydrogen isotope – has to be produced within the fusion device by neutron irradiation of lithium targets (${}^{6}_{3}Li$ and ${}^{7}_{3}Li$) resulting in ${}^{3}_{1}T$.

An inherent disadvantage of the fusion reaction described in Equation (1) is the appearance of induced radioactivity because of the emission of fast neutrons. Consecutively, these emitted neutrons interact with the surrounding matter resulting in neutron capture and radioactive processes are initiated. Other fusion reactions, which do not induce any radioactivity, do not offer the same yield or would require even more rare isotopes, such as ${}^{3}_{2}He$ [Reb05]:

$$ {}^{2}_{1}D + {}^{3}_{2}He \rightarrow {}^{4}_{2}He(3.6MeV) + {}^{1}_{1}H(14.7MeV) \quad (2) $$

Stressing a very holistic point of view, the generation of the elements this thesis is concentrated on, is based on such fusion processes. The origination of heavier elements than hydrogen and helium up to iron and nickel by fusion processes is an intermediate step towards evolution of heavier elements during e.g. supernovas.

One possibility to fuse atoms is to confine them magnetically; other ways are to confine them inertially (laser, z-pinch) or to use muon-catalyzed fusion. For ITER and DEMO, the way of magnetic confinement is chosen. The plasma is confined by magnetic fields originating from toroidal and poloidal coils and furthermore from the plasma current itself. Liquid helium cooled superconducting coils are necessary, conventional copper coils would need more electric power.

These coils have to be shielded from radiation. The blanket and the divertor (Figure 1-1), both parts constituting the so-called first wall that faces the hot plasma, realize the mechanical enclosure. Magnetic fields do not confine uncharged neutrons, rather they can transfer energy to the first wall via inelastic collisions. In addition, charged particles follow the field line into the vacuum vessel's lower part and interact with material constituting the divertor. In general, the heat flux is high; hence, all plasma-facing components need to be actively cooled for large-scaled fusion devices. For ITER the coolant will be water [FDR01], for DEMO helium is an option [Ihl05]. Helium, being chemically inert, offers the advantages of inertness to neutrons and the possibility to operate at higher temperatures and lower pressures [Nor08]. These new coolant technologies for ITER and DEMO are in contrast to existing experimental fusion facilities, where owing to the small power and short pulse times no active cooling is necessary.

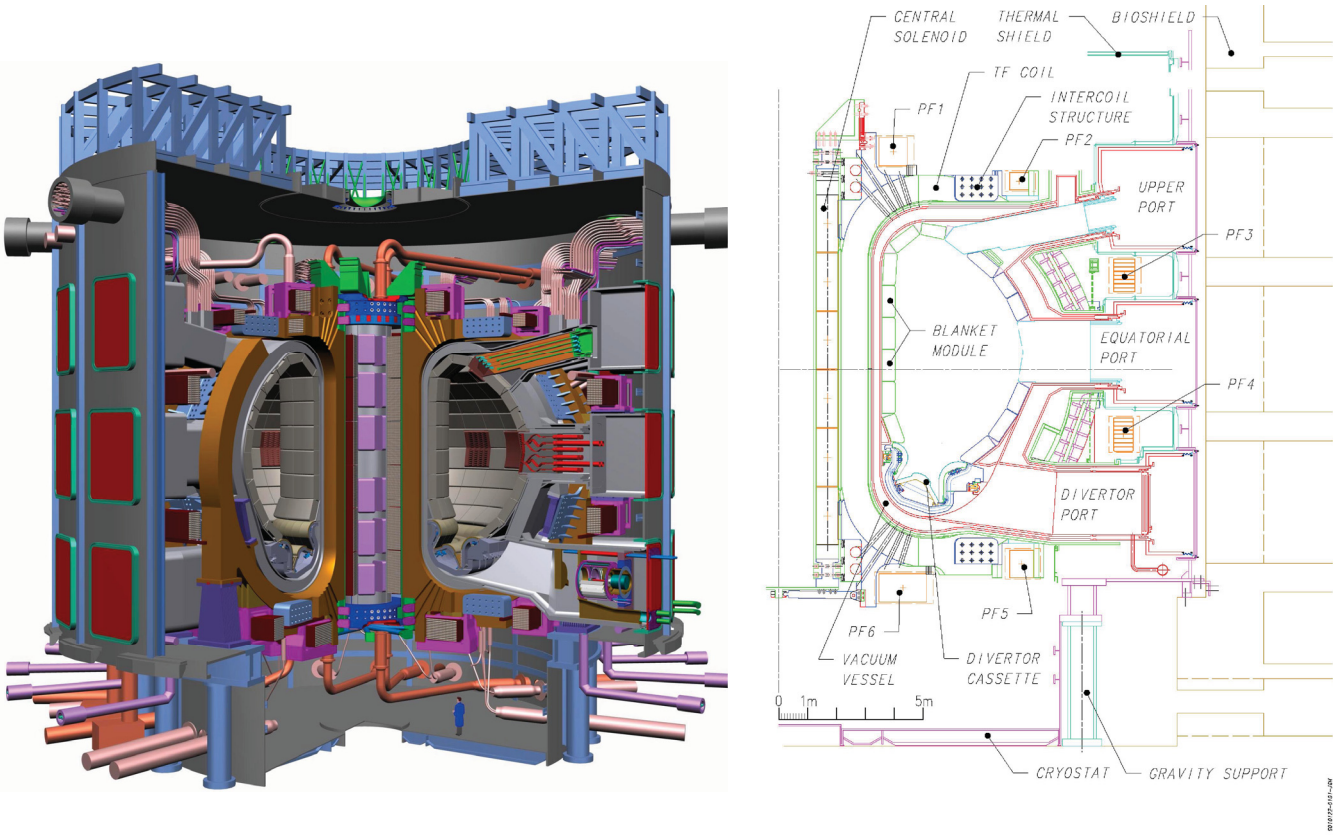

Figure 1-1: ITER tokamak cutaway (left) and cross-sectional view (right). taken from [FDR01].

Several different structural and plasma facing materials are proposed for fusion technologies [Zin05]. The divertor concept for ITER and a proposed divertor design concept for DEMO are shown in Figure 1-2. The design for DEMO consists of tungsten as the plasma facing material brazed on a thimble made of lanthanum-oxide dispersion strengthened tungsten (WL10 containing 1 wt% of La_2O_3), which is then again fixed to oxide dispersion strengthened (ODS) EUROFER steel [Ihl05, Nor08]. Helium enters at a pressure of 10 MPa with 600 °C and leaves at a temperature of

700 °C. Joining tungsten-based materials (WL10) to steel is somewhat tricky, due to the large mismatch in thermal expansion coefficient. This might be compensated with tungsten-based functionally graded materials, e.g. with large amounts of vanadium [HohJ10, Wur11], which adjust the coefficient of thermal expansion [HohJ10].

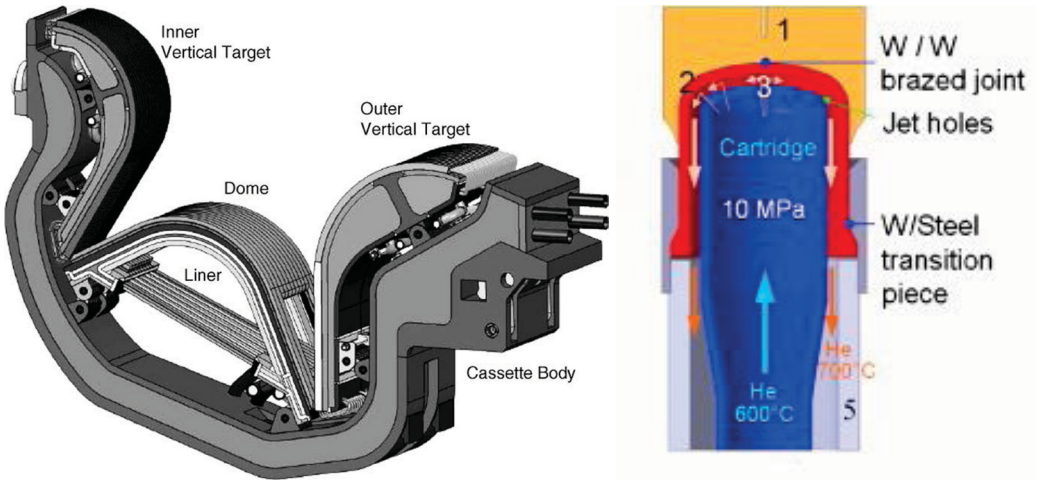

Figure 1-2: Left: Design of the divertor for ITER. Taken from [Mer06]. Right: He-cooled modular divertor with jet cooling (HEMJ), W tile (1), WL10 thimble (2), He (jet flow) (3), ODS Eurofer structure (5), [Ihl05, Nor08].

The most important requirements for these plasma facing and structural materials are to be resistant – at least up to a certain point – against radiation damage, such as evolution of transmutation elements and helium / hydrogen production, leading to swelling and embrittlement. Impacts of fast 14 MeV-neutrons (Equation (1)) lead to collision cascades, where a large number of atoms are displaced and interstitials and vacancies evolve. After the cascades – lasting for very short times – fade away, most of the atoms return to lattice sites, but some vacancies and interstitials are left behind. Irradiation damage of materials is expected to be two orders of magnitudes higher for first generation fission reactors (~100 dpa [Zin05]) than for ITER (~1 [Mer06]). Displacements per atom (dpa) are a measure for radiation damage, giving the average number of displacements of atoms from their lattice sites. One dpa means that on average each atom was displaced one time from its lattice site. The evolving damage is of course not just a question of energy and type of irradiating particles but also of irradiated matter. Some advantageous properties of nanocrystalline materials regarding their irradiation resistance will be discussed in Publication A.

Ultimately avoiding almost all long-lived radioactive waste would be a big advantage and a strong argument for future fusion reactors. An important difference between fusion and fission power plants is the following: whereas for fission power plants, the inventory of radioisotopes is quite large – as observed after serious accidents in Three Mile Island, United States of America (1979),

Chernobyl, Ukraine (1986) and recently in Fukushima, Japan (2011) – the situation for fusion power plants is a bit different. In contrast to fission, fusion does not rely on the usage of heavy nuclei (^{235}U, ^{239}Pu), which lead due to the fission process to the production of radioisotopes of intermediate mass (^{137}Cs, ^{131}I, ^{90}Sr …) and transuranic elements. Contrary, accumulation of large and long-living inventories of radioisotopes, which complicates decommission of power plants and final disposal of radioactive waste, is avoidable for fusion. Nevertheless, it is inevitable that a certain amount of radioactive tritium has to be used as fuel (half-life $\tau_{1/2,\ ß-}$ ~ 12.3 years) and materials are activated by neutron irradiation. However, designing the alloying contents of the surrounding material is feasible. Hence, materials for fusion applications have to be composed in a way not to produce long-lived radioisotopes. Certain elements such as molybdenum, aluminum, nickel, niobium and cobalt must not be used in pure form nor as alloying elements, because they would lead to an increased neutron capture induced radioactivity of structural and plasma facing materials. Reduced activation structural materials, which are proposed to be used for fusion applications, can be divided in three groups [Ehr00, Zin05]:

- Ferritic / martensitic steels with chromium as the main alloying element
    - Oxide dispersion strengthened steels [Uka02]
- Vanadium alloys, e.g. V-Cr-Ti [Muro02]
- SiC_{fibre}/SiC_{matrix} composites [Kat07, Ricc00]

Furthermore, beryllium, carbon fiber reinforced carbon composites and tungsten based materials are under consideration for the first wall.

In the upcoming ITER, beryllium, a low-Z element, will be used for the largest part of the first wall due to its good plasma compatibility [FDR01]. According to reference [Jan01], it cannot be used for larger reactors. The blanket in ITER will consist of a beryllium armor assembled on a steel frame, the divertor will consist of carbon fiber reinforced composites and tungsten [Jan01, Tiv01]. The function of the divertor is to remove the remaining α-particles, the so-called helium ash – remnant from the fusion process – and impurities from the plasma [Mer06]. For astrophysicists a “metal” is defined to be an element having a mass larger than the mass of helium, the same holds true for impurities within the plasma. Magnetic field lines are not closed in the divertor region of the plasma chamber and charged particles will strike the inner and outer vertical targets in their lower regions (Figure 1-2, left), these are the regions where application of carbon is considered. During normal operation conditions, the divertor is the only region where the plasma stays in direct contact with the first wall. Hence, divertor components are exposed to higher heat fluxes, the divertor heat load is about 15% of the total fusion power [Nor08].

Tungsten does not possess the same plasma compatibility as carbon and beryllium. Thus, high Z-impurities may not be fully ionized, and the remaining possibility of electronic transitions leads to further plasma power losses. In ITER’s starting configuration, tungsten will be used just for the upper regions of the inner and outer vertical target and for the dome [Mer06]. These components

act as baffles for uncharged particles. However, in a later stage of the ITER-project when it changes from its initial phase to the deuterium-tritium-burning phase, carbon is planned to be replaced by tungsten and consequently full-tungsten divertors will be used [RafAR10]. This is due to the higher tritium retention when using carbon-based materials. Beside of physical sputtering, chemical erosion at low energies by knock-on particles is also possible. Radioactive tritium is co-deposited with carbon and accumulates inside the plasma vessel, which might lead to safety related problems, as eroded, re-deposited and loosely bound material would easily be released in case of an accident. Thus, the higher erosion rate of carbon, leading to shorter lifetimes of components, is disadvantageous for the operation of commercial fusion power plants. This is not the case for tungsten, which has lower tritium retention and erosion rates. Nevertheless, one has to be aware of the formation of tungsten oxide at high temperature and presence of oxygen (e.g. air ingress).

Several fusion groups have already demonstrated the applicability of tungsten for plasma facing components: the ASDEX[2] Upgrade project [Dux09], TEXTOR[3] [Pos01] and Alcator C-Mod [Barn11]. Tungsten as a plasma facing material will also be used after the recent refurbishment campaign at EAST[4] [LuoGN11]. The ITER-like wall project at JET[5] [Pam07] aims at mimicking the whole first wall of ITER, which means the first wall will be made of beryllium except the divertor region being covered with tungsten. JET is now, summer 2011, starting to operate with this ITER-like wall, first plasma operation is planned to be achieved in August 2011 [Matt11]. The goals are to investigate the influence of the tungsten divertor on the plasma performance, the erosion of tungsten, the melt layer formation and the interaction with beryllium.

Another large-scaled irradiation and testing laboratory, being an important milestone on the roadmap to DEMO, is the upcoming IFMIF-facility (International Fusion Materials Irradiation Facility) [Kon98, Moe06]. It is inevitably necessary to gain a comprehensive understanding of the interaction of a high flux of fast 14 MeV neutrons with matter. Thus, IFMIF is an essential part of the worldwide fusion R&D program; however, this facility still needs to be constructed. Fast neutrons will be generated by hitting a liquid lithium target with deuterium beams. The affected volume of the high neutron flux region, experiencing 20-55 dpa per full power year (fpy) is rather small: 500 cm³ [Moe06]. The volumes of the medium flux region (1 – 20 dpa/fpy) with 6,000 cm³ and of the low flux region (< 1 dpa/fpy) with more than 1 m³ increase accordingly [Moe06]. Therefore, a research program on specimen miniaturization was set up for determination of various bulk mechanical properties in a space-saving manner [Wak11]. Publication F, dealing with micrometer-sized fracture experiments will address this topic again.

[2] Axially Symmetric Dicertor Experiment at Garching (Munich), www.ipp.mpg.de

[3] Tokamak Experiment for Technology Oriented Research, www.fz-juelich.de

[4] Experimental Advanced Superconducting Tokamak, For more information see [Wu07]

[5] Joint European Torus, www.jet.efda.org

1.2. Tungsten Materials for Fusion

> *"It is now clear to all that our original beliefs that the doors into the desired region of ultra-high temperatures would open smoothly at the first powerful pressure exerted by the creative energy of physicists have proved as unfounded as the sinner's hope of entering Paradise without passing through Purgatory."* Lev Andreevich Artsimovich at the IAEA Conference on Plasma Physics and Controlled Nuclear Fusion at Salzburg, Austria, September 1961 [IAE62]

1.2.1. Paradise

Tungsten and tungsten-based materials feature several advantageous properties, which make them very interesting for fusion applications. Important beneficial properties of tungsten are: a high melting point (3422°C [Nag91]), a good thermal conductivity, high creep resistance, high-temperature strength, low vapor pressure ($1.3*10^{-7}$ Pa at T_{melt} [Smid98]), a high threshold energy for physical sputtering, hence a low sputtering yield, low tritium retention and a low hydrogen solubility. In addition, the decay time for activation products is comparatively short. Noda et al. [Nod89] listed tungsten together with titanium, vanadium and chromium as materials of low induced activation. What has to be categorically kept in mind when discussing the material's properties of tungsten is the strong dependence of some properties on testing conditions – especially strain rate and testing temperature – but also on the processing history and, thus, on the microstructure of the material. Regarding fracture properties, the ratio of transcrystalline / intercrystalline fracture, ductile-to-brittle transition temperature (DBTT) and fracture toughness experience severe influences from the microstructure (grain size, grain aspect ratio, dislocation density, etc.). For a summary of physical properties of tungsten being independent from microstructure, the reader is referred to appendix II in [Pink89].

1.2.2. Purgatory

A general problem of materials exposed to high neutron fluxes, which are inevitably for actual fusion power plant technologies, is that the chemical composition of these materials is not constant. Fast neutrons, products of Equation (1), transmute atoms of the surrounding matter and induce radioactivity. This leads not only to heavier atoms, quite possibly radioisotopes, but also to the formation of lighter elements such as hydrogen and helium. This topic is less of a problem for ITER, as it experiences a low amount of irradiation damage. The facility will not be as trimmed for acceptable productiveness and a low number of downtimes as it is expected from first generation

fusion power plants. Nevertheless, one has to be aware that the materials composition of materials changes with time. According to [Nod98], the integrated cross section – considering all natural isotopes of tungsten – for the (n,γ)-reaction is higher than for the (n,2n)-reaction. Thus, tungsten tends to transmute to heavier elements (Re, Os). For the divertor region, Cottrell [Cot04] calculated the transmutation of pure tungsten into 75.1 at% of tungsten, 12.8 at% of osmium and 11.9 at% of rhenium after five years (Figure 1-3). These calculations are based on the assumption of irradiating a tungsten wall with 14 MeV neutrons with a wall loading of 2 MW m^{-2}. Linear extrapolation of the W-Os and W-Re phase diagrams to a ternary phase diagram shows that this composition could be close to the pure sigma phase, a brittle and hard component [Hall66]. Compositional changes in ITER are small [Cot04]: about 2 at% of Re and less than 1 at‰ of Os. Transmutation does of course not just take place for pure tungsten, but also has to be considered for tungsten as an alloying element in certain types of steels.

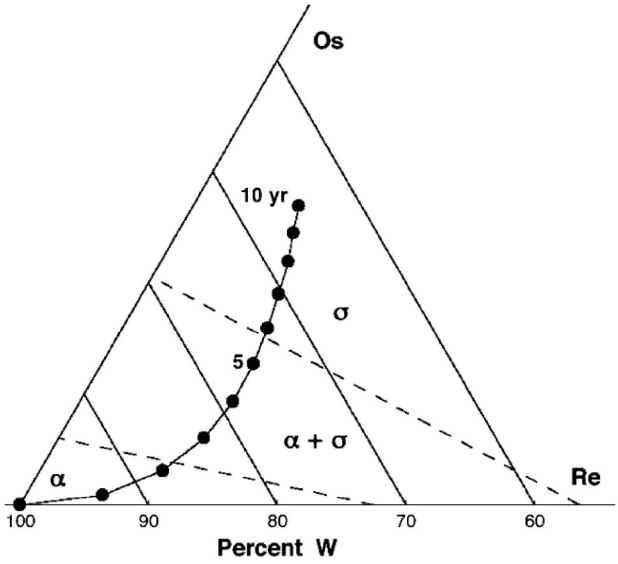

Figure 1-3: Due to irradiation of a pure tungsten wall with fast 14 MeV neutrons, transmutation of tungsten into rhenium and osmium takes place, approaching and entering the sigma phase field with increasing operational time. Ternary phase fields are extrapolated from binary phase diagrams. Taken from [Cot04].

Gilbert and Sublet recalculated transmutation induced changes in materials composition according to the neutron energy spectra expected for ITER and a conceptual nuclear power plant [GilMR11]. These calculations also take into account resonance self-shielding – the cross sections for neutron reactions of different isotopes are not constant with changing neutron energy but show giant resonances at low neutron energies. Consideration of this self-shielding effect leads to a marked decrease in the transmutation rate in comparison to older work of Gilbert [GilMR10], which is a paper cited in Publication C and [Cot04]. Consequently, the material's composition, when starting from pure tungsten, is not as close to the sigma phase field after five years of power plant

operation as was stated before. The atomic concentration of transmutation products in ITER after 14 years of scheduled operation is lower by more than an order of magnitude in comparison to the nuclear power plant after five years of operation. A fact that remains unchanged is the increased production of hydrogen and helium in light alloying elements (Ti, V) in comparison to heavy elements (Ta, W, Re), this is despite a lower overall transmutation rate of these lighter elements. A way that is proposed by Gilbert and Sublet [GilMR11] is to alter the type and quantity of the resulting transmutation isotopes and to tailor the concentration of isotopes in the starting materials. As outlined there, the tungsten isotope ^{183}W would result in the lowest possible amount of transmutation products after five years of power plant operation.

A point to be aware of is that the atoms being present after the transmutation process are not necessarily stable. Of concern are the long-living radioisotopes are when questioning decommissioning of fusion facilities and disposal of radioactive waste. The rhenium radioisotopes ^{186m}Re and ^{186}Re mainly govern the long-term induced radioactivity of tungsten; however, they “are not significant from the viewpoint of safety activity level” [Nod98].

The applicability, the useful operation temperature window of tungsten and tungsten-based materials is principally confined by two limits. The lower bound is given by the ductile-to-brittle transition (DBT) and recrystallization prohibits usage at very high temperatures due the to accompanying change of microstructure and increasing brittleness. The existence of a DBTT well above room temperature constitutes a problem in case of recurring temperature changes; any damage (erosion, cracking, melting) done to the material during high heat loading might become fatal in the case of cooling down. Thermal stresses in flaw-containing components might lead to their immediate failure. Neutron irradiation tends to increase the DBTT, but the interrelations of ductility, fracture and irradiation are far away from being completely understood. This brings us back to the need for IFMIF, investigating the materials’ response to high flux neutron irradiation. Before going on with outlining the influence of irradiation on tungsten, it should be mentioned that a description of DBTT is not easy. As will be discussed in Section 1.4., DBTT is not a simple material constant but especially depends on strain rate, hence, on the type of experiment used. A rather large difference will become obvious in comparing impact-like Charpy tests and Three-Point Bending (3PB) and Four-Point Bending (4PB) experiments of much lower strain rates. In addition, the situation gets more complicated: irradiation experiments, preceding to mechanical tests, can be made using different neutron spectra, fluences (particles per area), fluxes (particles per area and time) and irradiation temperatures. A higher irradiation temperature tends to heal irradiation-induced defects but can also change the type of defects created. Furthermore, DBTT can be defined in many different ways. In the next paragraph, the transition temperature will be determined via the results from tensile tests. Krautwasser et al. [Kra90] defined the DBTT as the temperature where a 3PB specimen could be bent to an angle of 90°. In contrast, in Section 1.4. DBTT will be defined by the fracture behavior of tungsten. More precisely, it will be determined from an increase in fracture toughness with increasing temperature, respectively a change from brittle to ductile

material's response in a fracture experiment. Hence, one has to be careful when comparing values of DBTT even for the same material.

Younger and Wrights irradiated tungsten with neutrons at a maximum irradiation temperature T_{irr} of 122 °C, being rather low, and neutron energies of more than 1 MeV, described in [YouCL70]. They outline that the DBTT, defined as the temperature where 40% of reduction in area during tensile tests occurred, increases with increasing neutron fluence. In addition, the temperature range of this transition becomes smaller with increasing fluence. Non-irradiated material had its DBTT at 316 °C. Up to irradiation with fluences of $1.2*10^{20}$ neutrons cm^{-2}, the DBTT increased by 28 °C for each increase of $1*10^{19}$ neutrons cm^{-2}. At the highest neutron fluence of $1.53*10^{20}$ neutrons cm^{-2}, DBTT was found to be at 794 °C. Megusar and Garner [Meg98] also detected, by handling the specimens, an extreme embrittlement of pure tungsten when irradiating it at a maximal neutron fluence of $1.44*10^{23}$ neutrons cm^{-2} (423 °C < T_{irr} < 600 °C) but did not present any experimental data on mechanical behavior. Further results [Ale79, Kra90] confirm an increase in DBTT with neutron fluence (Figure 1-4). Alloying with rhenium, thereby ductilizing the material in the unirradiated condition (see Section 1.5.1), is detrimental in the irradiated state according to results presented in the figure. The tungsten-based heavy metal Densimet, also presented there, is not suitable for fusion applications because of its nickel content. Unfortunately, a binder phase consisting of pure iron does not seem to be feasible.

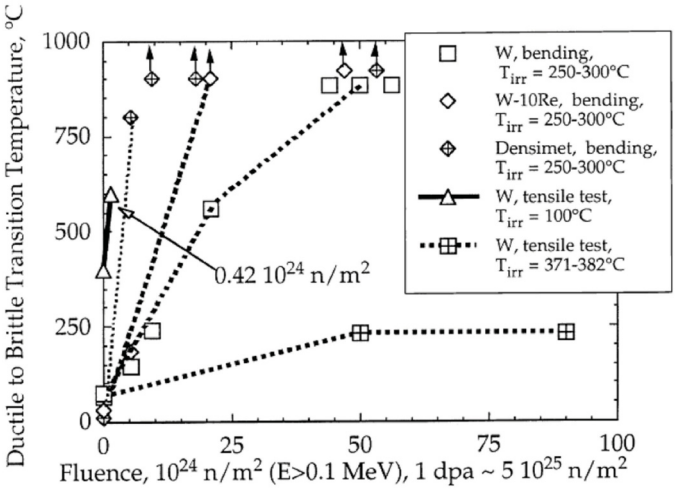

Figure 1-4: Neutron irradiation induced embrittlement of several tungsten-based materials (W, Densiment W3.4Ni1.6Fe, W-10%Re), diagram taken from [Bara00], data from [Ale79, Kra90]. Neutron fluences are rather low in comparison to DEMO- and power-plant-relevant conditions.

Barabash et al. [Bara00, Bara03] summarize the interaction of neutrons with plasma facing materials (Be, C, W) and its consequences. They outline that the neutron irradiation in ITER equivalent to 0.3 MW*a m^{-2} causes irradiation damage of about 0.3 dpa to 0.5 dpa [Bara00] or 0.1 dpa [Bara03] in case of exchange of divertor cassettes, respectively. Due to an increasing number

of transmuted atoms [Tan09] and these lattice defects, electrical conductivity is decreased and, according to the Wiedemann-Franz law (Equation (3)), thermal conductivity is reduced.

$$\frac{\text{thermal conductivity}}{\text{electrical conductivity}} = \text{const} \times \text{Temp.} \tag{3}$$

Tanno et al. [Tan09] further describes neutron irradiation of different W-Re and W-Os alloys between 0.17 dpa and 1.54 dpa and temperatures ranging from 400 °C to 750 °C. The increase in thermal conductivity is more pronounced for increasing alloying elements and to a lesser extent governed by irradiation induced defect generation. The irradiation temperature is of course a very crucial parameter; annealing rate of irradiation-induced defects will be higher at high temperatures. Summarizing for ITER, the rates of generation of transmutation products and changes in conductivity are low. A further important thermo-mechanical parameter is the coefficient of thermal expansion. The large mismatch of tungsten's thermal expansion coefficient ($\alpha_W \approx 4.5*10^{-6}$ [Smit76]) to possible structural materials (e.g. steel) will be addressed in the appended Publication C.

An easier addressable topic compared to neutron irradiation induced changes in materials' properties is the behavior of tungsten, and plasma facing materials in general, under high thermal loadings. The maxima of steady state heat loads are in the regime of 5 to 20 MW m^{-2}, which is less compared to a rocket nozzle of a European Ariane 5 rocket (85 MW m^{-2} [Lin11]). However, plasma-facing components should operate for years while rocket nozzles have a much shorter lifetime. In addition to steady heat load, transient events such as disruptions, vertical displacement events (VDE) or edge localized modes (ELMs) will also take place [RafAR10].

Considering ELMs, which are recurring instabilities of the plasma [Reb05, Con98]: energy of more than 1 MJ m^{-2} is deposited in short times of less than 1 ms and at frequencies of 1 Hz to 30 Hz. In other words, these ELMs deposit thermal loads in the regime of GW m^{-2}. More than 10^6, maybe up to 10^7 ELMs are expected to occur during the operational lifetime of the ITER divertor, which is set up for 3000 pulses with pulse duration of 400 s each [Lin11]. ELMs represent high cycle thermal fatigue loads superimposed to the low cycle thermal fatigue loads from the 3000 operational pulses. The high amount of energy deposited during ELMs in a very short time leads to a rapid increase of the surface temperature. Thereby, the material experiences elastic and plastic deformation at a high strain rate and an increase of DBTT (see Section 1.4). These high heat loads lead to surface roughening, cracking and melting, which will be discussed in the next paragraphs.

Several types of testing facilities such as electron beam guns [Fuj96, Hira09, Pint11a, Uyt07], quasi-stationary plasma accelerators [Gark05, Wit09, Zhit07] or lasers [Ued05, Ums09] exist in order to simulate the influence of ELM-like heat loadings on tungsten materials. Summarizing the cited references, there is an influence of the tungsten microstructure and material's composition on the temperature and energy threshold of cracking. Below a certain heat load and above a certain

base temperature of the irradiated material, the stress imposed by the transient heat loads stay in the elastic regime. Therefore, no crack formation can be found in this regime; at lower temperatures and higher absorbed power densities surface modifications and cracks appear [Pint11a]. The alignment of the grains in respect to the heat loading direction is very important: cracking of grain boundaries for a microstructure that is aligned along the direction of heat transfer (from plasma facing to cooling) would not lead to an immense decrease in heat transfer capability, but it would in case of cracks perpendicular to the heat loading direction.

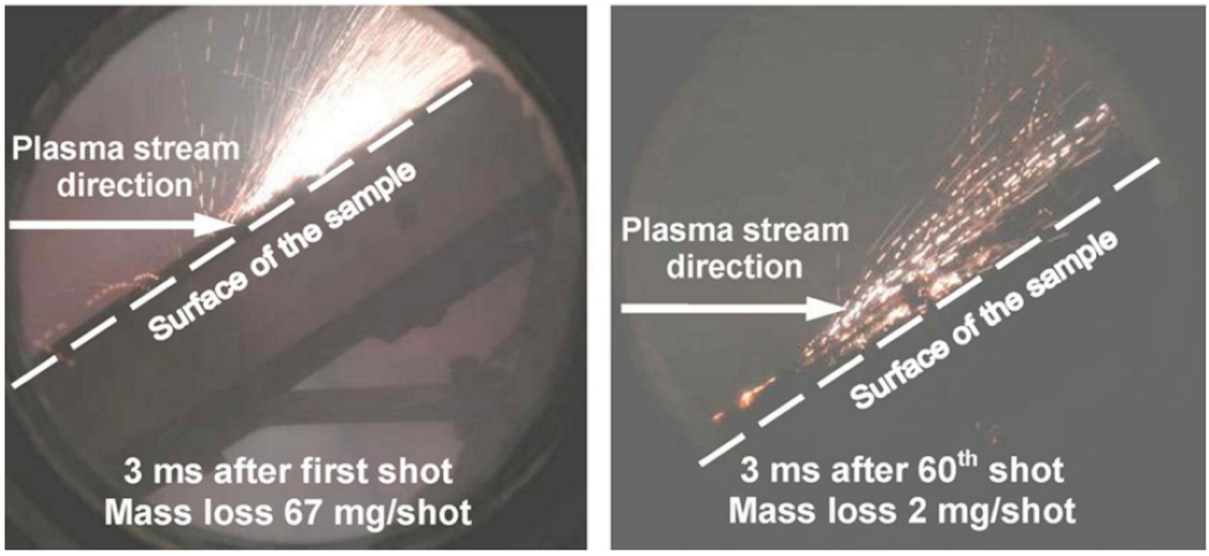

Figure 1-5: Photographs of tungsten specimens in a quasi-stationary plasma accelerator, showing the loss of tungsten material by droplet formation at an energy density of 1.6 MJ m^{-2}. Left: first plasma shot. Right: 60^{th} plasma shot, less tungsten is lost compared to the first shot due to a smoothening of surface edges. Pictures are taken from [Zhit07].

Uytdenhouwen et al. [Uyt07] demonstrated a better thermal shock resistance of tungsten in its sintered state compared to as-worked tungsten, while recrystallization degraded the properties in both cases. At higher thermal loadings, melting and re-solidification occur and melt layer movement along the plasma stream or perpendicular to it due to magnetic forces might bridge castellations of tungsten components. These castellations are necessary in plasma facing components to cope with the differences in thermal expansion of tungsten and the heat sink made of copper (ITER). At higher power densities, erosion of the melt layers takes place, melt droplets are ejected (Figure 1-5), contaminating plasma's outer layer and possibly even the plasma core [Wit09, Zhit07]. To get a glimpse of the dimensions shown in Figure 1-5, the specimen sizes used in [Zhit07] were 9.5 x 9.5 x 3 mm^3 and 19.5 x 19.5 x 3 mm^3, respectively.

Fujitsuka et al. [Fuj96] irradiated different tungsten based materials including W-5wt%Re and W-25wt%Re with a high current of low energy electrons. In contrast to superior mechanical properties of tungsten alloys containing rhenium – as will be outlined in Section 1.5.1. – the erosion behavior of W-25wt%Re is inferior to pure tungsten; the damaged area is large and weight losses are high. This might be related to the significantly lower thermal conductivity.

Recent, not completed and unpublished experiments by Pintsuk et al. [Pint11b] indicate an increased thermo-shock resistance of fine-grained tungsten with TiC dispersoids strengthening the grain boundaries (see Section 1.6.1.). This is due to an optimum combination of tungsten grain size, TiC dispersoid size and TiC amount and distribution. Similar results can be expected for other strengthening additions, e.g. for Y_2O_3.

A fact that has to be mentioned is the increasing price of tungsten raw materials. The price of tungsten oxides and ammonium paratungstate increased by about 100% within the last year [www11a]. The question arises to what extent this increase in tungsten price is artificially made and what comes from a shortage of raw materials. So, will there be enough base material to produce more than 400 power plants, to replace all fission power plants [IAE11]? To get an idea of the amounts of material needed, 53 tons or a bit less than 3 m^3 of tungsten will be used for the ITER divertor [Hira11].

1.3. Fracture Mechanics – A short introduction

Fracture mechanics is a rather young, but important part of materials science investigating the mechanical behavior of materials and components containing defects. This part of the introduction shall give a short summary of the most important fracture mechanical approaches. Fracture mechanical properties are determined from e.g. standard tension, compression and bending samples containing artificial defects. Sample geometries used in this thesis for fracture experiments are:

- Three Point Bending (3PB)
- Compact Tension (CT)
- Round Compact Tension (RCT)
- Micrometer sized cantilevers

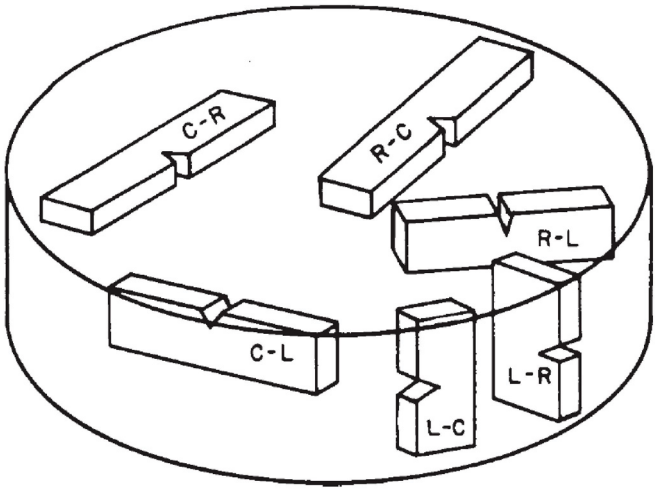

Figure 1-6: Code for describing crack plane and expected direction of crack propagation according to ASTM E 399-90 [AST90]. taken from [AST90].

It is of great importance – especially for tungsten and tungsten alloys – to know the spatial arrangement of the crack, which can be represented by its expected crack propagation direction and its crack plane normal, both in relation to the microstructure. The American Standard for Plane-Strain Fracture Toughness Testing of Metallic Materials ASTM E 399 [AST90] recommends to describe the crack system by a two-letter code. In the case of producing fracture specimens out of a bar – the material assumably of as-worked and hence elongated microstructure – the first letter of this code represents the normal of the crack plane and the second letter the direction of expected crack propagation. C stands for circumferential, R for radial and L for longitudinal direction. Some sample alignments are shown in Figure 1-6 for a cylinder (rod material). For materials not showing this elongated grain structure after rolling and drawing, other descriptions and codes can be defined [AST90, HohA10, Wur11]. In case of material deformed by High Pressure Torsion (HPT),

where the deformation takes place by shear, another code was used to account for the peculiarities of the microstructure present after this type of deformation as will be described in Publication C.
Based on the applicability of linear elastic fracture mechanics (LEFM), conditional fracture toughness values K_Q for different sample types are calculated the using following equations [AST90]:

$$K_Q = \frac{P_Q * S}{B * W^{3/2}} f(a/W) \tag{4}$$

$$f(a/W) = \frac{3(a/W)^{1/2}[1.99 - (a/W)(1-a/W)(2.15 - 3.93(a/W) + 2.7(a/W)^2]}{2(1+2a/W)(1-a/W)^{3/2}} \tag{5}$$

for 3PB – specimens,

$$K_Q = \frac{P_Q}{B * W^{1/2}} * f(a/W) \tag{6}$$

$$f(a/W) = \frac{(2+a/W)(0.886 + 4.64a/W - 13.32(a/W)^2 + 14.72(a/W)^3 - 5.6(a/W)^4}{(1-a/W)^{3/2}} \tag{7}$$

for CT-specimens,

$$K_Q = \frac{P_Q}{B * W^{1/2}} * f(a/W) \tag{8}$$

$$f(a/W) = \frac{(2+a/W)(0.76 + 4.8a/W - 11.58(a/W)^2 + 11.43(a/W)^3 - 4.08(a/W)^4}{(1-a/W)^{3/2}} \tag{9}$$

for RCT-specimens and

$$K_Q = \frac{P_Q * L}{B * W^{3/2}} f(a/W) \tag{10}$$

$$f(a/W) = 4 * \frac{3(a/W)^{1/2}[1.23 - (a/W)(1-a/W)(-6.09 - 13.96(a/W) + 14.05(a/W)^2}{2(1+2a/W)(1-a/W)^{1/2}} \tag{11}$$

for micrometer sized notched cantilevers [Wur10a].

S represents the span width of 3PB samples, *L* the bending length of cantilevers, *B* the specimen thickness, *a* the crack length and *W* the specimen width. The values, which were taken for the force P_Q (e.g. first load drop, maximum force) are described for each set of experiments within this thesis. Equations (10) and (11) for micrometer-sized and FIB-notched cantilevers are based on finite element computer simulations using ABAQUS software, they are described in detail in Publication E. It will be shown that the results are in good agreement with the evaluation of 3PB-experiments according to ASTM E 399 [AST90]. In addition, a matching comparison with other

solutions for the geometry function *f(a/W)* found in Murakami's Stress Intensity Factor Handbook [Mura87] will be presented in Section 2.5.

To perform valid evaluation of K_{IC} based on Equations (4) – (11), several requirements have to be fulfilled, e.g.:

$$B, a > 2.5 \frac{K_{IC}^{\ 2}}{\sigma_y^{\ 2}} \tag{12}$$

σ_y is the 0.2% offset yield strength of the material at the temperature of the fracture experiments, K_{IC} is the plane strain fracture toughness in crack opening mode I. Equation (12) takes into account that the specimen has to be significantly thicker than the plastic zone which develops in front of the crack tip. The right side of Equation (12) is proportional to the plastic zone size, which is a region where plastic deformation and other irreversible processes due to the high stresses take place. This region originates from singularities of stress fields close to cracks, flaws and defects being inevitably present within samples and components. They act as stress concentrators and the stress field close to the crack tip can be described in an ideal linear elastic case by

$$\sigma_{ij}(\Theta, r) = \frac{K}{\sqrt{2\pi r}} f_{ij}(\Theta) + O(r)\,. \tag{13}$$

K is the stress intensity factor, *i* and j represent *x* and *y* in a two-dimensional coordinate system. *r* and Θ are polar coordinates. Within these coordinate systems, the crack is located at the negative x-axis (Θ = π) and the crack propagation direction is along the positive x-axis (Θ = 0). The situation in front of a crack tip, including different loading conditions, is represented in Figure 1-7. Terms of higher order do not significantly influence the stress field close to the crack tip, which is ideally described with a crack tip radius of zero. The dimensionless function $f_{ij}(\Theta)$ accounts for the type of loading.

What simplifies linear elastic fracture mechanics is the existence of *K* – the stress intensity factor – completely describing the stress field around a crack tip, at least for a distinct loading condition. Three loading conditions, mode I, II and III are discriminated. Mode I leads to crack opening; forces normal to the crack plane are applied. In mode II and mode III, the crack surfaces slide against each other, for mode II shear is applied within the above-mentioned x-y-plane (Figure 1-7). For mode III, shear is applied out of this plane. In case of loading a flawed component, a real crack respectively, the loading will most certainly reflect a superimposition of two or three modes.

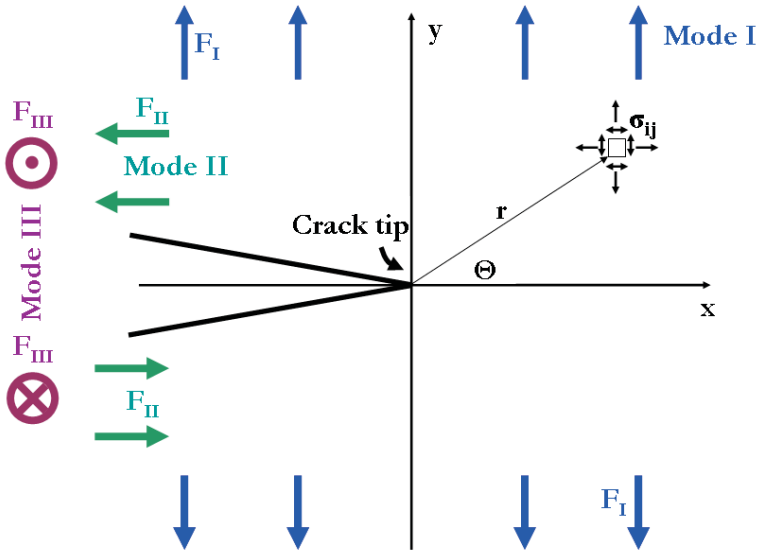

Figure 1-7: 2D – description of the situation in front of the crack tip using both, the *x*-*y* and *r*-*Θ* coordinate system. The application of forces for achieving pure Mode I (blue), Mode II (green) in paper plane and Mode III (purple) out of the paper plane, respectively are also indicated.

In case irreversible processes take place at a stress lower than the fracture stress, there exists a certain distance x_y in front of the crack tip, where an equivalent stress which can be obtained from the stresses σ_{ij}, indicated in Equation (13), reach the yield strength, as they increase with $x^{-1/2}$ when approaching the crack tip. Hence, it is obvious that the plastic zone is determined (in Equation (12)) solely by a critical stress intensity K_{IC} and the yield strength – which is in a more general case replaceable by any other stress value indicating the first occurrence of irreversible processes (phase transformations, micro-cracks, secondary cracks, friction and interlocking, etc. [Pip]). The crack length, *a*, and the length of the ligament, *W*-*a*, have to be significantly larger than the plastic zone. This is to ensure that the fracture process and the *K*-dominated field are not affected by the plastic zone. Consequently, in case of fracture at a certain load, a critical stress intensity factor (K_{IC}, K_{IIC}, K_{IIIC}, whereas $K_{IC} \neq K_{IIC} \neq K_{IIIC}$) can be derived. This critical value K_C is depending on loading conditions; it is a material constant and independent of the sample shape.

Going back to Equation (12), the thickness of the sample has to be larger than the plastic zone size in order to realize plane strain conditions within the largest part of the sample. On the free specimens' surfaces, the plastic zone is determined by plane stress conditions defined by $\sigma_{zz} = 0$. Plane strain conditions in the interior are defined by $\sigma_{zz} = \nu\,(\sigma_{xx} + \sigma_{yy})$.

Another way to analyze fracture processes is based on an energetic approach; however, it is equivalent to the *K*-approach. The potential energy *U* stored within the sample is given by the stress- and strain fields and by external forces. A change in potential energy is compared to the energy needed for generation of two new surfaces. The energy per area *G* that is released upon crack propagation for an infinitesimal distance *da* is given as

$$G = -\frac{dU}{da}. \tag{14}$$

Hence, *G* is called energy release rate; rate refers to the newly generated fracture surface and not to time. With increasing loading, the energy that would be released approaches a critical value G_C, where in its simplest case – just breaking of atomic bonds – the surface energy $\gamma_{surface}$ is considered; this does not take into account irreversible processes.

$$G_C = 2\gamma_{surface} = R \tag{15}$$

R is the crack resistance, which is the energy that has to be released in order that crack propagation takes place. Irreversible processes can be accounted by the term $\gamma_{irreversible}$:

$$\gamma_{total} = \gamma_{surface} + \gamma_{irreversibe} \tag{16}$$

The relationship between *K* and *G* is for mode I loading under plane stress:

$$G_I = \frac{K_I^{\,2}}{E} \tag{17}$$

and

$$G_I = \frac{K_I^{\,2}(1-\nu^2)}{E} \tag{18}$$

for plane strain with *E* being the Young's modulus and ν the Poisson's ratio. Again, distinctions for different loading conditions (I, II, III) have to be made.

Linear elastic fracture mechanics cannot be applied when regions that are affected by non-linear elastic behavior span large volumes within the sample. Fracture is not described by the K-dominated zone anymore; elastic-plastic fracture mechanics concepts are needed. Considering ductile material, large volume fractions of the samples might experience plastification, the crack tip blunts and at a certain load the crack will propagate, but this process is now governed by the plastic zone. For tungsten, this change takes place when testing small samples at room temperature or when experiments are conducted at higher temperatures, where the fracture

toughness increases and the material's strength decreases. This lead to an increase in plastic zone size (Equation (12)). A way to describe this situation was proposed by J.R. Rice [Rice68a]. A path-independent line integral along a curve Γ – the J-integral – going around the crack tip describes the conditions at the crack tip.

$$J = \oint_{\Gamma} \left[\left(\int_{0}^{\varepsilon_{ij}} \sigma_{ij} d\varepsilon_{ij} \right) dy - \sigma_{ij} n_j \frac{\partial u_i}{\partial x} ds \right]. \tag{19}$$

ε_{ij} and σ_{ij} are the strain and stress tensors, n_j the components of the normal vector on the curve Γ and u_i the components of the displacement vector. Again, J can be used to describe stress and strain fields and their singularities close to the crack tip – as it was the case for K. The region around the crack is now governed by the HRR-field, named after Hutchinson [Hut68] and Rice & Rosengren [Rice68b], who first showed that the conditions around the crack tip can be described by J.

The value of this integral can be determined experimentally by taking into consideration areas within the force – displacement – diagram recorded during the fracture experiment, the sample geometry and geometry factors. However, for identifications of a critical J-value, it is necessary to derive J as a function of crack propagation. This can be done either by applying a single specimen technique – as it will be described in Publication F – or by using the multiple specimens technique. Crack propagation, which necessarily has to be observed for the single specimen technique, can either be deduced from a decreasing compliance of the specimen or from direct observation or by the potential drop method. The decreasing compliance is determined by repeated unloading. For the potential drop method, the electrical resistance of the specimen increases with decreasing ligament length *(W-a)*. This method is hardly feasible for samples on the micrometer scale, as several electric connections to the specimens would be necessary. The multiple specimen approach for determination of J_c was also not deemed applicable to the research performed at micrometer-sized samples, as it involves testing of many samples up to various crack propagation lengths. As will be shown in Publication F, unloading procedures during in-situ experiments are a practicable way to determine elastic-plastic fracture parameters at the micrometer scale.

1.4. Fracture Behavior of Tungsten

Within the last five decades, tungsten based materials were subjected to varying scientific attention; the number of published papers seems to correlate to the number of proposed applications of tungsten. As outlined in Section 1.2., the environment to which tungsten materials are planned to be exposed to in future fusion power plants is rather harsh. The low toughness of tungsten at low temperatures – leading to brittle fracture – is one of the main drawbacks regarding the usage as plasma facing material. Such brittle fracture is dangerous to any component, as it would lead to failure at relatively small load. Thus, understanding the fracture behavior is an important issue when judging the (non-) applicability of any material, forecasting its load at fracture, (fatigue) lifetime and security aspects of flaw-containing materials. Hence, the fracture behavior of tungsten, especially single crystalline tungsten serving as a model material, was and still is of great interest [Arg66b, Bea65, Cor72, Gia07, Gum98, Hul65, LiuJM83, Ried94, and Ried96]. Before going on with this chapter, it should be mentioned that there is an elaborate review by Gumbsch discussing brittle fracture and the ductile-to-brittle transition [Gum03].

Tungsten single crystals preferentially cleave on {100} planes [e.g. Hul65, Bea65, Sch65, Ried94]. Liu and Shen [LiuJM83] tried to introduce cracks on {110} and {111} planes by electrical discharge machining, but they did not succeed for planes different from {100}. Hull et al. [Hul65] used single crystalline samples of arc-melted tungsten, which was purified by zone melting, for tensile experiments. Purification by zone melting relies on subsequent passes of the desired material through a high-heat zone and is also applicable to high-melting point materials [Gea59]. In [Hul65], {100} planes constitute all specimens' surfaces. The samples were pre-cracked by a spark-machining technique on (010) planes. During tensile testing in [010] direction, the specimens cleave on the same crystallographic plane where the crack was introduced. Samples that were fractured at room temperature and above showed signs of slow crack growth, preceding to catastrophic cleavage fracture. The amount of slow crack propagation increased with increasing temperature. Cordwell et al. [Cor72] expanded the investigations of cleavage as a function of crystallography to samples having the tensile axis oriented along <110>. Starting cracks, produced again by spark discharges, were located on {100} planes, and after fracture significantly more {100} cleavage planes were found than {110} planes.

According to stress vs. elongation curves found in [Hul65], a certain amount of plastic deformation took place even when testing at room temperature, at least at a low strain rate of $4*10^{-4}$ s^{-1}. Tensile tests using polycrystalline tungsten (grain size: 30 µm to 50 µm) performed by Wronski and Fourdeux [Wro64] starting from swaged and annealed single crystals showed an increase of the onset of detectable plastic deformation to 60 °C to 100 °C. The strain rate of $8.4*10^{-5}$ s^{-1} was even lower than in [Hul65].

Beardmore and Hull [Bea65] investigated single crystalline tensile samples of [110]- and [111]-tensile orientations – not having spark-machined pre-cracks. The authors report a strong dependency of yield strength and work hardening on crystallographic orientation and temperature. Cleavage planes were again of {100} type in most of the cases. The persisting appearance of cleavage on {100}-planes is somewhat odd. In case of pure brittle fracture the relation of the energy release rate *G* with generation of two new surfaces would result in preferred cleavage of closer packed {110} planes. However, this approach does not take into account any plasticity. Kohlhoff et al. [Koh91] explained the preferred cleavage on {100} planes by a larger number of orthogonal and easy crack propagation direction in relation to {110} planes. Easy crack propagation is achieved for both planes when the crack front is of <110> direction, tough directions have a crack front of <100> type, which was determined experimentally by Riedle et al. [Ried96]. In the case of {100}-cleavage, the tough directions enclose an angle of 45° to easy directions, the crack can thus changes more easily into a crack having crack front components along <011>. This is not accomplishable for cleavage on {110} planes with a crack front in a <001> direction, as the angle to any easy direction would be 90°. Taking account of this importance of the crack systems, they will be denoted henceforth with {XYZ} - <ABC> with {XYZ} representing the crack plane and <ABC> the crack front direction.

Tungsten features a ductile-to-brittle transition (DBT) typical for body centered cubic (bcc) metals. This means that the material fails by brittle fracture at low temperature and becomes tougher when approaching and beyond the ductile-to-brittle transition temperature (DBTT). Comparing the experiments on single crystalline tungsten with results gained from different industrial tungsten products investigated by Rieth and Hoffmann [Riet10] using standardized Charpy test one has to notice that the DBTT is enormously shifted to higher temperatures with increasing strain rate. For polycrystalline pure tungsten samples, brittle fracture still occurs at 500 °C, the upper shelf of Charpy impact energy is reached for testing temperatures of 900 °C. The increase in transition temperature with increasing strain rate was comprehensively investigated by Giannattasio and Roberts [Gia07] using single- and polycrystalline tungsten. Pre-cracked four-point-bending (4PB) samples were loaded with strain rates varying over three orders of magnitude and at temperatures ranging from -196 °C to 277 °C. The low temperature fracture toughness of (2.7 ± 0.2) MPa $m^{1/2}$, which was independent of strain rate, coincides with the results from Riedle et al. [Ried96], which was (3.4 ± 0.6) MPa $m^{1/2}$, measured at -196 °C . Both investigations used tungsten single crystals oriented for a {100}-<001> crack system. As outlined in [Ried96], the crack system {100}-<011> gives the lowest fracture toughness values for 77 K and room temperature. They also investigated several other crack systems containing the {110}-plane, namely {110}-<001> and {110}-<1$\underline{1}$0>. Both crack systems had a higher fracture toughness at room temperature; at very low temperatures (-196 °C) the toughness levels are comparable.

Coming back to the fracture experiments of Roberts et al. [Gia07]: as depicted in the Arhenius plot shown in Figure 1-8, DBTT increases with an inverse linear relationship with increasing logarithm of strain rate. Differences in poly- and single crystalline materials appear to be insignificant. The activation energy for the transition was determined to be (1.05 ± 0.05) eV, which is five times higher than the value of 0.2 eV found by Gumbsch et al. [Gum98] using {110}-<1$\underline{1}$0> single crystals. The latter group explains the low values by the existence of two different mechanisms controlling either crack tip plasticity and bulk plasticity, whereas [Gian07] attributes the lower value rather to the glide of pure edge dislocations that would be possible according to the samples' crystallography. Taking 1.05 eV for the activation energy of the DBT, this correlates well with the effective enthalpy for the formation of kink pairs in screw dislocations. For bcc metals, screw dislocations are slower than edge dislocations at low temperatures, therefore they govern the expansion of dislocation loops and the emission of dislocations close to or at the crack tip. Formation of such kink pairs eases the movement of screw dislocations; as it is not necessary to move the whole screw dislocation at once. Rather the screw dislocation overcomes the Peierls potential only over a restricted length along the dislocation line, the rest of the dislocation follows later.

Care has to be taken when defining the DBTT for fracture. In [Gian07], DBTT is linked with non-fracturing of samples after plastic strains of more than 5%, while in [Gum98] this temperature is associated with the maximum in toughness. However, the latter point is more likely related to the sample size.

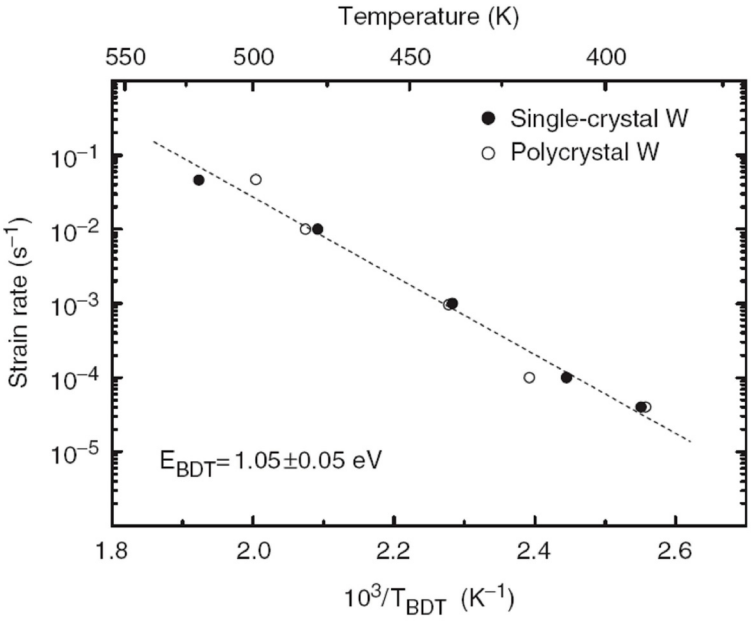

Figure 1-8: Arrhenius plot of strain rate vs. 1/DBTT. Taken from [Gia07].

Tarleton and Roberts [Tar09] explain the occurrence of a marked transition from ductile to brittle behavior by the stress fields from emitted dislocation, which shields the crack tip, and reduces the stress intensity K_{tip} at the crack tip due to external loading. Cleavage fracture takes place when this K_{tip} reaches a critical value, $K_{Griffith}$ (K_G). Dislocation sources close to the crack tip are activated due to the high stresses (Equation 13) and the crack tip itself can also serve as a source for dislocation as it was shown by Hirsch et al. [Hirs92],

In [Tar09] it was assumed that the emitted dislocations move on two slip planes ±45°, symmetrically inclined to the crack plane. Once a dislocation is emitted, back stresses act on the dislocation source and further dislocation nucleation is shut down until the emitted dislocation moves a certain distance and the stress acting on the dislocation source declines. The results presented in [Tar09] are based on a two-dimensional dislocation dynamics model, where the mobility of these emitted dislocations is governed by the double-kink nucleation mechanism. In the case that K_{tip} does not reach the value of K_G, either because of a high testing temperature (DBTT) that increases the dislocations' velocity, and/or a low strain rate that allows the dislocation to move away from the crack tip, the material is regarded to be ductile. For an increased strain rate, the fast increase of K_{tip} has to be overcome by more and faster dislocations, i.e. by decreases in shutdown time of sources, thus requiring a higher testing temperature.

1.5. Tungsten-based Alloys

1.5.1. Tungsten – Rhenium Alloys

Rhenium, having a hexagonal-close-packed (hcp) crystal structure, has the highest melting point (3186 °C) of all metals except of tungsten (3422 °C). The highest solubility of rhenium in tungsten is about 37 at% at a temperature of 3000 °C, it declines to 27.5 at% at a temperature of 1500 °C [Nag91] (Figure 1-9). Jaffee et al. [Jaf58] determined the terminal solubility to be 24 wt% to 25 wt% Re. More information on the alloy at lower temperatures is not available. When assuming a linear extrapolation of the solubility line of rhenium in tungsten, the solubility limit will further decrease, hence, the highest available tungsten-rhenium alloys (W-26Re) might be in the form of a supersaturated crystal at room temperature. Diffusion processes are not significant at temperatures below ~1000 °C (~0,4*T_{3273K}), therefore, segregation is not supposed to take place. Thus, the crystal remains in or close to a composition where it would rather transform into sigma phase. The sigma phase field becomes thinner for lower temperatures (Figure 1-8) and it might vanish for low temperatures as it happens for the sigma phase field in the Mo-Re phase diagram [Pre,a]. There, the sigma phase decomposes eutectoidally into the solid solution phase and a chi-phase. Using CALPHAD, Liu and Chang compute this narrowing of the sigma phase for lower temperatures; at about 800°C, the phase vanishes [LiuZK00]. For W-Ru and W-Ir, a disappearance of the sigma phase is also observed [Nag91].

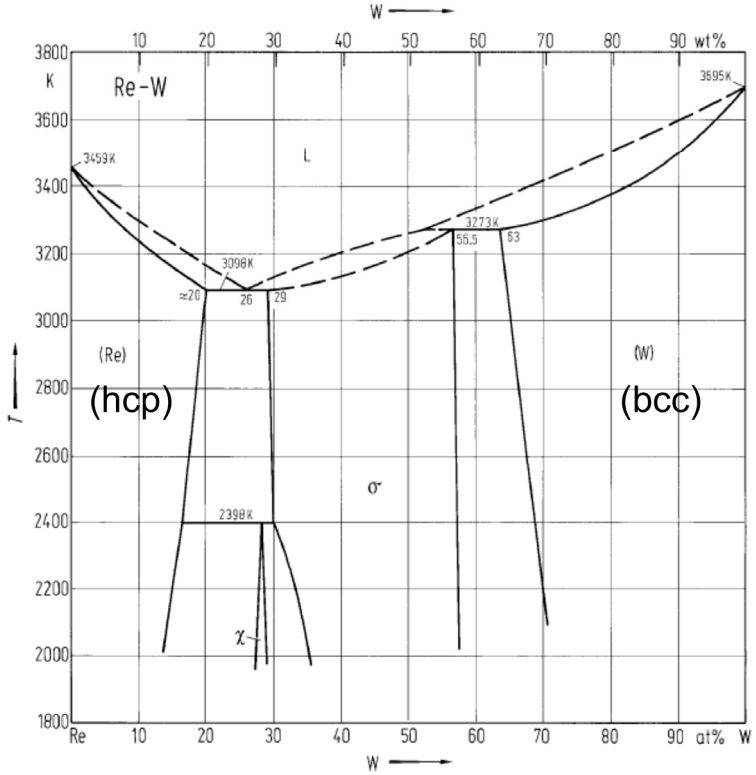

Figure 1-9: Rhenium – tungsten binary phase diagram. Taken from [Pre,b], basing on [Nag91]

Herschitz and Seidman [Her84] conducted neutron irradiation experiments on W-25at%Re (irradiation temperature 575 °C – 675 °C, $E_{neutron}$ > 0.1 MeV, 8.6 dpa) and found homogeneously nucleated WRe_3-precipitates and voids. It was assumed that helium atoms were produced by neutron interaction with impurity atoms (B, C, N, O, and S). They found a high content of rhenium very close to a grain boundary; the half width of the rhenium concentration profile crossing the grain boundary is very small and the nominal composition of 25 at% is reached within a few atomic planes. Concentration of rhenium close to the grain boundary was determined as high as 75 at%; hence, the χ-phase had formed by a radiation-induced segregation process. They conclude that the solid solution phase and sigma phase are in equilibrium at the irradiation temperature; in contrast to what was calculated in [LiuZK00]. Thus, no final statement on the appearance of a stable sigma phase field at low temperatures down to room temperature can be made.

Until the middle of last century, high-melting point materials including tungsten were used in the field of electrical components (incandescent lamps). Other applications of tungsten were rare, more often as alloying elements than in its pure form. From the mid-fifties to the mid-seventies, aerospace- and nuclear-driven research programs drastically amplified the interest in refractory metals, the number of scientific publications on this topic increased. It does not come by surprise that the advantageous effect of rhenium alloying to tungsten (and molybdenum) was published at that time. In the late fifties, several groups [Gea55, Jaf58] reported on alloys of tungsten with rhenium that have an increased high temperature strength, good machinability and ductility, which can be attributed neither to pure tungsten nor to rhenium. The discovery of this effect can be assigned to Geach and Hughes (1955) [Gea55], who found this increase in ductility (increased reduction on rolling before cracking, respectively) at room temperature with increasing rhenium content. At about 30 wt% of rhenium the ductility drops, but as the solubility limit of rhenium is a bit lower, a certain amount of brittle sigma phase seems to be acceptable.

A few years after, Booth et al. [Boo64] summarized previous work together with explanations for the ductilizing effect of rhenium alloying to group VI-A metals (Cr, Mo, W). There is a higher sustainable limit of oxygen content at least for molybdenum – rhenium is supposed to lead to a reduced wetting of grain boundaries by the formation of a complex $MoReO_4$ oxide. At low temperatures, the materials deform by mechanical twinning, but the good ductility was not attributed to this fact. Furthermore, a decrease in DBTT and an increase in resistance to cleavage fracture were found. This is contradictory to [GilA66], where a change of grain boundary fracture in unalloyed tungsten to predominant cleavage fracture for tungsten-rhenium alloys was reported. The ratio of transcrystalline to grain boundary fracture might be related to microstructural features [Glu10a], such as grain aspect ratio and testing direction rather than to the rhenium content. Without detailed knowledge of grain size, grain shape, working conditions and according testing directions in relation to this possibly anisotropic microstructure, one should be careful in drawing conclusions on trans- and intercrystalline fracture behavior. Whether the superior behavior of tungsten – rhenium alloys is determined by the relationship of solubility of interstitial impurities, the

interaction of dislocations with stress fields, changes of surface energies in rhenium alloys, increasing occurrence of twins, the vicinity to the sigma phase for high rhenium containing alloys or a change in electronic structure could not be finally determined in [Boo64]. Furthermore, Pink and Eck describe in their review [Pink96] on refractory metals and their alloys that there exist two minima in the curve showing DBTT vs. rhenium content. The first one located at low rhenium content is due to solid solution softening, which will be addressed later within this chapter. The second one is located at high rhenium contents, where it is more adequate to talk about the real rhenium ductilizing effect. First, solid solution softening vanishes for increasing rhenium alloying content and increasing testing temperature, and secondly solid solution softening was observed for other elements (e.g. tantalum [Ste70]) but only for dilute additions. As a consequence, two different mechanisms have to ductilize tungsten by rhenium additions.

Simpson et al. [Sim74] performed Auger Electron Spectroscopy (AES) studies of potassium-doped and undoped tungsten and tungsten-rhenium alloys. They did not find a systematical variation of potassium, oxygen and carbon impurity content with rhenium content when comparing Auger peak-to-peak height ratios. Klopp [Klo68] summarized a list of references (Ref. 9-15 within [Klo68]), which do not validate the hypothesis that the ductilizing effect of rhenium for VI-A metals comes from a decrease in solubility of interstitial atoms. More important might be the change of the preferred slip plane from {110} to {112}, which will be discussed in the following paragraphs.

For face centered cubic (fcc) materials slip takes place on closely packed {111}-planes, but for bcc metals, the description of preferred slip planes is not as straightforward. Due to the lack of closely packed planes, both {110}-planes and {112}-planes can serve as glide planes. In principle, glide on planes of {123}-type is also possible, but to the author's knowledge this has not been observed yet for tungsten-based materials. Several planes of each above-mentioned type intersect along <111>-zone axes. Furthermore, the glide plane does not necessarily have to be the one experiencing the highest Schmid factor, the highest resolved shear stress respectively, [Grö08]. At least the direction of slip is defined, it is along the close-packed <111>-direction.

Many characteristic features of plastic deformation of bcc metals in general [Chr83] and tungsten in particular are now explained by peculiarities of non-planar 1/2 <111> screw dislocations, which have a core spread in several planes. This was first proposed by Hirsch [Hirs60]. Slip planes, or lines respectively after surface intersection, often are not well defined because the screw dislocations easily cross slip, resulting in so-called wavy slip lines. Which glide plane will be the preferred one during experiments depends on the sample's crystallography, type of deformation, strain rate, alloying elements and of course the temperature. Plastic behavior and glide planes of tungsten and different tungsten alloys have experimentally been investigated by many groups, for example see [Arg66a, Garf66, Ste70, and Wro64]. The general trend is that both slip systems, {110} and {112}, have been observed for pure tungsten at room temperature [Arg66a, Garf66, and Wro64]. Alloying tungsten with rhenium allows now to compare the properties of dislocations in

pure and rhenium-alloyed tungsten materials to better understand the deformation behavior. A change in dislocation properties – especially of screw dislocations – seems to lead to improved mechanical properties. Computer simulations based on Bond Order Potentials by Gröger et al. [Grö08] show that the {110}-planes are the main glide planes for tungsten and molybdenum at lowest temperatures. Romaner et al. [Rom10] outline using density functional theory calculations that alloying rhenium to tungsten changes screw dislocations from a symmetric to an asymmetric core structure, furthermore the Peierls stress is lowered and other slip planes than {110} might be activated. Investigations comparing tungsten and tungsten-rhenium single crystals of various crystallographic orientations [Garf66, Ste70] depicted that rhenium additions promote slip at room temperature on {112}-planes. Stephens [Ste70] also found dislocations related to {112}-slip for dilute tungsten-tantalum alloys, but the effect was less pronounced. He explained the effect of rhenium and tantalum by a change of the ratio of critical resolved shear stress of different types of glide planes.

Another feature observed for dilute tungsten-rhenium alloys is solid solution softening, as previously mentioned. In general, alloying a small amount of rhenium to group VI-A metals leads to a decrease in hardness, but the effect diminishes at higher homologous temperatures (Figure 1-10) [Ste71]. As can be clearly seen, there is hardly any softening effect for tungsten-rhenium alloys at temperatures above about 457 °C (730 K). With decreasing testing temperature, the minimum in hardness is shifted to higher rhenium contents. Pink and Arsenault [Pink79] conducted a survey on solid solution of bcc alloys at low temperatures and data for all alloys of rhenium with tungsten, chromium and molybdenum is summarized in [Klo68]: above a homologous temperature T_m of 0.16 (~ 320°C, Figure 1-10), the softening effect vanishes for tungsten-rhenium alloys. With increasing rhenium content, depending on base material and testing temperature, solid solution hardening becomes the dominant mechanism and the hardness increases. The maximum rhenium content for change from a softening to hardening was found to be 16 at%. In [Pink79], intrinsic and extrinsic mechanisms are elucidated. The extrinsic explanation bases on scavenging of impurity atoms by additions of alloying elements leading to a softening. However, it does not seem consistent with investigations on materials of different impurity contents, especially with materials of very high purity. As an intrinsic mechanism, the easier formation of double kinks in screw dislocations is proposed.

The same behavior was observed by Raffo [RafPL69]: at low temperatures, the yield stress decreases with increasing rhenium content, at high temperatures yield stress increases (Figure 1-11). The increase in yield strength for a decrease in temperature is less steep for higher amounts of rhenium, furthermore the strain rate sensitivity is smaller. In [RafPL69] it is outlined that the decrease in DBTT is due to a decrease in Peierls stress and double kink formation energy. Both changes result in an increase of dislocation mobility, dislocation multiplication rates and hence in a more pronounced crack tip blunting.

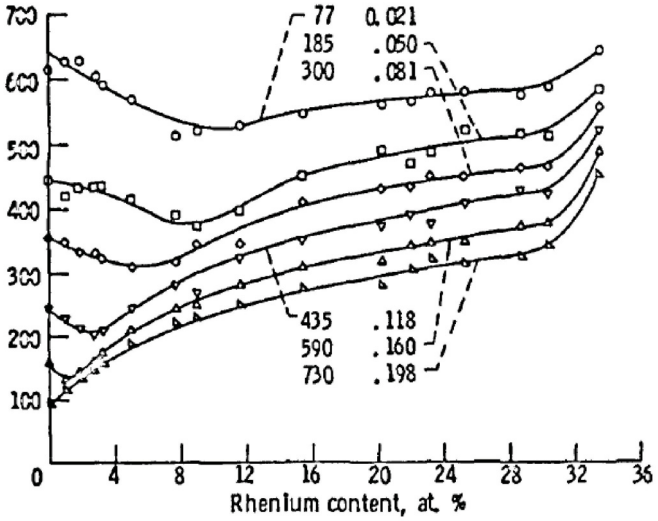

Figure 1-10: Hardness HV 1 of electron beam melted tungsten-rhenium alloys as a function of temperature (left row within the diagram, in K) and homologous temperature (right row) and rhenium content. A decrease in softening with increasing temperature and rhenium content can be seen. Taken from [Ste71].

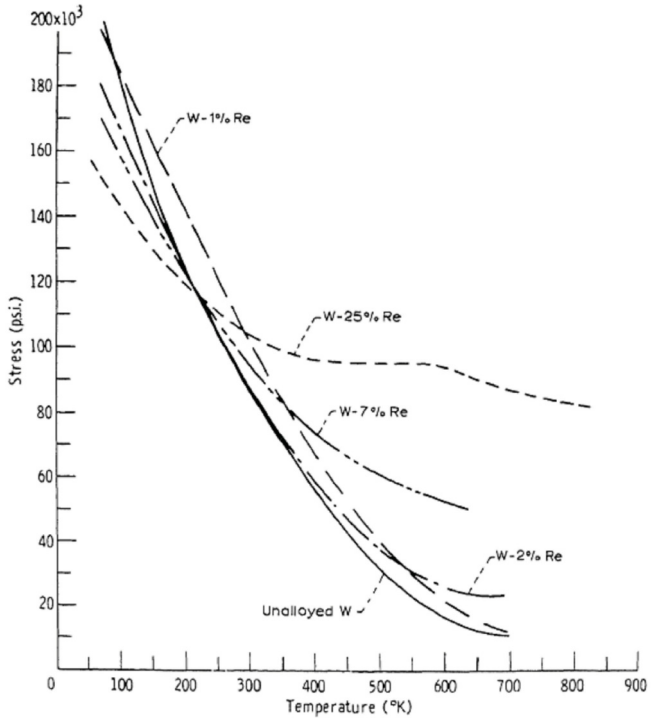

Figure 1-11: Yield stress vs. temperature for arc-melted pure tungsten and tungsten-rhenium alloys (W-1at%Re, W-2at%Re, W-7at%Re and W-25at%Re). Taken from [RafPL69].

To the author's knowledge, Mutoh et al. [Mut95] were the first to perform fracture mechanical experiments using tungsten-rhenium alloys. See Section 2.1. for a comparison of their results with other fracture experiments on tungsten-rhenium alloys, including the ones of this thesis. In [Mut95], plane strain fracture toughness values K_{IC} at room temperatures up to 600 °C and elastic-plastic fracture toughness J_{IC} at higher temperature up to 1600 °C were determined. The Japanese group used standard and sidegroved 3PB-specimens of various tungsten – rhenium alloys containing 0 wt%, 5 wt% and 10 wt% rhenium. The starting microstructures were not reported, only a "difference in forging ratio during the manufacturing of the specimens" [Mut95] is mentioned. At low temperatures, fracture toughness values K_{IC} are about the same for all investigated materials, with increasing temperature, rhenium alloys became tougher, the same is valid for J_{IC} although pure tungsten is nearly as tough as W-10Re in a temperature regime of about 1000 °C to 1200 °C. The increase and drops (at even higher temperatures) in fracture toughness for pure tungsten are much steeper, going to lower values than for both rhenium alloys. At 800 °C, where ductile dimple fracture is already visible on fracture surfaces of rhenium alloys, pure tungsten still shows quasi-cleavage fracture indicating that the experiment was conducted at a temperature below DBTT. At very high temperatures, up to 1600 °C, retarded recrystallization of rhenium alloys helps to avoid the generation of embrittled grain boundaries leading to a higher J_{IC} – value for higher rhenium content compared to pure tungsten. The increasing fracture toughness even for dilute rhenium alloying contents at low temperatures ([Mut95 and work described in Section 2.1.) might be attributable to the solid solution softening. At very high temperatures, retarded recrystallization leads to a comparatively higher ductility, but at intermediate temperatures, where neither process is acting, the ductilizing process has to be searched for in the change of the screw dislocations' cores [Rom10] and a decrease in double kink formation energy [Tar09], which would result in a decrease in DBTT.

Are there any more alloying elements with a beneficial impact on tungsten materials? Klopp [Klo75] concluded from the results of several non-rhenium systems also showing a rhenium-like ductilizing effect, e.g. chromium-based materials, that ductilizing elements are from groups VII-A and VIII-A, the alloying elements are sigma phase forming, solubility limits are rather high and maximal ductility at low temperatures occurs for saturated and supersaturated single phases. Extending these considerations for tungsten, taking at hand phase diagrams from [Nag91], technetium (5^{th} period, group VII-a), ruthenium (5^{th} period, group VIII-a), rhenium (6^{th} period, group VII-a) and osmium (6^{th} period, group VIII-a) are candidates. The latter one is even more expensive than rhenium, technetium is radioactive and does not have stable isotopes. The sigma phase is non existent at temperatures below 1667 °C in the ruthenium-tungsten phase diagram. From this point of view, rhenium seems to be the only ductilizing alloying element for tungsten, but it cannot be considered for the construction of a whole set of first generation fusion power plants, as its abundance in the earth crust is very low. This is of course reflected in the price: according to a publication from 1959 [Kir59] the price for one kilogram of rhenium powder was between 1,500 and 2,000 US-Dollar. Nowadays, the price is more than 5 times higher, reaching 10,000 $/kg [www1b].

1.5.2. Tungsten – Tantalum Alloys

Tantalum (T_m = 3020 °C [Nag91]) and tungsten are completely miscible in solid and liquid phases. The crystal structure of tantalum is bcc. In general, tantalum – tungsten alloys of technical importance are tantalum rich with a few weight percent of tungsten additions [Las99], mechanical properties of some of these materials were investigated in [Gou94]. Tantalum-based tungsten-containing materials combine elasticity and corrosion resistance of tantalum and strength of tungsten.

A decrease in DBTT for low tantalum alloying of tungsten was reported in [Ste70], the effect is most pronounced for 1 at% of tantalum and diminishes already for about 2 at%. This indicates a lower but existing ability of solid solution softening, which might be the reason for the rather good performance of the W-1Ta alloy in fracture experiments performed in this thesis (Publication C), at least in one testing direction. As will be presented in Publication C and was already reported from industrial [Hof] and EFDA-project partners [Riet11a], higher tantalum additions lead to a tremendous decrease in workability and fracture toughness respectively.

1.5.3. Tungsten – Vanadium Alloys

The tungsten-vanadium phase diagram also features complete solubility. Due to their high strength, ratio of strength to weight and good corrosion resistance, vanadium-based alloys containing certain amounts of titanium and chromium are typically used for air- and spacecraft as well as nuclear engineering applications [Pink96]. However, literature on fracture behavior of tungsten-vanadium is scarce, rather non-existent with the exception of a recent publication of Hohe and Gumbsch [HohJ10] on tungsten-vanadium composites and their possible application for fusion technology. Many different composite types were introduced: tungsten- or vanadium-particle reinforced composites, furthermore, short fiber reinforced composites of random and aligned fiber orientation and unidirectional infinite fiber reinforced materials with tungsten fibers and the vanadium phase constituting the matrix. Calculations regarding their thermal conductivity, thermal expansion, elastic properties, creep resistance, yield curves and fracture toughness enhancement were performed. In the divertor region, the high erosion resistance of tungsten would be needed when facing the plasma. When it comes to the question of how to join the plasma facing material to a steel structure (e.g. EUROFER), a material of adjusted coefficient of thermal expansion is preferred. Hence, functionally graded materials of varying tungsten and vanadium content are proposed in [HohJ10].

1.5.4. Tungsten – Iridium Alloys

Within this thesis, no results of tungsten – iridium alloys will be presented. Furthermore, iridium does not belong to the group of elements introduced by Klopp [Klo75]. Nevertheless, due to similarities between iridium and rhenium in electronic structure and thus in the phase diagram, some of these similarities and according investigations will be briefly outlined. The tungsten – iridium phase diagram shows a small sigma phase field at about 25 wt% Ir. The sigma phase is not stable below temperatures of about 1800 °C [Nag91]. Two publications by Luo et al. [LuoA91a, LuoA91b] describing alloys containing 0.4 wt% and 0.8 wt% Ir in two different temperature regimes are considered there. The first one investigates the mechanical behavior at room temperature [LuoA91a] the other one at ultrahigh temperatures [LuoA91b]. At room temperature, the softening mechanism – determined by Vickers hardness measurements and tensile tests – is more pronounced for W-Ir alloys in comparison to W-Re alloys, also investigated in [LuoA91a]. Less iridium (~0.4 wt% Ir) than rhenium is required to achieve a maximum in solid solution softening. This effect vanishes for iridium alloys at ultrahigh temperatures (1600 K to 2600 K) [LuoA91b]. Solid solution strengthening occurs, leading to increasing yield strength with increasing iridium content. Summarizing the little known for W-Ir alloys, the same behavior was observed as for tungsten-rhenium alloys. Nevertheless, due to the rarity and the high price of iridium, these alloys will not be of any importance for large technical applications.

1.6. Measures for increased fracture toughness of advanced tungsten-based materials

Besides the possibility of alloying tungsten, there are other means to achieve an increase in fracture toughness. In the following, two ways will be described. The first one (Section 1.6.1.) relies on a microstructural design approach, comparable to working of tungsten materials, which results in an elongated grain structure and two tough testing directions [Glu10a]. In detail, the present approach involves a microstructural / composite design strategy by severe plastic deformation using high pressure torsion as will be discussed in Publication C. The second possibility (Section 1.6.2.) is to toughen the material by producing a tungsten fiber – tungsten matrix composite. This offers several ways for the material to dissipate energy during crack propagation.

1.6.1. Microstructural Design

It is beyond the scope of the introduction of this thesis to give a comprehensive overview on subtleties of Severe Plastic Deformation (SPD) by High Pressure Torsion (HPT). The reader is forwarded to elaborate reviews on this topic [Haf07, Pip10, Val00 and Zhil08]. Summarizing the technique shortly, it uses a high hydrostatic pressure to deform rather small amounts of materials by shear. Thereby this method allows deformation even of brittle materials (e.g. tungsten based materials [Kec07, Fal07a, Sab05, Sab07, Wei06, Wur11], including Publication C) to large strains, which are not achievable by conventional methods (forging, rolling, drawing). Deformation temperatures can be very low in respect to the warm forming temperature regime. Disks of the starting material, either in bulk or powderous form, are put between two anvils into conical cavities; the anvils are pressed together and one is rotated against the other. As a rule of thumb, the used pressure has to be at least three times the flow stress of the undeformed material. This leads to a limitation in deforming large samples. The resulting microstructure is ulftrafine-grained (< 1 µm) or even nanocrystalline (< 100 nm). The potential of microstructures in the nanocrystalline regime regarding their resistance to radiation damage, is discussed in Publication A.

The applied shear strain γ, and the equivalent plastic strain ε, respectively, can be calculated according to

$$\gamma = \frac{2\pi nr}{h} \tag{20}$$

$$\varepsilon = \frac{2\pi nr}{h\sqrt{3}} \tag{21}$$

The distance from the – in an ideal case – non-deformed center of the sample is represented by *r*, *n* is the number of anvil revolutions and *h* the sample height. Thus, the applied strain and the resulting microstructure are dependent on the radius. The microstructure consists of elongated grains having a small angle of inclination of the long grain axis towards shear direction; for an elaborate review on microstructural evolution during high pressure torsion, see [Pip10].

Faleschini et al. [Fal07a] found an increasing fracture toughness with increasing strain until a saturation region is reached (see Figure A.2 in Publication A). Samples with crack propagation in the radial direction, according to the HPT-samples of cylindrical shape were used. Reasons for this behavior is the fact that at large strains a saturation of grain refinement is reached. Consequently, hardness also saturates with strain and the curve showing fracture toughness vs. strain (radius, respectively) is similar to hardness vs. strain. The reversed situation of grain size development is expected when starting from a level which is smaller than the saturation grain size. In this case, grain size is expected to increase [Yan08]. The saturation grain size is affected by deformation temperature, impurity and alloying contents. A higher temperature and less impurity / alloying content lead to a larger stable microstructural size.

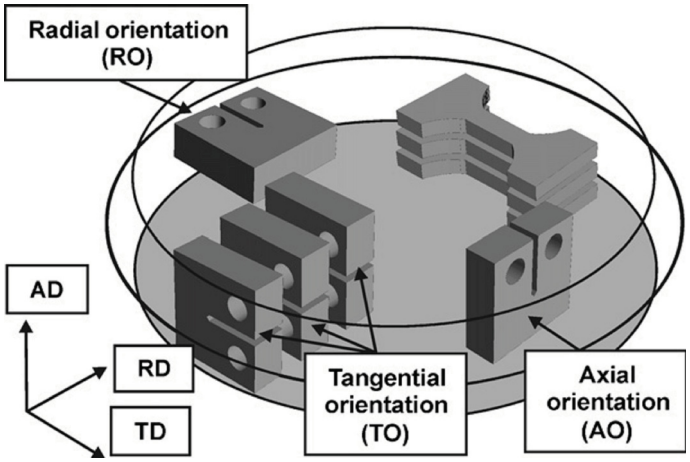

Figure 1-12: Different fracture toughness testing directions using CT-specimens, accounting for the anisotropic microstructure after HPT. Taken from [HohA10].

Hohenwarter and Pippan [HohA10] investigated the fracture behavior of HPT-deformed bcc iron and detected a strong dependency of fracture toughness on testing direction in relation to the direction of shear deformation. Referring to Figure 1-12, fracture toughness was low for tangential oriented samples, where the crack propagates along inclined and elongated grain boundaries. For axial orientation, fracture toughness was more than twice as high – the crack propagated perpendicular to mode I loading, following the elongated grain boundaries within the shear plane. Hence, the mode I fracture toughness in axial direction has to be at least twice the toughness of the tangential direction, as the crack would not deflect otherwise. Fracture toughness of specimens

of radial orientation is even higher, due to delaminations on the low toughness shear plane being perpendicular to the crack plane. The same behavior was observed for tungsten-based composites (Publication C), showing two tough testing directions, and the material still remains brittle in tangential testing direction.

It is of great importance to stabilize the ultra-fine grained or nanocrystalline microstructure at elevated temperatures, as recrystallization would degrade the advantageous properties. The most prominent material is potassium-doped tungsten, where finely dispersed potassium bubbles retard recrystallization [Pink89]. Further dopants at the start of the tungsten production route are aluminum and silicon. The possibilities to use other particles, for example carbide or oxide particles, are manifold: La_2O_3 [Mab96, Yar11a], TiC [Kit99, Kur09], a combination of La_2O_3 and TiC [Che08], HfC [Klo71], Y and Y_2O_3 [Vel09, Yar11b], ZrC [Son02] and ThO_2. Thorium was previously used for welding electrodes but nowadays it has to be avoided due to its radioactivity. Publication A will especially address nanocrystalline tungsten materials with TiC dispersoids. Kurishita et al [Kur07, Kur09], used material received from mechanical alloying of W and TiC powder and subsequent hot isostatic pressing and demonstrated a decrease in grain size with increasing TiC-content [Kit99]. Furthermore, a decrease in DBTT – determined by impact experiments – and an increase of recrystallization temperature was observed. TiC particles hinder recrystallization by hampering grain boundary migration. For instance, tungsten containing 0.2 wt% TiC (average grain size in as-hipped state: 1.6 µm) showed recrystallized microstructures after annealing at 2200 °C for 1 h. A batch of tungsten containing 0.5 wt% TiC (average grain size in as-hipped state: 0.05 µm) did not show any signs of recrystallization after 1 h at 2200 °C [Kit99]. Kurishita et al. also found improved properties such as reduced hardening under neutron irradiation of the ultra-fine grained materials [Kur07] and most recently an increased thermo-shock resistance [Pint11b].

1.6.2. Toughening by fiber-reinforced matrix composites

Alloying or microstructural optimizations can lead to an enhanced inherent toughness, but might, in turn, get embrittled by recrystallization at high temperatures and/or changes in alloying content because of transmutations at high neutron fluxes. In contrast to this, the method of fiber-reinforced metal-matrix composites can cope with brittle base materials. These composites rely on providing interfaces perpendicular to the expected crack propagation direction. The principal idea originates from ceramic composites: Ceramics are high-strength materials capable of withstanding high temperatures but showing a brittle behavior – not much different to tungsten. In [And95], the fiber-toughening mechanism is first-listed regarding its enhanced toughening capability. Other mechanisms rely on ductile networks, martensitic phase transformations, whisker reinforcement and microcracks.

The fiber-reinforced toughening is based on a mechanism as follows: a crack propagates within a brittle material (e.g. tungsten) containing a fiber (e.g. a thin tungsten wire) perpendicular to the crack propagation direction and the fiber axis is parallel to the normal of the crack plane. It is not necessarily disadvantageous when both materials are brittle. When the crack hits the fiber, energy dissipates by debonding of the fiber-matrix interface. To enable this process for a tungsten-tungsten-composite where both materials have the same Young's Modulus, the ratio of critical energy release rates G_{fiber} and $G_{interface}$ have to fulfill $G_{interface}/G_{fibre} < 0.25$ and the corresponding fracture toughness values $K_{interface}/K_{fiber} < 0.5$, respectively (Section 1.3.). On the one hand, if the interface is too strong, the overall behavior will be brittle and the crack will penetrate the fiber without debonding of fiber. On the other hand, if the interface is too brittle, not much energy is consumed during interfacial debonding. Subsequently to the failure of the interface, the additionally generated fracture surfaces where matrix and fiber had been in contact, being perpendicular to the original crack and thus experiencing mode II loading, dissipate energy by frictional sliding. Energy is also consumed by deformation and failure of the fiber. Furthermore, crack tip opening, taking place when the original crack propagates onward, is restricted. As outlined in a separate chapter on tungsten fiber reinforced composites in [Las99], this idea is not new, although other matrix materials have been used until now, e.g. superalloys, niobium, copper and silver.

You et al. were the first to design W_{fiber}–W_{matrix} composites and the applicability of the above-mentioned toughening mechanism for these new materials was successfully demonstrated [Du10a, Du10b, Du11, Ries]. The metal fiber – metal matrix composites used by You et al. consisted of commercially available, thin tungsten wires (150 µm), various kinds of magnetron sputtered interfacial coatings and a tungsten matrix produced by chemical vapor deposition (CVD). These interface coatings – in case of [Du10b] copper single layer coatings were chosen – might be advantageous, as plastically deformable interfaces contribute to enhanced energy dissipation. Furthermore, they act as mechanical barriers in order that the tungsten fiber does not join to the full tungsten matrix; the composite character would be lost [YouJH11]. As the volume fraction of interfaces is very small, they should not pose a problem in terms of changed chemical composition, transmutation in case of fusion applications and subsequent radioactive waste management. It should also pose no problem in respect of irradiation embrittlement due to the very high temperatures. Mechanical properties of interfaces were determined by fiber push-out experiments [Du10b]. Direct observation of the mechanism [Du10a] was made possible by use of dedicated specimens containing a single fiber with the geometry of a half cylinder cut along the longitudinal symmetry plane in order to display internal crack deflection and bridging (inlay in Figure 1-13). The three-point-bending (3PB) samples were loaded in-situ within a scanning electron microscope (SEM). It was demonstrated that the tungsten fiber did not fracture and interface debonding took place – as forecasted according to the criterion of crack deflection expressed by the ratio of fracture toughness values of fiber and interface. The same beneficial fracture behavior was recently confirmed for multi-fiber composites (Figure 1-14) [Ries, YouJH11].

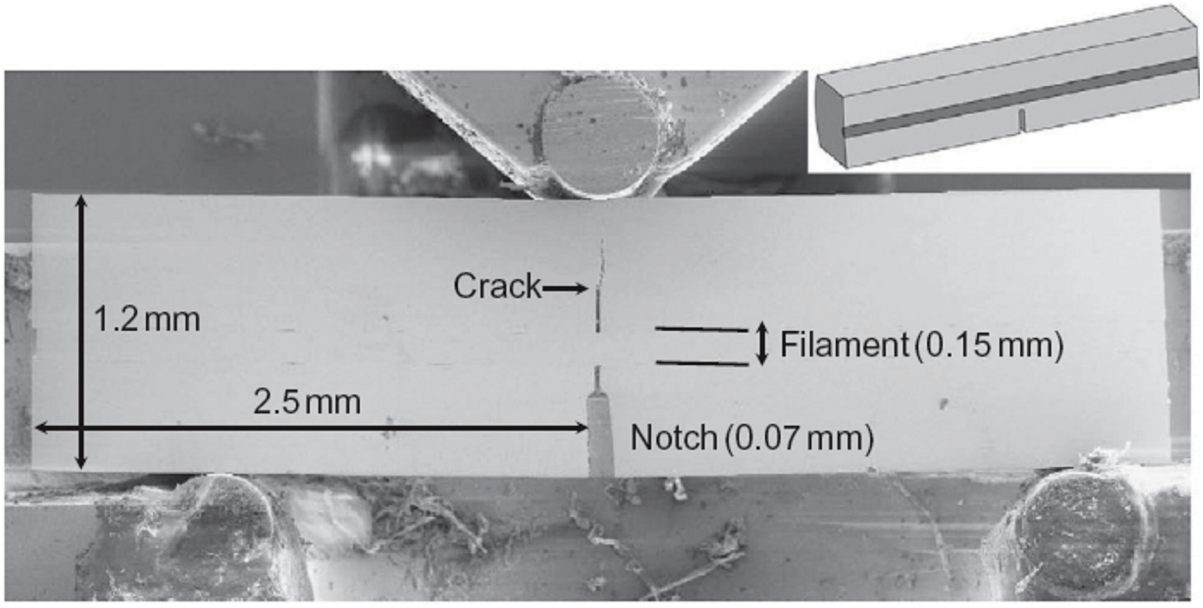

Figure 1-13: Secondary electron micrograph of a 3PB-sample consisting of a tungsten composite containing a single fiber, Zr/ZrO_x multilayer interface and CVD tungsten matrix. The sample was polished in order to display one half of the single fiber. The picture was taken during an in-situ experiment and shows the unfractured tungsten fiber and the crack extending beyond. Taken from [Du10a]

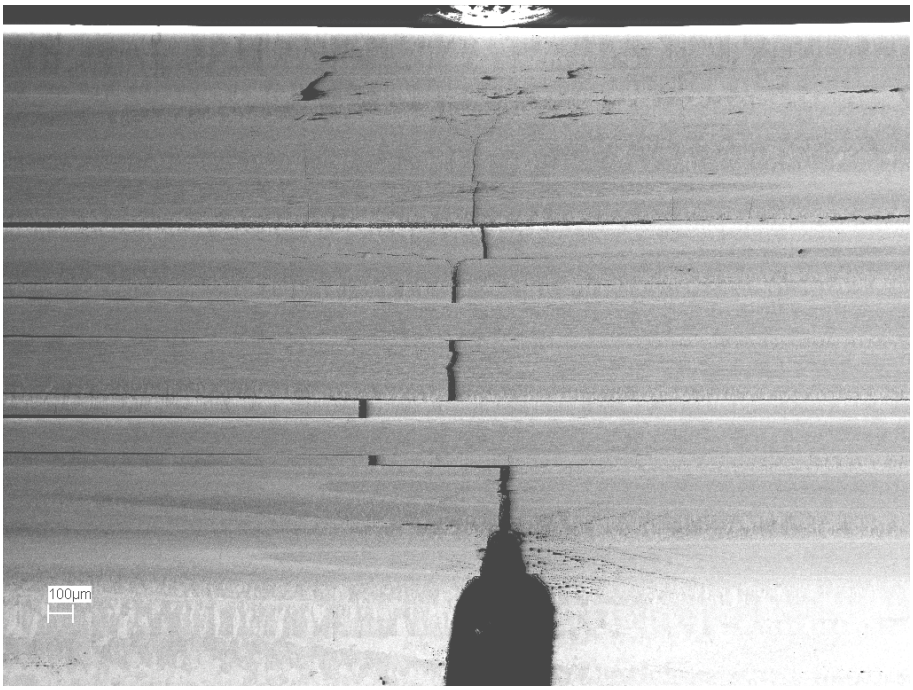

Figure 1-14: Backscattered electron image during an in-situ 3PB-experiment using a multi-fiber composite, containing several tungsten wires, surrounded by a CVD tungsten matrix. Picture provided by and property of Johann Riesch (Max-Planck Institute for Plasma Physics, Garching). Contrast and brightness were adjusted for better visibility.

1.7. Fracture Experiments on the Micrometer Scale

Several scientific groups, using various brittle materials, have already performed fracture experiments using samples on the micrometer scale. They are summarized in Table F.1 in Publication F, taken from [Wur]. In general, it is possible to apply bending of notched cantilevers and tensile tests involving notched tensile samples for determination of fracture toughness values. For determination of fracture stresses un-notched samples (e.g. [Mato09, Klü11]) have been used. Other sample geometries that are commonly used for macroscopically large samples such as CT, 3PB and 4PB do not seem to be applicable as they would require freestanding samples and subsequent micro-manipulation.

After specimen production – for the most part this work is performed using a Focused Ion Beam (FIB) workstation – they are tested by various techniques. Some authors [DiM05, Mato09] use nanonindentation, where the fracture process itself cannot be depicted. In-situ experiments using scanning electron microscopy [Mas09, Wur] have the advantage of direct observation of the experiment. Several techniques for generation of pre-cracks in macro-samples, such as cyclic compression, compound bending and electrical-discharge machining, are summarized in [Glu10a, Glu]. Cyclic compression is also possible for micrometer-sized samples [Tak05]; however, for this work, the FIB was used for producing a sharp notch. It is a common approach to produce sharp crack-like notches (see Table F.1 in Publication F). In general, line milling with low currents (pA) is used and some reported crack tip radii are in the regime of 10 nm [DiM05, Mas06, Mato09].

Matoy et al. [Mato09] investigated chemical vapor deposited amorphous silicon oxide, oxynitride and nitride. Fracture stresses for silicon nitride were beyond 7 GPa and fracture toughness values did not exceed ~1.7 MPa $m^{1/2}$. Hence, these are ideal materials to utilize linear elastic fracture mechanics, with the plastic zone limit mentioned in 1.3. (Equation (12)) being below 200 nm. Although, one should rather speak of a process zone instead of a plastic zone for these amorphous, dislocation-free but not defect-free materials. As this zone extends less than half a micrometer from the crack tip, it is possible to produce samples large enough to give meaningful results using LEFM, even when considering the most unfavorable combination of material's strength and toughness.

In [Miy09], the authors report on very low fracture toughness values (1.5 – 3.6 MPa $m^{1/2}$) for interlamellar crack orientation, which is – at least for the lower bound – in accordance to energy calculations for cleavage fracture. For the latter crack orientation, resulting in a toughening mechanism akin to the one described in Section 1.6.2., the fracture toughness was higher (5.0 – 8.1 MPa ^{½}), but low compared to macroscopical large samples. For interlamellar crack orientation, the crack plane coincides with the plane of lamellas; whereas for translamellar orientation, the initial crack – or in this case – notch, is perpendicular to the plane of lamellas.

The authors argued that extrinsic toughening mechanisms are not activated. Alternatively, the small specimens' size in relation to toughness and strength might lead to a reduced value of K_Q, as it is reported in Publication F. The same decrease in fracture toughness values was found in [Half05], where micrometer-sized samples fractured at stress intensities of 1.4 – 6.9 MPa $m^{1/2}$, whereas the toughness of large samples is in the range of 17.8 MPa $m^{1/2}$. Thus, to extend fracture investigations to more ductile materials, it is necessary to perform evaluations according to elastic-plastic fracture mechanics. This will be demonstrated in Publication F.

2. Results and Discussion

The second chapter shall outline the results of this thesis and includes a discussion regarding their consequences for the application of tungsten based materials for fusion applications. This part will present the most important findings, which have already been published (Publications A – F) together with unpublished work, relevant for elaborating an outlook on further work.

2.1. Fracture Investigations on Tungsten – Rhenium Alloys

Rhenium has been known for a long time to ductilize tungsten materials (see Section 1.5.1.) One part of this work was devoted to understand better the influence of rhenium alloying on tungsten and the results gained on fracture experiments of tungsten rhenium alloys shall be compared to existing ones. RCT samples made of porous materials (porosity: 22%, provided by Plansee SE) of three different rhenium contents (weight percentage) were fractured at room temperature [unpublished work]. Unless noted otherwise, all succeeding alloying compositions will be given in weight percentage[6]. Starting materials were cylinders of 6 mm in height and 7.2 mm in diameter, they were bisected in order to receive RCT-preforms. Notches were produced by diamond wire saw cutting and a fatigue crack was introduced by cyclic compression [Pip87]. The specimens' dimensions are given in Table 1 and the results of fracture experiments are depicted in Figure 2-1,a. LEFM [AST90] was used for evaluation of conditional fracture toughness values K_Q. Increasing toughness with increasing rhenium alloying content is evident. Data points show a linear relation of fracture toughness data in the composition regime of 2 wt% Re to 10 wt% Re (correlation coefficient R = 0.979). The linear interpolation leads to an increase of toughness by about 0.5 MPa $m^{1/2}$ for adding 1 wt% of rhenium. However, stressing Figure 1-10 in Section 1.5.1., a quadratic form of the curve showing fracture toughness versus rhenium alloying content with a shallow declination of fracture toughness when approaching 10 wt% Re can be expected. Nevertheless, the as-expected increase of fracture toughness [Fal07b, Mut95 and Wur10b] with increasing rhenium content is demonstrated, even for a porous material. An Inverse Pole Figure (IPF) map (Figure 2-1,b) from Electron Backscatter Diffraction (EBSD) analysis depicts the microstructure in a side view of specimen W-10Re No.1 in its as-sintered state. The EBSD scan was made after the fracture experiment; the mean grain size was determined to be 6 µm. Subsequent EBSD analysis of other specimens did not give the same low amount of misorientation within the grains, which is most likely due to problems in preparation of a porous structure of a rather high strength base material.

[6] Due to the proximity of tantalum (73), tungsten (74) and rhenium (75) in the periodic system of elements, the differences between atomic percentage and weight percentage are rather small.

Table 1: Measurements of porous W-Re specimens and results of fracture experiments. Force F_Q, width W, thickness B, overall crack length a and resulting conditional fracture toughness values K_Q are given.

Alloying Content & Specimen No.	F_Q [N]	W [mm]	B [mm]	a [mm]	K_Q [MPa $m^{1/2}$]
W-2Re No.1	35.1	5.20	1.95	2.86	3.0
W-2Re No.2	56.2	5.20	2.87	2.85	3.2
W-5Re No.1	82.1	5.16	2.31	2.41	4.5
W-5Re No.2	94.4	5.16	2.38	2.24	4.6
W-5Re No.3	76.7	5.12	2.43	2.49	4.3
W-10Re No.1	137.0	4.82	2.55	2.33	7.5
W-10Re No.2	114.4	5.20	2.11	2.71	8.2
W-10Re No.3	128.6	5.20	2.52	2.53	6.9

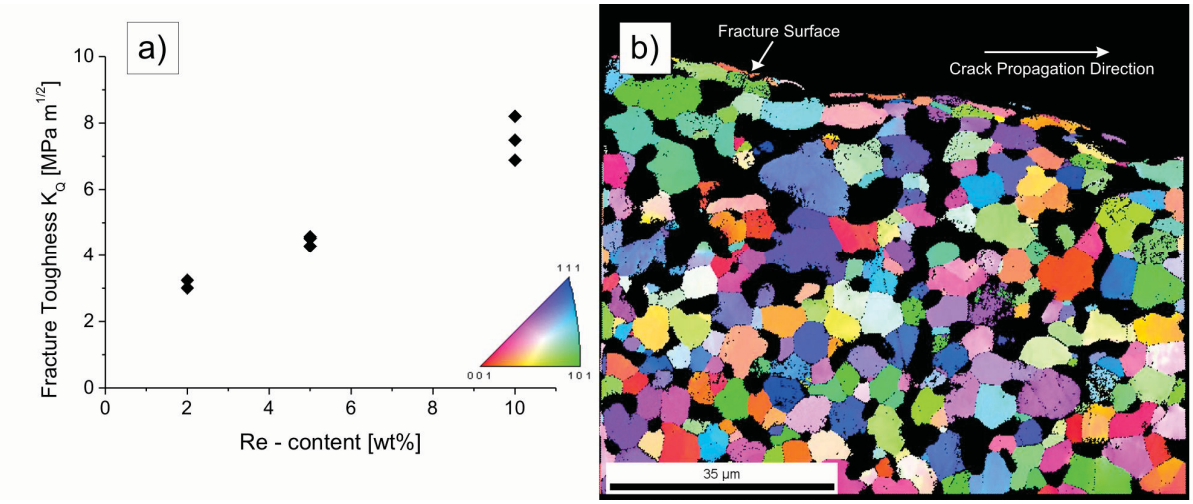

Figure 2-1: a) Conditional fracture toughness values K_Q of porous W-Re RCT specimens at room temperature as a function of rhenium content. Color code for b) is included in a). b) Inverse Pole Figure Map from EBSD analysis of W-10Re sample No.1 after fracture. Noise was removed by non-showing points of low confidence index and very small grains.

Further work focused on temperature-dependent fracture behavior of a recrystallized W-26Re alloy. The experimental temperature regime spans from -196 °C to 870 °C. The specimen broken at the highest temperature did not fail completely, see remarks in Publication B. Recrystallization of the W-26Re alloy took place for 2 h at 2000 °C in hydrogen atmosphere. For comparison, results of this alloy in the as-worked condition were taken from [Fal07b, Kre06]. In the as-worked state, different testing directions due to the elongated microstructure have been taken into account.

Application of linear elastic fracture mechanics gives lower bounds for the critical fracture toughness values at high testing temperatures; this is indicated where necessary. All results on fracture investigations are summarized in Figure 2-2, where the fracture toughness of W-26Re is shown as a function of temperature for different testing direction and microstructures. The toughness of the recrystallized material stays well below the toughness of the material in as-worked condition, DBTT seems to be shifted to higher temperatures. Apparent superior toughness of the recrystallized material at high temperatures cannot be ensured as the values marked with asterisks in Figure 2-2 give lower bounds K_Q, for critical fracture toughness values K_{IC}. Nevertheless, the fracture toughness of this alloy is high, even in its as-recrystallized state, in comparison to e.g. tungsten in the as-recrystallized state [Glu10a]. Fracture surfaces show a large amount of grain boundary fracture with a slight increase in the amount of intercrystalline fracture with increasing temperature (Figure 2-3). Up to the highest testing temperature of 870 °C no micro ductile fracture surface was observed.

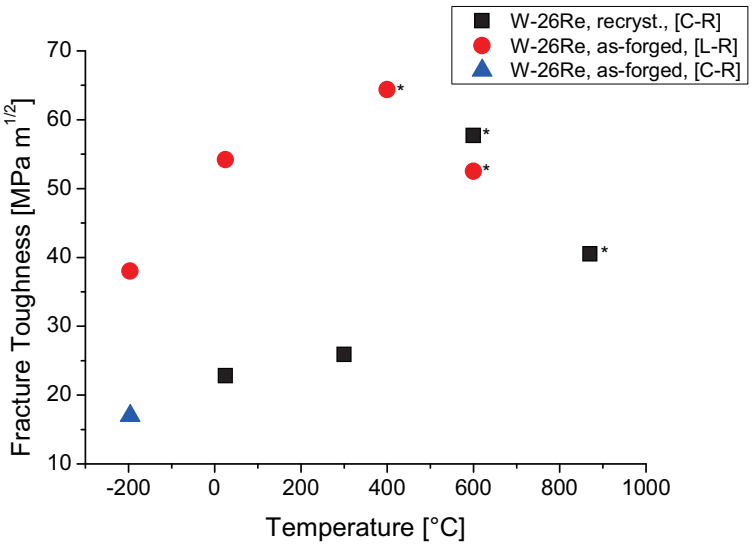

Figure 2-2: Compilation of results on fracture toughness of a W-26Re alloy in as-forged and recrystallized states taking into account different crack systems (Section 1.3., Figure 1-6). Toughness values marked with an asterisk are not valid according to ASTM E 399 [AST90]. Data taken from [Fal07b, Kre06, Wur10b].

Fracture experiments were performed for a W-13Re alloy in as-sintered and deformed state. CT-specimens were taken from the as-received, sintered rod material in order to show the C-R crack system. Material was provided by Plansee SE. The sample dimensions and results from the fracture experiments are summarized in Table 2 and Figure 2.4. Fracture toughness values of the sintered material are low compared to the W-26Re material, also in comparison to the recrystallized state. Fracture surfaces (Figure 2-5) of specimens tested at different temperatures show large amount of grain boundary fracture. Even for experiments conducted at the highest

testing temperature of 900°C the fracture surfaces do not show much difference compared to the fracture surface of a specimen tested at room temperature. The reason for the low toughness of a material, whose toughness was expected to be higher (see results on porous tungsten rhenium alloys presented above, Figure 2-1), is unclear.

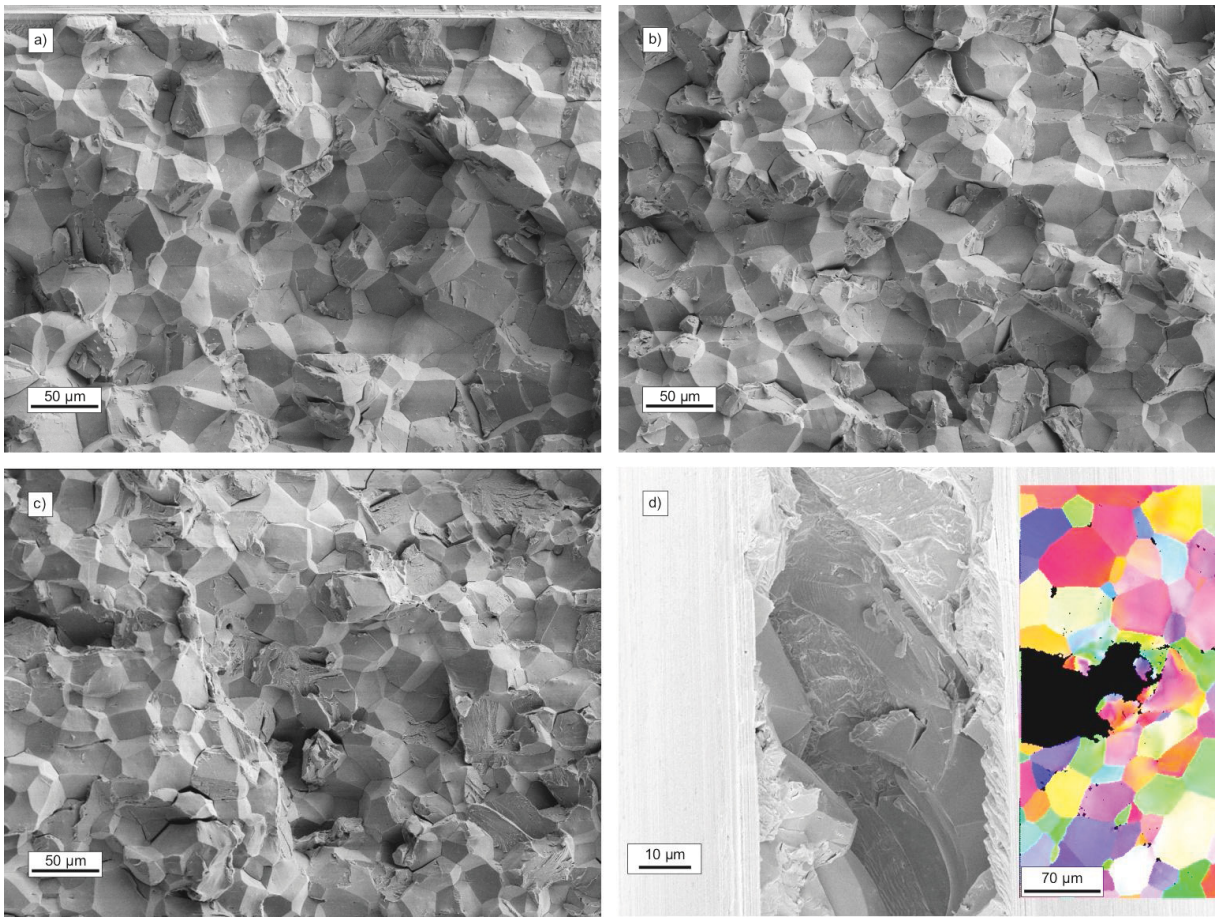

Figure 2-3: SE micrographs of the fracture surfaces of recrystallized W-26Re specimens fractured at a) room temperature, b) 300 °C, c) 600 °C and d) 870 °C. d) was made with viewing direction coinciding with crack propagation direction. The colored inlay in d) shows the amount of crack propagation from left to right by use of an IPF map made in the interior of the bisected specimen. For color code, see Figure 2-1 or Figure 2-11.

In addition to testing the as-sintered state, a cylinder of the sintered material ($h_{initial}$ = 16.2 mm, Ø = 19.5 mm) was compressed at high temperatures (inductive heating, without thermocouple hence temperature measurement) to a final height of h_{final} = 10.5 mm. Notice that oxidation took place at the surface, heating and compression was performed in air. Small 3PB specimens were produced from the deformed material, crack propagation direction was either perpendicular (Type 1) or parallel to compression direction (Type 2), as it was also done for as-forged, solid solution tungsten tantalum alloys (Publication C). Measurements and results are collected in Table 2. After

razor blade sharpening, precracks were introduced by cyclic compression. 3PB specimens were tested at room temperature. Compression of the cylinder brings tendencies towards plate-like grain shapes (Figure 2-6,d) and a pronounced anisotropy of fracture toughness (Figure 2-4). The toughness in one testing direction (Type 2) markedly increases, whereas the toughness of the other direction with compression direction being a normal vector of the originating fracture surface further decreases to a very low value.

Table 2: Measurements of W-13Re specimens taken from sintered and deformed material and results of fracture experiments. Force F_Q, width W, thickness B, overall crack length a and resulting conditional fracture toughness values K_Q are given.

Specimen type & Test temperature	F_Q [N]	W [mm]	B [mm]	a [mm]	K_Q [MPa $m^{1/2}$]
W-13Re, CT, RT	170.4	6.60	3.19	3.42	6.7
W13Re, CT, 600 °C, I	256.1	6.62	3.15	3.19	9.1
W13Re, CT, 600 °C, II	192.0	6.53	2.76	3.40	8.9
W13Re, CT, 900 °C	246.0[(7)]	6.59	2.95	3.31	10.0[(7)]
W13Re, 3PB, RT. Type 1	4.9	1.03	0.80	0.59	2.9
W13Re, 3PB, RT, Type 2	29.3	1.01	1.01	0.50	10.9

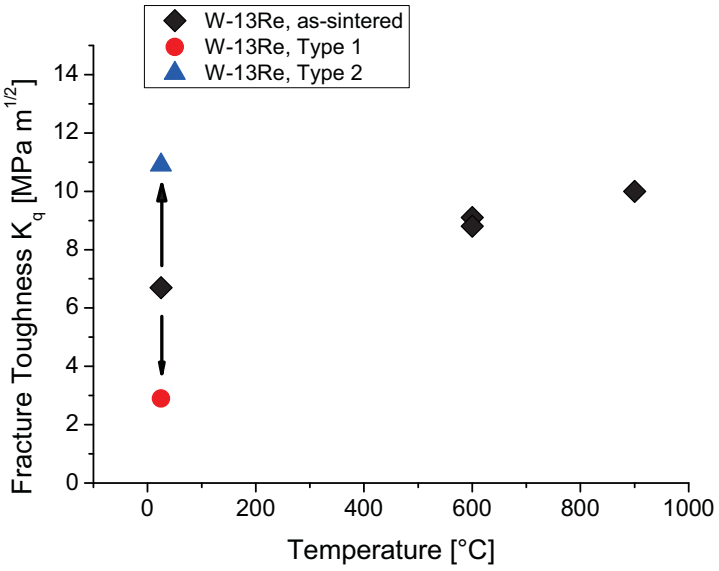

Figure 2-4 Fracture toughness values for 3PB and CT specimens made of W13Re from two different processing routes (as-sintered and after compression at high temperature). After compression, the direction of crack propagation has a marked influence on the fracture toughness. Type 1: Crack propagates in compression direction, Type 2: Compression direction is a normal vector of the crack plane.

[(7)] For this specimen F_{max} was taken for calculation of conditional K_Q, F_Q would lead to a lower K_Q.

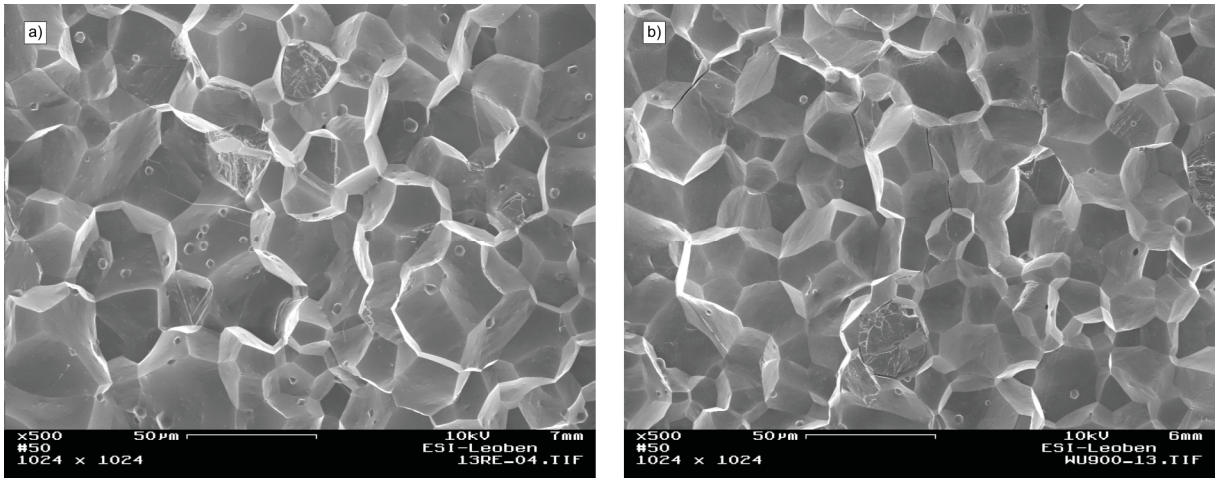

Figure 2-5: SE micrographs of the fracture surface of two different specimens made of W-13Re alloy in its sintered state. a) CT specimen, tested at RT; b) CT specimen, tested at 900 °C.

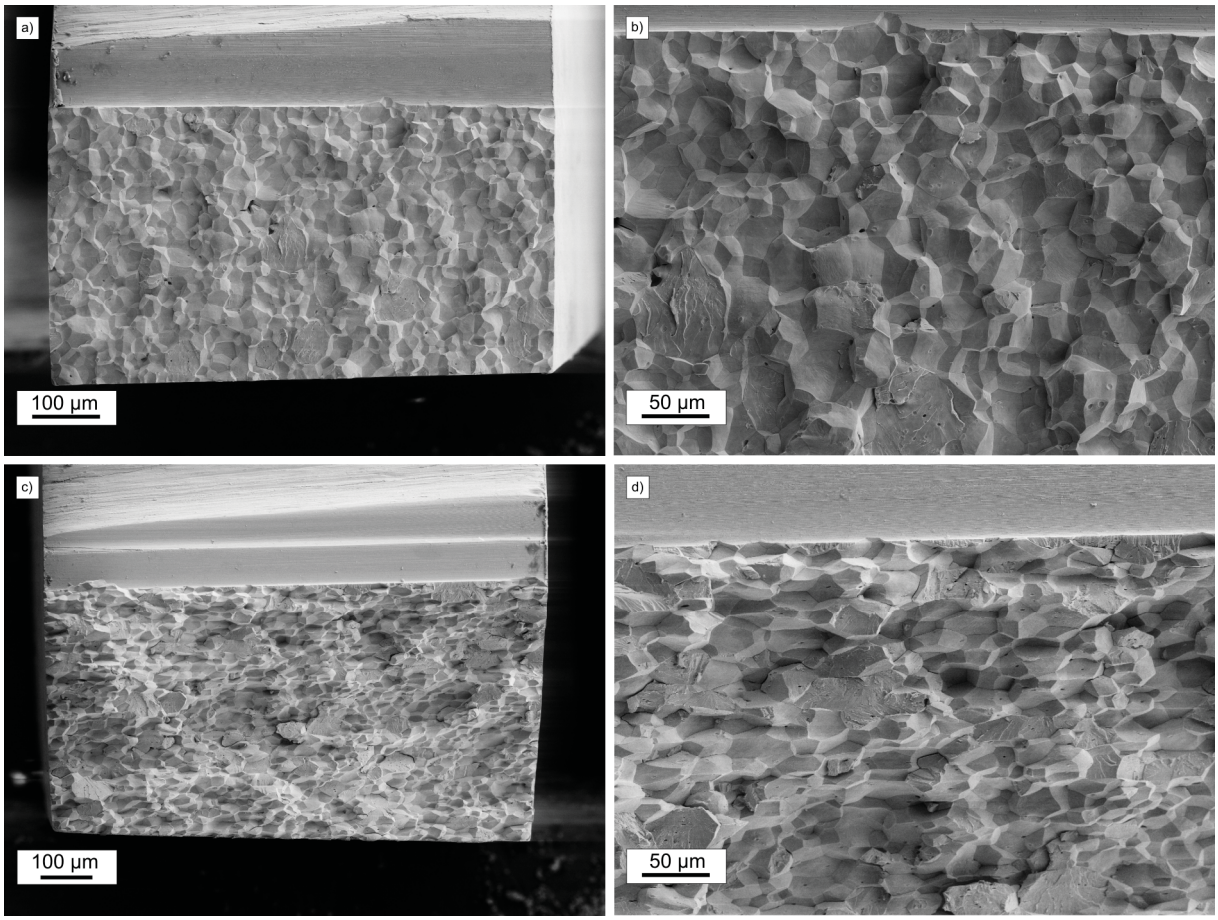

Figure 2-6: SE micrographs of the fracture surface of 3PB specimens made of the deformed W-13Re alloy. First line: Type 1 – testing direction; second line: Type 2 with an increased fraction of transcrystalline fracture and larger deviations in and out of predefined notch plane. Both samples were fractured at room temperature.

The general trend found for fracture experiments of tungsten rhenium alloys is in accordance to Mutoh et al. [Mut95] who compared W-5Re and W-10Re alloys with pure tungsten. According to Figure 1-10, some influence from solid solution softening is expectable at room temperature together with low rhenium compositions, but this effect vanishes for higher rhenium content – especially for W-26Re – and increasing testing temperatures. Maximum test temperatures were 870 °C for this work and 1600 °C for [Mut95]. Including this aspect to the results gained for a high-alloyed W-26Re, which should be almost the highest concentration of rhenium without obvious formation of brittle sigma phase (Section 1.5.1., [Jaf58]), leads to the conclusion that there has to be another toughening mechanism beside the one leading to solid solution softening and up to now it seems to be unique to tungsten rhenium alloys.

As pointed out by Gludovatz et al. [Glu10b], there tends to be a higher crystal misorientation in the vicinity of the crack flanks, indicating the more pronounced plastic deformation. Roughly speaking, there is a higher dislocation density within grains compared to pure tungsten. This was demonstrated by Electron Backscatter Diffraction (EBSD) analysis. However, to quantify this behavior in an absolute manner it would be necessary to use samples in as-recrystallized or as-sintered state having the same grain size distribution or even better to compare grains of the same crystallographic orientation towards the propagating crack. This could be done more easily by micrometer-sized fracture and bending samples using single crystals or recrystallized material showing grains of desired crystallography and adequate size.

This increase in dislocation density is in accordance with Romaner et al. [Rom10]. By using density functional theory (DFT) they calculated a decrease in Peierls potential and a change of symmetric to asymmetric core structure of ½ <111> screw dislocations for high-alloying contents of rhenium (W-25Re). This change was not found up to now for any other alloy (e.g. WTa, WV, WTi [Rom]) according to similar calculations. This non-finding (up to now) of any other alloying elements changing the screw dislocations' core structure is in agreement with experimental results collected over decades. No other element showing the same ductilizing / toughening behavior at high alloying concentrations was found – rhenium alloys seem to be the only one. Therefore, it can be stated that the improved fracture behavior of rhenium-rich tungsten alloys correlates most probably with the changed screw dislocation structure.

As these computer simulations are performed at 0 K, the question remains, which mechanism these computer simulations [Rom10] depict. Is it a mechanism that works in addition to solid solution softening or do these calculations extrapolate solid solution softening to very low temperatures and to very high rhenium alloying content? One could assume, when extrapolating the results shown in Figure 1-10, to lower temperatures that the minima in hardness can be found at these very high rhenium contents. However, attributed to the change in dislocation core structure, there is an increase in the number of possible slip planes [Rom10]. Glide on {112} planes becomes more likely, as it was elucidated in Section 1.5.1. An upcoming publication by Li, Wurster

et al. [Li] will demonstrate and explain this increase in number of slip planes by combination of DFT computer simulations and experimental work. Bending experiments using micrometer-sized cantilevers (Figure 2-14) of pure, as-sintered tungsten and recrystallized tungsten alloys (WRe, WTa) show a change of detected slip planes of a W-26Re alloy in recrystallized state. Glide does not take place on {110} anymore as it was found for pure tungsten and a tungsten-tantalum alloy. Whether glide takes place on {112} or {123}, which is also possible but less likely according to previous results found in literature, cannot be distinguished. As these experiments have been performed at room temperature, the DFT-results found at 0 K seem to be transferable to higher temperatures and this change in core structure influences the deformation behavior of tungsten-rhenium alloys far within the temperature- and compositional-regime where no solid solution softening is supposed to happen.

2.2. Tungsten-based Composites

Summarizing the last chapter, additions of certain weight percentages of rhenium have a beneficial effect on fracture behavior. However, the production of very large batches of tungsten rhenium alloys for fusion applications (e.g. some first generation fusion power plants) is impracticable – rather impossible – due to the low worldwide output of rhenium. Hence, other solutions have to be searched for.

Advantageous properties of both nanocrystalline materials in general and HPT-deformed materials in particular (see e.g. Section 2.4.) are now the reason why this work was also focused on HPT-deformed tungsten-based materials. It was already shown by Faleschini et al. [Fal07a, Fal07b] that the HPT-method is able to process brittle and high-strength tungsten base materials to produce ultrafine-grained microstructures showing an increased toughness. In [Fal07a], one single fracture toughness testing direction was investigated because of the limited sample size. Using a new HPT-tool, capable of applying a force of 4 MN (a tenfold increase in comparison to the previous tool), larger samples of tungsten-based composites can be processed and their fracture toughness values were determined taking into account three general crack propagation directions. These composite materials are produced by powder mixing, feeding the mixed powder in a retaining ring, which is placed between the anvils. There is in principle no restriction to the overall chemical composition of the composites. Subsequent application of a high pressure and deformation, which could in principle be done at different temperatures (RT – 300 °C), leads to compaction and consolidation of the material. The deformation temperature was chosen to be 300 °C. A slight increase in temperatures is expected due to the HPT-processing. The higher temperature is necessary because of the pronounced increase in tungsten-based materials' strength with decreasing temperature. Nevertheless, this is a very low temperature to apply a large amount of strain compared to industrially used forming processes. All produced HPT-deformed samples had diameters of 30 mm, including rings made of steel, ARMCO-iron or copper. All HPT-deformed samples were stress relieved for 1 h at 1000°C in a vacuum furnace.

Room temperature fracture experiments on tungsten composites were performed on two different materials:

- A composite of W-30Ta was chosen to extend the investigations made on industrially produced, solid solution tungsten-tantalum alloys of 1 wt%, 5 wt% and 10 wt%, which were received from Plansee SE. Furthermore, based on DFT calculations, there seems to be a decline in Peierls stress at tungsten alloys with a high tantalum content [Rom] anticipating an improved fracture behavior. However, one has to be aware of the high transmutation rate of tantalum into tungsten considering fusion relevant neutron loading [GilMR10, GilMR11] in case of application of tantalum rich alloys. Taking at hand the transmutation

simulation including resonance shielding leading to a reduced transmutation rate, pure tantalum in the first wall of a fusion power plant transmutes into 61.5 at% Ta and 36.7 at% W after five years of operation [GilMR11].

- A W-25V composite was produced in order to direct the work towards functionally graded materials [HohJ10], as an increase in the coefficient of thermal expansion eases the joining of tungsten materials to ODS steels.

3PB samples were manufactured out of the stress relieved composite materials at different radii (Publication C). The investigated directions of crack propagation directions were radial, axial and shear in respect to the cylindrical sample shape. Instead of introducing cracks by cyclic compression, sharp notches were introduced with the FIB. A comprehensive study of equivalence of FIB made notches and cracks produced by cyclic compression is lacking. The results, which are outlined in detail in Publication C and [Wur11], are summarized in Figure 2-7, left. For both tungsten composite materials, W-30Ta and W-25V, axial and radial testing direction were found to be of high toughness, about 2 to 5 times higher than the fracture toughness when the crack plane coincides with the shear plane. The toughness values of shear direction are comparable to values of tungsten [Glu10b] in as-sintered or recrystallized state, where predominantly grain boundary fracture takes place. Comparison of the results with fracture toughness measurements performed by Faleschini et al. [Fal07a] shows that toughness values are about the same at strain levels below 10. Higher strain rates were not investigated in this thesis. Scatter is high for both cases. The saturation in toughness with higher strains ([Fal07a], Figure 2-7,right) can be attributed to a saturation of the microstructure at higher strains, as will be discussed in the next paragraph.

When applying a large amount of strain, samples tend to show cracks within the shear plane (Figure 2-8) and close to the retaining ring, which is thought to come from the fact that the applied pressure and/or the HPT-temperature are too low. Accordingly, HPT-deformation was not successfully applied to strains where saturation of the microstructural size takes place. For pure tungsten and potassium doped tungsten the saturation regime was determined to start at strains of about 30 ([Fal07b], Figure 3.10, therein). As a consequence, the fracture experiments outlined in [Wur11] were not performed on a material whose microstructure is only determined by HPT-deformation. At these comparatively low strains, an influence of the microstructure of the original powder is still existent. As it is shown at the right side in Figure 2-7 fracture toughness values of materials in their saturated states tend to be higher. New anvils including insets of WC/Co – withstanding high compressive stresses – shall enable application of higher pressure and circumvent crack formation. However, what has to be accepted is a certain decrease in sample size (Ø ~ 20mm) when applying higher pressures.

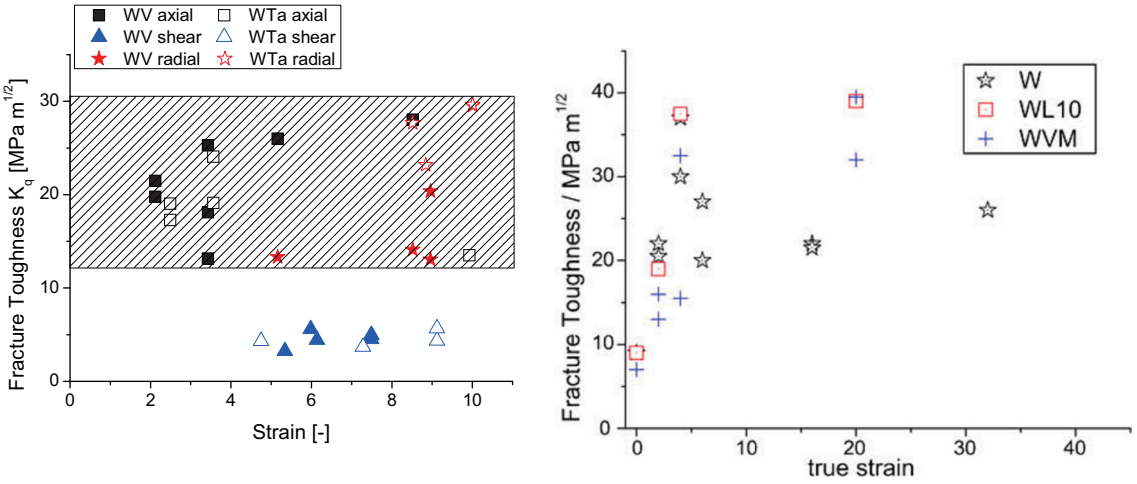

Figure 2-7: Left: Results of fracture toughness measurements for two tungsten-based composite materials, showing the increased fracture toughness for crack propagating in axial and radial direction (dashed area) in comparison to shear direction. Note that depiction of three fracture toughness values being larger than 30 MPa $m^{1/2}$ was omitted. Right: Results of fracture experiments on pure tungsten (W), tungsten containing 1 wt% La_2O_3 (WL10) and potassium doped tungsten just taking into account radial-oriented samples (WVM). Data from Faleschini et al. [Fal07a] and redrawn in [Wur09]

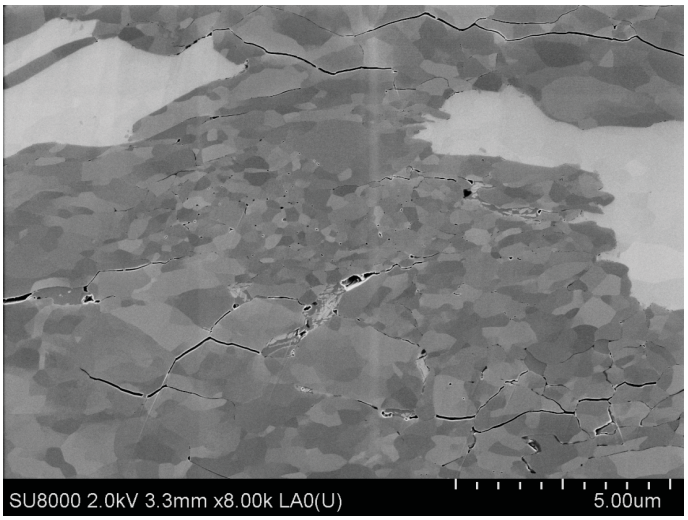

Figure 2-8: Cross-section polished surface of a W-30Ta composite showing cracks lying within the shear plane.

Changing the topic to the microstructural size of phases: as it can be seen in Publication C, tantalum and tungsten powder particles conglomerate (Publication C, Figure C.10,a and Figure 2-11 within this chapter) and do not necessarily break up during simple powder mixing procedures. Vanadium powder particles are rather loosely bound (Figure 2-11,d). Applying strains below 10 is

not enough to result in strong intermixture of phases – this results in a rather coarse-grained "phase microstructure" within the range of tens of micrometers.

A qualitative chemical analysis can be performed using the EBSD method. The identification of bright and dark regions in Figure 2-11,b with tungsten and tantalum rich regions is proven in Figure 2-9. In general, EBSD can be used for phase analysis directly from certain features of the recorded Kikuchi patterns but due to the same crystal structure and a small difference in lattice parameters (a_{Ta} = 0.330 nm, a_W = 0.317 nm [Nag91]) it is difficult to perform. A simple Image Quality (IQ) analysis using the software OIM – Orientation Imaging Microscopy v5.31, shown in Figure 2-9, helps to fasten the qualitative chemical analysis of composite phase microstructure. IQ describes the quality of the Kikuchi pattern; the crystalline regions experiencing more distortions are represented in dark grey or black. Within Figure 2-9, bright regions correspond to tungsten and darker regions correspond to tantalum.

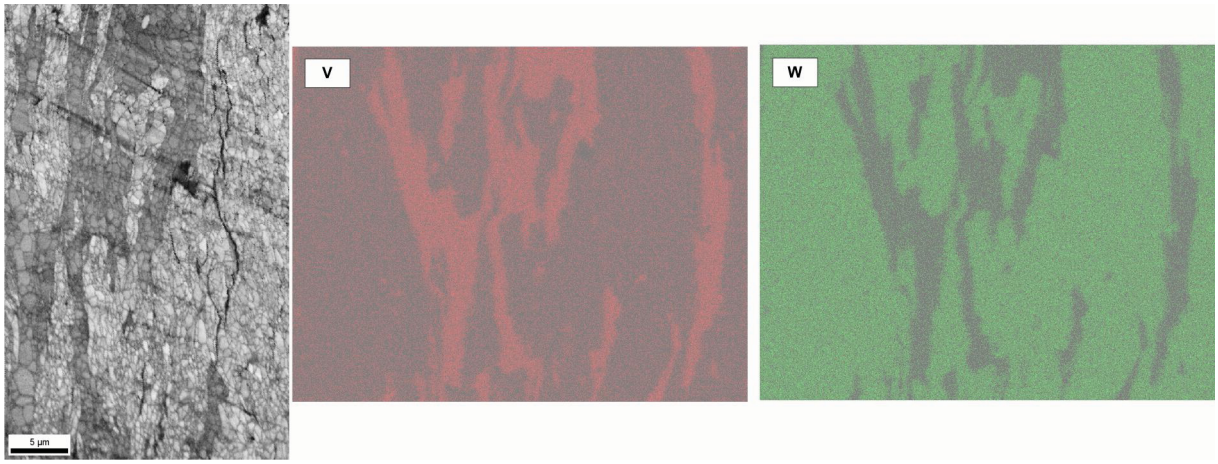

Figure 2-9: IQ map from EBSD analysis of the HPT – deformed W-30Ta composite, surface preparation: cross-section polishing with HITACHI E-3500. The comparison of IQ map with EDX – mapping of tungsten and tantalum demonstrates: darker regions represent vanadium rich regions, brighter regions represent tungsten rich regions. For better visibility, brightness and contrast was adjusted.

Milling, replacing simple powder mixing, shall become a new method leading to smaller, chemically homogeneous regions. Alternating phases on a smaller scale inhibit crack propagation within brittle phases (i.e. tungsten) over long distances – hence, an improved fracture behavior is expected. Nevertheless, one has to be aware of diffusion processes at high temperatures. Preferential pathways for diffusion within these ultra-fine grained materials will be along large areas of grain boundaries. Composite materials of, e.g. randomly distributed grains of tungsten and other elements, with the grains being in the regime of hundreds of nanometers, might loose their composite character. This will be especially detrimental, when the change in chemical composition

leads to intermetallic phases or alloying compositions that are more brittle than the original materials.

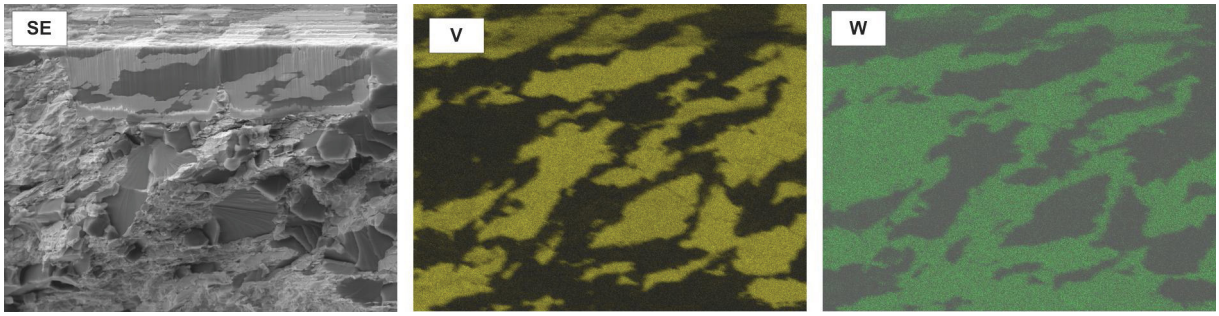

Figure 2-10: Depicting the "phase microstructure", introduced in the text above. a) SE image of FIB-notched region of a 3PB specimen made of W-25V composite material (specimen tested in [S-A] orientation, K_Q = 13.1 MPa $m^{1/2}$. More information in 15th row in Table C.1. in Publication C), the length of the FIB – notch is about 100 µm. The figure is completed with EDX mappings of vanadium and tungsten. Contrast and brightness of tungsten – mapping was adjusted for visibility.

Faleschini [Fal07b] reports on pure, bulk tungsten that was HPT-deformed within the same range of strains as investigated in Publication C and annealed at 1000 °C for 1 h. This annealing procedure results in grain sizes of about 2 µm. However, as it can be seen in Publication C, the grain size is in the regime of hundreds of nanometers. Impurities within the powder and on the large powder surface are expected to be present and furthermore a thin tungsten oxide layer developing during the heating of the samples to 300°C might be the reasons for hampering grain growth during annealing. The open porosity of the sample was determined to be zero by comparing bulk density and the density without any open porosity using a helium pycnometer [Garc]. Nevertheless, there is a certain amount of oxygen entrapped during compaction (closed porosity) and this leads to formation of oxide layers when keeping the sample at 300 °C for about 1 h while the HPT processing is performed.

2.3. The high content WTa and WV alloys

For investigating solid solution alloys based on composite production, suitable thermo-mechanical treatments are necessary. A simple annealing at very high temperatures, ideally close to the melting point of the lower-melting material because of short processing time, leads to remarkable diffusion and a chemical homogenization of the material (Publication C) but also to increased porosity supposedly because of the Kirkendall effect. This effect is a consequence of differences in diffusion constants of tungsten in element X and element X in tungsten at the annealing temperatures. The vanadium composite was annealed for 1 h at 1800 °C and the tantalum composite for 1 h at 2500 °C resulting in compositions of 18 to 30 wt% V at selected points on a fracture surface. The tantalum composite had a composition of 30 to 38 wt% Ta. Chemical compositions were determined with energy dispersive X-ray spectroscopy (EDX). Due to its brittleness, the solid solution treated tungsten-vanadium material could not have been tested under defined conditions. The tantalum composite shows a decrease in toughness to about 4 MPa $m^{1/2}$, this is even less in relation to the worst testing direction regarding HPT-deformed composite samples.

Other possibilities to achieve solid solution, such as electron beam melting, powder production and subsequent runs of powder compaction and HPT, as well as hot isostatic pressing of composites at very high temperatures are still under investigation. Electron-beam melting of W-25V and W-50V was already performed successfully ($T_{liquidus,\ W\text{-}25V}$ ~ 2900 K [Nag91], $T_{liquidus,\ W\text{-}50V}$ ~ 2500 K [Nag91]), complete melting of W-2Ti could not have been achieved ($T_{liquidus,\ W\text{-}2Ti}$ ~ 3500 K [Nag91]) in a first approach. The vanadium content of the W-25V composite was reduced by about 50% due to evaporation of vanadium during electron beam melting in argon atmosphere, resulting in a W-12V alloy. The vanadium content of the W-50V composite did not change. Figure 2-12 depicts the microstructure of the W-12V alloy; the vanadium content was determined with EDX at several points to be about (12 ± 2) wt%. The recrystallized and large-grained microstructure is in contrast to the dendritic microstructure of the electron beam melted W-50V alloy shown in Figure 2-13. This figure presents the microstructure and an EDX mapping of the elements tungsten and vanadium. 3PB samples as they were used for WV- and WTa-composites outlined in Publication C, were used. The fracture toughness of the alloy containing low vanadium was found to be (5.6 ± 0.3) MPa $m^{1/2}$.

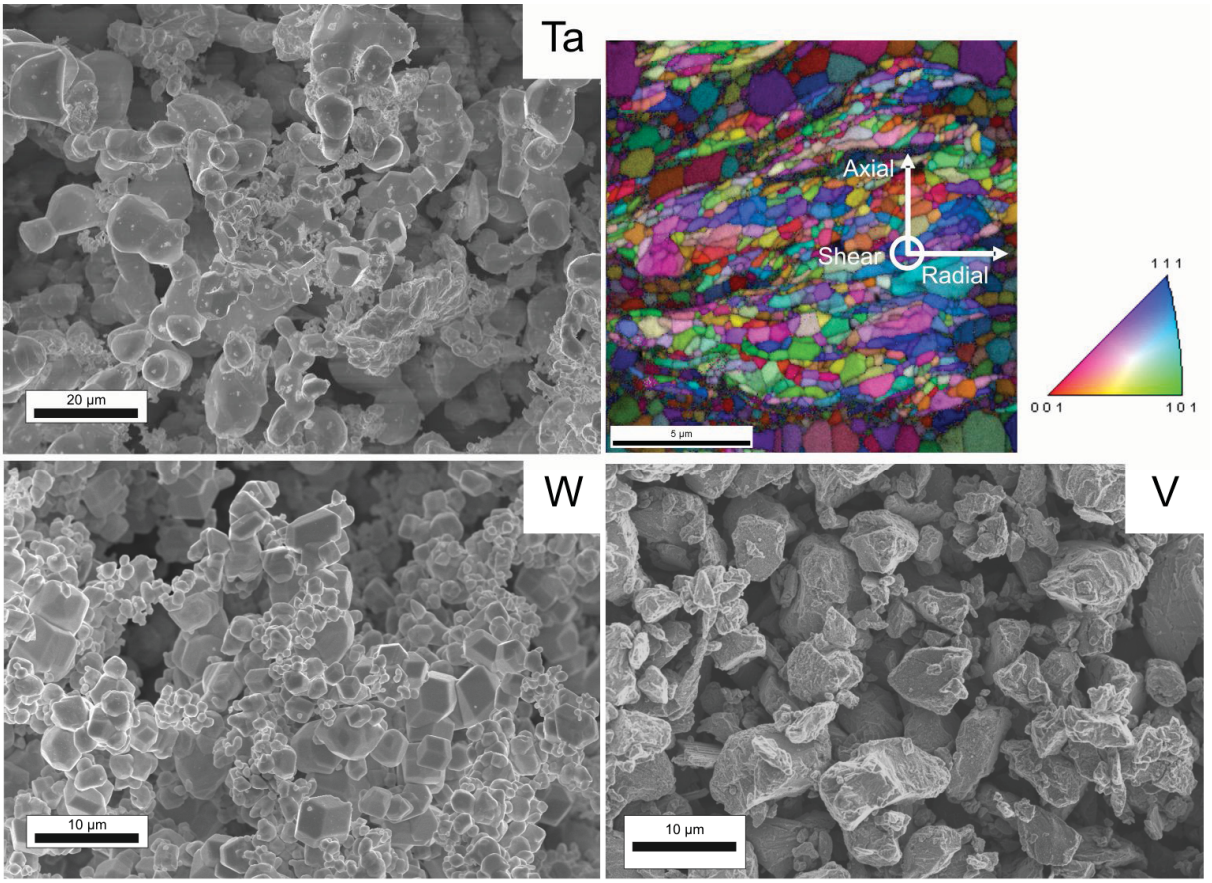

Figure 2-11: SEM micrographs of tantalum (a), tungsten (c) and vanadium (d) powders used for composite production, showing the conglomeration of tungsten and tantalum powders. b) Inverse Pole Figure combined with a grayscale overlay representing the image quality. Bright regions: tungsten rich, dark: tantalum rich; Material: HPT – deformed W-30Ta composite at a radius of r ~ 3 mm, surface preparation: cross-section polishing with HITACHI E-3500.

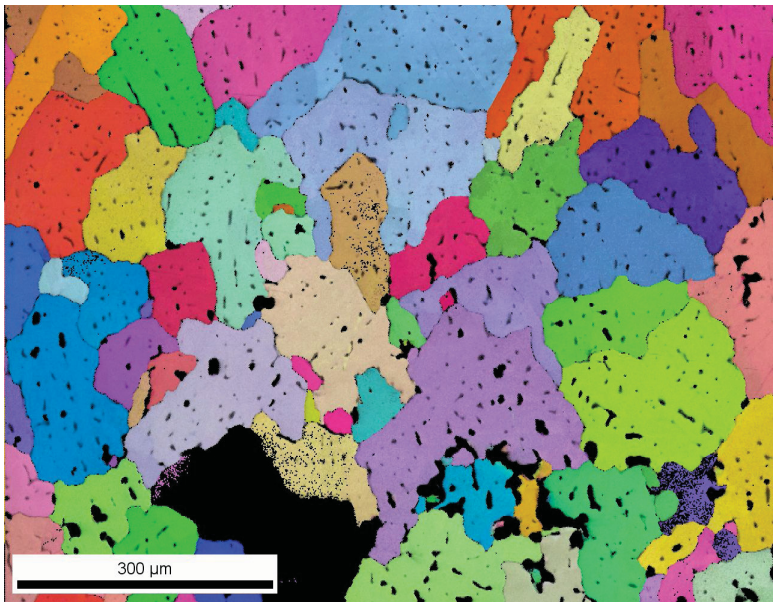

Figure 2-12. IPF with an grey – scale overlay of IQ, showing the microstructure of the electron beam melted W-12V alloy (original composition W-25V). One grain in the lower region was not successfully indexed; thus, it is shown in black.

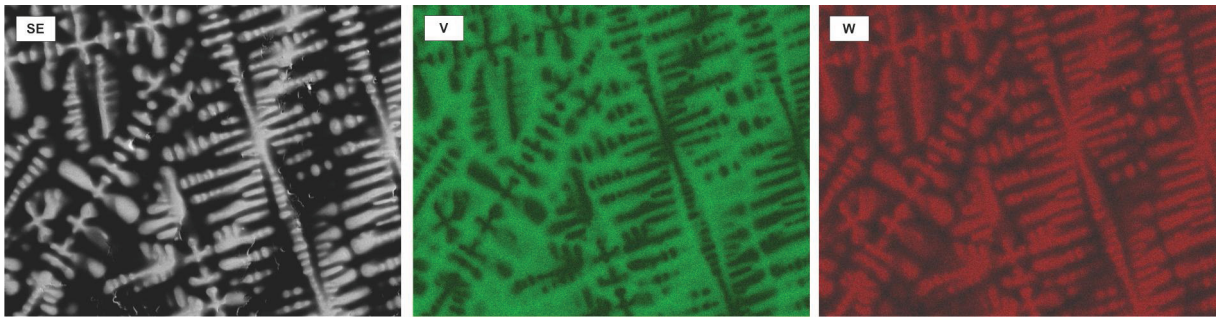

Figure 2-13: a) SE image of the polished surface of the electron beam melted W-50V composite. The figure is completed with EDX mappings of vanadium and tungsten showing the dendritic microstructure. Contrast and brightness of tungsten – mapping was adjusted for visibility.

As already pointed out, there is a decrease in Peierls stress at high tantalum contents [Rom], but an improved (fracture) mechanical behavior was not found for the W-30Ta alloy, as first experiments on annealed material show. The low fracture toughness is in marked contrast to an increased toughness of tungsten-rhenium alloys (W-26Re) in recrystallized state.

These results on fracture behavior can be confirmed by bending of micrometer-sized cantilevers (Figure 2-14) cut from the 2500 °C – treated W-30Ta composite [Li]. EDX analysis on the base support of a cantilever show a mean tantalum concentration of about 24 wt%; the decrease in tantalum concentration, starting from a W-30Ta composite might be due to still existent compositional differences after the heat treatment. Two cantilevers made of tantalum containing

material were tested and brittle failure along grain boundaries took place with unstable crack propagation. This type of failure was observed neither for notched and un-notched micrometer-sized cantilevers made of single crystalline tungsten nor for technically pure tungsten nor for W-26Re. The W-30Ta composite, which was annealed for 1 h at 2500°C showed an increasing amount of pores, weakening the un-notched cantilever in the highly stressed region. However, as pores were also found in a (tested) pure tungsten material in as-sintered state [Li], where no unstable crack propagation took place, this is more likely to explain crack initiation than crack propagation. An increase in toughness of W-30Ta can be expected to take place after applying deformation, as it was the case for W-1Ta and W-5Ta (Publication C). However, this is just in the case that forging is possible at all – forging of W-10Ta resulted in fracture of the material [Hof].

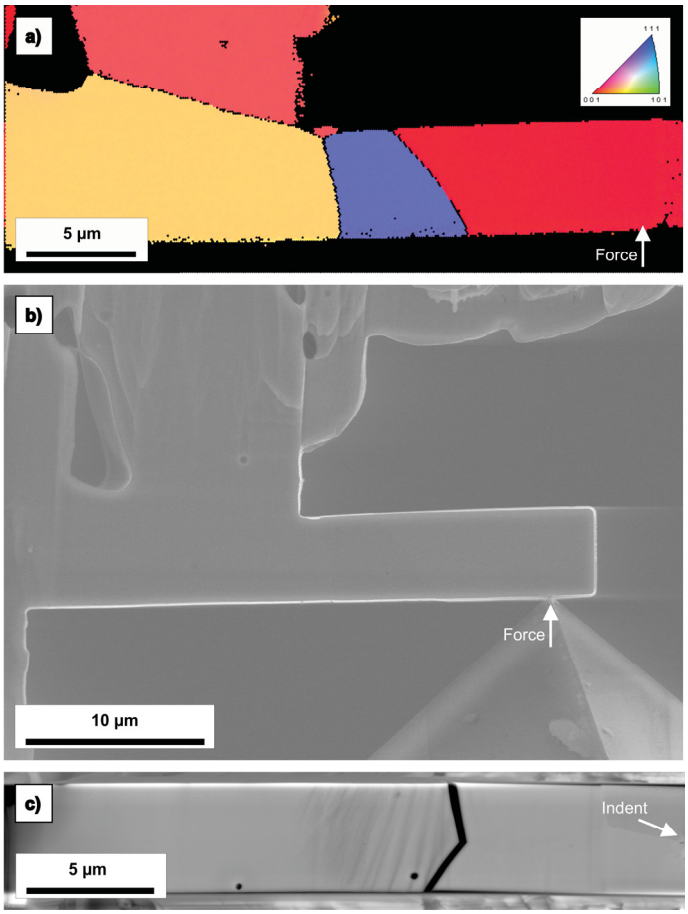

Figure 2-14: a) IPF map of an un-notched WTa cantilever. Direction of loading is also depicted. b) shows an SE-image of the experimental set-up for the same cantilever prior to in-situ-loading with a cube corner indenter. c) Backscattered electron micrograph showing the top surface of the same cantilever. The image shows the crack propagating along the grain boundaries and the traces of the slip planes within the grain shown in orange. Taken from [Li], being in preparation.

2.4. Nanocrystalline Materials and Irradiation Effects

Nanocrystalline materials, not necessarily containing any ductilizing agent, processed by Severe Plastic Deformation (SPD) using High Pressure Torsion (HPT) combine the possibilities of achieving a high toughness in at least two testing directions [HohA10, Wur11]; furthermore, they might show an increased resistance against irradiation. Irradiation (neutrons, alpha particles …) degrades material properties, e.g. increases the hardness, and lowers the ductility and the DBTT. This was the motivation to summarize recent results on irradiation resistance of nanocrystalline and ultra-fine grained fusion relevant materials like reduced-activation ferritic / martensitic (RAFM) steels and tungsten-based material (Publication A).

According to Shen [She08], there is an optimum grain diameter in respect of a general phase transition (e.g. changing the crystallographic structure or amorphization, as described therein), which is material dependent. Using the wording, presented in this publication, “smaller” necessarily is not better but “smaller” can be better. The free energy from grain boundaries goes with 1/d and this has to be outbalanced by the free energy from point defects, increasing with d^2. *d* is the grain diameter. Consequently, the smallest grains do not necessarily constitute the highest irradiation resistance. It should – in principle – be possible to achieve the material dependent, optimum grain size by computer simulations (e.g. molecular dynamics) or experimental work.

The high grain boundary area per unit volume increases the tendency to heal out point defects generated by collision cascades originating from irradiation with high energetic particles. However, one has to be aware of a potentially deteriorated creep behavior, which is also of great importance as plasma facing components have to withstand high temperatures for long times. Furthermore, heat loading of (tungsten) plasma facing materials in fusion reactors must not automatically lead to grain growth. Thus, usage of dispersion-strengthened tungsten (Section 1.6.1.) has to be envisaged. Recent successful results regarding thermal shock resistance of tungsten with TiC dispersoids [Pint11b] show that it is possible to find new combinations of materials with improved properties. However, the processing of such materials – including HPT-deformed tungsten based material, described above – is far from industrial scale. This still constitutes a big challenge.

2.5. Micrometer – Sized Fracture Experiments

Experiments using micrometer-sized samples should be of high interest for the fusion community. Material experiencing a defined irradiation process for experimental purposes is limited in volume. This holds true for samples irradiated with neutrons and even more for materials irradiated with heavier particles (alpha particles, ions …). The penetrating depth of tungsten ions in tungsten is just a few hundreds of nanometers [Arm11], fracture experiments using such small volumes is at the moment beyond the method that will be introduced here. For homogeneously irradiated volumes in the range of micrometers, however, it is applicable. These micrometer sized fracture experiments enable us to gain additional information from the same amount of material. The limitation in sample size has a further beneficial effect. Testing of large samples (i.e. samples of standard size) sometimes necessitates the usage of hot cells, which might be avoided as regulations regarding radiation protection should be obeyed more easily.

In general, it is possible to produce samples out of electrolytically etched needles [Kie08]. In this case, the long, thin and compliant needle would complicate bending of a cantilever sitting on top of the needle. Manufacturing of samples out of bulk material – as it was already successfully demonstrated either at the edge [Mot05] or centrally located within the material [DiM05] – is also possible. However, this is a time consuming method, especially when cutting tungsten based materials. In advance, long milling steps using high currents are needed to cut trenches around the specimens. Hence, a new idea was developed in the framework of this study (Publication D) to quicken the production of micrometer-sized samples. An “Ion Slicer”, typically used for transmission electron microscopy sample production, prepares very thin lamellas, which are preforms for subsequent FIB-cutting. The FIB is still needed, however the milling time is shortened and consequently, the ion irradiation damage is expected to be lower. All ion-sliced samples that will be described in this thesis were prepared at the Institute of Metals and Technology (Ljubljana, Slovenia) utilizing an EM-09100IS Ion Slicer from JEOL. Argon ions, accelerated by up to 6 kV, remove large amounts of material and leave behind lamellas with several hundreds of micrometers in length but just a few micrometers in thickness.

Giving a short outlook on further work, the acquisition of a cross section polisher (HITACHI E-3500), normally used for scanning electron microscopy sample preparation will be applied to perform the same task as the ion slicer does and maybe even more. Again, argon ions with energies below 6 keV are used to polish macroscopically large areas (~ 1 mm²). By design of improved shielding structures, the generation of thin lamellas for subsequent FIB-cutting, maybe even of the specimens themselves is envisaged. Ideally, these specimens do not have to be cut with the FIB and furthermore this should enable the fabrication of small samples made of materials which cannot be processed with the FIB using a gallium beam, e.g. aluminum.

With increasing interest in the mechanical behavior of FIB-made samples, the interest in the nature and consequences of damage induced by ion milling also increased [Kie07, Shi09]. Thus, the usage of argon ion produced samples create a new potential to compare results from argon milled and gallium milled samples. Argon ions (atomic mass ~ 40) of low energy are less detrimental (i.e. less penetrating) to e.g. tungsten than high energy gallium ions (atomic mass ~ 70). This is confirmed with the help of simulations using the SRIM[8] code [Zie85], the results are shown in Figure 2-15. There, a decrease in penetrating depth for slow argon ions (6 kV) in comparison to fast gallium ions (30 kV) is shown, both for perpendicular and grazing (parallel to the surface) impact of the ion beam on a tungsten target. Ion ranges are about twice as large for gallium ions compared to argon ions.

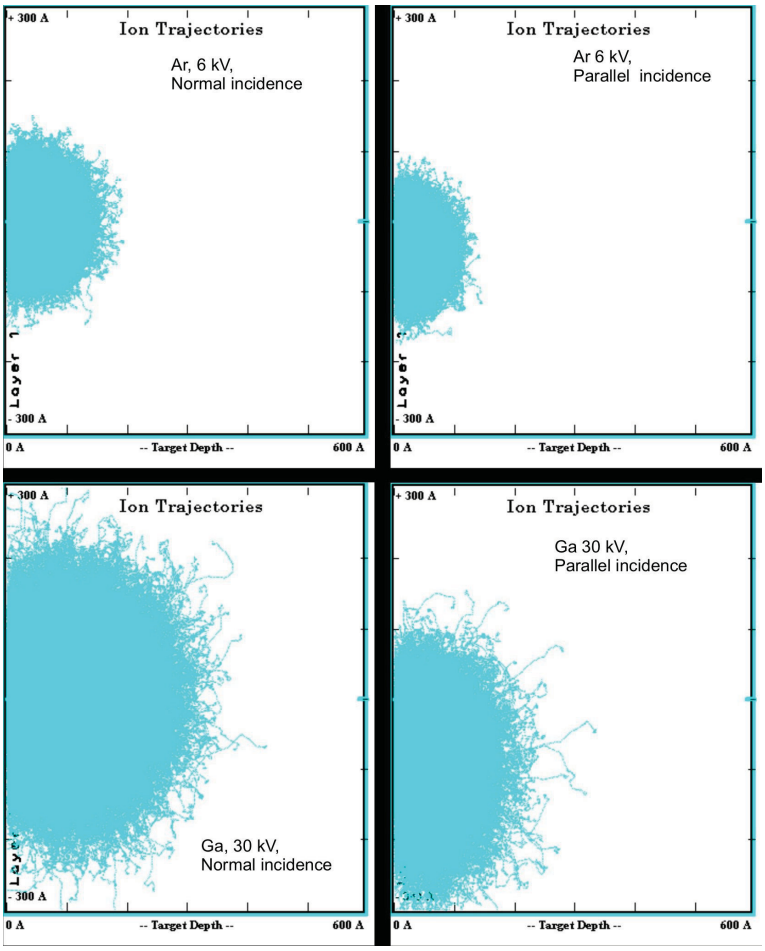

Figure 2-15: Simulations basing on the SRIM code [Zie85] for Ar-ions (6 kV) with W target (normal and parallel incidence, upper row) and Ga-ions (30 kV) with W target (normal and parallel incidence, lower row).

[8] Stopping and Range of Ions in Matter

The main goal of the work dealing with micrometer-sized samples was to investigate, evaluate and hence to better understand the brittle fracture of tungsten. Single crystalline specimens were produced with their crystallography being close to the one of macroscopic specimens showing the lowest fracture toughness at room temperature [Ried, Ried96]. Several small samples with FIB-made notches and natural crack were loaded in the in-situ experiments. The FIB-made notches were aligned at different angles towards the cleavage plane, the crack front direction respectively. Scanning electron microscopy facilitated detailed observation of the fracture process.

Publication F describes the evaluation and results of conditional fracture toughness values, K_Q, which were derived from load vs. displacement diagrams according to Equations (10) and (11). This evaluation is based both on linear elastic fracture mechanics based on ASTM E399 [AST90] and elastic plastic fracture mechanics. As already mentioned in the introduction (Section 1.3.) and later on in the corresponding Publication E, the determination of geometrically necessary factors f(a/W), which are sample shape dependent (equations (5), (7), (9) and (11)) relies on finite element computer simulations using ABAQUS software. Within this chapter, the results for $f(a/W)$ for notched cantilevers are compared with results for single edge crack pure bending specimens [Mur87]. As it is shown in Figure 2-16, the values of $f_{cantilever}(a/W)$ and $f_{[Mur87]}(a/W)$ are in good agreement. Within the range of 0.2 to 0.7 for a/W the results differ by less than 5 %.

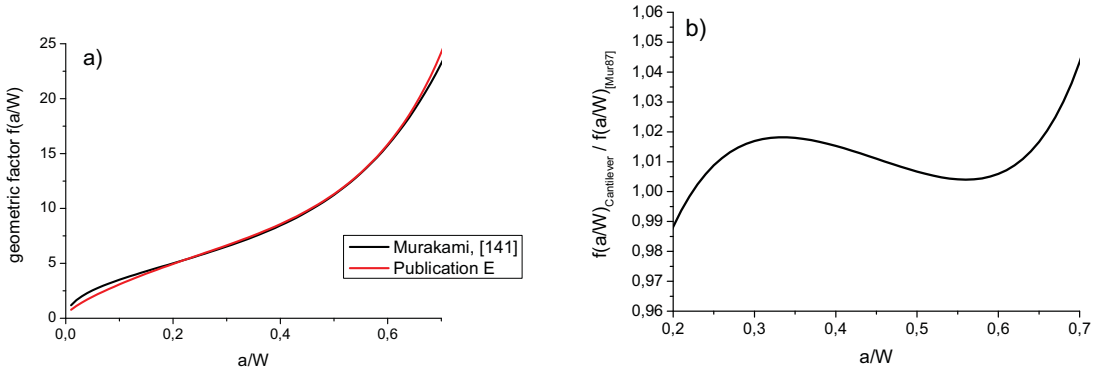

Figure 2-16: a) Sample-shape-dependent geometry factors for determination of fracture toughness values. Results from Publication E [Wur10a] compared to results given in Murakami [Mur87]. b) Ratio of values of $f(a/W)$ taken from [Mur87] and [Wur10a].

The approach to evaluate micrometer – sized fracture experiments basing on LEFM results in lower bounds, several requirements regarding sample size cannot be fulfilled. Therefore, they are denominated as $K_{Q,\ LEFM}$. Production of larger samples would circumvent the problem of specimen size to a certain extent but this would increase the machining time with the FIB and would somewhat be contradictory to the above-mentioned advantages and the general idea of this method. Although tungsten is generally attributed to be of low toughness at room temperature, the combination of toughness and yield stress (Equation (12)) in combination with the small sample

size makes it necessary to determine conditional fracture toughness values basing on specimens' crack tip opening displacement (*CTOD*) and *J*-integrals, i.e. to apply elastic-plastic fracture mechanics.

Crack tip opening displacements were determined considering a hinge model [Brit72] (Publication F, Figure F.5 therein) and resulted in typical CTOD-Δa-curves. J-integrals were calculated from curves showing force versus corrected indenter displacement. In advance, these curves were adjusted according to a translation of the lamella the specimens are located on and furthermore, according to the generation of an indent. Again, typical J-Δa-curves can be drawn. Knowledge on crack growth, which is necessary to end up with the above-mentioned curves, was gained both by direct observation of the fracture process in the SEM and by determination of the unloading compliance. Crack propagation leads to an increase in cantilevers' compliance. From both curves, CTOD-Δa and J-Δa, conditional fracture toughness values were calculated. They are depicted in Figure 2-17, together with results from LEFM and $K_{Q,J}$ from the 2nd unloading compliance. For a detailed description of the evaluation and a elaborate discussion of the results, the reader is forwarded to Publication F.

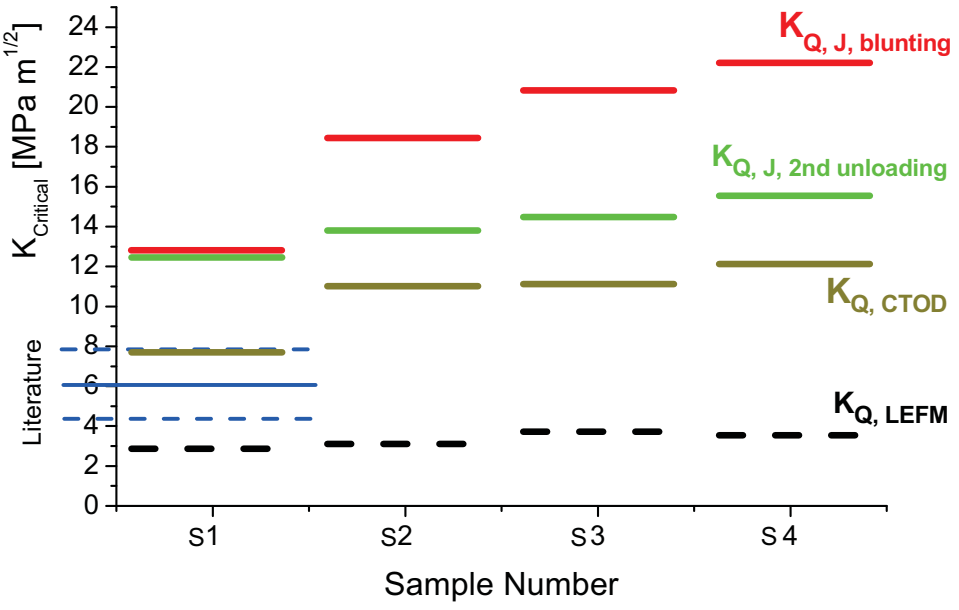

Figure 2-17: Conditional, critical stress intensity factors showing $K_{Q,\ LEFM}$ giving lower limits for fracture toughness together with results from elastic plastic evaluation ($K_{Q,\ J,\ blunting}$, $K_{Q,\ J,\ 2nd\ unloading}$ and $K_{Q,\ CTOD}$). Fracture toughness values from [Ried, Ried96], based on LEFM, are indicated with blue lines. The sample numbers 1 to 4 correspond to increasing deviation of notch plane from cleavage plane (No.1: coinciding, No.2: 5°, No.3: 15°, No.4: 25°). Taken from Publication F.

As expected $K_{Q,\ LEFM}$ represent lower bounds for valid K_{IC}-values. All results from evaluations involving the J-integral that can be compared with values from literature (Sample No.1) are higher by a factor of two. If this phenomenon is an intrinsic effect of the sample size in the case of semi-brittle fracture or a question of the correct determination of the transition from blunting to stable crack growth, has to be investigated in the future by varying the size of the samples. Fracture toughness values from CTOD – evaluation are in good accordance with values found in literature. Furthermore, it can be expected to increase the accuracy of the methods presented in Publication F, when increasing the number of unloading steps, thus acquiring more data on crack growth, CTOD and J-values.

The appearance of stable fracture for all samples tested in the micrometer regime might be explained with a model from Hirsch et al. [Hir92], describing stable crack growth by micro-cleavage in semi brittle materials. Shielding and anti-shielding dislocations are emitted close to or at the crack tip. The latter type forces the crack to grow due to high tensile stresses acting on the crack tip, whereas shielding dislocations move away from the crack tip and stabilize the crack propagation. The free length of movement for shield dislocations is much higher for millimeter-sized samples than for micrometer-sized ones. There, dislocations are affected by repulsive compressive stresses below the neutral axis of bending. Thus, the crack tip shielding stress intensity declines quicker for larger samples and more dislocations can be emitted; this also includes anti-shielding dislocations supposedly triggering fracture in tungsten single crystals.

A second point that was treated by using these small samples was to demonstrate the equivalency of FIB-made notches and natural cracks. Cantilevers made of single crystalline tungsten were produced out of bulk material, where natural cracks due to a thermal treatment during cutting the crystal were introduced. It has to be emphasized that the crack front did never experience any FIB-cutting and ion irradiation damage. As can be seen in Section 3.3. in Publication F, the general appearance of the force vs. indenter displacement curve and crack propagation mechanisms do not change. Crack growth is stable. Evaluation of critical fracture toughness values from both linear elastic and elastic plastic fracture mechanics is difficult due to several reasons: 1) The crack length is not constant with specimen thickness. 2) Bending length was short compared to specimen width. 3) The crack is not straight but inclined, thus experiencing a mixed loading condition. Nevertheless, it can be stated that conditional fracture toughness values are comparable to the ones of FIB-notched cantilevers.

3. Summary

In this short section, important questions will be answered, but maybe more have risen:

Rhenium alloying was shown to be an alloying element not just ductilizing but also toughening tungsten. Recrystallization, which is unavoidable in highly heat loaded areas e.g. at the fusion reactor's first wall, lowers the fracture toughness in comparison to the one of an as-worked microstructure; nevertheless, the fracture toughness is high and outclasses pure, recrystallized tungsten. Fracture surfaces show a large amount of grain boundary fracture but these grain boundaries are strengthened by the rhenium additions. However, due low the low abundance of this element, any use of tungsten – rhenium alloys for several large fusion power plants is not recommendable. The improved mechanical properties seem to be attributable to a change in core structure of screw dislocations. Unfortunately, according to density functional computer simulations this was not found for any other alloying element up to now [Rom]. Alloying tungsten with tantalum, showing a completely different phase diagram compared to W-Re, is not detrimental for low tantalum alloying contents – solid solution softening can be expected at very low contents and low temperatures. Higher tantalum additions did not enhance the solid solution alloy's fracture properties. There are hints of a decrease in Peierls stress for higher tantalum compositions than were investigated in this study for solid solution alloys. Transmutation – seriously affecting tantalum – will shift the composition again towards a tungsten rich regime. Composite materials, prepared by consolidation via an HPT-process, are promising regarding their fracture behavior. Ultra-fine grained material showed high toughness in two out of three testing directions. This accentuates the point that it is possible, rather necessary to design the (fracture) properties of tungsten and tungsten based materials by microstructural design and anteceding forming steps. Any forming step leading to a microstructural anisotropy is advisable. Furthermore, ultra-fine grained and nanocrystalline materials show an increased irradiation resistance, because of the fact that the vast amount of grain boundaries act as sinks for defects. For a complete understanding of the interrelation of irradiation – 14 MeV neutron irradiation, in particular – a large number of experiments are required and this is the point where experiments on the micrometer scale are a meaningful assistance to standard sized experiments with standard samples. Up to now, fracture experiments on micrometer sized samples made of different materials, not including tungsten, were based on linear elastic fracture mechanics. As the scientific research on fusion materials is directed towards finding tough and ductile materials, this is not sufficient anymore and elastic plastic fracture toughness was successfully introduced to small-scaled fracture experiments with tungsten single crystals serving as a model material. Of course, further research has to be performed in order to determine the absolute limit in sample size as a function of strength and toughness to give meaningful results using this method.

4. Outlook

What are the measures that have to be taken in order to make tungsten applicable for new fusion technologies?

Scientific research, including this thesis, has not increased the number of alloying elements, which enhance tungsten's material properties. Titanium gave some hints to do so, and this will be pursued; nevertheless, "pure tungsten seems to be the best tungsten" (© M. Rieth) – excluding minor additions of oxides, nitrides, etc. as will be outlined soon.

From the fracture mechanical point of view, the microstructure has to be designed in a way to end up with small, plate-like grains. This shape offers the advantage of the presence of an increased number of tough testing directions compared to globular or needle-shaped grains. The size of the grains should be in the range of several hundreds of nanometers, with the thickness being about 100 nm to 200 nm and an aspect ratio grain diameter versus thickness of about 5 to 10.

This small grain size is beneficial for increased fracture toughness and it is expected to be beneficial for an increased irradiation resistance. The microstructure is achievable via the technique of High Pressure Torsion. HPT – processing is a very versatile tool to process a variety of materials and to end up with ultra-fine grained or nanocrystalline grains, often leading to improved material properties. However, an inherent disadvantage of this HPT is the impossibility to modify the method in order to process substantially larger amount of material. Consequently, it is recommended to search for and apply processes resulting in the same microstructural outcome for example by rolling or other deformation processes.

The microstructure has to be stabilized by addition of e.g. yttrium oxide and lanthanum oxide or titanium carbide or immiscible elements (K,…) leading to grain boundary strengthening and hampering of the recrystallization process. Furthermore, a point that still lacks very detailed examination, and thus understanding, is the interaction of particle irradiation (e.g. fast neutrons) with matter in general, and in this special case with tungsten based materials. That is, the final qualification of any new small – grained tungsten material has to be determined by irradiation tests.

References

[And95] T.L. Anderson, Fracture Mechanics – Fundamentals and Applications, Boca Raton, Ann Arbor, London, Tokyo, 2nd edition, CRC Press, 1995, p. 343 ff.

[Arg66a] A.S. Argon, S.R. Maloof, Plastic deformation of tungsten single crystals at low temperatures, Acta Metall. 14 (1966) 1449 – 1462

[Arg66b] A.S. Argon, S.R. Maloof, Fracture of tungsten single crystals at low temperatures, Acta Metall. 14 (1966) 1463 – 1468

[Arm11] D.E.J. Armstrong, Micro-Mechanical Testing, oral presentation at the 13th International Workshop for Plasma-Facing Materials and Components for Fusion Application & 1st International Conference on Fusion Energy Materials Science, Rosenheim, 9th – 13th of May, 2011

[Ale79] I. Alexandrow, I.V. Gorynin, Metallovedenie 22 (1979) 35

[AST90] Annual Book of ASTM Standards – Standard Test Method for Plane-Strain Fracture Toughness of Metallic Materials (ASTM E399-90), reapproved 1997, American Society for Testing and Materials

[Bara00] V. Barabash, G. Federici, M. Rödig, L.L. Snead, C.H. Wu, Neutron irradiation effects on plasma facing materials, J. Nucl. Mater. 283 – 287 (2000) 138 – 146

[Bara03] V. Barabash, G. Federici, J. Linke, C.H. Wu, Material/plasma surface interaction issues following neutron damage, J. Nucl. Mater. 313 – 316 (2003) 42 – 51

[Barn11] H.S. Barnard, B. Lipschultz, D.G. Whyte, A study of tungsten migration in the Alcator C-Mod divertor, J. Nucl. Mater (2011), in press, doi:10.1016/.j.jnucmat.2010.12.317

[Bea65] P. Beardmore, D. Hull, Deformation and fracture of tungsten single crystals, J. of Less-Common Metals, 9 (1965) 168 – 180

[Boo64] J.G. Booth, R.I. Jaffee, E.I. Salkovitz, The mechanisms of the rhenium-alloying effect in group VI-A metals, Proceedings of the 5th Plansee Seminar, Reutte (1964) 547 – 570

[Brit72] Methods for Crack Opening Displacement (COD) Testing DD 19:1972, British Standards Institutions, London, 1972

[Cam05] D. Campell, Magnetic confinement fusion: tokamak, in: K. Heinloth (Editor), Landolt-Börnstein Numerical Data and Functional Relationships in Science and Technology Group VIII: Advanced Materials and Technologies, Vol. 3. Energy Technologies, Subvolume B: Nuclear Energy, Berlin, Heidelberg, New York, Springer, 2005

[Che08] Y. Chen, Y.C. Wu, F.W. Yu, J.L. Chen, Microstructure and mechanical properties of tungsten composites co-strengthed by dispersed TiC and La_2O_3 particles, Int. J. of Refr. Met. Hard Mater. 26 (2008) 525 – 529

[Chr83] J.W. Christian, Some surprising features of the plastic deformation of body-centered cubic metals and alloys, Met. Trans. A 14A (1983) 1237 – 1256

[Con98] J.W. Connor, Review model for ELMs, Plasma Phys. Contr. Fusion 40 (1998) 191 – 213

[Cor72] J.E. Cordwell, D. Hull, Observation of {110} cleavage in <110> axis tungsten single crystals, Phil. Mag. 26 (1972) 215 – 224

[Cot04] G.A. Cottrell, Sigma phase formation in irradiated tungsten, tantalum and molybdenum in a fusion power plant, J. Nucl. Mater. 334 (2004) 166 – 168

[DiM05] D. Di Maio, S.G. Roberts, Measuring fracture toughness of coatings using focused-ion-beam-machined microbeams, J. Mater. Res. 20 (2005) 299 – 302

[Du10a] J. Du, T. Höschen, M. Rasinski, S. Wurster, W. Grosinger, J.-H. You, Feasibility study of a tungsten wire-reinforced tungsten matrix composite with ZrO_X interfacial coatings, Composites Science and Technology 70 (2010) 1482 – 1489

[Du10b] J. Du, T. Höschen, M. Rasinski, J.H. You, Interfacial fracture behavior of tungsten wire / tungsten matrix composites with copper-coated interfaces, Mat. Sci. Eng. A 527 (2010) 1623 – 1629

[Du11] J. Du, T. Höschen, M. Rasinski, J.-H. You, Shear debonding behavior of carbon-coated interface in a tungsten fiber-reinforced tungsten matrix composite, J. of Nucl. Mater. (2011) doi:10.1016/j.jnucmat.2010.12.254 (article in press)

[Dux09] R. Dux, V. Bobkov, A. Herrmann, A. Janzer, A. Kallenbach, R. Neu, M. Mayer, H.W. Müller, R. Pugno, T. Pütterich, V. Rohde, A.C.C. Sips, ASDEX Upgrade Team, Plasma-wall interaction and plasma behaviour in the non-boronised all tungsten ASDEX upgrade, J. Nucl. Mater. 390 – 391 (2009) 858 – 863

[Ehr00] K. Ehrlich, E.E. Bloom, T. Kondo, International strategy for fusion materials development, J. Nucl. Mater. 283 – 287 (2000) 79 – 88

[Fal07a] M. Faleschini, H. Kreuzer, D. Kiener, R. Pippan, Fracture toughness investigations of tungsten alloys and SPD tungsten alloys, J. Nucl. Mater. 367 – 370 (2007) 800 – 805

[Fal07b] M. Faleschini, Severe Plastic Deformation of Tungsten Alloys and its Influence on Fracture Behaviour, PhD thesis, Leoben, 2007

[FDR01] Summary of the ITER Final Design Report, July 2001

[Fuj96] M. Fujitsuka, I. Mutoh, T. Tanabe, T. Shikama, High heat load test on tungsten tungsten containing alloys, J. Nucl. Mater. 233 – 237 (1996) 638 – 644

[Garc] C. Garcia-Rosales, CEIT, Spain, personal communication

[Garf66] M. Garfinkle, Room-temperature tensile behaviour of <100> oriented tungsten single crystals with rhenium in dilute solid solution, NASA Technical Note, NASA TN D-3190. Washington DC, January 1966

[Gark05] I.E. Garkusha, A.N. Bandura, O.V. Byrka, V.V. Chebotarev, I.S. Landman, V.A. Makhlaj, A.K. Marchenko, D.G. Solyakov, V.I. Tereshin, S.A. Trubchaninov, A.V.

Tsarenko, Tungsten erosion under plasma heat loads typical for ITER type I ELMs and disruptions, J. Nucl. Mater. 337 – 339 (2005) 707 – 711

[Gea55] G.A. Geach, J.E. Hughes, The Alloys of Rhenium with Molydenum or with Tungsten and Having Good High Temperature Properties, Proceedings of the 2nd Plansee Seminar, Reutte (1955) 245 – 253

[Gea59] G.A. Geach, F.O. Jones, The zone melting of refractory metals including rhenium and tungsten, J. of Less-Common Metals, 1 (1959) 56 – 59

[Gia07] A. Giannattasio, S.G. Roberts, Strain-rate dependence of the brittle-to-ductile transition temperature in tungsten, Phil. Mag. 87 (2007) 2589 – 2598

[GilA66] A. Gilbert, A fractrographic study of tungsten and dilute tungsten-rhenium alloys, J. of Less-Common Metals 10 (1966) 328 – 343

[GilMR10] M.R. Gilbert, Transmutation and He Production in W and W-alloys, CCFE-R10(01) Culham Centre for Fusion Energy, http://www.ccfe.ac.uk/assets/Documents/CCFE-R(10)1.pdf, (2010), access on 20th of June 2011

[GilMR11] M.R. Gilbert, J. Ch. Sublet, Neutron-induced transmutation effects in W and W-alloys in a fusion environment, Nucl. Fusion 51 (2011) 1 – 13

[Glu] B. Gludovatz, S. Wurster, A. Hoffmann, R. Pippan, A study into the crack propagation resistance of pure tungsten, (in preparation)

[Glu10a] B. Gludovatz, Fracture behaviour of tungsten, PhD thesis, University of Leoben, October 2010

[Glu10b] B. Gludovatz, S. Wurster, A. Hoffmann, R. Pippan, Fracture toughness of polycrystalline tungsten alloys, Int. J. of Ref. Met. Hard Mater. 28 (2010) 674 – 678

[Gou94] W.H. Gourdin, D.H. Lassila, M.M. Leblanc, A.L. Shields, The influence of tungsten alloying on the mechanical properties of tantalum, Journal de Physique IV, Colloque C8, supplement au Journal de Physique III, Volume 4, septembre 1994, C8-207 – C8 212

[Grö08] R. Gröger, A.G. Bailey, V. Vitek, Multiscale modeling of plastic deformation of molybdenum and tungsten: I. Atomistitc studies of the core structure and glide of ½ <111> screw dislocations at 0K, Acta Mater. 56 (2008) 5401 – 5411

[Gum98] P. Gumbsch, J. Riedle, A. Harmaier, H.F. Fischmeister, Controlling factors for the brittle-to-ductile transition in tungsten single crystals, Science 282 (1998) 1293 – 1295

[Gum03] P. Gumbsch, Brittle fracture and the brittle-to-ductile transition of tungsten, J. Nucl. Mater. 323 (2003) 304 – 312

[Haf07] M. Hafok, Aufklärung der Verformungsvorgänge bei der Hochverformung, PhD thesis, in German, University of Leoben, April 2007

[Hall66] E.O. Hall, S.H. Algie, The sigma phase, Metallurgical Reviews, 11 (1966) 61 – 88

[Half05] T.P. Halford, K. Takashima, Y. Higo, P. Bowen, Fracture tests of microsized TiAl specimens, Fatigue Fract. Engng. Mater. Struct. 28 (2005) 695 – 701

[Her84] R. Herschitz, D.N. Seidman, An atomic resolution study of radiation-induced precipitation and solute segregation effects in a neutron-irradiated W-25 at% Re alloy, Acta Metall. 32 (1984) 1155 – 1171

[Hirs60] P.B. Hirsch, Proceedings to the 5th International Conference on Crystallography, Cambridge University, 1960

[Hirs92] P.B. Hirsch, A.S. Booth, M. Ellis, S.G. Roberts, Dislocation-driven stable crack growth by microcleavge in semi-brittle crystals, Scripta Met. et Mat. 27 (1992) 1723 – 1728

[Hira09] T. Hirai, G. Pintsuk, J. Linke, M. Batilliot, Cracking failure study of ITER-reference tungsten grade under single thermal shock loads at elevated temperatures, J. Nucl. Mater. 390 – 391 (2009) 751 – 754

[Hira11] T. Hirai, Engineering of In-Vessel Components for ITER, oral presentation at the 13th International Workshop for Plasma-Facing Materials and Components for Fusion Application & 1st International Conference on Fusion Energy Materials Science, Rosenheim, 9th – 13th of May, 2011

[Hof] A. Hoffmann, Plansee SE, personal communication

[HohJ10] J. Hohe, P. Gumbsch, On the potential of tungsten-vanadium composites for high temperature application with wide-range thermal operation window, J. Nucl. Mater. 400 (2010) 218 – 231

[HohA10] A. Hohenwarter, R. Pippan, Anisotropic fracture behaviour of ultrafine-grained iron, Mat. Sci. Eng. A 527 (2010) 2649 – 2656

[Hul65] D. Hull, P. Beardmore, A. Valintine, Crack propagation in single crystals of tungsten, Phil. Mag. 12 (1965) 1021 – 1041

[Hut68] J.W. Hutchinson, Singular behaviour at the end of a tensile crack in a hardening material, J. Mech. Phys. Solids 16 (1968) 13 – 31

[IAE62] “Towards Nuclear Fusion”, IAEA Bulletin (1962) Volume 04, Issue 1, http://www.iaea.org/Publications/Magazines/Bulletin/Bull041/04105100306.pdf, access on 29th of June 2011

[IAE11] IAEA, Power Reactor Information System, http://www.iaea.org/programmes/a2/ access on 29th of April 2011

[Ihl05] T. Ihli, R. Kruessmann, I. Ovchinnikov, P. Norajitra, V. Kuznetsov, R. Giniyatulin, An advanced He-cooled divertor concept: Design, cooling technology and thermohydraulic analyses with CFD, Fus. Eng. Des. 75 – 79 (2005) 371 – 375

[ITE11] www.iter.org, access on 20th of June 2011

[Jaf58] R.I. Jaffee, C.T. Sims, J.J. Harwood, The effect of rhenium on the fabricability and ductility of molybdenum and tungsten, Proceedings of the 3rd Plansee Seminar, Reutte (1958) 380 – 411

[Jan01] G. Janeschitz, ITER JCT and HTs, Plasma-wall interaction issues in ITER, J. Nucl. Mater. 290 – 293 (2001) 1 – 11

[Kat07] Y. Katoh, L.L. Snead, C.H. Henager Jr., A. Hasegawa, A. Kohyama, B. Riccardi, H. Hegeman, Current status and critical issues for development of SiC composites for fusion application, J. Nucl. Mater. 367 – 370 (2007) 659 – 671

[Kec07] L.J. Kecskes, K.C. Cho, R.J. Dowding, B.E. Schuster, R.Z: Valiev, Q. Wei, Grain size engineering of bcc refractory metals: Top-down and bottom-up – Application to tungsten, Mat. Sci. Eng. A 467 (2007) 33 – 43

[Kie07] D. Kiener, C. Motz, M. Rester, M. Jenko, G. Dehm, FIB damage of Cu and possible consequences for miniaturized mechanical tests, Mat. Sci. Eng. A 459 (2007) 262 – 272

[Kie08] D. Kiener, W. Grosinger, G. Dehm, R. Pippan, A further step towards an understanding of size-dependent crystal plasticity: In situ tension experiments of miniaturized single-crystal copper samples, Acta Mater. 56 (2008) 580 – 592

[Kir59] K. Kirner, Bemerkungen zu Rhenium-Wolfram Legierungen, in German, Planseeberichte für Pulvermetallurgie 7 (1959) 117 – 119

[Kit99] Y. Kitsunai, H. Kurishita, H. Kayano, Y. Hiraoka, T. Igarashi, T. Takida, Microstructure and impact properties of ultra-fine grained tungsten alloys dispersed with TiC, J. Nucl. Mater. 271 & 272 (1999) 423 – 428

[Klo68] W.D. Klopp, Review of ductilizing of group VI-A elements by rhenium and other solutes, NASA Technical Note NASA TN D-4955, Washington D.C., December 1968

[Klo71] W.D. Klopp, P.L. Raffo, W.R. Witzke, Strengthening of Molybdenum and Tungsten Allloys with HfC, J. of Metals, (1971) 27 – 38

[Klo75] W.D. Klopp, A review of chromium, molybdenum and tungsten alloys, J. of Less-Common Metals 42 (1975) 261 – 278

[Klü11] T. Klünsner, S. Wurster, P. Supancic, R. Ebner, M. Jenko, J. Glätzle, A. Püschel, R. Pippan, Effect of specimen size on the tensile strength of WC-Co hard metal, Acta Mater. 59 (2011) 4244 – 4252

[Koh91] S. Kohlhoff, P. Gumbsch, H.F. Fischmeister, Crack propagation in b.c.c. crystals studied with a combined finite-element and atomistic model, Phil. Mag. A 64 (1991) 851 – 878

[Kra90] P. Krautwasser, H. Derz, E. Kny, Influence of fast neutron fluence on the ductile-brittle transition of W, W10Re and W3.4Ni1.6Fe, High Temperatures – High Pressures 22 (1990) 25 – 32; also appearing in Proceedings of the 12th International Plansee Seminar 1989 Reutte, RM 77, 673

[Kre06] H. Kreuzer, M. Faleschini, B. Gludovatz, R. Pippan, Report for TASK of the EFDA Programme TW5-TTMA-002 “Tungsten Alloy Development”, 2006.

[Kon98] T. Kondo, IFMIF, its facility concept and technology, J. Nucl. Mater. 258 – 263 (1998) 47 – 55

[Kur07] H. Kurishita, Y. Amano, S. Kobayashi, K. Nakai, H. Arakawa, Y. Hiraoka, T. Takida, K. Takebe, H. Matsui, Development of ultra-fine grained W-TiC and their

mechanical properties for fusion applications, J. Nucl. Mater. 367 – 370 (2007) 1453 – 1457

[Kur09] H. Kurishita, S. Matsuo, H. Arakawa, M. Narui, M. Yamazaki, T. Sakamoto, S. Kobayashi, K. Nakai, T. Takida, K. Takebe, M. Kawai, N. Yoshida, High temperature tensile properties and their application to toughness enhancement in ultra-fine grained W-(0-1.5)wt% TiC, J. Nucl. Mater. 386 – 388 (2009) 579 – 582

[Las99] E. Lassner, W.D. Schubert, Tungsten – Properties, Chemistry, Technology of the Element, Alloys and Chemical Compounds, New York, Boston, Dordrecht, London, Moscow, Kluwer Academic / Plenum Publishers, 1999

[Li] H. Li, S. Wurster, C. Motz, L. Romaner, C. Ambrosch-Draxl, R. Pippan, Dislocation core symmetry and slip planes in W alloys, (in preparation)

[Lin11] J. Linke, Testing of plasma facing materials and components, oral presentation at the 13th International Workshop for Plasma-Facing Materials and Components for Fusion Application & 1st International Conference on Fusion Energy Materials Science, Rosenheim, 9th – 13th of May, 2011

[LiuJM83] J.M. Liu, B.W. Shen, Crack nucleation in tungsten on crystallographic planes and on grain boundaries of twist misorientation, Scripta Metall. 17 (1983) 635 – 638

[LiuZK00] Z.K. Liu, Y. Austin Chang, Evaluation of the thermodynamic properties of the Re-Ta and Re-W systems, J. of Alloys and Compounds 299 (2000) 153 – 162

[LuoA91a] A. Luo, D.L. Jacobson, K.S. Shin, Solution softening mechanism of iridium and rhenium in tungsten at room temperature, Ref. Met. Hard Mater. 10 (1991) 107 – 114

[LuoA91b] A. Luo, K.S. Shin, D.L. Jacobson, Ultrahigh temperature tensile properties of arc-melted tungsten and tungsten-iridium alloys, Scripta Met. et Mat. 25 (1991) 2411 – 2414

[LuoGN11] G.N. Luo, Development of W/Cu Divertor Components for EAST, oral presentation at the 13th International Workshop for Plasma-Facing Materials and Components for Fusion Application & 1st International Conference on Fusion Energy Materials Science, Rosenheim, 9th – 13th of May, 2011

[Mab96] M. Mabuchi, K. Okamoto, N. Saito, M. Nakanishi, Y. Yamada, T. Asahina, T. Igarashi, Tensile properties at elevated temperature of W-1%La_2O_3, Mat. Sci. Eng. A 214 (1996) 174 – 176.

[Mai08] D. Maisonnier, European DEMO design and maintenance strategy, Fus. Eng. Des. 83 (2008) 858 – 864

[Mas09] S. Massl, W. Thomma, J. Keckes, R. Pippan, Investigation of fracture properties of magnetron-sputtered TiN films by means of a FIB-based cantilever bending technique, Acta Mater. 57 (2009) 1768 – 1776

[Mato09] K. Matoy, H. Schönherr, T. Detzel, T. Schöberl, R. Pippan, C. Motz, G. Dehm, A comparative micro-cantilever study of the mechanical behaviour of silicon based passivation films, Thin Solid Films 518 (2009) 247 – 256

[Matt11] G. Matthews, The JET ITER-like wall status and experimental programme, oral presentation at the 13th International Workshop for Plasma-Facing Materials and Components for Fusion Application & 1st International Conference on Fusion Energy Materials Science, Rosenheim, 9th – 13th of May, 2011

[Meg98] J. Megusar, F.A. Garner, Response of dynamically compacted tungsten to high fluence neutron irradiation at 423-600°C in FFTF, J. Nucl. Mater. 258 – 263 (1998) 940 – 944

[Mer06] M. Merola, J. Palmer, The EU ITER Participating Team, EU activities in preparation of the procurement of the ITER divertor, Fus. Eng. Des. 81 (2006) 105 – 112

[Miy09] D. Miyaguchi, M. Otsu, K. Takashima, M. Takeyama, Microscale fracture toughness testing of TiAl PST crystals, Mater. Res. Soc. Symp. Proc. 1128 (2009) 197 – 202

[Moe06] A. Moeslang, V. Heinzel, H. Matsui, M. Sugimoto, The IFMIF test facilities design, Fus. Eng. Des. 81 (2006) 863 – 871

[Mot05] C. Motz, T. Schöberl, R. Pippan, Mechanical properties of micro-sized copper bending beams machined by the focused ion beam technique, Acta Mater. 53 (2005) 4269 – 4279

[Mura87] Y. Murakami (editor), Stress Intensity Factors Handbook, Volume 1, 1st edition, Oxford, New York, Beijing, Frankfurt, Sao Paulo, Sydney, Tokyo, Toronto, Pergamon Press, 1987

[Muro02] T. Muroga, T. Nagasaka, K. Abe, V.M. Chernov, H. Matsui, D.L. Smith, Z.-Y. Xu, S.J. Zinkle, Vanadium alloys – overview and recent results, J. Nucl. Mater. 307 – 311 (2002) 547 – 554

[Mut95] Y. Mutoh, K. Ichikawa, K. Nagata, M. Takeuichi, Effect of rhenium addition on fracture toughness of tungsten at elevated temperatures, J. Mat. Sci. 30 (1995) 770 – 775

[Nag91] S.V. Nagender Naidu, P. Rama Rao (editors), Monograph Series on Alloy Phase Diagrams, Phase Diagrams of Binary Tungsten Alloys, The Indian Institute of Metals, Calcutta (1991)

[Nod89] T. Noda, F. Abe, Y. Hiraoka, H. Araki, T. Fujii, M. Okada, Low activation first wall materials for fusion reactors, Fus. Eng. Des. 10 (1989) 463 – 467

[Nod98] T. Noda, M. Fujita, M. Okada, Transmutation and induced radioactivity of W in the armor and first wall of fusion reactors, J. Nucl. Mater. 258 – 263 (1998) 934 – 939

[Nor08] P. Norajitra, S.I. Abdel-Khalik, L.M. Giancarli, T. Ihli, G. Janeschitz, S. Malang, I.V. Mazul, P. Sardain, Divertor conceptual designs for a fusion power plant, Fus. Eng. Des. 83 (2008) 893 – 902

[Pam07] J. Paméla, G.F. Matthews, V. Philipps, R. Kamendje, JET-EFDA Contributors, An ITER-like wall for JET, J. Nucl. Mater. 363 – 365 (2007) 1 – 11

[Pink79] E. Pink, R.J. Arsenault, Low-temperature softening in body-centered cubic alloys, Prog. Mater. Sci. 24 (1979) 1 – 50

[Pink89] E. Pink, L. Bartha (editors), The metallurgy of doped / non-sag tungsten, London, New York, Elsevier Applied Science, 1989

[Pink96] E. Pink, R. Eck, Refractory Metals and Their Alloys, in: R.W. Cahn, P. Haasen, E:J. Kramer (editors) Materials Science and Technology, Vol.8, Structure and Properties of Nonferrous Alloys, pp 591 – 638, Weinheim, New York, Basel, Cambridge, Tokyo, VCH, 1996

[Pint11a] G. Pintsuk, A. Prokhodtseva, I. Uytdenhouwen, Thermal shock characterization of tungsten deformed in two orthogonal directions, J. Nucl. Mater. (2011), in press, doi: 10.1016/j.jnucmat.2010.12.109

[Pint11b] G. Pintsuk, Thermal shock response of fine and ultra fine grained tungsten based materials, oral presentation at the 13th International Workshop for Plasma-Facing Materials and Components for Fusion Application & 1st International Conference on Fusion Energy Materials Science, Rosenheim, 9th – 13th of May, 2011

[Pip] R. Pippan, Ausgewählte Kapitel der Festkörpermechanik (in German), lecture notes

[Pip87] R. Pippan, The growth of short cracks under cyclic compression, Fatigue Fract. Eng. Mater. Struct. 9 (1987) 319 – 328

[Pip10] R. Pippan, S. Scheriau, A. Taylor, M. Hafok, A. Hohenwarter, A. Bachmaier, Saturation of fragmentation during severe plastic deformation, Annu. Rev. Mater. Res. 40 (2010) 319 – 343

[Pos01] A. Pospieszczyk, T. Tanabe, V. Philipps, G. Sergienko, T. Ohgo, K. Kondo, M. Wada, M. Rubel, W. Biel, A. Huber, A. Kirschner, J. Rapp, N. Noda, Operation of TEXTOR-94 with tungsten poloidal main limiters, J. Nucl. Mater. 290 – 293 (2001) 947 – 952

[Pre,a] B. Predel, Mo-Re (Molybdenum-Rhenium). O. Madelung (editor), SpringerMaterials - he Landolt–Börnstein Database (http://www.springermaterials.com). DOI: 10.1007/10522884_ 2089

[Pre,b] B. Predel, Re-W (Rhenium-Tungsten). O. Madelung (editor), SpringerMaterials - The Landolt-Börnstein Database (http://www.springermaterials.com). DOI: 10.1007/10551312_2604

[RafPL69] P.L. Raffo, Yielding and fracture in tungsten and tungsten-rhenium alloys, J. of Less-Common Metals 17 (1969) 133 – 149

[RafAR10] A.R. Raffray, R. Nygren, D.G. Whyte, S. Abdel-Khalik, R. Doerner, F. Escourbiac, T. Evans, R.J. Goldston, D.T. Hoelzer, S. Konishi, R. Lorenzetto, M. Merola, R. Neu, P. Norajitra, R.A. Pitts, M. Rieth, M. Roedig, T. Rognlien, S. Suzuki, M.S. Tillack, C. Wong, High heat flux components – Readiness to proceed from near term fusion systems to power plants, Fus. Eng. Des. 85 (2010) 93 – 108

[Reb05] E. Rebhan, D. Reiter, R. Weynants, U. Samm, W.J. Hogan, J. Raeder, T. Hamacher, Controlled nuclear fusion: general aspects, in: K. Heinloth (Editor), Landolt-Börnstein Numerical Data and Functional Relationships in Science and

Technology Group VIII: Advanced Materials and Technologies, Vol. 3. Energy Technologies, Subvolume B: Nuclear Energy, Berlin, Heidelberg, New York, Springer, 2005

[Ricc00] B. Riccardi, P. Fenici, A. Frias Rebelo, L. Giancarli, G. Le Marois, E. Philippe, Status of the European R&D activities of SiC_f/SiC composites for fusion reactors, Fus. Eng. Des. 51 – 52 (2000) 11 – 22

[Rice68a] J.R. Rice, A Path Independent Integral and the Approximate Analysis of Strain Concentration by Notches and Cracks, Trans ASME J. of Appl. Mech. 35 (1968) 379 – 386

[Rice68b] J.R. Rice, G.F. Rosengren, Plane strain deformation near a crack tip in a power-law hardening material, J. Mech. Phys. Solids 16 (1968) 1 – 12

[Ries] J. Riesch, IPP Garching, Germany, personal communication, unpublished results

[Ried] J. Riedle, Bruchwiderstand in Wolfram-Einkristallen: Einfluss der kristallographischen Orientierung, der Temperature und der Lastrate, PhD thesis, in German, University of Stuttgart

[Ried94] J. Riedle, P. Gumbsch, H.F. Fischmeister, V.G. Glebovsky, V.N. Semenov, Fracture studies on tungsten single crystals, Mat. Lett. 20 (1994) 311 – 317

[Ried96] J. Riedle, P. Gumbsch, H.F. Fischmeister, Cleavage anisotropy in tungsten single crystals, Phys. Rev. Lett. 76 (1996) 3594 – 3597

[Riet10] M. Rieth, A. Hoffmann, Influcence of microstructure and notch fabrication on impact bending properties of tungsten materials, Int. J. Ref. Met. Hard Mater. 28 (2010) 679 – 686

[Riet11a] M. Rieth, Microstructure and fracture behaviour of tungsten, Presentation at MAT-W&WALLOY Monitoring Meeting, Garching, 9^{th} – 10^{th} of February 2011

[Riet11b] M. Rieth, J.L. Boutard, S.L. Dudarev, T. Ahlgren, S. Antusch, N. Baluc, M.-F. Barthe, C.S. Becquart, L. Ciupinski, J.B. Correia, C. Domain, J. Fikar, E. Fortuna, C.-C. Fu, E. Gaganidze, T.L. Galán, C. Garcia-Rosales, B. Gludovatz, H. Greuner, K. Heinola, N. Holstein, N. Juslin, F. Koch, W. Krauss, K.J. Kurzydlowski, J. Linke, Ch. Linsmeier, N. Luzginova, H. Maier, M.S. Martinez, J.M. Missiaen, M. Muhammed, A. Munoz, M. Muzyk, K. Nordlund, D. Nguyen-Manh, P. Norajitra, J. Opschoor, G. Pintsuk, R. Pippan, G. Ritz, L. Romaner, D. Rupp, R. Schäublin, J. Schlosser, I. Uytdenhouwen, J.G. van der Laan, L. Ventelon, S. Wahlberg, F. Willaime, S. Wurster, M.A. Yar, Review of the EFDA programme on tungsten materials technology and science, J. Nucl. Mater. (2011) in press, doi: 10.1016/j.jnucmat.2011.01.075

[Rom] L. Romaner, H. Li, Erich Schmid Institute of Materials Science, Austria, personal communication

[Rom10] L. Romaner, C. Ambrosch-Draxl, R. Pippan, The effect of rhenium on the dislocation core structure in tungsten, Phys. Rev. Lett. 104 (2010) 195503

[Sab05] I. Sabirov, R. Pippan, Formation of a W-25%Cu nanocomposites during high pressure torsion, Scripta Mater. 52 (2005) 1293 – 1298

[Sab07] I. Sabirov, R. Pippan, Characterization of tungsten fragmentation in a W-25%Cu composite after high pressure torsion, Mater. Char. 58 (2007) 848 – 853

[ScA10] “12 events that will change everything”, Scientific American, June 2010, Vol. 302, No. 6, p.20 ff.

[Sch65] R.H. Schnitzel, Deformation of tungsten single crystals from -77°C to 800°C, J. of Less-Common Metals, 8 (1965) 81 – 89

[She08] T.D. Shen, Radiation tolerance in a nanostructure: Is smaller better?, Nucl. Instrum. Method B 266 (2008) 921–925.

[Shi09] S. Shim, H. Bei, M.K. Miller, G.M Pharr, E.P. George, Effects of focused ion beam milling on the compressive behvior of directionally solidified micropillars and the nanoindentation response of an electropolished surface, Acta Mater. 57 (2009) 503 – 510

[Sim74] R.P. Simpson, G.J. Dooley III, T.W. Haas, Study of grain boundary fracture surfaces in doped tungsten-rhenium alloys, Met. Trans. 5 (1974) 585 – 591

[Smid98] I. Smid, M. Akiba, G. Vieider, L. Plöchl, Development of tungsten armor and bonding to copper for plasma-interactive components, J. Nucl. Mater. 258 – 263 (1998) 160 – 172

[Smit76] C.J. Smithells, E.A. Brandes (editors), Metals Reference Book, p: 941, 5th edition, London & Boston, Butterworths, 1976,

[Son02] G.-M- Song, Y.-J. Wang, Y. Zhou, The mechanical and thermophysical properties of ZrC/W composites at elevated temperatures, Mat. Sci. Eng. A 334 (2002) 223 – 232

[Ste70] J.R. Stephens, Dislocation Structures in Single-Crystal Tungsten and Tungsten Alloys, Met. Trans. 1 (1970) 1293-1301

[Ste71] J.R Stephens, W.R. Witzke, Alloy softening in group VIA metals alloyed with rhenium, J. of Less-Common Metals, 23 (1971) 325 – 342

[Tad00] H. Tada, P.C. Paris, G.R. Irwin, The Stress Analysis of Cracks Handbook, 3rd edition, American Society of Mechanical Engineers, New York, 2000

[Tak05] K. Takashima, Y. Higo, Fatigue and fracture of a Ni-P amorphous alloy thin film on the micrometer scale, Fatigue Fract. Engng. Mater. Struct. 28 (2005) 703 – 710

[Tan09] T. Tanno, A. Hasegawa, J.C. He, M. Fujiwara, M. Satou, S. Nogami, K. Abe, T. Shishido, Effects of transmutation elements on the microstructural evolution and electrical resistivity of neutron-irradiated tungsten, J. Nucl. Mater. 386 – 388 (2009) 218 – 221

[Tar09] E. Tarleton, S.G. Roberts, Dislocation dynamic modelling of the brittle-ductile transition in tungsten, Phil. Mag. 89 (2009) 2759 – 2769

[Tiv01] R. Tivey, M. Akiba, D. Driemeyer, I. Mazul, M. Merola, M. Ulrickson, ITER R&D: Vacuum vessel and in-vessel components: Divertor cassette, Fus. Eng. Des. 55 (2001) 219 – 229

[Ued05] Y. Ueda, M. Toda, M. Nishikawa, K. Kondo, K.A. Tanaka, Effects of repetitive ELM-like heat pulses on tungsten surface morphology, Fus. Eng. Des. 82 (2007) 1904 – 1910

[Uka02] S. Ukai, M. Fujiwara, Perspective of ODS alloys application in nuclear environments, J. Nucl. Mater. 307 – 311 (2002) 749 – 757

[Ums09] K.R. Umstadter, R. Doerner, G. Tynan, Enhanced erosion of tungsten plasma-facing components subject to simultaneous heat pulses and deuterium plasma, J. Nucl. Mater. 386 – 388 (2009) 751 – 755

[Uyt07] I. Uytdenhouwen, M. Decréton, T. Hirai, J. Linke, G. Pintsuk, G. van Oost, Influence of recrystallization on thermal shock resistance of various tungsten grades, J. Nucl. Mater. 363 – 365 (2007) 1099 – 1103

[Val00] R.Z. Valiev, R.K. Islamgaliev, I.V. Alexandrov, Bulk nanostructured materials from severe plastic deformation. Prog. Mater. Sci. 45 (2000) 103 – 189

[Vel09] L. Veleva, Z. Oksiuta, U. Vogt, N. Baluc, Sintering and characterization of W–Y and W–Y_2O_3 materials, Fus. Eng. Des. 84 (2009) 1920 – 1924

[Wak11] E. Wakai, S. Nogami, R. Kasada, A. Kimura, H. Kurishita, M. Saito, Y. Ito, F. Takada, K. Nakamura, J. Molla, P. Garin, Small specimen test technology and methodology of IFMIF/EVEDA and the further subjects, J. Nucl. Mater. (2011) doi:10.1016/j.jnucmat.2011.02.011

[Wei06] Q. Wei, H.T. Zhang, B.E. Schuster, K.T. Ramesh, R.Z. Valiev, L.J. Kecskes, R.J. Dowding, L. Magness, K. Cho, Microstructure and mechanical properties of super-stong nanocrystalline tungsten processed by high pressure torsion, Acta Mater. 54 (2006) 4079 – 4089

[Wit09] K. Wittlich, T. Hirai, J. Compan, N. Klimov, J. Linke, A. Loarte, M. Merola, G. Pintsuk, V. Podkovyrov, L. Singheiser, A. Zhitlukhin, Damage structure in divertor armor materials exposed to multiple ITER relevant ELM loads, Fus. Eng. Des. 84 (2009) 1982 – 1986

[Wro64] A. Wronski, A. Fourdeux, Slip-induced cleavage in polycrystalline tungsten, J. of Less-Common Metals 6 (1964) 413 – 429

[Wu07] S. Wu, the EAST Team, An overview of the EAST project, Fus. Eng. Des. 82 (2007) 463 – 471

[Wur] S. Wurster, C. Motz, R. Pippan, Describing fracture on the micrometer scale employing single crystalline notched cantilevers (in preparation)

[Wur09] S. Wurster, R. Pippan, Nanostructured metals under irradiation, Scripta Mater. 60 (2009) 1083-1087

[Wur10a] S. Wurster, C. Motz, R. Pippan, Notched-cantilever testing on the micrometer scale – Effects of constraints on plasticity and fracture behaviour, Proceedings of the 18th European Conference on Fracture, Dresden, 2010

[Wur10b] S. Wurster, B. Gludovatz, R. Pippan, High temperature fracture experiments on tungsten-rhenium alloys, Int. J. Ref. Met. Hard Mater. 28 (2010) 692-697

[Wur11] S. Wurster, B. Gludovatz, A. Hoffman, R. Pippan, Fracture behaviour of tungsten-vanadium and tungsten-tantalum alloys and composites, J. Nucl. Mater. 413 (2011) 166 – 176

[www11a] http://www.metal-pages.com/metalprices/tungsten access on 28th of April 2011

[www11b] http://www.metalprices.com/FreeSite/metals/re/re.asp access on 29th of April

[Yan08] B. Yang, H. Vehoff, A. Hohenwarter, M. Hafok, R. Pippan, Strain effects on the coarsening and softening of electrodeposited nanocrystalline Ni subjected to high pressure torsion, Scripta Mater. 58 (2008) 790 – 793

[Yar11a] M.A. Yar, S. Wahlberg, H. Bergqvist, H.G. Salem, M. Johnsson, M. Muhammed, Chemically produced nanostructured ODS-lanthanum oxide-tungsten composites sintered by spark plasma, J. Nucl. Mater. 408 (2011) 129 – 135

[Yar11b] M.A. Yar, S. Wahlberg, H. Bergqvist, H.G. Salem, M. Johnsson, M. Muhammed, Spark plasma sintering of tungsten-yttrium oxide composites from chemically synthesized nanopowders and microstructural characterization, J. Nucl. Mater. 412 (2011) 227 - 232

[YouCL70] C.L. Younger, G.N. Wrights, Effect of reactor irradiation on ductile-brittle transition and stress-strain behaviour of tungsten, NASA Technical Note, NASA TN D-5991, Washington D.C., September 1970

[YouJH11] J.-H. You, Tungsten wire-reinforced tungsten matrix composites: Proof of principle, oral presentation at the 13th International Workshop for Plasma-Facing Materials and Components for Fusion Application & 1st International Conference on Fusion Energy Materials Science, Rosenheim, 9th – 13th of May, 2011

[Zie85] J.F. Ziegler, J.P. Biersack, U. Littmark, The Stopping Range of Ions in Matter, Pergamon Press, New York, 1985

[Zhit07] A. Zhitlukhin, N. Klimov, I. Landman, J. Linke, A. Loarte, M. Merola, V. Podkovyrov, G. Federici, B. Bazylev, S. Pestchanyi, V. Safronov, T. Hirai, V. Maynashev, V. Levashov, A. Muzichenko, Effects of ELMs on ITER divertor armour materials, J. Nucl. Mater. 363 – 365 (2007) 301 – 307

[Zhil08] A.P. Zhilyaev, T.G. Langdon, Using high-pressure torsion for metal processing: Fundamentals and applications, Progess in Materials Science 53 (2008) 893 – 979

[Zin05] S.J. Zinkle, Advanced materials for fusion technology, Fus. Eng. Des. 74 (2005) 31 – 40

List of appended publications & proceedings

[A] S. Wurster, R. Pippan, Nanostructured metals under irradiation, Scripta Materialia, 60 (2009) 1083 – 1087

[B] S. Wurster, B. Gludovatz, R. Pippan, High temperature fracture experiments on tungsten-rhenium alloys, International Journal of Refractory Metals and Hard Materials, 28 (2010) 692 – 697

[C] S. Wurster, B. Gludovatz, A. Hoffman, R. Pippan, Fracture behaviour of tungsten-vanadium and tungsten-tantalum alloys and composites, Journal of Nuclear Materials, 413 (2011) 166 – 176

[D] S. Wurster, C. Motz, M. Jenko, R. Pippan, Micrometer-sized specimen preparation based on ion slicing technique, Advanced Engineering Materials, 12 (2010) 61 – 64

[E] Conference Proceeding: S. Wurster, C. Motz, R. Pippan: “Notched-cantilever testing on the micrometer scale – Effects of constraints on plasticity and fracture behaviour”, Proceedings of the 18th European Conference on Fracture, Dresden, 2010, (non peer-reviewed)

[F] S. Wurster, C. Motz, R. Pippan, Describing fracture on the micrometer scale employing single crystalline tungsten notched cantilevers, in preparation

Remark

In the appended papers, I, Stefan Wurster performed all experiments, data analyses and was the primary author with the following exceptions.

- Wolfgang Schiller and Thomas Leitner assisted in sample preparation and experimental work for Publication B and Publication C.
- Bernd Gludovatz supported the construction of experimental setup, conduction of experiments and analysis of results for Publication B and C.
- Miroslav Pečar from the Institute of Metals and Technology (Ljubljana, Slovenia) performed the ion slicing sample preparation for all tungsten preforms used for Publication D, E and F. These are the publications on experiments using micrometer – sized samples.
- Christian Motz contributed to publications D, E and F with helpful advises on sample preparation with the Focused Ion Beam workstation, realization of in-situ experiments in the scanning electron microscope and analysis and interpretation of results.
- Reinhard Pippan contributed to all publications with principal ideas from design of experiments to final analysis and interpretation of results.

In order to stay with the published versions, no modifications according to British English and American English have been made.

Publication A: Nanostructured metals under irradiation

Nanostructured metals under irradiation

Stefan Wurster[a,*] and Reinhard Pippan[a,b]

[a] Erich Schmid Institute of Materials Science of the Austrian Academy of Sciences, Jahnstrasse 12, A-8700 Leoben, Austria

[b] Christian Doppler Laboratory of Local Analysis of Deformation and Fracture, Jahnstrasse 12, A-8700 Leoben, Austria

Abstract

Particle irradiation has a pronounced influence on the mechanical and thermal properties of materials, largely due to the generation of point defects. Owing to their large free surface to volume ratio, nanostructured metals show improved irradiation resistance. This nanostructuring can negatively impact the creep resistance of these materials, but by introducing fine precipitates this effect can be balanced.

Keywords: Nanocrystalline material; Grain boundary; Point defects; Irradiation

1. Introduction

The environment to which materials are exposed in nuclear facilities requires specific material properties. It is not an easy task to find materials capable of withstanding irradiation damage, and elevated temperatures may aggravate this situation in certain respects. Internal stresses due to component production will then be superimposed by thermal stresses. In addition, nuclear power plants operate for decades, and so materials require increased ductility and fracture toughness in the relevant temperature window, creep resistance over long intervals and apparently irradiation resistance. Considering fusion reactor applications, materials should have high erosion resistance – for achieving higher durability and a better quality of plasma – as well as good thermal conductivity; with increasing entrapment of defects the thermal conductivity may be lowered.

High-energy particle radiation removes atoms from their lattice sites during a collision cascade lasting some picoseconds; this process leaves behind vacancy–interstitial Frenkel pairs. A first step towards increasing the radiation resistance of materials is to provide chances for extinguishing radiation-induced and freely migrating interstitial atoms and vacancies. Primarily, this means offering solid–vapour or solid–solid interfaces and having short diffusion paths towards a grain boundary. A variety of nanostructured materials thereby show improved properties [1–7], owing to the high density of dislocations and the large volume fraction of grain boundaries compared to a ‘‘conventional” material, i.e. materials with grains larger than the micrometer scale. This enhancement is also supported by the existence of fine dispersed precipitates and/or oxides. Both small grains and embedded particles lead to a large free surface to volume ratio and a larger percentage of atoms affected by these interfaces. These sites act as points of annihilation for migrating point defects, mainly for more mobile interstitials, leading to a lower net defect production in the grain compared to coarser-grained material. However, in some other cases, as mentioned in Ref. [8], the generation of defects may even be enhanced in nanocrystals as the formation energy for vacancies is lowered in the amorphous, less densely packed region of grain boundaries.

Ovid‘Ko and Sheinerman [8] summarized four different possibilities by which the defect structure in nanocrystals could be modified under irradiation:

1. irradiation-driven generation of point defects,
2. absorption of these point defects at the grain boundaries,
3. annihilation of vacancies and interstitial atoms, and
4. formation of stable clusters of point defects,

where 1 and 2 play the most significant role. Accumulation of point defects usually leads to severe degradation of a material’s macroscopic properties, such as irradiation hardening, loss of ductility and decreasing fracture toughness, increase in the ductile-to-brittle transition temperature and amorphization; a transition from crystalline to glass-like structure and volume expansion may also occur.

2. Computer Simulations and Thermodynamics compared with Experimental Results

Molecular dynamics simulations on nanocrystalline nickel with grain sizes in the range of 5 – 10 nm by Voegeli et al. [9] indicated that radiation, simulated by a primary knock-on atom with an energy of 5 keV, may change the grain size when the volume affected by the thermal spike of the cascade is of the same size or larger than the grain size. Voegeli et al. compared the change in the microstructure after irradiation with the effect of heat treatment of the same material, and concluded that the kinetic activation for both processes is different. Grain growth was also found in experiments [7] with ultrafine-grained austenitic stainless steel, e.g. as used for internal structures of pressurized water reactors, where the mean grain diameter grew from 40 to 60 nm after receiving a dose of 5 displacements per atoms (dpa) 150 keV Fe^+ ions. In general, radiation experiments often make use of neutrons, protons or heavier ions (e.g. Fe^+, Ar^+), so it has to be remembered that different radiation settings and types of radiation involved may lead to different results.

The advantageous effect of a high grain boundary density was also confirmed by Samaras et al. [11, 12], who compared the effect of irradiation on nanocrystalline and single-crystalline face-centred cubic (fcc) Ni and body-centred cubic (bcc) Fe by molecular dynamics computer simulations. These materials are appropriate for analyzing the localized primary damage states. Primary knock-on atoms with energies in the range of several keV produce a certain number of Frenkel defects within the grains that will mostly recombine. The remaining interstitial atoms are more mobile than vacancies and migrate to regions of tensile pressure detectable at grain boundaries, leaving behind a surplus of vacancies; hence annihilation of point defects in the grain is suppressed. In Ref. [12], which deals just with nickel, the authors describe the mass transport occurring due to a large number of replacement collision sequences directed towards the grain boundaries, termed ‘‘funnelling”. The grain boundaries themselves are found to be mobile in order to assimilate incoming interstitials, and the grain boundary may be moved by incoming cascades close to or at the boundary. It is notable, but somehow obvious, that this process does not happen in simulations with a perfect fcc Ni crystal. Experimental results on the improved radiation resistance of a nanocrystalline Ni–Ti alloy [2] will be addressed below. The experimentally investigated grain size is about twice as large as the one investigated by computer simulations, 20 – 30 nm compared to 5 – 10 nm, but according to the work of Shen [13], these may be in the same regime as they bear the same dominant features.

Recent X-ray diffraction experiments by Kilmamentov et al. [2] compared a fully dense bulk nanocrystalline Nitinol (TiNi) alloy with a grain size in the range of 20 – 30 nm, produced by high-pressure torsion (HPT), with a coarse-grained TiNi alloy after irradiation with 1.5 MeV Ar^+ ions at room temperature up to a dose of 5.6 dpa. The authors showed that the fine-grained alloy can

preserve long-range order and crystalline structure up to higher doses than the coarse-grained alloy, i.e. the coarser-grained material is amorphized at lower doses. Nanocrystalline TiNi showed no amorphous background in X-ray diffractograms at twice the dose that leads to significant amorphization of coarse-grained material. Kilmamentov et al. elucidated that the ion damage needed to disturb the long-range ordering of bulk nanocrystalline TiNi is at least one order of magnitude higher than that for coarse-grained material. Earlier experiments comparing single-phased nanocrystalline and conventional polycrystalline $MgGa_2O_4$ by Shen et al. [4] reported the same facts: the nanocrystalline specimen resisted amorphization under 300 keV Kr^{++} radiation to at least 8 times the dose needed for the coarse-grained specimen to amorphize. No amorphization for nanocrystalline magnesium gallium oxide was detected for the highest dose of 96 dpa. However, as shown by Meldrum et al. [10] on ceramic zirconia nanoparticles with an average radius of approximately 1.5 nm, there could be an opposite size effect of irradiation-induced amorphization. At room temperature the small particles were amorphized at a dose of 0.9 dpa. This is about three magnitudes lower than the dose for ZrO_2 bulk material, which did not show significant amorphization even at 680 dpa. The authors presumed that the high free surface energy of the nanoparticles facilitated amorphization. The type of material, the grain size, temperature regime and dose seem to determine whether or not amorphization occurs.

Thermodynamical considerations highlighted by Shen in Ref. [13] combined with experimental data from Ref. [3] outline that defect annihilation in a nanocrystalline material is primarily driven by grain boundary sinks. Furthermore, Shen derives a sequence of grain sizes where phase transitions, i.e. amorphization or change of crystallographic structure, may or may not occur. In the smallest grains phase transitions can occur at low irradiation levels or even without irradiation, due to the large free energy of the existing grain boundaries. Larger but still nanocrystalline grains up to about 100 nm exhibit a higher free energy due to an increased density of intragranular point defects. The annihilation of point defects is dominated by intercrystalline vacancy–interstitial interactions instead of grain boundary sink effects. The ability to manage irradiation damage will decrease with a further increased grain size. There should be an optimum grain diameter d (see Figure A.1) leading to a minimum of the sum of free energy of grain boundaries ($\propto d^{-1}$) and free energy of point defects ($\propto d^2$). In summary, the smallest grains will not always show the highest resistance against particle irradiation, and the grain diameter, d, has to be optimized for each material and application.

Concerning amorphization of nanocrystals resulting from defect accumulation, Ovid'ko and Sheinerman [8] derived concentrations of point defects during and after irradiation, based on a theoretical model using kinetic equations for densities of point defects. They opposed the hypothesis that the nanosized grains enhanced amorphization because the total energy of the system is elevated, enabling the interfaces to incorporate defects, thereby hindering amorphization. They explained the experimentally found fact that nanocrystalline materials are in some cases more susceptible (e.g. [10]) to amorphization in comparison to coarse-grained materials. Ovid'Ko and Sheinerman discussed amorphization-enhancing and amorphization-suppressing processes at

the grain boundaries in a theoretical model. The more dominant factor decides whether or not a solid state amorphizing transformation takes place. They concluded that if irradiation-induced amorphisation, generated by accumulation of point defects, does not happen before the irradiation has stopped – i.e. the moment when the concentration of point defects reaches its maximum – it will never occur. When stopping irradiation, the source of point defects vanishes; however, the grain boundary, which acts as a drain, is left.

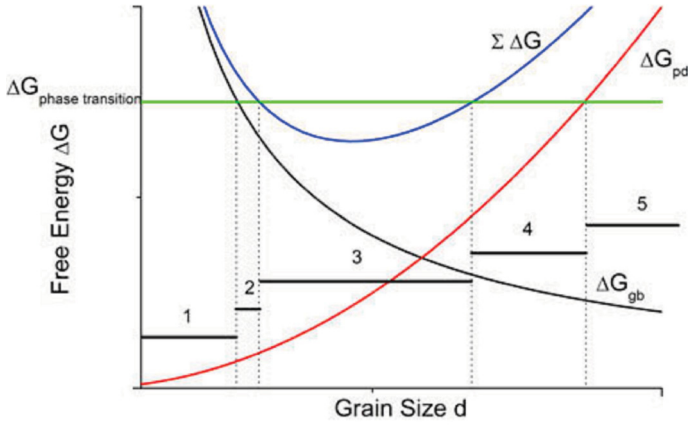

Figure A.1: Contribution of point defect-free energy (ΔG_{pd}) and grain boundaries (ΔG_{gb}) to the total free energy ($\Sigma\Delta G$) compared with the free energy of phase transition, according to Ref. [13].

3. Recent Experiments on Tungsten Alloys

Plasma-facing components in fusion reactors will have to withstand incident particles and high thermal loads; thus tungsten alloys are frequently considered as materials for fusion applications. With their high melting points, low vapour pressures and low sputtering yields, tungsten and tungsten alloys are proposed for plasma-facing material in certain regions in the future International Thermonuclear Experimental Reactor (ITER) [15] and the planned DEMO fusion reactor. In contrast to tungsten's excellent high-temperature properties, it exhibits a ductile-to-brittle transition (DBT) of fracture at elevated temperatures, which complicates its handling at room temperature and lessens the material's usefulness under thermal cyclic loading. Moreover, tungsten is also embrittled by recrystallization at higher temperatures and/or irradiation. Submicron-crystalline tungsten experiences ductilization and the DBT temperature (DBTT) is lowered. Faleschini et al. [16] showed that severe plastic deformation (SPD) of tungsten by HPT at 400 °C has a beneficial effect on its fracture toughness (see Figure A.2). The grain size after HPT was around 300 nm. Experiments on three different SPDed tungsten materials illustrate that the production of ultrafine-grained tungsten increases the fracture toughness 2 to 3-fold. The explanation might be the generation of additional, mobile, edge dislocations. Regarding the DBT of fracture in nanocrystalline metals, Yang and Yang [17] quantitatively compared the competing mechanisms of

crack propagation and crack stopping in a material with grains smaller than 25 nm. Grain boundary cavitation is regarded as responsible for crack propagation and grain boundary-dominated creep, resulting in crack blunting. Whether the material performs in a ductile or brittle manner depends on the competition between these two mechanisms.

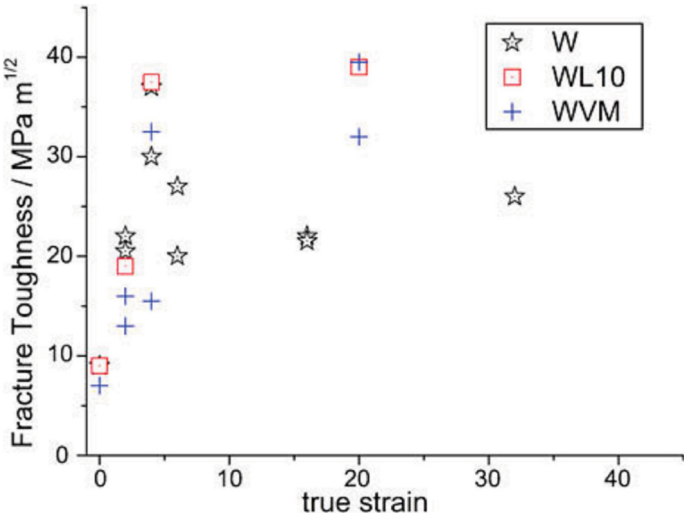

Figure A.2: The effect of high-pressure torsion on fracture toughness values for different tungsten alloys tested at room temperature; W: tungsten of technical purity (99.98%); WL10: lanthanum oxide dispersion strengthened tungsten; WVM: potassium-doped tungsten. Values were taken from Ref. [16].

Kurishita et al. [1] performed neutron and helium-ion irradiation experiments on tungsten with different additions of TiC (0.3 – 0.7 wt.%), with grain sizes in the range of 50 – 200 nm. Titanium carbides reduce the size of the otherwise coarse-grained structure and improve the strength of the grain boundaries. It has been demonstrated that W–TiC alloys produced by mechanical alloying (MA) under different atmospheres and subsequent hot isostatic pressing, leading to ultrafine-grained tungsten, exhibit a higher performance under neutron and 3 MeV helium irradiation environments than commercially available pure tungsten. The density of voids in normal tungsten after neutron irradiation at 600 °C is 3 – 4 times higher than that in ultrafine-grained W–0.5 wt.% TiC, whereas there is no significant difference in the number of irradiation-induced interstitial-type dislocation loops. Hardening under neutron irradiation, as observed for normal tungsten, is suppressed; on the contrary, for a certain addition of TiC the material softens when irradiated. Ultrafine-grained tungsten also suppresses the evolution of surface damage due to helium irradiation, so it is assumed that grain boundaries can retain a certain amount of helium. Thus, the finegrained material lowers the helium concentration inside the grain. The deformation of W–TiC materials is not solely dependent on the grain size but also on the mechanical alloying atmosphere, e.g. Ar and H_2 [18]. Ar-filled bubbles develop, coalesce and lead to intercrystalline fracture. The right amount of TiC is crucial for producing a ductile material, because tungsten/titanium carbide interfaces are regarded to be argon cavitation suppressors.

4. Recent Experiments on Steel

The details as to which mechanisms dominate the deformation of nanocrystalline materials are still under discussion. Several components, e.g. grain boundary sliding, influence of triple junctions, pores, operation of dislocation sources, impurities – possibly due to contamination during mechanical alloying by means of ball milling – and grain boundary diffusion creep, may be part of the cause. The same grain boundary-dominated considerations can be made for creep.

Creep deformation is an important deformation mechanism that needs to be considered when exposing components to higher temperatures for longer times. Compared to conventional materials, nanocrystalline components may exhibit creep at lower temperatures. Thus, aside from tungsten, nanostructured oxide dispersion strengthened (ODS) Fe–Cr ferritic and martensitic steels are also candidates for applications involving spallation, fusion and fission. Compared to austenitic steels, ODS steels are less susceptible to swelling; in addition, they have good high-temperature properties, e.g. a higher creep resistance than conventional reduced-activation ferritic–martensitic (RAFM) steels and good thermal conductivity. These attributes lead to higher operational temperature regimes and derive from a high density of nanometer-scale precipitates and oxides (nanofeatures) of yttrium and/or titanium, stabilizing the small grain size.

More latent energy is stored in a fine-grained material and the mechanical properties derive to a large extent from nanofeatures; hence the thermal stability of the nanofeatures and the microstructure is a critical issue. In-use temperatures will be up to 1200 °C in the divertor region of fusion reactors. Miao et al. [19] performed aging experiments on MA957, a nanostructured ferritic alloy containing 14 wt% Cr, 0.9 wt% Ti, 0.3 wt% Mo and 0.25 wt% Y_2O_3. These aging experiments at 900 °C, 950 °C and 1000 °C, lasting for 3000 h, revealed that the ferrite grain size and the dislocation density are not affected, while only limited softening was observed. However, sublimation of Cr from the surface may lead to localized coarsening, identified through transmission electron microscopy (TEM) and small-angle neutron scattering (SANS). The precipitates and oxides show only slight coarsening at 950 °C and 1000 °C. This was also found earlier by Miller et al. [20], who investigated three different ODS alloys, including the above-mentioned MA957, at higher temperatures. They found that annealing at 1300 °C for 24 h did not increase the grain size considerably, whereas the density of Y-, Ti- and O-rich particles decreased by more than one order of magnitude, and a significant amount of particle coarsening was observed. A lack of data on long-term creep experiments remains, which might be a source for new knowledge about the behaviour of nanocrystalline material under conditions of service in a fusion or fission reactor.

The major feature of ODS steels – oxide dispersions – is not influenced very much by irradiation. Atom probe investigations on Fe-ion irradiated ODS ferritic alloy, described in Ref. [25], show that 1800 displacements in 10^4 nm^3, representing about 0.7 dpa, do not influence the properties of

nano-oxides. Yamashita et al. [26] irradiated martensitic and ferritic steels between 670 K and 807 K at a dose of 2.5 – 15 dpa with neutrons; insignificant changes in average grain size and oxide density were observed. They believed that the irradiation temperature, in addition to the type of complex oxides, is the main factor influencing oxide stability as oxide particles dissociated in DT2203Y05 irradiated with neutrons at 81 dpa, whereas the oxides in MA957, irradiated at 200 dpa at lower temperature, did not. However, Schäublin et al. [27] stated that the irradiation temperature seems to have no influence on the hardening of EUROFER 97 based alloys. For more information we suggest readers peruse Refs. [25 – 27] and future reports of irradiation experiments performed on these types of materials.

The microstructure, and hence the material properties, depends on the method of nanostructured material production. One major problem with ODS steels made by mechanical alloying, during subsequent consolidation processes and deformation steps, is the anisotropic grain structure, resulting in deformation–orientation dependent mechanical properties. Ref. [21] describes the orientation dependence of fracture toughness for the nanocomposite ferritic alloy MA957, which exhibits a highly anisotropic texture after hot extrusion. Three different specimen orientations are tested. The L–R direction has the highest fracture toughness in comparison to the circumferential orientations C–R and C–L. This two-letter code describes reference directions (longitudinal, radial and circumferential) for cylindrical sections. The first letter specifies the direction normal to the crack plane; the second letter specifies the expected direction of crack propagation. Alamo et al. [22] also showed that the mechanical properties of ODS steels are highly dependent on the microstructure. They compared two different microstructures and metallurgical conditions of MA957, a fine-grained and anisotropic material with a grain size of approximately 500 nm, resulting from hot extrusion and cold deformation, and a recrystallized microstructure with grains of 10 – 50 μm. Recrystallization raises ductility, specified as reduction in area to rupture, but the DBTT value rises too. At 650 °C the fine-grained material has a superior creep resistance compared to the recrystallized one, when staying below a rupture time of 10,000 h.

There are several important issues related to the topic of nanostructured metals, one of which is the joining technology used. The usual welding methods would dissolve nanometer-sized oxides and precipitates by melting and resolidification. Miao et al. [14] investigated the effects of friction stir welding (FSW) and electrospark deposition (ESD) welding on the nanostructure of an ODS steel, revealing FSW as a more promising method for joining this material. FSW, a solid-state joining process without melting, involves mixing of the base material under SPD; the highest temperatures reached are 1300 – 1400 °C. Dynamic recrystallization during FSW refines the grain size and SPD introduces a high dislocation density. In contrast to FSW, ESD leads to localized melting by rapid heating using short-duration current pulses, which might affect nanosized particles. Both FSW and ESD decrease the number density and volume fraction of nanofeatures while their size is increased, resulting in a reduction of the strength of the joint. The effect of ESD is more pronounced than that of FSW.

5. Conclusion

In summary, nanostructured materials seem to be promising for nuclear applications because the grain boundaries act as sinks for interstitial atoms, diminishing the degradation of mechanical and thermal properties. However, the long-term behaviour under medium- and high-temperature irradiation of nanocrystalline materials has not been investigated sufficiently. Furthermore, only very few of the possible materials and combinations of materials with a certain nanostructure have so far been analyzed for this type of use. Until now, only a few existing materials have been modified and processed to obtain a relatively stable nanostructure. There should be a large variety of possible nanocrystalline materials or nanocomposites and improved processing routes which should permit the development of materials with improved irradiation resistance. For example, thermally stable nanocomposites, e.g. CuW alloys or CuCr alloys [23, 24], might be interesting materials for selected parts in high heat flux components. For the development of such new optimized nanostructured materials, a fundamental understanding of the irradiation behaviour, degradation of mechanical properties, thermal stability and creep behaviour of these types of materials is necessary.

Disclaimer

This work, supported by the European Communities under the Contract of Association between EURATOM and the Austrian Academy of Sciences, was carried out within the framework of the European Fusion Development Agreement. The views and opinions expressed herein do not necessarily reflect those of the European Commission.

References for Publication A

[1] H. Kurishita, S. Kobayashi, K. Nakai, T. Ogawa, A. Hasegawa, K. Abe, H. Arakawa, S. Matsuo, T. Takida, K. Takebe, M. Kawai, N. Yoshida, Development of ultra-fine grained W-(0.25-0.8)wt%TiC and its superior resistance to neutron and 3MeV He-ion irradiation, J. Nucl. Mater. 377 (2008) 34 – 40

[2] A.R. Kilmamentov, D.V. Gunderov, R.Z. Valiev, A.G. Balogh, H. Hahn, Enhancedion irradiation resistance of bulk nanocrystalline TiNi alloy, Scripta Mater. 59 (2008) 1027 – 1030

[3] M. Rose, A.G. Balogh, H. Hahn, Instability of irradiation induced defects in nanostructured materials, Nucl. Instrum. Method B 127/128 (1997) 119 – 122

[4] T.D. Shen, S. Feng, M. Tang, J.A. Valdez, Y. Wang, K.E. Sickafus, Enhanced radiation tolerance in nanocrystalline $MgGa_2O_4$, Appl. Phys. Lett. 90 (2007) 263115

[5] N. Nita, R. Schaeublin, M. Victoria, Impact of irradiation on the microstructure of nanocrystalline materials, J. Nucl. Mater. 329 – 333 (2004) 953 – 957

[6] Y. Chimi, A. Iwase, N. Ishikawa, M. Kobiyama, T. Inami, S. Okuda, Accumulation and recovery of defects in ion-irradiated nanocrystalline gold, J. Nucl. Mater. 297 (2001) 355 – 357

[7] B. Radiguet, A. Etienne, P. Pareige, X. Sauvage, R. Valiev, Irradiation behavior of nanostructured 316 austenitic stainless steel, J. Mater. Sci. 43 (2008) 7338 – 7343

[8] I.A. Ovid'Ko, A.G. Sheinerman, Irradiation-induced amorphization processes in nanocrystalline solids, Appl. Phys. A 81 (2005) 1083 – 1088

[9] W. Voegeli, K. Albe, H. Hahn, Simulation of grain growth in nanocrystalline nickel induced by ion irradiation, Nucl. Instrum. Method B 202 (2003) 230 – 235

[10] A. Meldrum, L.A. Boatner, R.C. Ewing, Size effects in the irradiation-induced crystalline-to-amorphous transformation, Nucl. Instrum. Method B 207 (2003) 28 – 35

[11] M. Samaras, P.M. Derlet, H. van Swygenhoven, M. Victoria, Atomic scale modeling of the primary damage state of irradiated fcc and bcc nanocrystalline metals, J. Nucl. Mater. 351 (2006) 47 – 55

[12] M. Samaras, P.M. Derlet, H. van Swygenhoven, M. Victoria, Computer simulation of displacement cascades in nanocrystalline Ni, Phys. Rev. Lett. 88 (2002) 125505

[13] T.D. Shen, Radiation tolerance in a nanostructure: Is smaller better?, Nucl. Instrum. Method B 266 (2008) 921 – 925

[14] P. Miao, G.R. Odette, J. Gould, J. Bernath, R. Miller, M. Alinger, C. Zanis, The microstructure and strength properties of MA957 nanostructured ferritic alloy joints produced by friction stir and electro-spark deposition welding, J. Nucl. Mater. 367–370 (2007) 1197 – 1202

[15] K. Ioki, V. Barabash, J. Cordier, M. Enoeda, G. Federici, B.C. Kim, I. Mazul, M. Merola, M. Morimoto, M. Nakahira, M. Pick, V. Rozov, M. Shimada, S. Suzuki, M. Ulrickson, Yu. Utin, X. Wang, S. Wu, J. Yu, ITER vacuum vessel, in-vessel components and plasma facing materials, Fus. Eng. Des. 83 (2008) 787 – 794

[16] M. Faleschini, H. Kreuzer, D. Kiener, R. Pippan, Fracture toughness investigations of tungsten alloys and SPD tungsten alloys, J. Nucl. Mater. 367 – 370 (2007) 800 – 805

[17] Fan Yang, Wei Yang, Brittle versus ductile transition of nanocrystalline metals, Int. J. Solids Struct. 45 (2008) 3897 – 3907

[18] S. Matsuo, H. Kurishita, H. Arakawa, T. Takida, M. Kato, Y. Yamamoto, K. Takebe, M. Kawai, N. Yoshida, Deformability enhancement in ultra-fine grained Ar-contained W compacts by TiC additions up to 1.1%, Mater. Sci. Eng. A 492 (2008) 475 – 480

[19] P. Miao, G.R. Odette, T. Yamamoto, M. Alinger, D. Klingensmith, Thermal stability of nano-structured ferritic alloys, J. Nucl. Mater. 377 (2008) 59 – 64

[20] M.K. Miller, D.T. Hoelzer, E.A. Kenik, K.F. Russel, Stability of ferritic MA/ODS alloys at high temperatures, Intermetallics 13 (2005) 387 – 392

[21] M.J. Alinger, G.R. Odette, G.E. Lucas, Tensile and fracture toughness properties of MA957 Implications to the development of nanocomposited ferritic alloys, J. Nucl. Mater. 307 – 311 (2002) 484 – 489

[22] A. Alamo, V. Lambard, X. Averty, M.H. Mathon, Assessment of ODS-14%Cr ferritic ally for high temperature applications, J. Nucl. Mater. 329 – 333 (2004) 333 – 337

[23] I. Sabirov, R. Pippan, Formation of a W-25%Cu nanocomposites during high pressure torsion, Scripta Mater. 52 (2005) 1293 – 1298

[24] X. Sauvage, P. Jessner, F. Vurpillot, R. Pippan, Nanostructure and properties of a Cu-Cr composite processed by severe plastic deformation, Scripta Mater. 58 (2008) 1125 – 1128

[25] P. Pareige, M.K. Miller, R.E. Stoller, D.T. Hoelzer, E. Cadel, B. Radiguet, Stability of nanometer-sized oxide clusters in mechanically-alloyed steel under ion-induced displacement cascade damage conditions, J. Nucl. Mater. 360 (2007) 136 – 142

[26] S. Yamashita, N. Akasaka, S. Ohnuki, Nano-oxide particle stability of 9-12Cr grain morphology modified ODS steel under neutron irradiation, J. Nucl. Mater. 329 – 333 (2004) 377 – 381

[27] R. Schäublin, A. Ramar, N. Baluc, V. de Castro, M.A. Monge, T. Leguey, N. Schmid, C. Bonjour, Microstructural development under irradiation in European ODS ferritic-martensitic steels, J. Nucl. Mater. 351 (2006) 247 – 260

Publication B: High temperature fracture experiments on tungsten-rhenium alloys

High temperature fracture experiments on tungsten–rhenium alloys

Stefan Wurster[a] , Bernd Gludovatz[a,b] , Reinhard Pippan[a,b]

[a] Erich Schmid Institute of Materials Science of the Austrian Academy of Sciences, Jahnstraße 12, A-8700 Leoben, Austria

[b] CD Laboratory of Local Analysis of Deformation and Fracture, Jahnstraße 12, A-8700 Leoben, Austria

Keywords: Tungsten–rhenium alloys, Recrystallization, Fracture toughness, High temperature fracture experiments

Abstract

A big problem when using tungsten as plasma facing components in a future fusion reactor is the very low fracture toughness at low temperatures. Tungsten–rhenium alloys outclasses other tungsten-based materials in terms of increased ductility. We study the reason for this positive effect by investigating the influence of rhenium on the fracture process of tungsten–rhenium alloys at different temperatures (between room temperature and 900 °C). The experiments are performed in a furnace-equipped tensile testing machine with a vacuum chamber, which allows us to perform fracture experiments at elevated temperature without oxidizing the material. Antecedent and subsequent electron backscattered diffraction scans are used to analyse the extent of plastic deformation and the interaction of plastic deformation and the fracture process. Furthermore, the consequences of recrystallization on the fracture process of tungsten–rhenium alloys will be analysed.

1. Introduction

Tungsten materials are considered to be implemented in the International Thermonuclear Experimental Reactor (ITER) in Cadarache, France, and in future fusion reactors as plasma facing materials in the main chamber, other proposed materials are beryllium and carbon fibre composites. Tungsten-based components, either in the shape of bulk or coated parts, will be placed in the divertor region [1]. The first wall, enclosing the plasma, is exposed to challenging conditions: high thermal fluxes up to several MW m^{-2}, high operational temperatures and large temperature gradients. Exposure to radiation has to be considered too. Bolt et al. [2] estimate the neutron flux at the first wall of first commercial fusion power reactors after ITER to lead to 150 displacements per atoms (dpa). Beside good mechanical properties at high temperatures, tungsten and tungsten alloys feature high melting points and other superior thermal properties such as good thermal shock resistance and good thermal conductivity. In comparison to low-Z materials like beryllium and carbon, tungsten has a lower erosion rate. A disadvantage of high-Z materials in general is the lower tolerable impurity concentration inside the fusion reactor's plasma; otherwise, the radiation losses of the plasma would be too high. This fact might be outbalanced by the lower sputtering yield of tungsten. Another disadvantage of tungsten in particular is its low fracture toughness, low elongation and small reduction in area at fracture at low temperatures, respectively its high ductile to brittle transition temperature (DBTT), complicating its machinability at room temperature. Nevertheless, the capability of application of tungsten as a plasma facing material has already been proven in the ASDEX (Axially Symmetric Divertor EXperiment) Upgrade tokamak [2].

It has been well known since the sixties and seventies, after intense research programmes related to aircraft and spacecraft technique, that alloying of tungsten with rhenium improves the mechanical behaviour of tungsten, which means lowering of DBTT [3–6]. In the following decades, the information on e.g. fracture behaviour of W–Re alloys is rather sparse [7], which might be related to the fact that Re is a very scarce – its abundance is more likely to be measured in ppt instead of ppm – and thus expensive metal. It is not planned to be used at high concentrations at a large, industrial scale. Nevertheless, not negligible amounts of rhenium and in succession osmium will be produced by transmutation of W due to neutron irradiation [8], implicating the existence of Re within the fusion reactor even when assuming pure W to be the used. However, the development of a strategy to enhance the mechanical behaviour of tungsten alloys is the main reason why the investigation is of interest.

2. Experimental procedure

For fracture toughness experiments, we used an alloy of nominally 26% Re. Closer examination of the as-received material with energy-dispersive X-ray spectroscopy (EDX) determined the rhenium content to be 26.8 wt% corresponding to 26.5 at%. The small difference in atom- and weight-percent is related to the close proximity of tungsten (No. 74) and rhenium (No. 75) in the periodic system of elements. No evidence was found that rhenium and tungsten are no solid solution, although the composition of the presented alloy is quite close to the brittle phase. Out of an as-forged rod with a diameter of 18 mm, compact tension (CT) specimens with thicknesses of $B \approx 3$ mm and widths $W \approx 6$ mm were manufactured.

In this study, we compare the fracture behaviour of the as-worked and subsequently stress-relieved W26Re alloy with the recrystallized alloy. After recrystallization of the specimens for 2 h at 2000 °C in hydrogen atmosphere, notches (length ≈ 3 mm) were produced with a cutting disc in C–R-direction according to ASTM E399-90 [9]. The first letter of this code – used for describing crack geometry in relation to the rod axis – represents the direction normal to the crack plane and the second letter represents the direction of expected crack propagation. Assuming a cylinder, representing the starting material, circumferential (C), longitudinal (L) and radial (R) directions form an orthogonal coordinate system, in which the crack system is positioned. After recrystallization, the previously chosen crack orientation should not have a significant influence on the fracture behaviour due to the more globular shape of the grains and low crystallographic texture. The blunt notches were sharpened by succeeding razor blade polishing technique and cyclic compression [10] up to several 10,000 cycles; the result was a sharp pre-crack penetrating the whole width of the specimen. The influence of recrystallization on the microstructure is visible when checking Figure B.3(a) against Figure B.3(b) and (c). The well recrystallized microstructure is clearly evident from the uniform colour of the grains. Forging induces significant changes crystal orientation in the grains and the formation of a subgrain structure becomes visible in Figure B.3(a).

In addition to the standard microstructural characterization, electron backscatter diffraction scans (EBSD) were made before and after recrystallization of the fracture mechanics samples by use of a Zeiss 1525 scanning electron microscope equipped with an EDAX EBSD system. Evaluation of scans was made with Orientation Imaging Microscopy (OIM) software. Using the support of image quality maps, provided by OIM software, the ends of cyclic compression-induced cracks are easily allocatable. Scans made after recrystallization and before breaking the specimens can then be compared with scans made after the experiment (Figure B.3(c)). This picture permits to estimate the amount of plastic deformation and the size of the plastically deformed region at different temperatures.

Specimens were tested in atmosphere at room temperature and at 300 °C and in a furnace- and vacuum chamber equipped tensile testing machine (Figure B.1) at higher temperatures. The vacuum chamber is capable of reaching pressures of $2*10^{-5}$ mbar. During the experiments, when reaching temperatures up to about 900 °C, the pressure increases but does not exceed 10^{-2} mbar. 1000 °C is the as-designed temperature limit of the furnace. Temperature is measured with thermocouples of type K. Force, temperature, time and – owing to a constant crosshead speed – the displacement of the crosshead are recorded. The crosshead speed was set at 0.4 mm min^{-1} for all experiments. An example for recorded load vs. time diagram is shown in Figure A.2, for a specimen tested at 300 °C in atmosphere. As it is shown there, the maximal difference in force, representing P_{max}, is taken for evaluation of a conditional K_Q value for fracture toughness according to following Equation (B.1) [9].

$$K_Q = \frac{P_Q}{B*W^{1/2}} * \frac{(2+a/W)/(0.886+4.64*a/W-13.32*(a/W)^2+14.72*(a/W)^3-5.6*(a/W)^4)}{(1-a/W)^{3/2}} \quad \text{(B.1)}$$

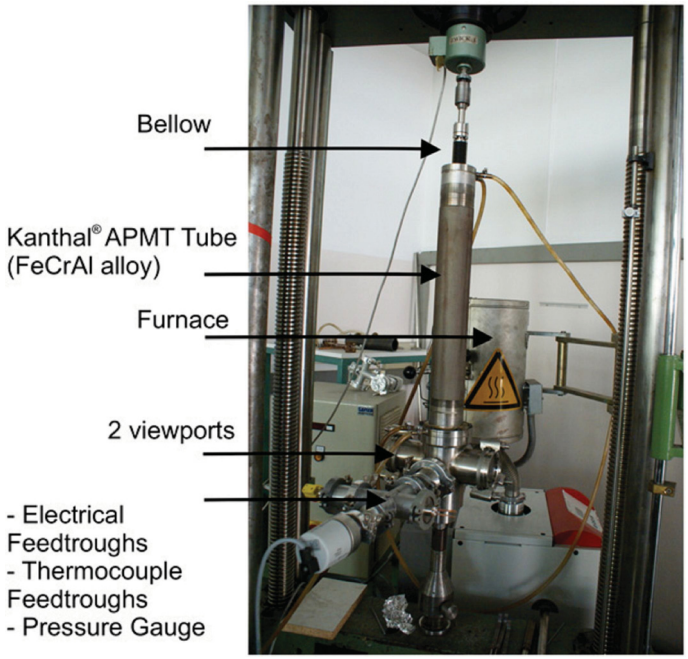

Figure B.1: Assembly of the cylindrical vacuum chamber mounted inside the furnace equipped tensile testing machine. The device is also equipped with a potential drop method measurement to determine the crack extension during loading.

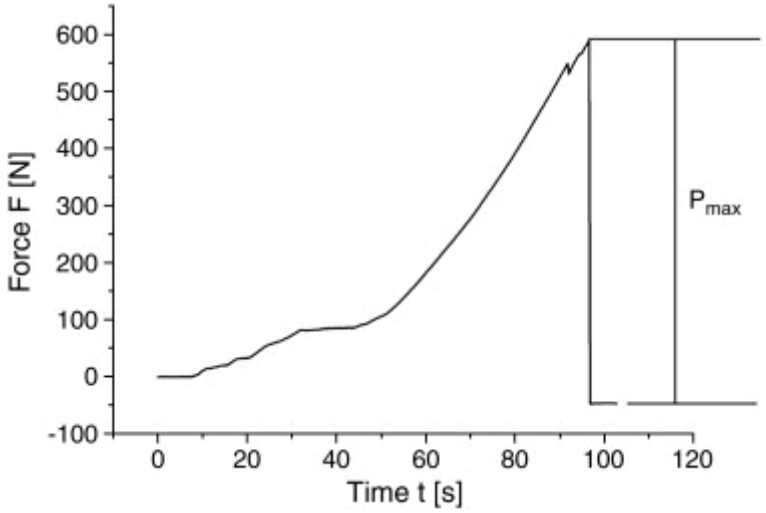

Figure B.2: Load vs. time recording for specimen tested in atmosphere at 300 °C, P_{max} is taken for evaluation of K_Q.

This test value, K_Q, as well as the experiment itself has to fulfill certain requirements to represent a valid K_{IC} value. The size of the specimen has to fulfill: B and $a > 2.5\ (K_{IC}/\sigma_{YS})^2$. σ_{YS} is the 0.2% offset yield strength of the material for the temperature and loading rate of the test. The results from these experiments are compared with earlier experiments [11], which were made with the as-forged and stress-relieved tungsten–rhenium alloy, representing the initial condition of the used recrystallized alloy. Three-Point-Bending (3PB) specimens, sizing 3 x 6 x 24 mm^3, were fabricated in L–R orientation out of the rod. L–R sample geometry can be described as follows: the normal on the crack plane is equivalent to the rod axis and the expected crack propagation direction is along the radius of the rod. Again, the pre-cracks were prepared with the diamond wire saw and razor blade, prior to final fatigue crack initiation under cyclic compression. These 3PB specimens were tested at room temperature and up to 600 °C according to [9]. Heating was carried out by radiation heating and the crosshead speed was 0.03567 mm min^{-1}, about 9% of speed used for testing of recrystallized material.

3. Results and discussion

The results of fracture toughness experiments are summarized in Table B.1. The yield strength σ_{YS} was taken from [3], where the influence of temperature on the yield stress of a W25Re alloy, recrystallized at 2255 K for 1 h, is presented. For higher temperature, yield stresses where linearly extrapolated based on yield stresses for temperatures ranging from 330 to 580 °C. With this data it is possible to estimate whether the K_Q values fulfill the above mentioned criterion for being valid K_{IC} values or not. The specimen fractured at 300 °C is 30% too small to accommodate the plane strain conditions, for 600 and 870 °C, the specimens are too small by one order of magnitude to fulfill this requirements of linear elastic fracture mechanic (LEFM). Regarding the experiments on 3PB-

specimens, the K-values measured at 400 and 600 °C are not valid according LEFM. But, all these determined values can be used at least as a lower limit for fracture toughness.

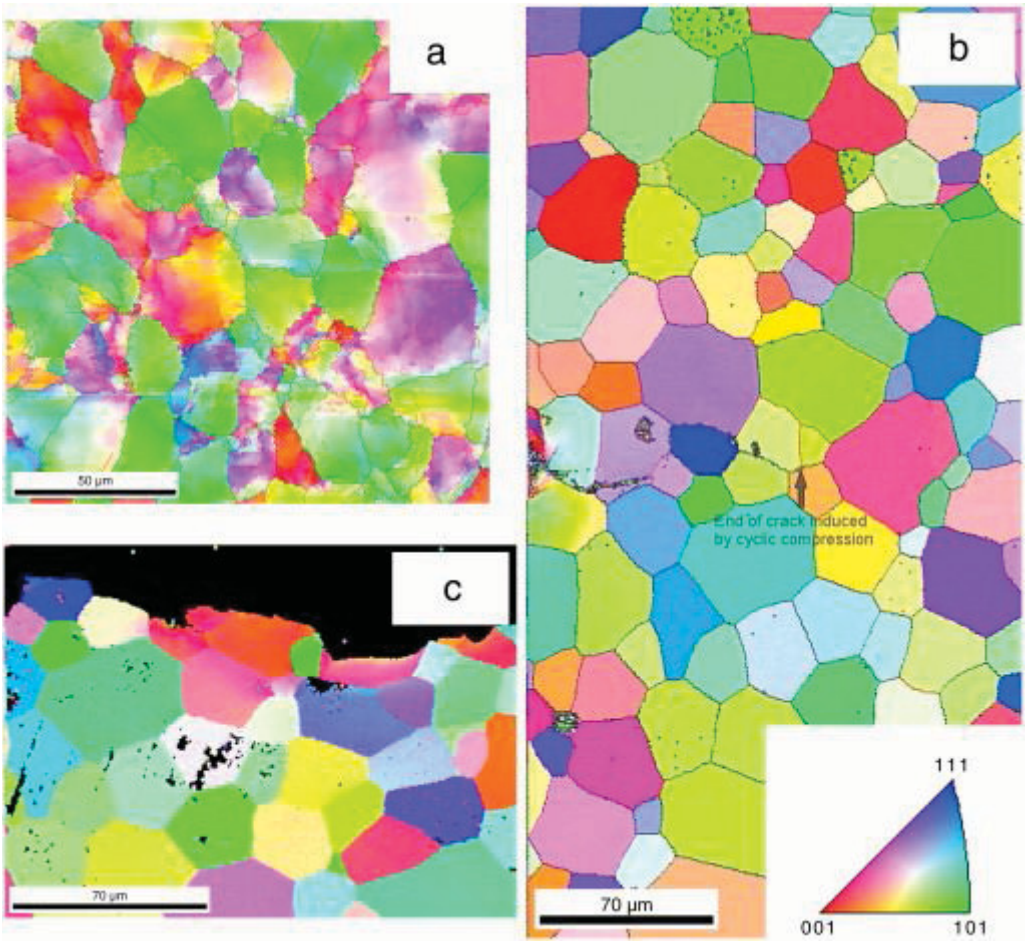

Figure B.3. (a) Inverse Pole Figure (IPF) compiled by an EBSD – scan in longitudinal direction of W26Re alloy in as-worked condition showing a larger amount of misorientation within the grains in comparison to recrystallized material depicted in (b) which shows an IPF of as-recrystallized material (2 h at 2000 °C in hydrogen atmosphere). Insert shows the colour code for IPF. (c) IPF of one half of the specimen after breaking at 300 °C in atmosphere showing plastically deformed grains close to the crack path. Cleanup of all IPFs were conducted with OIM software.

The bolts, made of lanthanum-doped tungsten, utilized for an experiment at 870 °C failed at the maximum load, as the diameter of the bolts, which agreed to ASTM E399-90, is too small. In fact, it was not possible to fracture the specimen in two parts, nevertheless first crack propagation took place. So, the experiment was successful in terms of obtaining a lower limit value for fracture toughness. This resulting fracture toughness is regarded to be the crack initiation fracture toughness. Scanning electron micrographs taken in alignment of the propagated crack were taken (Figure B.4(e) and (f)). Appearing maximum load was used for evaluating a preliminary fracture

toughness value. Due to this behaviour, a 3PB-bending apparatus capable of working in vacuum at high temperatures is going to be constructed.

Table B.1: Fracture toughness values for four recrystallized W26Re CT-specimens, tested at different temperatures, in atmosphere for room temperature – 300 °C, in vacuum for 600 °C – 870 °C, in comparison with K_Q – values for tungsten–rhenium alloy in as-forged condition, 3PB – specimens. Those marked with (↑) represent lower limits for fracture toughness. Value of K_Q for liquid nitrogen temperature was taken from Figure 14 in [12].

Testing temperature (°C)	K_Q, recrystallized (MPa $m^{1/2}$)	K_Q, forged (MPa $m^{1/2}$)
-196		38
20	22.8	54.2
300	25.9	-
400	-	65.4 (↑)
600	57.7 (↑)	52.5 (↑)
870	40.5 (↑)	

The fracture toughness of the as-forged material does not show an isotropic behaviour, as it is lowered by about more than a factor of 2, from 38 MPa $m^{1/2}$ to 17 MPa $m^{1/2}$ [12], when changing the sample geometry from L–R to C–R. In case of C–R sample geometry, the crack front does not propagate perpendicular to the elongated grain structure but these elongated grains are now parallel to the crack front. As the recrystallized samples were tested in C–R sample geometry too, it should be stated that the decrease of fracture toughness is not because of a changed testing direction, as the aspect ratio of the recrystallized grains is much closer to one.

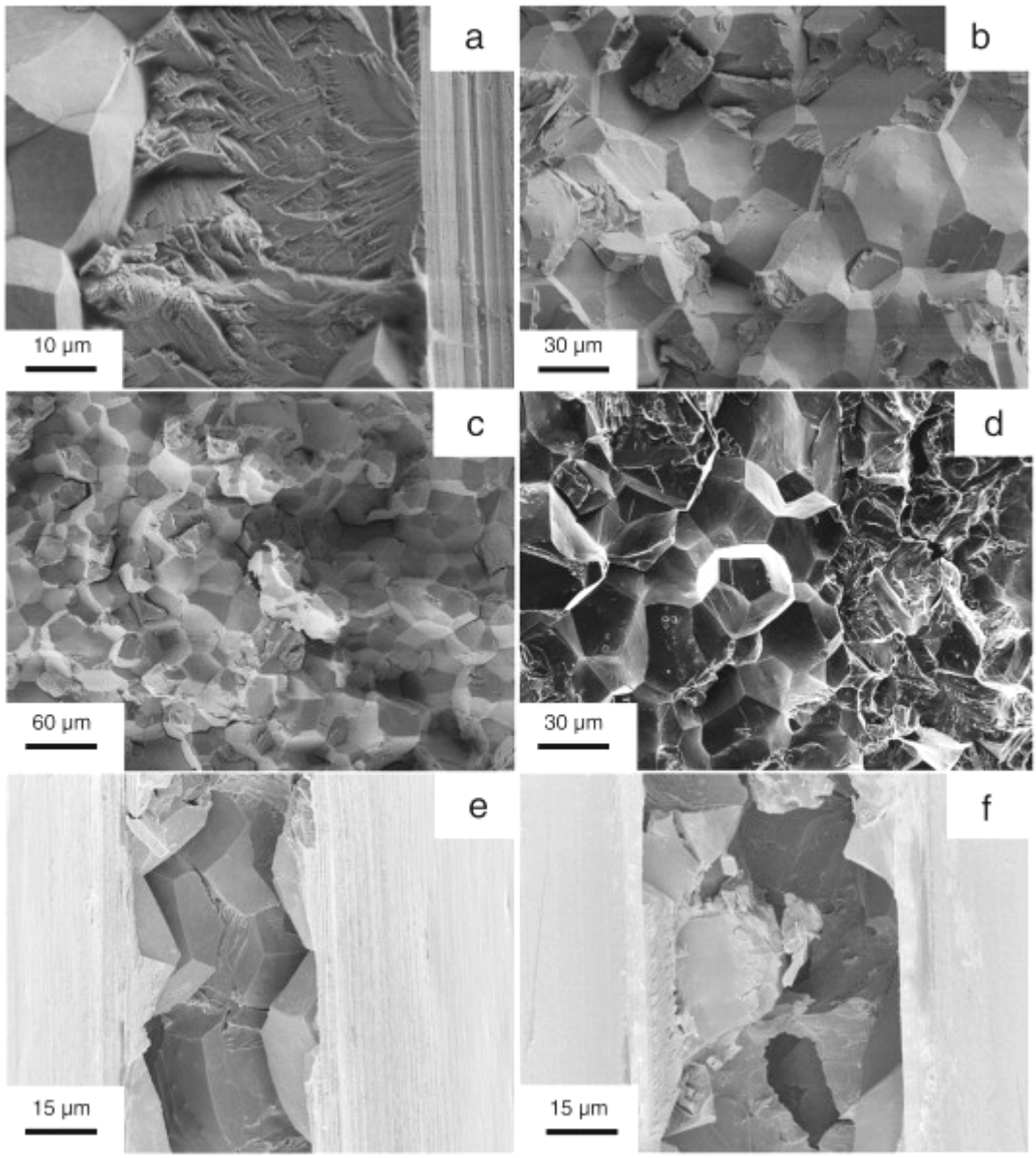

Figure B.4: (a) crack induced by cyclic compression; (b), (c) and (d) fracture surfaces of specimens tested at room temperature, 300 °C and 600 °C showing an increasing part of transcrystalline fracture for 600 °C; (e) and (f) scanning electron micrographs taken of the opened up notch of the specimen tested at 870 °C, showing again both transcrystalline and intercrystalline fracture.

EBSD scans were made before and after breaking the specimens and it is possible to recognize grains in both Inverse Pole Figures (IPF). For instance, the blue grain in the centre of Figure B.3(b) is also identifiable on picture (c) at top left, which was made after fracturing. Slight changes of basic colouring of grains originate from a somewhat changed angle of fitting of the specimen. These IPFs can reveal the plastic deformation of grains, respectively orientation changes inside a grain near the crack path. Scans made for samples tested at room temperature show plastic deformation just very close to the crack path. When fracturing at 300 °C, (Figure B.3(c)) more grains experience

plastic deformation, also those which are one grain diameter away from the crack path are affected. The size of the plastically deformed areas and the amount of misorientation increases when experiments are conducted at higher temperatures. Measuring the crystallographic orientation within one grain makes it possible to compare the amount of plastic deformation at different temperatures and for different tungsten alloys. When relating the orientation changes in a previously recrystallized grain with the amount of emerging dislocation, the combination of dislocation nucleation and dislocation movement seems to be enhanced the in tungsten–rhenium alloy than in other recrystallized tungsten materials. We plan to treat this topic in a more detailed way in a forthcoming publication.

The fracture surfaces of all recrystallized specimens reveal both intercrystalline and transcrystalline fracture with an increasing tendency towards transcrystalline fracture at elevated temperatures. The fact that specimens broken at room temperature and 300 °C feature almost similar fracture toughness is supported by the fact that they show the same kind of fracture – mostly along the grain boundaries. Fracture toughness for specimens tested at elevated temperatures is higher, which is reflected in the larger amount of transcrystalline fracture. Therefore, the amount of transcrystalline fracture seems to be correlated to the fracture toughness of the samples. Specimens made of the as-forged material show a by far larger extent of transcrystalline fracture (Figure B.5) even at room temperature with a larger plastic deformation of grain boundaries compared to recrystallized material. Fracture toughness is about twice as high.

4. Conclusion

Alloying tungsten with rhenium leads to an increase of fracture toughness of tungsten. In our case, this was verified for a W26Re alloy in both stress-relieved as-worked and recrystallized condition. Recrystallization, which might happen at high temperatures plasma facing materials are exposed to in a fusion reactor, changes the picture and lowers the fracture toughness again. In case of the recrystallized W26Re alloy, the fracture toughness was lowered by approximately 50% when taking at hand the samples, which were tested at room temperature and 300 °C. Nevertheless, this recrystallized material outclasses pure recrystallized tungsten by about a factor of 3. Inverse pole figures from EBSD scans reveal a higher crystal orientation gradient in the tungsten–rhenium alloy. Considering semi-brittle fracture, dislocations are emitted from the crack tip as the stress intensity is increased and before crack propagation takes place. These dislocations, are the reason for the tilting of the crystals close to the crack flanks in respect to the recrystallized grain, which shows the same crystallographic orientation everywhere. As the tilting of the alloyed material is higher, more dislocations have to be generated in tungsten–rhenium than in tungsten. For an increase in dislocation nucleation, the mobility of screw dislocation is of importance. Our group [13] has shown with simulations basing on density functional theory that alloying tungsten with rhenium leads to a

decrease in Peierls stress for the screw dislocations and hence to an increased mobility of dislocations. With increasing testing temperature, dislocation sources in grains at a certain distance from the crack flanks get activated and these grains experience plastic deformation too.

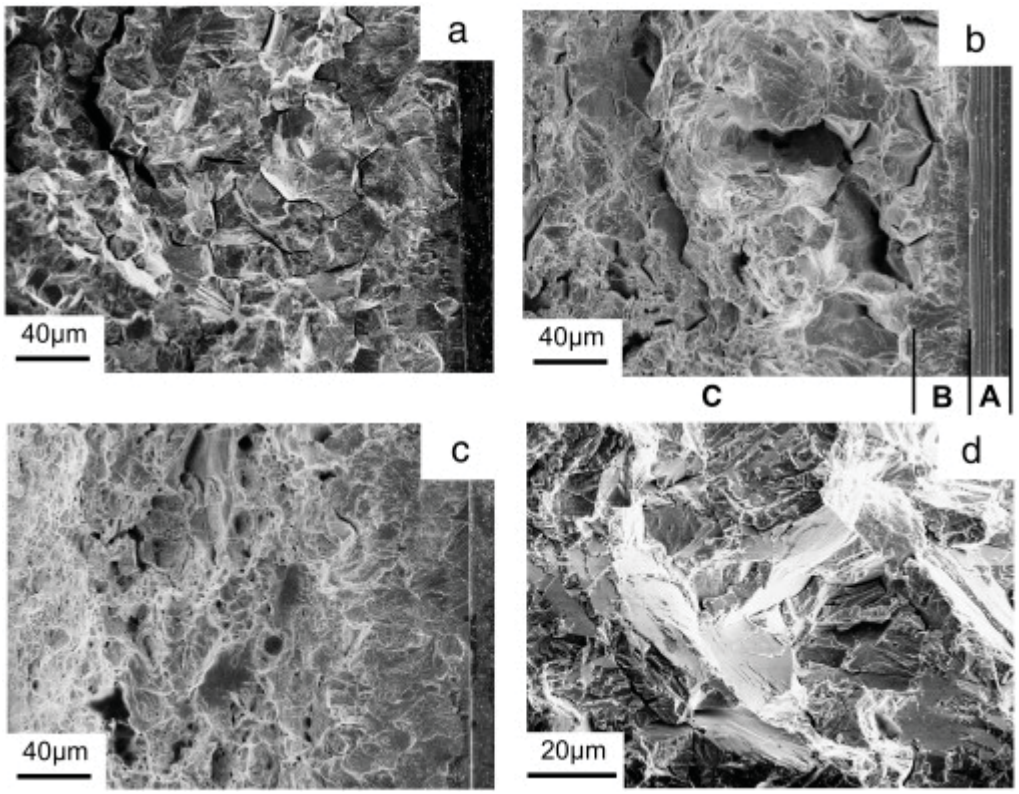

Figure B.5: Scanning electron micrographs of 3 PB specimens broken at (a) room temperature, (b) 400 °C, (c) 600 °C, (d) −196 °C. Intersections in (b) show pre-crack made by razor blade sharpening (A), fatigue crack induced by cyclic compression (B) as well as the fracture surface (C).

In addition, there is a marked difference of fracture morphology between the as-worked and the recrystallized tungsten–rhenium alloy. Scanning electron micrographs identify the grain boundaries of the recrystallized material to be the weakest link. Reasons for this behaviour are numerous. Impurities like oxygen, phosphorous, fluorine or sulfur, which might be uniformly dispersed in the as-worked material, may perhaps get accumulated during the recrystallization process at the moving grain boundaries. Furthermore, the marked difference in dislocation density, texture and subgrain structure may influence the fracture behaviour to a certain extent. Within the context of this work, it is not possible to conclude to what level the above mentioned parameters effect the fracture behaviour of these materials. More work will be carried out on these topics, especially regarding the impurities in tungsten alloys.

Disclaimer

This work, supported by the European Communities under the Contract of Association between EURATOM and the Austrian Academy of Sciences, was carried out within the framework of the European Fusion Development Agreement. The views and opinions expressed herein do not necessarily reflect those of the European Commission.

References for Publication B

[1] Hirai T, Maier H, Rubel M, Mertens P, Neu R, Gauthier E, et al. JET EFDA Contributors. R&D on full tungsten divertor and beryllium wall for JET IER-like wall project. Fusion Eng Des 2007;182:1839–45.

[2] Bolt H, Barabash V, Krauss W, Linke J, Neu R, Suzuki S, et al. ASDEX Upgrade Team. Materials for the plasma-facing components of fusion reactors. J Nucl Mater 2004;329–333:66–73.

[3] Raffo P. Yielding and fracture in tungsten and tungsten–rhenium alloys. J Less Common Metal 1969;17:133–49.

[4] Geach GA, Hughes JE. The alloys of rhenium with molybdenum or with tungsten and having good high temperature properties. In: Proc 2nd International Plansee Seminar; 1955. p. 245–53.

[5] Klopp WD, Witzke WR, Raffo PL. Mechanical properties of dilute tungsten–rhenium alloys. NASA Technical Note NASA TN D-3483, Washington, DC; 1966.

[6] Jaffee RI, Sims CT, Harwood JJ. The effect of rhenium on the fabricability and ductility of molybdenum and tungsten. In: Proc 3rd International Plansee Seminar; 1958. p. 380–411.

[7] Mutoh Y, Ichikawa K, Nagata K, Takeuchi M. Effect of rhenium addition on fracture toughness of tungsten at elevated temperatures. J Mater Sci 1995;30:770–5.

[8] Noda T, Fijita M. Effect of neutron spectra on the transmutation of first wall elements. J Nucl Mater 1996;233–237:1491–5.

[9] Annual Book of ASTM Standards. Metal test methods and analytical procedures, vol. 03.01; 1993; p. 509–39.

[10] Pippan R. The growth of short cracks under cyclic compression. Fatigue Fract Eng Mater Struct 1987;9:319–28.

[11] Kiener D, Kreuzer H, Pippan R. Report for TASK of the EFDA Programme TW4-TTMA-002, Tungsten Alloys Development, 2004.

[12] Kreuzer H, Faleschini M, Gludovatz B. Report for TASK of the EFDA Programme TW5-TTMA-002, Tungsten Alloy Development, 2006.

[13] Romaner L, Ambrosch-Draxl C, Pippan R. Effect of Rhenium on the Dislocation Core Structure in Tungsten. Phys Rev Lett 2010;104(19):195503.

Publication C: Fracture behaviour of tungsten – vanadium and tungsten – tantalum alloys and composites

Fracture behaviour of tungsten – vanadium and tungsten – tantalum alloys and composites

Stefan Wurster [a] , Bernd Gludovatz [a, b, d], Andreas Hoffmann[c], Reinhard Pippan [a, b]

[a] Erich Schmid Institute of Materials Science of the Austrian Academy of Sciences, Jahnstraße 12, A-8700 Leoben, Austria

[b] CD Laboratory of Local Analysis of Deformation and Fracture, Jahnstraße 12, A-8700 Leoben, Austria

[c] Plansee SE, A-6600 Reutte, Austria

[d] now at: Materials Sciences Division, Lawrence Berkeley National Laboratory, Berkeley, CA 94720, USA

Abstract

The influence of both microstructure and chemical composition on the fracture behaviour of tungsten-tantalum, tungsten-vanadium composites and alloys of varying chemical compositions are investigated. Industrial solid solution tungsten-tantalum alloys with different tantalum contents in the as-forged condition are investigated along with different tungsten-tantalum and tungsten-vanadium composites and alloys made by powder consolidation, severe plastic deformation using high pressure torsion and different subsequent heat treatments. To investigate the fracture behaviour, several crack propagation directions in relation to the forging direction and shear direction, respectively, are taken into account. Heat treatment of the composite material results in a more homogeneous distribution of the alloying element and the impacts of these specific heat treatments on microstructure and fracture toughness are discussed. The fracture experiments are performed within a temperature range from room temperature to 600 °C and reveal a strong dependence of the fracture toughness and fracture morphology on temperature and on the microstructure, and hence the processing history of the materials.

Keywords

Tungsten, vanadium, tantalum, fracture, severe plastic deformation

1. Introduction

Tungsten and tungsten-based materials are commonly used for high temperature applications in many different fields. Filaments for light bulbs, X-ray rotating anodes, welding electrodes and radiation protection techniques, just to name a few general ones, take advantage of the high melting point and good mechanical properties of tungsten materials at elevated temperatures. Furthermore, these materials are short-listed for future nuclear fusion reactors, for the International Thermonuclear Experimental Reactor (ITER) and especially for a demonstration power plant (DEMO) in the more distant future. The final divertor set of ITER, experiencing high thermal loadings, should be ideally consisting of tungsten. Divertors are high heat flux components within fusion reactors. For DEMO, tungsten materials might in addition be used for structural applications [1]. In the case of using tungsten as plasma facing material, outstanding properties like low sputtering yield and low plasma contamination become relevant too.

A very important point is the joining technology of tungsten to tungsten and other materials, mostly different types of steel. Independent of the exact design of divertors, either for experimental or demonstrational reactors, connections between tungsten structures and steel structures will have to be realised at some point. Generally, there is of course the option to use materials with low thermal expansion coefficients to decrease thermal stresses resulting from constrained thermal strains, as pointed out by Hohe and Gumbsch [2]. They also proposed to use functionally graded tungsten-vanadium composites. This would combine the benefits of pure tungsten close to the plasma-exposed region, while an increase in vanadium content close to the joining region adjusts some mechanical and thermal properties of the composite materials closer to steel. An increase in thermal expansion coefficients of tungsten materials, getting closer to the ones of e.g. oxide dispersion strengthened (ODS) ferritic steels, and hence a decrease in thermal stresses in the region of joining would help to produce a better connection of tungsten and steel. In [2], the production of a tungsten-vanadium composite via a powder metallurgical route using hot isostatic pressing is described. There, tungsten particles are embedded in a vanadium rich matrix. However, a certain porosity is unavoidable during the processing. In the work presented here, a new processing route will be described, resulting in a more dense structure of vanadium or tantalum particles embedded in a tungsten matrix. A high alloying content of tantalum and vanadium was chosen (30 wt% and 25 wt%, respectively) to achieve materials of markedly changed mechanical and thermal properties – as aforementioned – and furthermore to manufacture composites and alloys of chemical compositions inaccessible in industrial dimensions until now. The customisation of the thermal expansion coefficient is the reason for fabricating tungsten composites with a large alloying fraction.

A second important point and an unfortunate drawback for the usage of tungsten as a plasma facing material, is its low toughness. The brittle-to-ductile transition temperature (DBTT) of tungsten is high, this confines the application of tungsten to intermediate temperatures since recrystallisation with accompanying low toughness does not allow the application at very high temperatures. At low temperatures, existing cracks – pre-existing ones from production or cracks developed during the reactor's operation – might grow; at higher temperatures, recrystallisation can destroy the generated microstructure. The DBTT cannot be given as a simple number, but – depending on testing procedure and strain rate, material composition, production history, hence microstructure – it ranges over several hundred degrees [3-6]. The fracture behaviour of tungsten single crystals and polycrystalline tungsten based materials has already been subjected to extensive research by various scientific groups [3-11], revealing a strong dependency of fracture toughness on crystallography in the case of single crystals [7, 11], strain rate [3, 11], microstructure [4, 8, 9] and of course temperature. A way to increase the toughness is alloying, this works especially well with the addition of rhenium [5, 10, 12]. Now, a systematic investigation directed towards modifying the microstructure and alloying content in order to shift the DBTT to lower values and/or raise the low temperature fracture toughness is required. Romaner et al. [13] showed recently by using density functional theory calculations (DFT) that rhenium changes the core structures of screw dislocations

from symmetric to asymmetric and alters significantly the Peierls stress, this might be the reason for this promising effect of rhenium addition. Related to this work, DFT calculations have been performed for tungsten-tantalum [14] and tungsten-vanadium alloys in order to investigate whether similar effects appear. In this work, fracture experiments for tungsten-tantalum and tungsten-vanadium composites are presented, providing a comparison with this theoretical work.

In the case of very fine microstructures, appearing e.g. after wire drawing [8] or Severe Plastic Deformation (SPD) by Equal Channel Angular Pressing (ECAP) or High Pressure Torsion (HPT) [9], it is possible to achieve high fracture toughness, K_q. The work presented here investigates whether the positive effects of HPT-processing, as observed for bcc α-iron [15] and for lanthanum-oxide dispersion strengthened (WL10), potassium doped (AKS-W or WVM) and pure tungsten [9], can be found for other tungsten materials. In both publications, an increase in fracture toughness was observed. The HPT-process is an easy way to deform also brittle materials to very large strains, owing to the high hydrostatic pressure, which is present during the shear deformation. For this work, a combination of powder consolidation [16] and HPT [17] was used to generate different batches of tungsten-tantalum and tungsten-vanadium materials exhibiting considerably refined grain sizes. One of the advantages of this procedure is that consolidation of composite materials is easy; any chemical composition of materials – disregarding phase diagrams – is possible. When aiming at a fully dense alloy to be developed out of the composite by an adequate heat treatment, one should nevertheless take into account the corresponding phase diagrams. Tungsten materials have already been subjected to SPD by HPT [9, 18-20], but detailed analysis of fracture toughness experiments using SPD-deformed material in general [15, 21] and explicitly for tungsten materials [9] are rare. This is particularly valid for general tungsten-tantalum and tungsten-vanadium [2] materials. For detailed information on materials for fusion application, especially in terms of vanadium alloys, the work of Zinkle et al. [22-24] is recommended.

Hence, the two questions addressed in this investigation are:

- How can one generate dense tungsten-tantalum and tungsten-vanadium composites or alloys?
- Can such alloys or composites help to overcome the low temperature brittleness of tungsten?

2. Materials and experimental methods

2.1. Industrial alloys

Three different tungsten-tantalum alloys of nominally 1, 5 and 10 wt% of tantalum were received from the Austrian company PLANSEE SE in form of sections of disc-shaped specimens in as-forged condition. All alloy and composite compositions are given in weight percent. Figure C.1 shows examples of the microstructures of the as-forged alloys W-1Ta and W-10Ta, typically featuring disc-shaped grains spread in the radial and circumferential directions. The microstructure of W-5Ta is comparable with these results. A well-defined substructure within the grains is recognizable in Figure C.1 and later on in Figure C.4. The microstructure should have a cylindrical symmetry in the forged block. Compact Tension (C(T)) and Three-Point Bending (3PB) specimens were manufactured from all three alloys with the expected crack propagation direction perpendicular to the forging direction and the normal of the crack plane parallel to the forging direction (Type A). The second batch of samples had the normal of the crack plane perpendicular to the forging direction and the expected crack propagation direction parallel to the forging direction (Type B). The specimen size and support span varied between 2 x 4 x 16 mm^3 and 4 x 8 x 32 mm^3. Notches were made by diamond wire saw cutting, razor blade sharpening and, finally, fatigue pre-cracks were introduced by cyclic compression [25]. With the exception of W-10Ta type B samples, all specimens were tested at temperatures varying from room temperature up to 600 °C, using the experimental setup described in [10]. Crosshead speed was 0.4 mm min^{-1} independent of specimen size, resulting in a stress intensity rate of 0.26 – 0.9 MPa $m^{1/2}s^{-1}$. All experiments at temperatures above room temperature were performed in vacuum better than 10^{-2} mbar, preventing oxidation. In the case of W-10Ta, type B-specimens, the sample dimensions were 1 x 1 x 4.6 mm^3. These specimens were tested at room temperature, together with the specimens made of the severe plastically deformed material, described in Section 2.2.

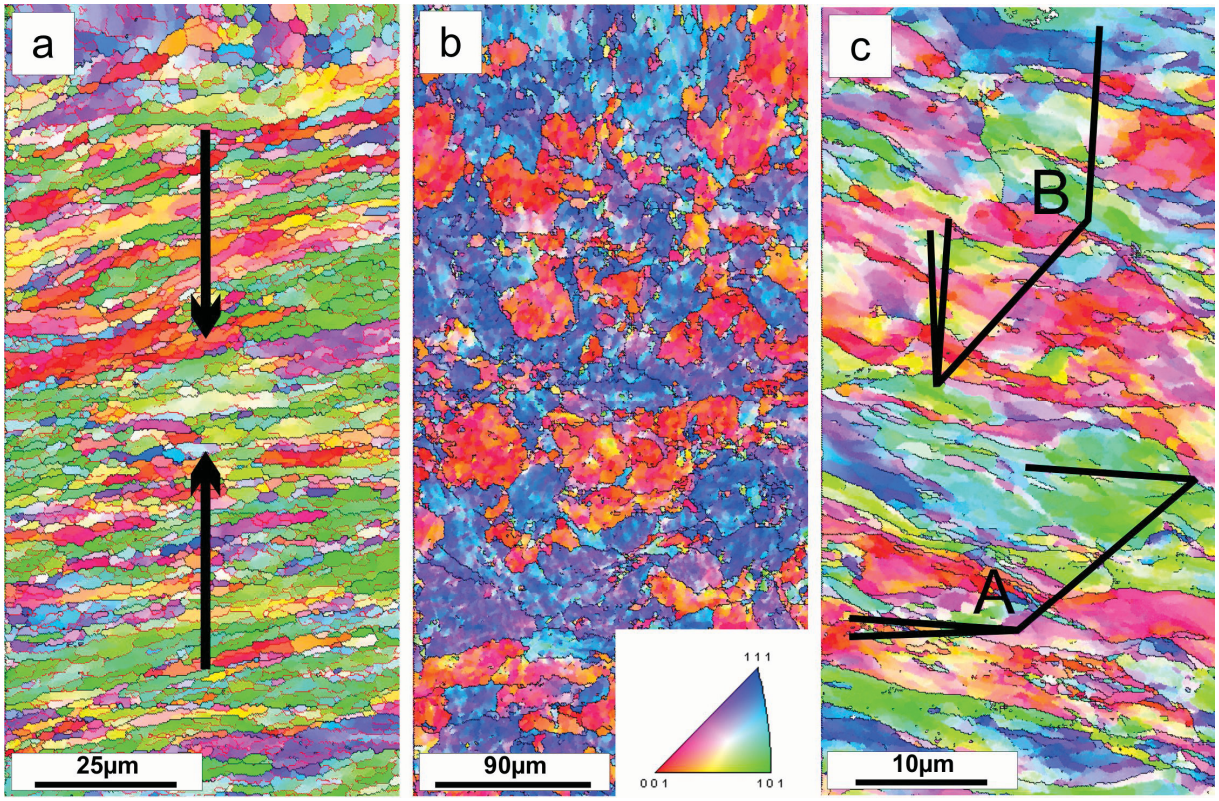

Figure C.1: a) Inverse Pole Figure (IPF) map from Electron Backscatter Diffraction (EBSD) analysis, showing the microstructure of the industrial W-1Ta alloy. High angle grain boundaries, HAGB (>15°, black lines), and small angle grain boundaries SAGB, (5°<α<15°, red lines), are indicated. Scan was made in circumferential direction. Black arrows indicate the forging direction. b) IPF of the same W-1Ta alloy shows the spread of grains along radial and circumferential direction. The scan was made along the forging direction and for the sake of clarity no SAGB are indicated. c) shows an IPF of the W-10Ta alloy. The two crack systems investigated for these industrial alloys are schematically depicted. Please notice the different length of micron bars

2.2. HPT-deformed materials

Two composite materials, W-30Ta and W-25V, were produced by powder mixing, powder consolidation and subsequent SPD by HPT. Mixed powder was put into an ARMCO-iron ring with an inner diameter of 20 mm and an outer diameter of 30 mm. The deformation process was conducted at a temperature of 300 °C. The temperature during deformation corresponds to a homologous temperature $T_{hom} = T/T_{melt}$ of 0.16 (!), thus really being a cold forming process. Both powder compaction and deformation were carried out in air. The anvils of the HPT facility, having the iron ring containing the powder in between, were pressed together and the lower anvil was rotated against the upper one; the anvil's rotation speed was kept constant at 1/15 min^{-1}. The final

specimen thickness, *t,* was 3.6 mm. After HPT, the specimens were stress relieved for one hour at a temperature of 1000 °C in vacuum; all successively described investigations were made after this heat treatment. Because of the comparatively high temperature, this thermal treatment lead to remarkable growth of vanadium grains within the composite, whereas the grain size of tungsten remains in the submicron regime. Micro-hardness measurements were made on bisected specimens with loading along the circumferential direction and samples for fracture experiments were taken at different radii. A characteristic feature of the HPT process, which has to be taken into account, is that the applied strain is radius dependent and so the resulting microstructure and state of consolidation after HPT-processing might also be. The equivalent strain or von-Mises strain respectively, at a certain distance *r* from the centre of the specimen is

$$\varepsilon_{eq} = \sqrt{\frac{4}{3}} \frac{\pi n r}{t}. \tag{C.1}$$

n is the number of revolutions, this was one for both composites in this investigation. Correspondingly, at the specimens' outermost region of *r* = 10 mm, the material experienced an equivalent strain of about 10. In Figure C.2, two Inverse Pole Figure (IPF) maps representing the microstructure at different radii are shown. At a small radius, the IPF map shows more subgrains, which diminishes for higher radii and higher strains. The grain sizes at regions of large deformation are equivalent to the subgrain size at smaller strains. Despite the differences in the microstructure at different radii, the microhardness as a function of the radius was relatively constant.

Owing to this large strain gradient, specimens to be used for fracture experiments were taken out at different radii. Miniaturised 3PB specimens of varying crack systems in relation to the direction of deformation were manufactured out of the stress relieved HPT-deformed material. Specimens will further on be described using the pair of [crack plane normal – expected crack propagation direction] notation. The investigated crack propagation directions were radial (R-type) and axial (A-type) and a third type of samples had the crack plane within the shear plane (S-type). Due to the production route of the specimens, which involves cutting slices normal to the radius, there is a certain deviation α (see Table C.1) of the real crack system from the designated one. As the set of specimens varies in size, crack plane orientation, radius at crack starting point and thus equivalent strain, of all specimens are summarised in Table C.1.

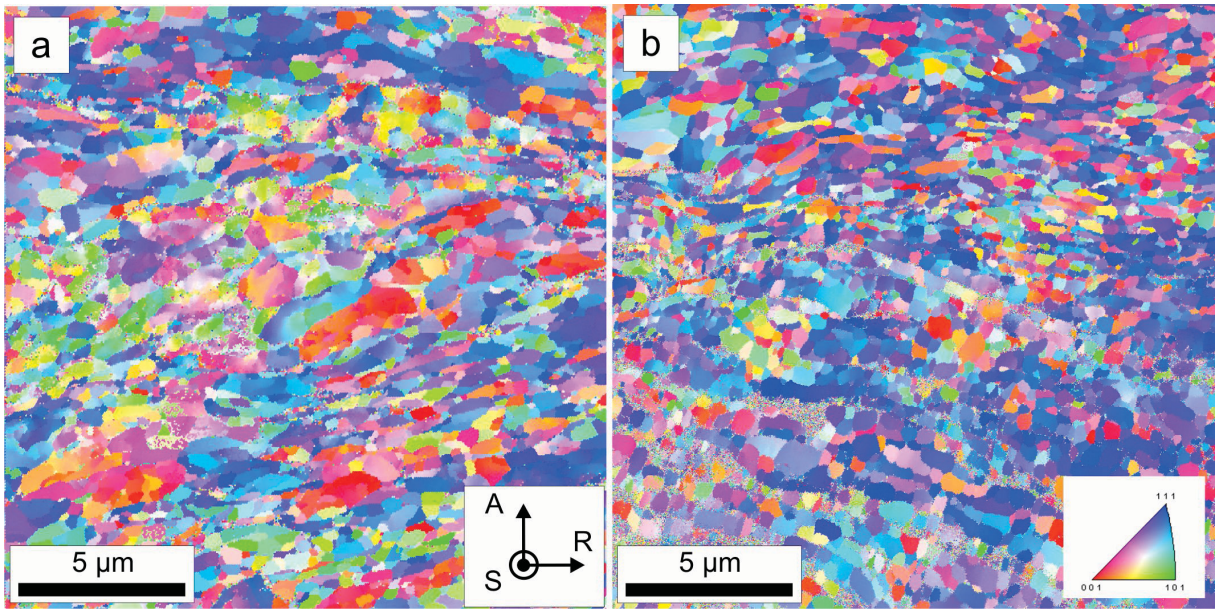

Figure C.2: IPF from EBSD analysis of the W-30Ta specimen, stress relieved for 1 h at 1000 °C, at different radii; (a) at r = 2 mm (ε_{eq} ~ 2) and (b) at r = 8 mm (ε_{eq} ~ 8). Shear, axial and radial directions are denoted. Both IPFs show tungsten rich regions.

The production of specimens' notches involved diamond wire saw cutting, razor blade sharpening and – in contrast to the large specimens made of solid solution tungsten alloys – Focused Ion Beam (FIB) milling. This modified production route was chosen because of the small specimen size and the brittleness of the material – at least in respect to certain testing directions (S-Type) and material conditions (porous microstructure after high-temperature annealing, see Section 2.3). Pre-cracking of such small and relatively brittle samples by cyclic compression often leads to premature failure, FIB-cutting promised a sample pass of 100%. The settings for producing fine FIB-made notches within the razorblade-sharpened notches were the same for all small samples. Two lines with a length of ~50 µm each were cut for 30 min each, using an ion current of 20 nA and 30 kV Ga^+-ions; the resulting trenches were separated by several micrometres. Refinement of the two coarse milled trenches, which were positioned in the centre of the specimen, took place by cutting a thinner line using an ion current of 1 nA (same acceleration voltage) for 10 min over both trenches. The resulting crack-like structure is displayed in Figure C.3 and the FIB-notches can also be seen on the resulting fracture surfaces of A- and R-type samples (Figure C.7 a) – d)). The very small ligament between the two large trenches experiences the highest tensile stresses under 3PB-loading, and fracture is expected to start there. This wall is used as a stress concentrator for crack initiation. It can be seen in the insert in Figure C.3, showing this part after the 1 nA – cut, that the notch tip radius is very small, thus it is presumable that FIB-made notches successfully mimic natural cracks. Any damaged area, resulting from gallium ion milling, is negligible in relation to the overall specimen size, even in relation to the small wall separating the larger trenches [26].

Table C.1: Set of 3PB specimens of HPT deformed materials, before and after thermal treatment.

Material	[Orient.]	α [°]	ε_{vM} [-]	S [mm]	B [mm]	W [mm]	a [mm]	K_Q [MPa m$^{1/2}$]
W-25V	[A-S]	8	6.1	2.94	0.66	1.09	0.39	4.4
W-25V	[A-S]	23	6.0	2.92	0.67	1.13	0.45	5.6
W-25V	[A-S]	7	7.5	2.88	0.96	0.98	0.37	4.9
W-25V	[A-S]	7	7.5	2.88	0.97	1.22	0.52	4.5
W-25V	[A-S]	7	7.5	2.88	0.96	1	0.50	5.0
W-25V	[A-R]	12	5.3	2.94	1.11	0.8	0.32	3.3
W-25V	[S-R]	15	9.0	2.9	1.67	0.7	0.28	20.3
W-25V	[S-R]	15	9.0	2.94	1.44	0.72	0.24	13.1
W-25V	[S-R]	17	5.2	4.52	1.08	0.79	0.44	13.3
W-25V	[S-R]	29	8.5	4.52	1.14	0.96	0.38	14.1
W-25V	[S-A]	66	2.1	2.9	1.08	1.41	0.42	19.8
W-25V	[S-A]	66	2.1	2.92	1.09	1.83	0.66	21.5
W-25V	[S-A]	47	3.3	2.94	1.12	1.56	0.58	25.3
W-25V	[S-A]	47	3.4	2.9	1.12	1.69	0.53	18.1
W-25V	[S-A]	47	3.4	2.92	1.12	1.53	0.45	13.1
W-25V	[S-A]	29	8.5	4.52	0.97	2.03	0.83	28.0
W-25V	[S-A]	17	5.2	4.52	0.78	2.2	0.83	26.0
W-30Ta	[A-S]	23	9.2	2.88	1.16	1.23	0.42	4.4
W-30Ta	[A-S]	23	9.2	2.88	1.15	1.74	0.76	5.7
W-30Ta	[A-S]	32	7.3	2.94	0.70	1.36	0.55	3.7
W-30Ta	[A-R]	10	4.8	2.94	0.93	0.67	0.26	4.3
W-30Ta	[S-R]	23	10.0	2.94	1.31	1.24	0.51	29.5
W-30Ta	[S-R]	23	10.0	2.9	1.64	1.04	0.47	29.6
W-30Ta	[S-R]	20	8.8	4.52	0.73	0.96	0.54	23.2
W-30Ta	[S-R]	20	8.8	4.52	1.10	1.13	0.54	27.7
W-30Ta	[S-A]	11	5.6	4.52	1.14	2.06	0.91	39.5
W-30Ta	[S-A]	70	2.5	2.92	0.91	1.31	0.44	19.0
W-30Ta	[S-A]	70	2.5	2.92	1.01	1.95	0.75	17.3
W-30Ta	[S-A]	49	3.6	2.9	1.12	1.95	0.91	24.1
W-30Ta	[S-A]	49	3.6	2.94	1.11	1.37	0.69	19.1
W-30Ta	[S-A]	11	5.6	4.52	1.04	2.10	0.91	39.8
W-30Ta	[S-A]	16	7.1	2.88	1.14	1.01	0.58	55.1
W-30Ta	[S-A]	22	9.9	4.52	1.24	0.95	0.41	13.3
W-30Ta	Recryst.	-	-	4.52	1.15	1.12	0.56	4.2
W-30Ta	Recryst.	-	-	4.52	1.02	1.21	0.59	3.2
W-30Ta	Recryst.	-	-	2.88	0.84	1.06	0.46	4.1

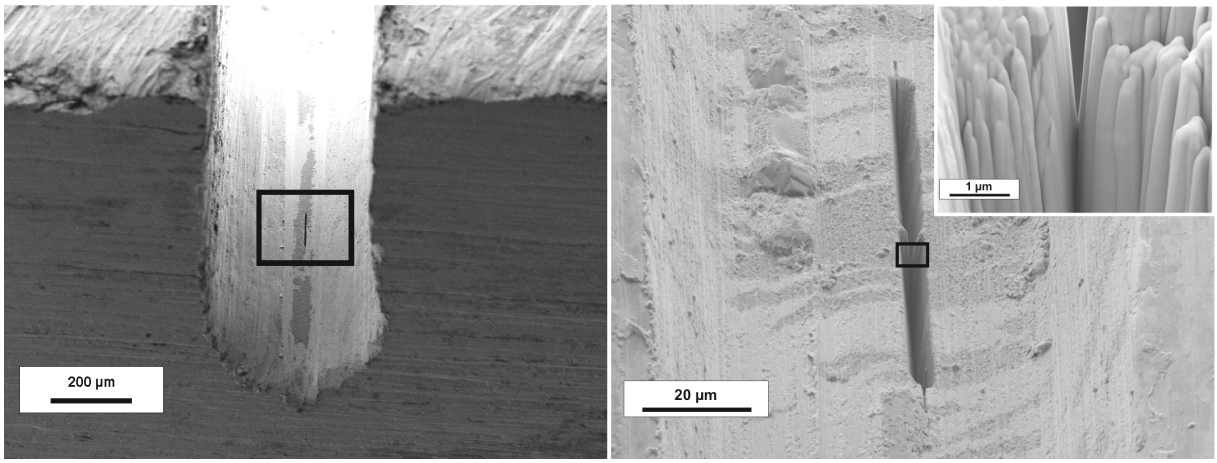

Figure C.3: FIB-made crack-like structure in the centre of the razor blade sharpened notch, 2 coarse milled trenches are refined and connected by a fine cut using a smaller ion current, the two-phase composite microstructure is easily recognisable in the razorblade-sharpened notch. The inlay shows the wall separating the two large trenches; this sharp notch is the result of 1 nA - cutting. The large dark areas in the right picture show debris from razor blade polishing.

2.3. Homogenised HPT-deformed materials

EDX measurements were conducted in order to determine the chemical composition at different sites within the HPT-deformed tungsten composites. As expected, no remarkable interdiffusion of tantalum and vanadium into tungsten was observed after HPT and annealing at 1000 °C; much higher strains would have been necessary to perform mechanical alloying. Hence, some parts of the HPT-deformed materials were annealed at 1800 °C (W-25V), being close to the melting temperature of vanadium, and 2500 °C (W-30Ta), respectively. Again, 3PB specimens for fracture experiments were machined; production was similar to specimens made material having the composite microstructure, described in Section 2.2. Due to the expected recrystallised microstructure after heat treatment, no specific measures were performed for testing specially arranged crack systems, as was done for the as-deformed material.

3. Result

3.1. Industrial alloys

All results of fracture toughness measurements on industrially produced solid solution treated tungsten-tantalum alloys at varying test temperatures are summarised in Figure C.5. K-values were calculated according to ASTM E399 [27] using the first load drop either originating from crack extension starting at the fatigue crack or originating from grain boundary delamination in front of the crack tip; this results in fracture initiation toughness values. Further increases in load after first load drops indicate an R-curve behaviour of the fracture toughness. The occurrence of crack deflection, which makes the R-curve analysis more complex, and the missing of an accurate crack extension measurement are reasons why only the crack initiation toughness is considered in the following. The diagrams (Figure C.5) show the expected increase in fracture toughness with increasing temperature for all investigated alloys. Specimens of type A show a low but steady increase in fracture toughness with increasing temperature and a decrease with increasing tantalum content – at least from W-1Ta to W-5Ta. This reflects the experiences gained from forging and machining of specimens. For specimens of type B an increase of K_q with temperature is recognisable, but unsteady, which will be discussed in greater depth later on. Fracture morphology shows very distinct differences, the fracture is either almost completely transcrystalline, when the crack propagates along the forging direction or intercrystalline, when propagating perpendicular to it. As an example for the “one-way” fracture morphology, the fracture surfaces of different W-5Ta specimens, tested under various conditions, are presented in Figure C.4. Fracture morphology is simply dependent on crack propagation direction, any differences according to temperature are hardly distinguishable. As with the EBSD results, the pronounced subgrain structure is visible on both kinds of fracture surfaces. As can be seen in Figure C.4 a) and b), it is most likely for type B samples – at least at low temperatures - that the crack does not propagate along subgrain boundaries, which would involve only slight deviations from straight propagation, but subgrains are cleaved.

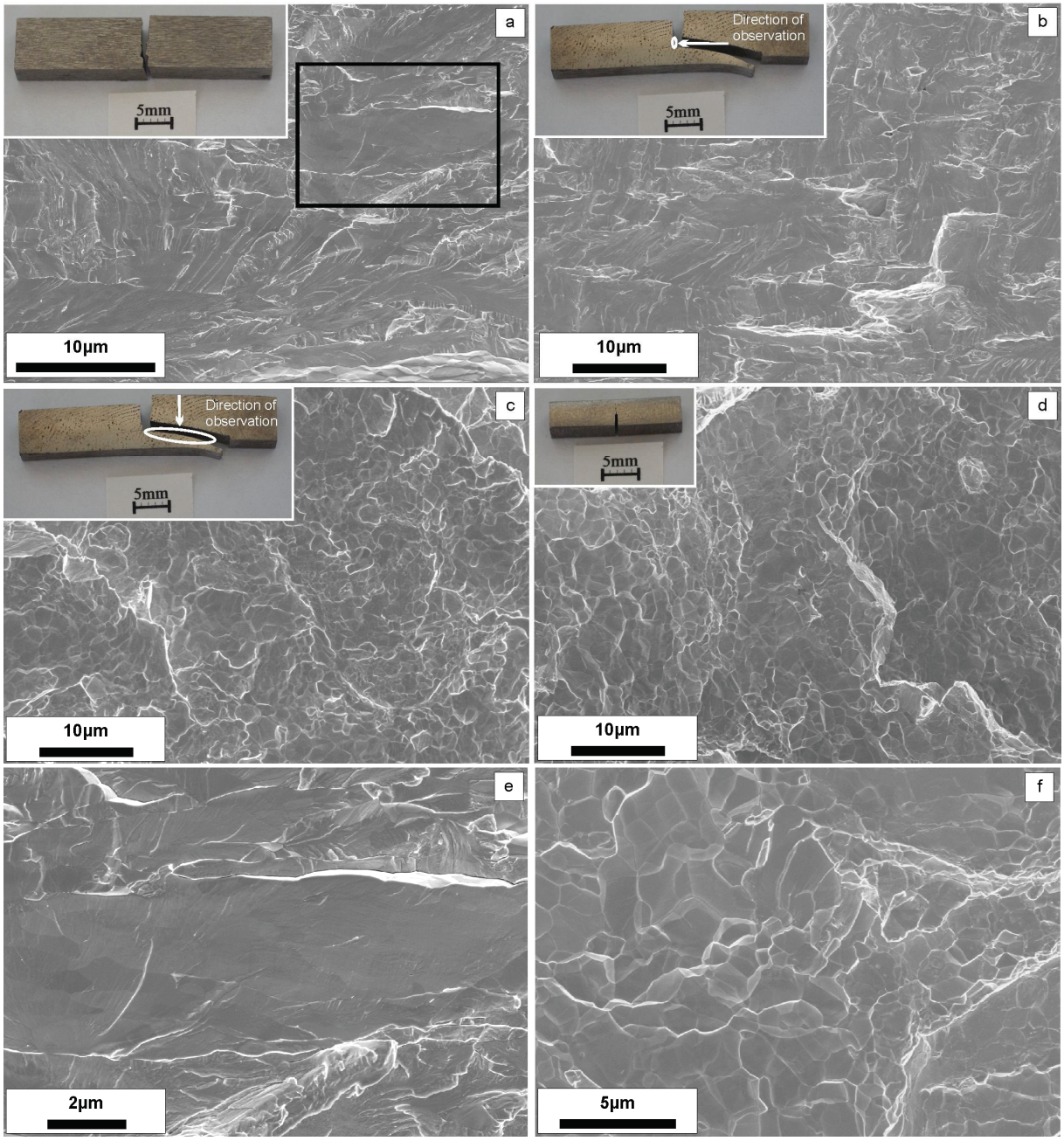

Figure C.4: Illustration of the fracture surfaces taken on 3PB specimens made of W-5Ta. a) tested at RT, crack propagation in the forging direction; b) tested at 600 °C, crack propagation in forging direction, transcrystalline fracture for small crack extension. (c) the same specimen as b) but micrograph was taken in the specimen's midsection, where the crack had deviated from the forging direction, resulting in pure intercrystalline fracture. d) specimen fractured at RT, crack perpendicular to forging direction, again pure intercrystalline fracture is observed. e) shows the transcrystalline fracture within the region highlighted with a black square in a) in greater detail. f) is a higher magnified picture from the sample shown in d). In both details, the subgrain structure is visible.

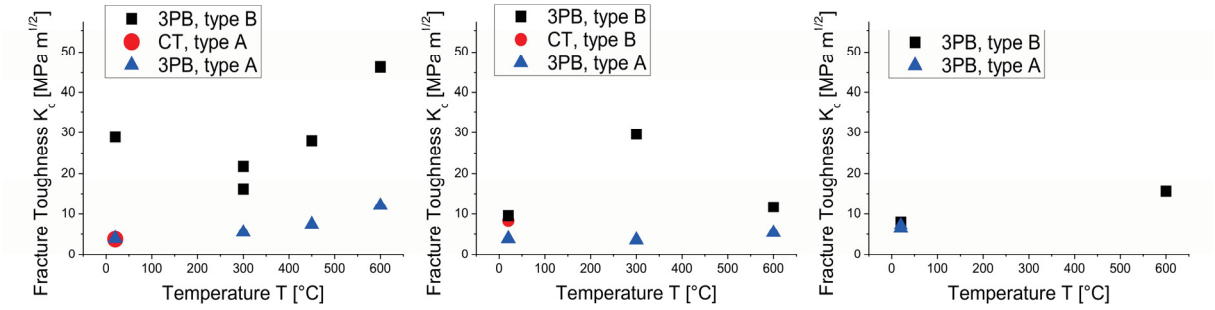

Figure C.5: Fracture toughness K_q as a function of temperature for different solid solution treated tungsten-tantalum alloys (W-1Ta, W-5Ta, W-10Ta from left to right) and as a function of notch direction

3.2. HPT-deformed materials

Figure C.6 summarises the results of fracture toughness experiments considering different HPT-deformed materials, different equivalent strains and different crack propagation directions. K_q-values were calculated according to [27]. As no load drops were observed, the maximum force was used instead. In the HPT-sample the applied strain increases linearly with radius. Assuming an accuracy of ±500 µm in determination of the radius within the cylindrical sample of the crack starting point the error margin in applied strain is about 0.5. Independent of the angle between shear direction and crack propagation direction, applied equivalent strain and material, the K-values of specimens with the crack plane lying in the shear plane are small and comparable with results gained for the solid solution tungsten-tantalum alloys for type A – testing. For all other specimens having the crack plane different from the shear plane, the fracture toughness is much higher, not less than 13 MPa $m^{1/2}$. An increase in K_q with higher equivalent strain for all of these four general types of samples (A-type, R-type, W-30Ta, W-25V) might be possible.

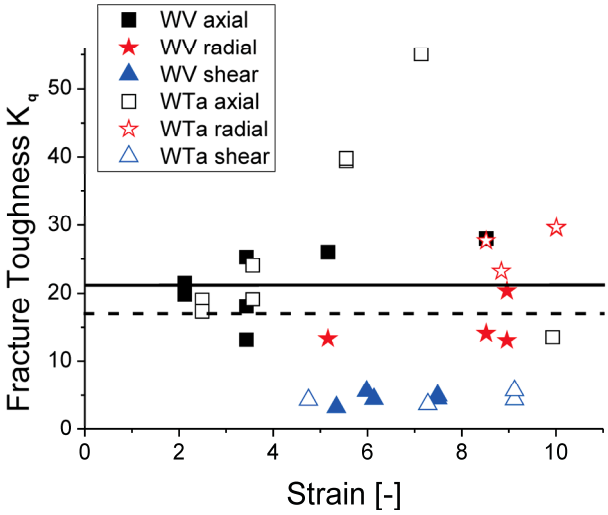

Figure 6: Fracture toughness values K_q for W-25V and W-30Ta considering different equivalent strains and crack propagation directions, measured at room temperature. The limits of validity according to [27] are shown for WTa (continuous line) and WV (dotted line) assuming a 3PB-sample with $B = a = W - a = 0.5$mm.

Results of fractography for all crack propagation directions (S, A, R) as well as both composite materials are summarised in Figure C.7. All fracture surfaces displayed there, exhibit brittle fracture; no signs of macroscopic plastic deformation are visible. The outcome regarding fracture morphology is typical for such HPT-deformed specimens, as the crack always tends to propagate towards (A and R) or stays within (S-type) the shear plane. In the case of radial specimens, this fact leads to serrated crack propagation fronts, whereas for axial specimens the crack propagation plane itself is serrated. On a smaller scale, the fracture surface appears fibrous. This can be seen best in the insets in Figure C.7 a) and c). In all of the figures displaying specimens of A- and R-type, the FIB-machined notch is visible. Large grains – in comparison to the tungsten microstructure – of vanadium are visible on all W-25V fracture surfaces (Figure C.7 (b), (d) and (e)). This is a result of annealing for 1 h at 0.58 T/T_m for vanadium.

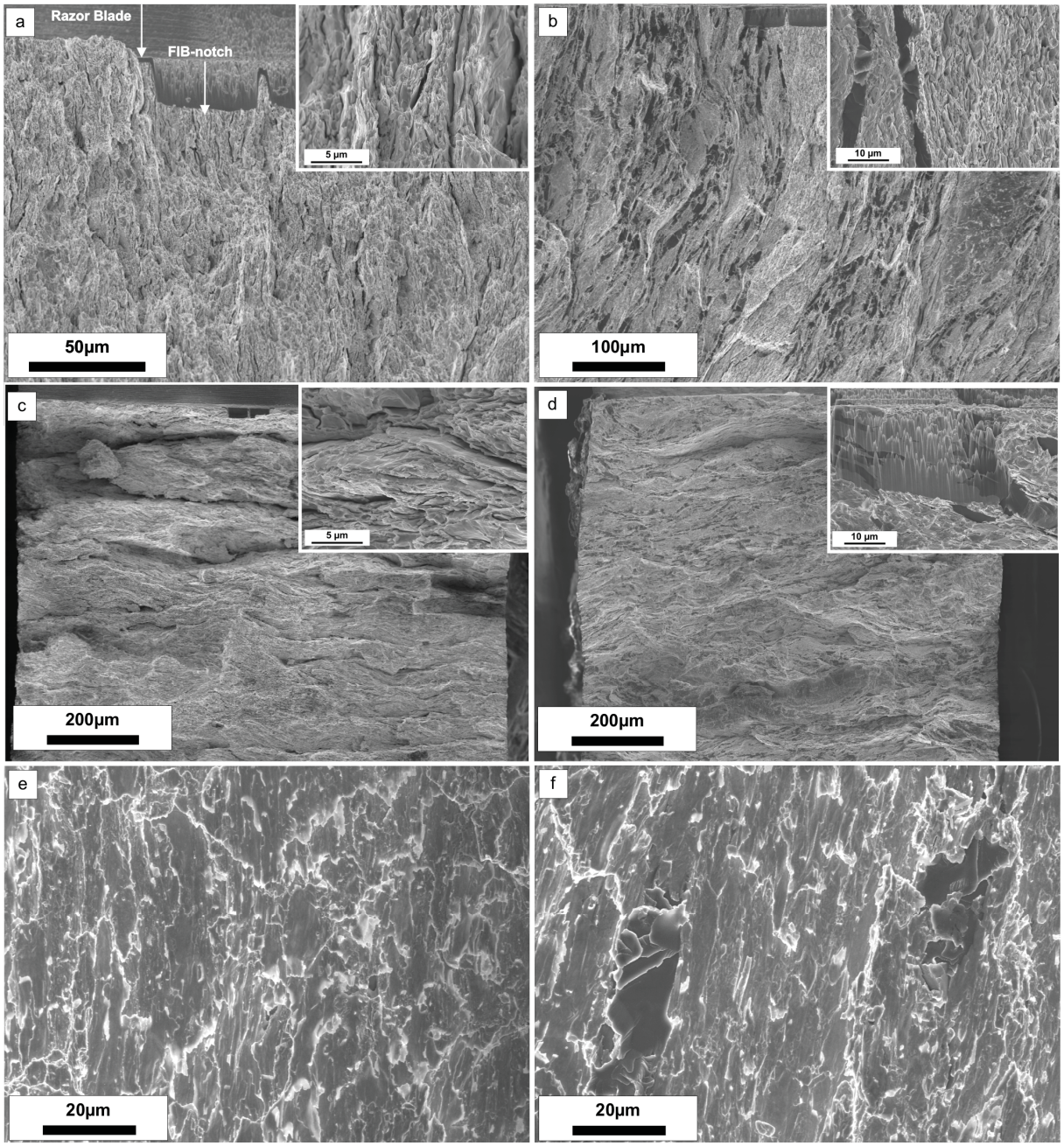

Figure C.7: Fracture surfaces of W-30Ta, (a), (c), and (e) and W-25V, (b), (d), and (f). (a) and (b) show radial specimens, (c) and (d) axial ones and (e) and (f) specimens with crack propagation in shear direction. Crack propagation direction within the SEM micrographs is always from top to bottom. In a), the razor blade- and FIB-notches are highlighted.

As the specimens in this work are small, the question arises whether these fracture toughness values can be considered valid. Applying the standard criteria that crack length *a* and specimen thickness *B* have to be larger than 2.5 K_q^2/σ_y^2 and assuming that σ_y is 1.2 GPa for W-25V and 1.5 GPa for W-30Ta, it turns out that many specimens for the axial and radial directions are too small, owing to their high fracture toughness. Yield stresses are deduced from micro-hardness measurements, using the rule of Tabor. Conservative specifications of hardness for both specimens after 1000°C annealing is 400 HV 1 for W-25V and 500 HV 1 for W-30Ta. Hence, the experimentally determined fracture toughness values of many specimens, gained from small 3PB-samples and calculated by using linear elastic fracture mechanics, can only considered to be lower bounds for a valid K_{IC}-value. In summary, all specimens with cracks within the shear plane are valid, whereas for the samples with the other crack systems, just a few failed at low stress intensities and deliver valid K_{IC}-values.

3.3. Homogenised HPT-deformed material

As expected after SPD and annealing at 1000 °C neither WTa- nor WV-composites achieve chemical homogeneity. Hence, the tantalum composite was annealed at 2500 °C for 1 h and the vanadium composite at 1800 °C, also for 1 h. The porosity is – due to the Kirkendall effect – larger for the W-25V composite. In this case, 1800 °C represents 0.95 T_{hom} for vanadium but just 0.56 T_{hom} for tungsten. The difference is smaller for the W-30Ta heat treatment at 2500 °C: 0.84 T_{hom} for tantalum and 0.75 T_{hom} for tungsten. EDX measurements performed at fracture surfaces of both types of heat-treated specimens show a relative homogeneous distribution of tantalum and vanadium. Homogenised W-25V shows a composition varying from 18 to 30 wt% V in selected regimes. W-30Ta shows a composition of 30 to 38 wt% Ta in selected regimes at the fracture surface.

None of the 3PB-specimens made of heat treated WV could have been tested successfully; all of them broke beforehand – revealing the material's very brittle nature. Fracture might be supported by the high porosity generated during the annealing at 1800 °C for 1 h (Figure C.8,a). Three specimens of W-30Ta were tested, resulting in an average fracture toughness value of (3.8 ± 0.6) MPa $m^{1/2}$. Despite the small specimen size, this is a valid K-value. Figure C.8, b presents the fracture surface one of the specimens tested with the crack propagation along the radial direction.

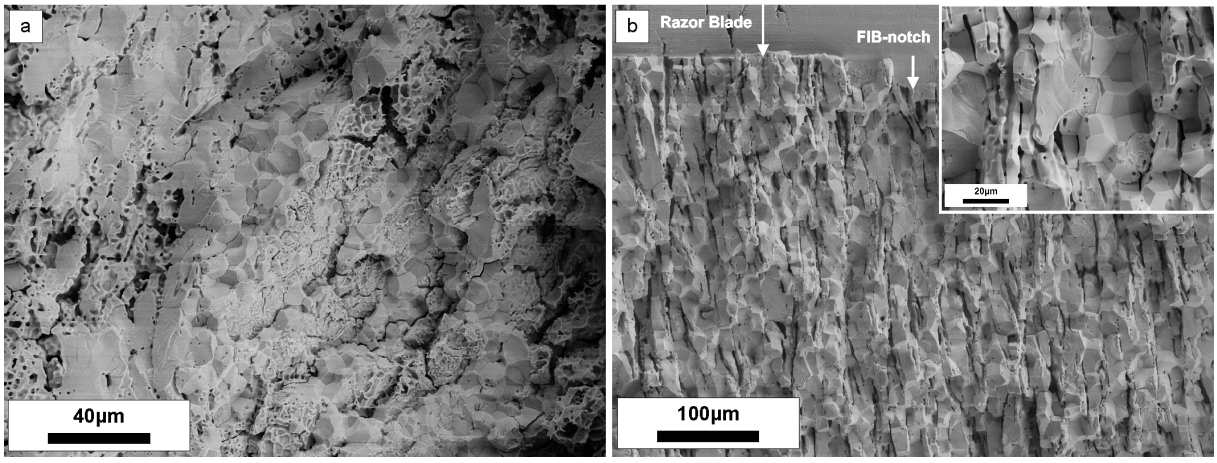

Figure C.8: Fracture surface of W-25V annealed at 1800°C for 1 h (a), showing the very porous microstructure, and W-30Ta annealed for 2500 °C for 1 h (b).

4. Discussion

4.1. Fracture behaviour

4.1.1. Industrially produced solid solution alloy

Two different types of samples were tested: One batch of samples had the expected crack propagation direction perpendicular to the forging direction / parallel to the elongated grains and the normal of the crack plane parallel to forging direction (Type A). The second batch of samples (Type B) had the normal of the crack plane perpendicular to forging direction and the direction of expected crack propagation parallel to forging direction, or perpendicular to the elongated grain respectively. Concerning specimens of type A of the solid solution alloy, the improvement in K_q with increasing temperature, starting from a very low level at room temperature, is as expected. Figures C.1 a) and b) shows many grain boundaries along the crack propagation direction; the fractograph in Figure C.5 d) shows pure intercrystalline fracture. Hence, the toughness of type A specimens can be considered as the intrinsic fracture toughness of grain boundaries of tungsten alloys with varying tantalum content. This low temperature toughness is in coincidence with S-type samples of the HPT-generated composite.

In contrast to type A, the behaviour of specimens of type B is different. The drop in fracture toughness vs. temperature can be related to the deflection of propagating cracks from the forging direction. Just looking at specimens tested above room temperature, none of these specimens, except for W-1Ta tested at 600 °C, showed a monotonic increase in load until catastrophic fracture occurs, but load drops appeared before F_{max} was reached. Not having in situ observation within the heated vacuum chamber available, the most probable cracking procedure has to be deduced from

light and scanning electron microscopy. Either, the crack starts directly at the fatigue crack or the material in front of the crack delaminates, hence leaving back material, which deforms and finally fractures by shear. It can be stated that the same macroscopic fracture behaviour is shifted with increasing tantalum content to higher temperature. The W-1Ta specimen fractured at room temperature shows crack branching in front of the notch, resulting in small cracks branched in the perpendicular direction – hence the high toughness – but as a general trend the crack follows the original notch direction and the macroscopic path is more or less within the forging direction. This is the same for the W-5Ta specimen, showing fewer branched cracks perpendicular to the propagation direction and a smoother fracture surface. W-10Ta shows the smoothest fracture surface of all. For higher temperatures, all W-1Ta specimens show crack deflection with a large fraction of intercrystalline fracture. 300°C-W5Ta shows the same behaviour as found for RT-W1Ta: macroscopic crack path coinciding with the notch but zigzag progress, alternating regions of trans- and intercrystalline fracture and crack branching at the crack's reversal points. For W-10Ta, no crack branching or deflection was observed, even for the highest temperature. Summarising, there is an increase in fracture toughness with temperature, until a change in fracture behaviour and a drop in global fracture toughness takes place. For pure, polycrystalline tungsten this has already been explored and discussed in greater detail by Rupp and Weygand [28], where they found a transition temperature of 275 °C for the change from trans- to intercrystalline fracture. This change was also associated with a change of the crack propagation from perpendicular into the direction of the aligned grains. They used material of similarly aligned microstructure. The transition in fracture mode discussed here should not be confused with the normally used term of "brittle-to-ductile transition" for tungsten. The results presented here are in agreement with [28], as for W-1Ta, the transition has already taken place at 300 °C and for W-5Ta it did not. The strong dependency of fracture mode on tantalum alloying content is evident, as for the W-10Ta alloy heating to 600 °C was not sufficient to reach the transition from the transcrystalline to intercrystalline fracture mode, which shall be explained by Figure C.9. There, the temperature-dependent fracture toughness for transcrystalline and intercrystalline fracture are schematically depicted. Transcrystalline fracture toughness for WTa is noticeable lower for higher temperatures in comparison to pure tungsten. The temperature for this transition is higher, the more brittle the grain interior is.

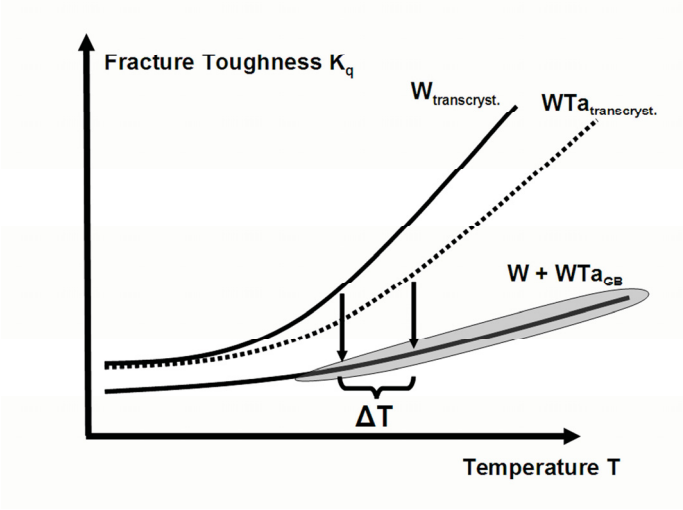

Figure C.9: Schematic Illustration of generals trends of fracture toughness K_q vs. temperature for pure tungsten and tungsten-tantalum alloys

4.1.2. HPT-deformed material

Three different types of HPT-consolidated composites were tested: For S-type samples, the crack plane coincides with the shear plane. For R-type and A-type samples, the expected direction of crack propagation is in radial and axial direction. Fracture experiments show that toughness is very low when the crack plane is in coincidence with the shear plane. Independent of composite, equivalent strain, angle between shear direction and crack propagation direction, the fracture toughness values are about 4 – 5 MPa $m^{1/2}$. The cracks stay – except for minor deflections – within the shear plane. This changes when testing radial and axial specimens, where major crack deflection takes place. In both cases, the crack tries to propagate along the shear plane resulting in a zigzag progress and the fracture surfaces have fibrous character. The reason for this is the elongated grain structure remaining after HPT, which can be seen best in the inset of Figure C.7 b).

One striking feature of the HPT-deformed tungsten materials is the very small grain size of tungsten – even after annealing at 1000 °C for 1 h, which is 0.34 T_m of tungsten. Typically, highly deformed materials are very prone to recrystallisation, as the amount of stored energy is large and the driving force for grain boundary migration is high. However, closer investigation of the microstructure of the tungsten-tantalum composite using EBSD showed that the majority of the grains have grain sizes ranging from 200 nm to 300 nm. This is assumed to be beneficial for the fracture toughness perpendicular to the elongated grains. Faleschini [29] used the same annealing procedure for bulk tungsten, which was HPT-deformed to even higher equivalent strains and also heat treated for 1 h at 1000 °C. The observation was that the grain size is about 2 µm for strain levels below 30. The fine microstructure of the tungsten matrix, processed by powder compaction instead of using bulk materials, might originate from impurities. This comes most likely from WO_3,

being present at the powder's surface before the deformation process starts, as described by Bachmaier et al. for pure nickel and aluminium [30]. There, the usage of an oxidised nickel powder for powder compaction and HPT led to a remarkable decrease in grain size and an increase of structural stability at higher temperatures. Here, the same process is proposed, as, according to [31], an oxide layer of 1 nm thickness develops on pure tungsten even at room temperature. A detailed analysis for 300 °C is not given in [31], but when heating up to 400 °C for 1 h, the tungsten oxide layer increased to more than 10 nm.

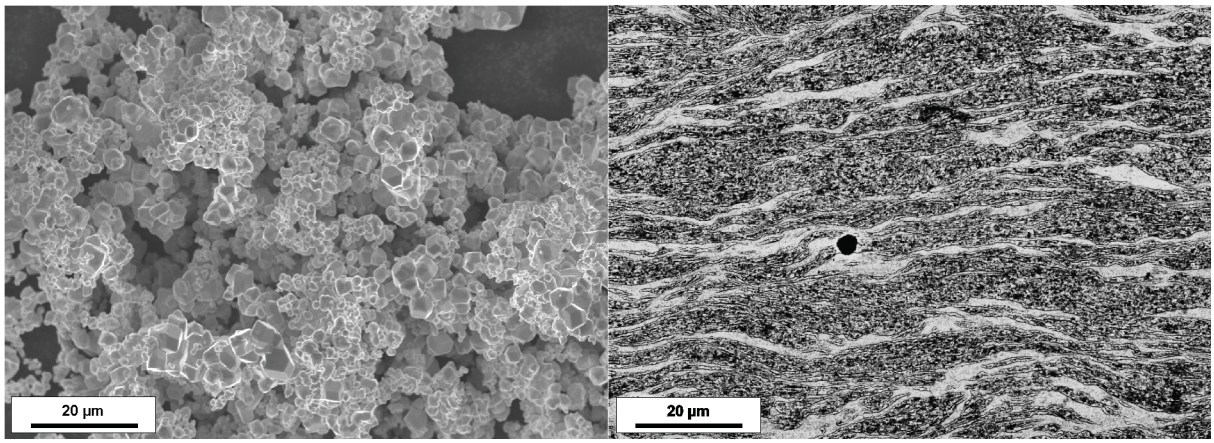

Figure C.10: a) SEM images of tungsten powder in the as-received condition. b) BSE image of the surface of the tungsten-tantalum composite, stress relieved at 1000 °C for 1 h, picture was taken at r ~ 10 mm (ε_{eq} ~ 10). Black areas show W-rich regions, brighter ones mainly consist of Ta.

On the one hand, the formerly powder-like material is indeed very dense after HPT powder compaction but on the other hand, there should be some oxygen at high pressure left within the sample, due to the closed porosity, which develops at a certain point during powder compaction. The heating of the powder-compacted HPT sample to 300 °C takes about 10 min, after allowing 15 min for temperature compensation, the HPT process then lasts for 15 min. This should be enough time to develop an oxide layer of a few nanometres in thickness. Furthermore, the small starting size of single grains should also be helpful to introduce a greater amount of oxide into the deformed material. An SEM image of tungsten powder in the as-received condition can be seen in Figure C.10; all single grains have sizes smaller than 10 µm but stick together into larger conglomerates. This results in a large reactive surface area. It is already well known that microstructures of tungsten based materials can be stabilised to higher temperatures by oxide dispersion strengthening, e.g. by lanthanum oxide or thorium oxide. The same process seems to work by the introduction of oxidised parental powder particles, without deteriorating the fracture toughness.

Faleschini et al. [9] demonstrated the increasing fracture toughness for increasing equivalent strain for pure tungsten, lanthanum-oxide dispersion strengthened tungsten and potassium doped tungsten. All of these materials were processed in bulk form and subjected to HPT – to even higher equivalent strains than used here. The specimens tested there, are equivalent to the [S-R]-orientation tested in this work. In a strain range of 2 – 10, the reported fracture toughness values are 13 – 37 MPa $m^{1/2}$. For the tungsten-tantalum composite material, the internal size of the "phase microstructure" is on the order of several micrometres up to several tens of micrometres (Figure C.10, b; Figure C.7, f), so we assume that the crack is triggered within the large and linked-up tungsten regions. This is confirmed by the fact that there is a coincidence in fracture toughness values of the above-mentioned HPT-deformed bulk tungsten material and the composite. A striking difference in fracture behaviour is expected when the size of the individual phases approach the submicron regime. Then, the crack cannot propagate within the more brittle phase over long distances, but diffusion might become a problem, as it would destroy the composite microstructure.

The increase in K_q with strain is not fully reproducible in this work as the investigated range of strain is not as large as in [9]. A slight increase in toughness values might be recognisable (see Figure C.6), but this might also come from large scatter. When starting with a very fine powder and a small microstructure, respectively, the microstructural size after HPT-process does not vary over a large range when comparing inner and outer radii. Hence, the increase in K_q, as observed in [9] is not detectable.

Another point when questioning the reliability of the results is the production of the notches with the FIB, as they are no natural cracks. In fact, the FIB-machined notches do not extend over the whole sample thickness. The probability to find defects, which trigger final fracture at or close to the FIB-notch roots would increase with longer FIB-notches. However, as the microstructure after HPT-deformation is in the regime of several hundreds of nanometres, the used notches with a length of about 100 µm affect a large number of grains. Nevertheless, it is possible that scatter of fracture toughness values of A-type and R-type samples (Figure C.6) can be attributed to artificial FIB-notches. Summarising the fractographs of all samples, just one out of the batch of specimens having the crack plane within the shear plane displayed the FIB-made notch on the fracture surface. Hence, there had to be pre-existing defects within the shear plane either being larger than the FIB-notches or having sharper crack tips. In contrast, just one out of the batch of specimens having the crack plane not within the shear plane did not display the FIB-made notch. It appears very unlikely that a crack starts elsewhere within the A- and R-type samples and then runs towards the FIB-notch. Hence, we assume the FIB-made notches to be adequate representatives of natural cracks.

4.1.3. Homogenized high content W-Ta and W-V materials

Evenly distributed tantalum and vanadium concentrations in HPT-samples might be accomplished by applying a higher number of revolutions, requiring a much higher equivalent strain. However, subsequent heat treatments also diminish these gradients of chemical composition. A drawback when just using a simple thermal treatment without applying any pressure is that the resulting microstructures entail many pores due to the Kirkendall effect as a consequence of different diffusion constants of V in W, W in V, Ta in W and W in Ta. Using such porous materials is of course not advisable in fusion applications, as thermal conductivity is reduced and without any adjusted microstructure, the fracture toughness is low too. Three subsequent production routes are possible to obtain composite materials without porosity.

- Hot forming of the as-received composite after sintering, if the workability allows for it.
- Hot isostatic pressing
- A double sintering process, involving the generation of powder out of the homogenised material and a successive second HPT process using the powder of the desired chemical composition.

4.2. Tungsten materials for fusion: thermal expansion and fracture toughness

For decades, alloying elements, which should feature a ductility enhancing effect like rhenium, have been pursued. Summarising this work, it can be stated that neither tantalum nor vanadium have this beneficial effect. However, it could be shown that deformation has an advantageous influence on the ductility, bringing the materials described in this work to a similar level of fracture toughness in comparison to other tungsten-based materials. Alloying tungsten with other elements might be of interest not only for striving for ductile materials but also for other purposes – such as joining – as will be discussed now.

Due to a large difference in thermal expansion of tungsten ($\alpha \approx 4.5*10^{-6}$ [32]) and reduced activation ferritic/martensitic steels ($\alpha \approx 10.4*10^{-6}$ [33]) high thermal stresses are caused by thermal cycling. Hohe and Gumbsch demonstrated in [2] by numerical simulation that a simple rule of mixture applies very well in determining the thermal expansion coefficient of tungsten-vanadium composites. Hence, as a rule of thumb, α increases linearly with vanadium ($\alpha \approx 8.3*10^{-6}$ [32]) and tantalum ($\alpha \approx 6.5*10^{-6}$ [32]) content. Expansion coefficients, used here, are valid for room temperature. The higher thermal expansion coefficient of vanadium in comparison to tantalum makes it more usable when coming back to the topic of joining. Tungsten-vanadium alloys will be especially tuneable over a large range; furthermore, vanadium is more stable under neutron irradiation. Gilbert [34] performed transmutation calculations for a large set of elements, assuming

a neutron spectrum according to a recent power plant conceptual study and for an irradiation time of 5 years.[9] Tantalum atoms transmute to a large part into tungsten atoms, whereas the atomic concentration of vanadium just drops to 99% after 5 years, only small amounts of other elements evolve. However, a disadvantage is the increased rate of production of helium in vanadium [34]. When compared to tungsten or tantalum, the production of helium is increased by more than one order of magnitude.

A suggestion for a tungsten material for fusion application consists of a very fine grained and aligned microstructure in the regime of several hundred nanometres, maybe even smaller, as small grains have positive effects on the material's irradiation resistance [35]. These materials will then develop good fracture toughness in two testing directions. This naturally takes place at the expense of the toughness in another loading direction, where many grain boundaries might be in front of the propagating crack. However, an increased toughness in all three directions relying on an improved microstructure does not seem to be achievable – the usage of high toughness, high-Re alloyed materials is not cost effective. Therefore, the components have to be made out of the tungsten-based materials in order that the high toughness directions are correctly aligned to the direction of loading.

5. Conclusion

The aim was to search for ways to improve the toughness of W alloys and to analyse the possibility of bridging the thermal expansion difference between W and steels, which is an essential task for fusion application. The fracture toughness of WTa and WV alloys have been investigated by using two different types of materials: An industrially produced WTa hot forged solid solution alloy and WV and WTa composites, generated by low temperature consolidation via severe plastic deformation. The later materials have been investigated in a multiphase and a solid solution treated microstructure.

- The standard powder metallurgical production of WTa and WV is limited to volume concentrations below 10% of Ta and V. A successful consolidation of WTa and WV powder is independent of Ta and W concentrations.
- The composites are stable up to 1000 °C. The thermal stability is somewhat better for Ta than for V.
- At temperatures larger then 1500 °C significant interdiffusion of W, Ta and V occurs. At higher concentrations of Ta and V, the Kirkendall effect results in pore generation during the homogenisation treatment, which leads to degradation of the mechanical properties. This limits the standard powder metallurgical production of such solid solution alloys.

[9] Note: There is a more recent publication by Gilbert and Sublet [GilMR11], see Section 1.2.2.

- The fracture toughness at room temperature of the investigated alloys is comparable to typically used W microstructures.
- The forged solid solution WTa alloys (Ta between 1 and 10 wt%) have a fracture toughness in the crack propagation direction parallel to elongated grains between 3.8 and 12.1 MPa $m^{1/2}$ and between 8.0 and 46.3 MPa $m^{1/2}$ perpendicular to the elongated grains.
- The anisotropy in toughness is more pronounced for both composites, WTa and WV, than for the solid solution industrial WTa alloys.
- The toughness for the crack propagation perpendicular to the aligned grain and composite microstructure is high. For composite materials, an increase in fracture resistance within the investigated regime of strains is not determinable. In the crack propagation direction along the aligned microstructure, the room temperature fracture toughness remains low.
- The results indicate that as with W microstructures, “good toughness” in WTa and WV alloys and composites can only be obtained by an appropriate microstructural design in one or two principal directions. In one direction, the investigated microstructure remains highly brittle at room temperature.

Disclaimer

Parts of this work, supported by the European Communities under the Contract of Association between EURATOM and the Austrian Academy of Sciences, were carried out within the framework of the European Fusion Development Agreement. The views and opinions expressed herein do not necessarily reflect those of the European Commission.

Acknowledgement

The authors thank Doris Luef for HPT–WTa and –WV sample production and Thomas Leitner for 3PB sample production.

References for Publication C

[1] A.R. Raffray, R. Nygren, D.G. Whyte, S. Abdel-Khalik, R. Doerner, F. Escourbiac, T. Evans, R.J. Goldston, D.T. Hoelzer, S. Konishi, O. Lorenzetto, M. Merola, R. Neu, P. Norajitra, R.A. Pitts, M. Rieth, M. Roedig, T. Rognlien, S. Suzuki, M.S. Tillack, C. Wong, High heat flux components – Readiness to proceed from near term fusion systems to power plants, Fus. Eng. Des. 85 (2010) 91-108

[2] J. Hohe, P. Gumbsch, On the potential of tungsten-vanadium composites for high temperature application with wide-range thermal operation window, J. Nuc. Mater. 400 (2010) 218-231

[3] A. Giannattasio, S.G. Roberts, Strain-rate dependence of brittle-to-ductile transition temperature in tungsten, Phil. Mag. 87 (2007) 2589-2598

[4] D. Rupp, R. Mönig, P. Gruber, S.M. Weygand, Fracture toughness and microstructural characterization of polycrystalline rolled tungsten, Int. J. Refract. Met. Hard Mater. 28 (2010) 669-673

[5] Y. Mutoh, K. Ichikawa, K. Nagata, M. Takeuchi, Effect of rhenium addition on fracture toughness of tungsten at elevated temperatures. J Mater Sci, 30 (1995) 770

[6] M. Rieth, A. Hoffmann, Influence of microstructure and notch fabrication on impact bending properties of tungsten materials, Int. J. Refract. Met. Hard Mater. 28 (2010) 679-686

[7] J. Riedle, P. Gumbsch, H.F. Fischmeister, Cleavage Anisotropy in Tungsten Single Crystals, Phys. Rev. Lett. 76 (1996) 3594-3597

[8] B. Gludovatz, S. Wurster, A. Hoffmann, R. Pippan. Fracture toughness of polycrystalline tungsten alloys, Int. J. Refract. Met. Hard Mater. 29 (2010) 674-678

[9] M. Faleschini, H. Kreuzer, D. Kiener, R. Pippan, Fracture toughness investigations of tungsten alloys and SPD tungsten alloys, J. Nuc. Mater. 367-370 (2007) 800-805

[10] S. Wurster, B. Gludovatz, R. Pippan, High temperature fracture experiments on tungsten-rhenium alloys, Int. J. Refract. Met. Hard Mater. 28 (2010) 692-697

[11] P. Gumbsch, J. Riedle, A. Hartmaier, H.F. Fischmeister, Controlling Factors for the Brittle-to-Ductile Transition in Tungsten Singly Crystals, Science 282 (1998) 1293-1295

[12] P. Raffo, Yielding and fracture in tungsten and tungsten-rhenium alloys, J. Less Common Met. 17 (1969) 133-149

[13] L. Romaner, C. Ambrosch-Draxl, R. Pippan, Effect of rhenium on the core structure in tungsten, Phys. Rev. Lett. 104 (2010) 195503

[14] H. Li, L. Romaner, R. Pippan, C. Ambrosch-Draxl, Modelling screw dislocations in W and W-based alloys, (in preparation)

[15] A. Hohenwarter, R. Pippan, Anisotropic fracture behaviour of ultrafine-grained iron, Mater. Sci. Eng. A 527 (2010) 2649-2656

[16] K. Xia, Consolidation of Particles by Severe Plastic Deformation: Mechanism and Applications in Processing Bulk Ultrafine and Nanostructured Alloys and Composites, Adv. Eng. Mater. 12 (2010) 724-729

[17] R.Z. Valiev, R.K. Islamgaliev, I.V. Alexandrov, Bulk nanostructured materials from severe plastic deformation. Prog. Mater. Sci. 45 (2000) 103-189

[18] I. Sabirov, R. Pippan, Formation of a W-25%Cu nanocomposites during high pressure torsion, Scripta Mater. 52 (2005) 1293-1298

[19] Q. Wei, H.T. Zhang, B.E. Schuster, K.T. Ramesh, R.Z. Valiev, L.J. Kecskes, R.J. Dowding, L. Magness, K. Cho, Microstructure and mechanical properties of super-strong

nanocrystalline tungsten processed by high-pressure torsion, Acta Mater. 54 (2006) 4079-4089

[20] L.J. Kecskes, K.C. Cho, R.J. Dowding, B.E. Schuster, R.Z. Valiev, Q. Wei, Grain size engineering of bcc refractory metals: Top-down and bottom-up – Application to tungsten, Mater. Sci. Eng. A 467 (2007) 33-43

[21] I. Sabirov, O. Kolednik, R.Z. Valiev, R. Pippan, Equal channel angular pressing of metal matrix composites: Effect on particle distribution and fracture toughness, Acta Mater. 53 (2005) 4919 - 4930

[22] S.J. Zinkle, Advanced Materials for fusion technology, Fus. Eng. Des. 74 (2005) 31-40

[23] T. Muroga, T. Nagasaka, K. Abe, V.M. Chernov, H. Matsui, D.L. Smith. Z.-Y. Xu, S.J. Zinkle, Vanadium alloys – overview and recent results, J. Nucl. Mater, 307-311 (2002) 547 – 554

[24] S.J. Zinkle, N.M Ghoniem, Operating temperature windows for fusion reactor structural materials, Fus. Eng. Des. 51-52 (2000) 55-71

[25] R. Pippan, The growth of short cracks under cyclic compression, Fatigue Fract. Eng. Mater. Struct. 9 (1987) 319-328

[26] D. Kiener, C. Motz, M. Rester, M. Jenko, G. Dehm, FIB damage and possible consequences for miniaturized mechanical tests, Mat. Sci. Eng. A 1-2 (2007) 262-272

[27] ASTM E399-90 (Reapproved 1997) Standard Test Method for Plane-Strain Fracture Toughness of Metallic Materials

[28] D. Rupp, S. Weygand, Anisotropic fracture behaviour and brittle-to-ductile transition of polycrystalline tungsten, Phil. Mag. 90 (30) (2010) 4055-4069

[29] M. Faleschini, Severe Plastic Deformation of Tungsten Alloys and its Influence on Fracture Behaviour, PhD Thesis, Leoben, 2006

[30] A. Bachmaier, A. Hohenwarter, R. Pippan, New procedure to generate stable nanocrystallites by severe plastic deformation, Scripta Mater. 61 (2009) 1016-1019

[31] Warren, A. Nylund, I. Olefjord, Oxidation of Tungsten and Tungsten Carbide in Dry and Humid Atmospheres, Int. J. Refract. Met. Hard Mater. 14 (1996) 345-353

[32] C.J. Smithells, E.A. Brandes, Metals Reference Handbook, fifth ed., Butterworths, London & Boston, 1976

[33] J. Reiser, P. Norajitra, R. Ruprecht, Numerical investigation of a brazed joint between W-1%La_2O_3 and ODS EUROFER components, Fus. Eng. Des. 82 (2008) 1126-1130

[34] M.R. Gilbert, Transmutation and He Production in W and W-alloys, CCFE-R10(01) Culham Centre for Fusion Energy, http://www.ccfe.ac.uk/assets/Documents/CCFE-R(10)1.pdf, (2010)

[35] S. Wurster, R. Pippan, Nanostructured metals under irradiation, Scripta Materialia 60 (2009) 1083-1087

Publication D: Micrometer-Sized Specimen Preparation Based on Ion Slicing Technique

Micrometer-Sized Specimen Preparation Based on Ion Slicing Technique

Stefan Wurster[1], Christian Motz[1], Monika Jenko[2] and Reinhard Pippan[1]

[1] Erich Schmid Institute of Materials Science of the Austrian Academy of Sciences, Jahnstrasse 12, 8700 Leoben, Austria

[2] Institute of Metals and Technology, Lepi pot 11, 1000 Ljubljana, Slovenia

Abstract

The ion slicing technique has been well known for producing samples for transmission electron microscopy (TEM) investigations. It will be shown that this method can also be used for producing different types of samples for micro-mechanical experiments. The capability of manufacturing thin freestanding lamellae with a width of some micrometers and subsequently cantilevers and tensile testing specimens on the micrometer-scale using the focused ion beam (FIB) technique will be demonstrated.

1. Introduction

Experiments in the size regime of several hundred nanometers to some micrometers become more and more important in order to better understand local mechanical properties and hence the mechanisms determining the material's behavior on that scale. These experiments shall also uncover the dependency of the material's properties on the size and preparation method of the specimen. Knowledge of the material's behavior at these small dimensions becomes increasingly significant due to development and usage of micro-electro mechanical systems, small medical devices, and nanocomposites. One possibility to fabricate specimens of adequate size is using a focused ion beam (FIB) workstation, [1–4] which is quite a powerful but costly and time-consuming method. Different types of specimens (e.g. notched and un-notched cantilevers, tensile, and compression testing specimen) may be produced out of the bulk material, whereas quite large amounts of material need to be removed. This can accumulate FIB damage [5–8] and alter the structure of the material by ion implantation as well as by introducing defects and surface-near amorphized regions. When assuming the quantity of removed material to be proportional to milling time, it becomes obvious that providing an already thinned lamella noticeably quickens the sample preparation. The aim of this paper is to show a way to produce such lamellae as preforms for further micro-machining. Nevertheless, working without any FIB induced damage-structures is not possible at the current stage. Using this ion slicing technique in the first step of the sample preparation will presumable reduce the ion damage in comparison to pure FIB milling, due to the lower acceleration voltage and the use of argon ions instead of gallium. This might contribute to less irradiation damage.

2. Preparation

A schematic summary of the ion slicing process is shown in Figure D.1(a). Low-energy argon ions incline perpendicular to the thinnest side and parallel to the largest side. The ion accelerating voltage is adjustable from 1 to 8 kV. Specimen ion current is in the range of several tens of mA, whereas the overall current is about five times as high. In comparison to ‘‘conventional’’ FIB microscopy and preparation, the ion current is three to six orders of magnitudes higher. A thin stainless steel band protects the specimen at the top, reducing the amount of material to be sputtered away from the top side. Instead, the material is removed from both large side faces, leaving behind a thinned-out and crescent-shaped area. Figure D.2(a) shows an example of a milled tungsten lamella. Due to the comparable low sputtering yield of tungsten, it takes several hours of argon ion bombardment to achieve a narrow bridge. The thickness is in the range of 5 – 10 mm. It is possible to observe the whole progress by means of a CCD camera inside the vacuum chamber. The ion gun pivots up to 4° across the specimen's longest side, so it is possible to adjust the shape of the cross-section of the remaining bridge. The use of appropriate tilting angles leads

to parallel flanks of the bridge; otherwise, the flanks would broaden or taper, which may result in a hole in the center of the specimen. It is possible to rotate the specimen by ±30° relative to the ion gun, using a rotation axis perpendicular to the largest sample side, yielding a smoother and larger thinned-out area. Subsequent to the slicing process, we fix the specimens on a copper support ring and mount them in a comparatively large brass holder for easier manipulation and further processing. Deviations of several degrees from desired crystal orientation develop due to a non-perfectly aligned single crystal and the sequenced production steps of cutting, grinding, polishing, ion slicing, and mounting of sample in the sample holder.

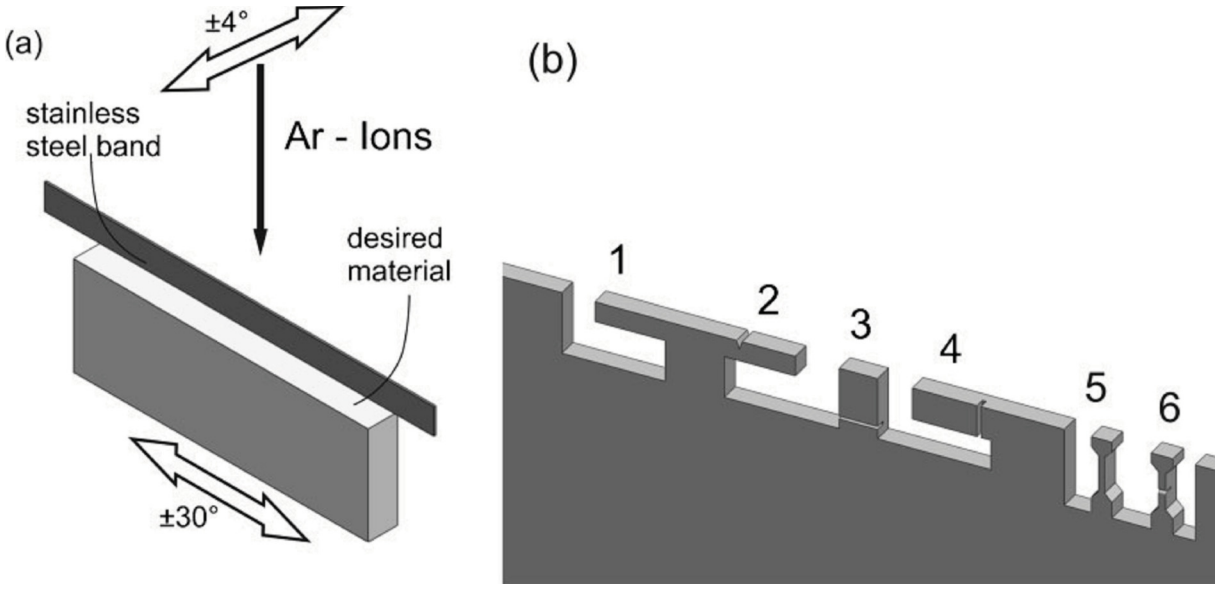

Figure D.1: (a) Sketch of the ion slicing procedure; (b) Sketch of some possible alignments of un-notched (1) and notched (2–4) cantilevers adjusted for different loading directions as well as a possible un-notched (5) and notched (6) tensile specimen configuration.

Starting with such ion sliced sheets it is easier to prepare several specimens for micro-mechanical experiments on one macroscopic sample. Figure D.1(b) depicts some possible sample geometries, especially introducing notched cantilevers in different testing directions. The ion slicing technique, acting as starting point for producing micrometer-sized samples, features several advantages in comparison to conventional FIB-sample preparation:

i) The length of the thin bridge, as can be seen in Figure D.2(a), is about 1 mm and leaves enough space for producing many specimens that can be placed next to each other.

ii) All specimens are made out of the same single- or polycrystalline macroscopic bulk material and consequently all samples feature the same crystallographic orientation.

iii) This procedure removes variations in crystallography of separate samples, which might happen when producing samples one by one. For this reason, results are well reproducible.

iv) It is easy to produce specimens of slightly altered geometry, i.e., tilted tensile axes or inclined crack planes and crack propagation directions. This is done by a change of notch orientation or by a rotated position of the whole sample within the lamella. Hence, comparison of determined physical properties in relation to sample alignment and crystal orientation is uncomplicated.

v) Furthermore, the time needed for FIB cutting is lowered considerably, as hardly any bulk material has to be removed. This certainty might be accompanied by a lower level of ion irradiation damage.

3. Experimental

As an example in this paper, we use tungsten single crystals with rod axis in <110>-direction. Cylinders with a thickness of 3 mm were cut from the tungsten single crystals using a cutting disc. The cylinder was cut in order to display later on the {001}-<110> crack system in relation to the loading direction. This crack system has the lowest fracture toughness according to Riedle et al. [9] Small rectangular sheets were made and mechanically polished, the final size was 3 x 1 x 0.1 mm^3. The samples were ion sliced using an EM-09100IS Ion Slicer from JEOL.

After testing different settings, a lower acceleration voltage of 5 kV at the final polishing step was used. Low-energy argon ions polish the surface and this leads to less damage on the thinned forefront of the sample. The ion slicing settings of a typical sample are: 2 h at 7 kV, tilting angle 1.3° then polishing for 1 h at 5 kV and 1.3°, respectively. The lamella reaches its thinnest point in the middle of the crescent-shaped area and widens in all the directions marked with arrows in Figure D.2(a). The final crystal orientation of the sample in order to machine the notch in the ideal crack plane is measured by electron backscatter diffraction (EBSD) analysis.

Succeeding with ion slicing we prepared all samples with a LEO XB 1540 workstation, using 30 keV gallium ions and currents of 500 – 2000 pA for cutting the contours of the micro-samples and 50 –100 pA, if needed, for cutting notches and fine pre-cracks inside the notches. The desired geometries are notched cantilevers for fracture experiments and, later on, notched tensile specimens. Regarding Figure D.1(b), cantilever number 2 turned out to be the most promising one, because of the much higher stiffness of the tungsten lamella under this load direction in comparison to, e.g., the cantilevers number 3 and 4.

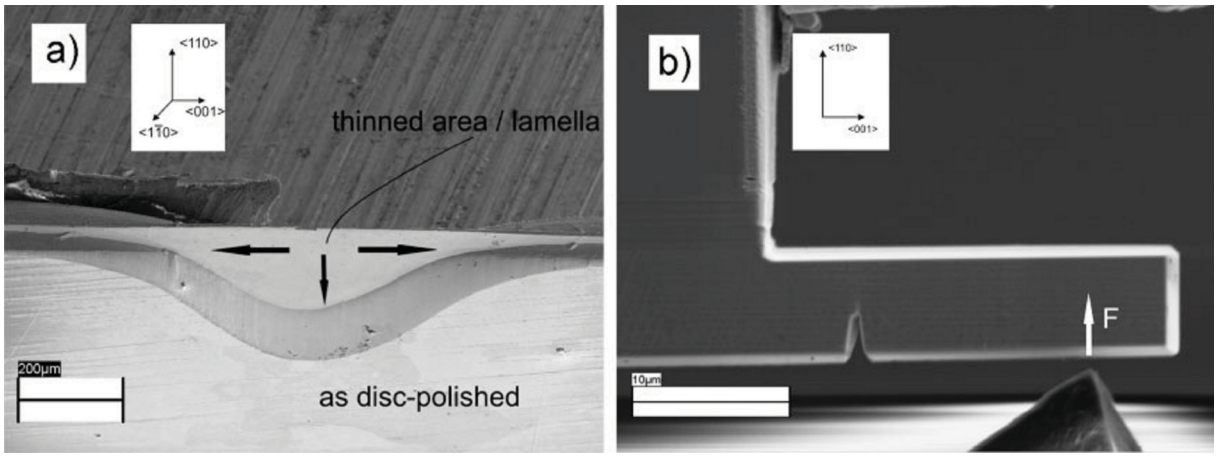

Figure D.2: (a) SEM image of the final ion sliced single crystalline tungsten specimen, showing the thin lamella (‘‘bridge’’). The thickness of lamella increases in direction of black arrows; (b) SEM image of notched cantilever with direction of expected crack growth in {001}-<110> orientation, before loading with indenter.

Figure D.2(b) depicts a notched cantilever prior to an in situ loading experiment. The diamond cube corner indenter is also visible. The width of the notched cantilever, W = 11.0 µm, is given by the thickness of the used lamella after ion slicing, but it is possible to produce thinner cantilevers either by using other settings for the ion slicing procedure or by doing the work with the FIB workstation. The other dimensions of the cantilever are: distance of loading point to notch (bending length): 14.9 µm; thickness of cantilever t = 6.7 µm; depth of triangular notch and the fine pre-crack cut with 100 pA: a = 3.1 µm. After milling, the micrometer-sized samples are tested in situ in a scanning electron microscope (LEO 982) using a piezoelectrically controlled in situ micro-indenter (ASMEC, UNAT). Displacement—time curves are predefined and the load—displacement response is recorded.

4. Discussion

This technique can now be used to answer many different questions in material science: size effect of plastic strength, hardening behavior, fatigue, and fracture of selected phases, interface properties, etc. In the following, some examples are shortly discussed, where we use this special technique for a better understanding of the cleavage phenomena of semibrittle materials, especially tungsten.

Future work will focus on the one hand on the investigation of notched cantilevers subjected to loading–unloading experiments, where it is possible to relate increasing compliance of specimen to crack growth. Necessarily, other effects, like the marked change of geometry when reaching bending angles up to 30°, have to be considered here. Figure D.3 shows results of a typical loading–unloading experiment: in (a) the obtained load versus displacement and in (b) the

extracted consecutive reloading curves are shown. From the change in the compliance in the load displacement curve at different reloadings, the crack length can be measured and the K-value or J-integral can be estimated. Detailed analyses of such experiments will be presented in a forthcoming paper.

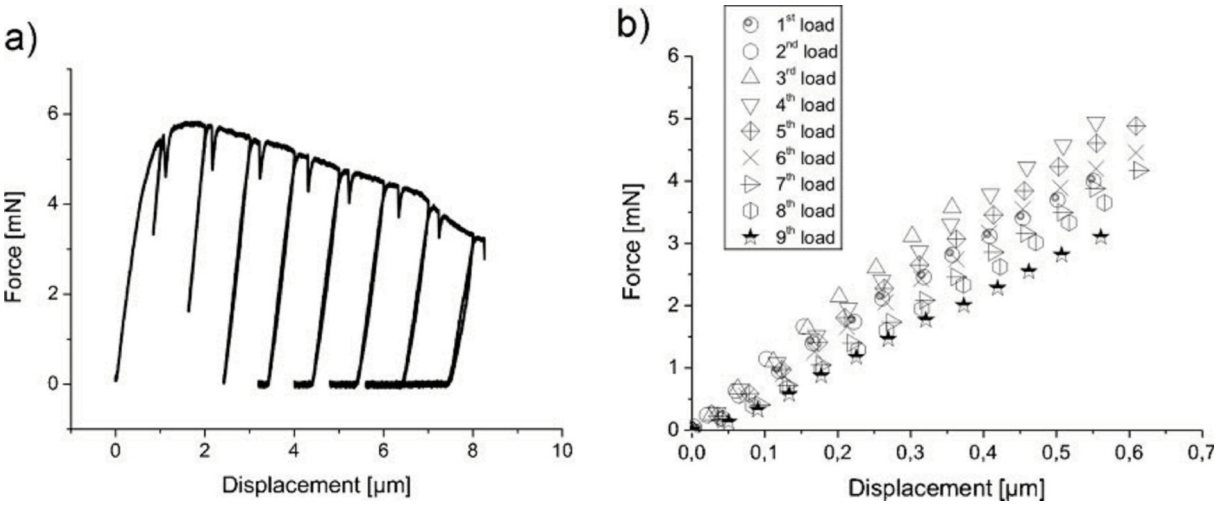

Figure D.3: (a) Load–displacement curve for a stepwise, displacement-controlled experiment. The small load drops originate from taking SE images due to relaxation of specimen-indentation system, large ones from unloading. (b) Extract of load–displacement curves for the first load and each subsequent reload.

On the other hand, future work will focus on experiments of notched tensile specimens (see Figure D.4(a)). The marked difference between expected dislocation structure in notched tensile and bending samples is illustrated in Figure D.4(b). In both cases, dislocations – emitted from the crack tip – move away from the crack tip. In a cantilever, the crack tip is located in the region of tensile stress. Dislocations pile up at the neutral axis of bending, as they perceive a repulsive force due to the existence of a region of compressive stresses in the cantilever's bottom side. This is not the case in notched tensile samples. No compressive stresses act there during the experiment. The dislocations can move freely through the whole sample and pile up is unlikely to happen. By changing the thickness of notched cantilevers, it is possible to gain insights in the effect of constraints in plasticity on cleavage fracture, as the free length of path for dislocation movement is variable. In both cases, it is possible to adjust the angle between FIB-produced notch and preferred cleavage plane. Comparableness of results is supported by the fact that both samples can easily be produced on one large sample, thus featuring the same crystallography. Taking experiments on both types of specimens in mind, we hope to learn more about the influence of different local dislocation structures in front of the crack tip on the brittle fracture behavior of body centered cubic metals like tungsten.

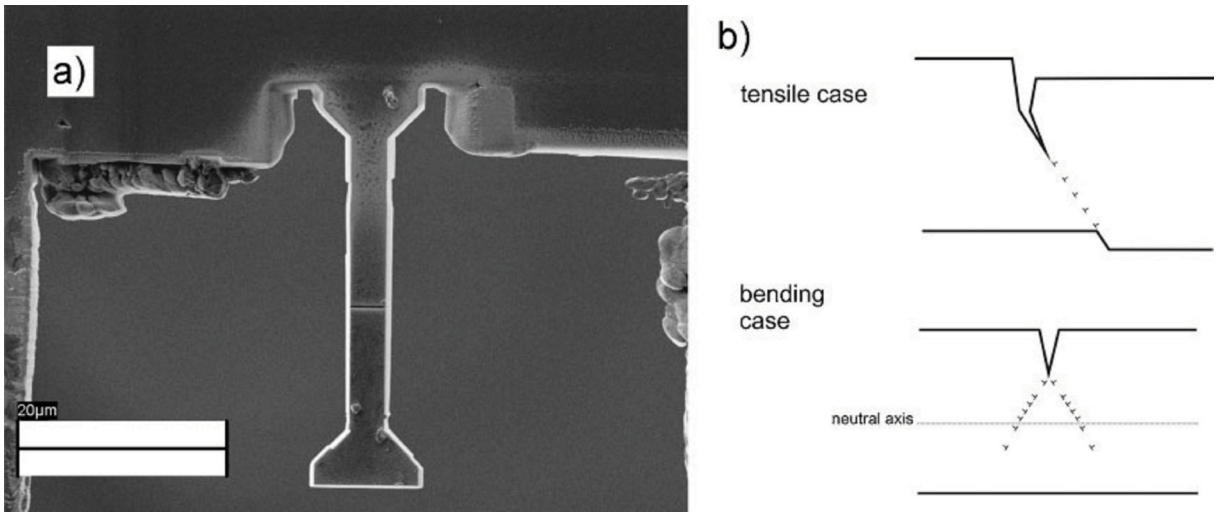

Figure D.4: (a) FIB image of a notched tensile specimen; (b) Schematic depiction of expected dislocation structure in case of notched tensile specimen and notched cantilever.

5. Conclusions

In this publication, we showed the feasibility of using an argon ion sliced specimen as an initial point for subsequent ‘‘mass’’ production of different micrometer-sized samples with the FIB workstation. This ion milling process saves time and costs during sample preparation and many identical samples – also from a crystallographic point of view – can be manufactured and tested on one macroscopic specimen. Producing desired deviation from as-received sample crystallography is easy. Due to the usage of low-energy argon ions instead of high-energy gallium ions for initial preparation, the ion damage is expected to be lower. First fracture toughness experiments using notched cantilevers display reproducible results. An outlook on future work on stepwise displacement controlled experiments for investigation of crack growth and on the comparison of notched bending and tensile samples is given.

Disclaimer

This work, supported by the European Communities under the Contract of Association between EURATOM and the Austrian Academy of Science, was carried out within the framework of the European Fusion Development Agreement. The views and opinions expressed herein do not necessarily reflect those of the European Commission.

Acknowledgements

The authors thank Miro Pecar from the Institute of Metals and Technology for sample preparation and Peter Gumbsch from the Karlsruhe Institute of Technology/Frauenhofer IWM for providing the tungsten single crystals.

References for Publication D

[1] D. Di Maio, S. G. Roberts, Measuring fracture toughness of coatings using focused-ion-beam-machined microbeams, J. Mater. Res. 2005, 20, 299.

[2] C. Motz, T. Schö berl, R. Pippan, Mechanical properties of micro-sized copper bending beams machined by the focused ion beam, Acta Mater. 2005, 53, 4269.

[3] J. McCarthy, Z. Pei, M. Becker, D. Attridge, FIB micromachined submicron thickness cantilevers for the study of thin film properties, Thin Solid Films 2000, 358, 146.

[4] S. Shim, H. Bei, M. K. Miller, G. M. Pharr, E. P. George, Effects of focused ion beam milling on the compressive behaviour of directionally solidified micropillars and the nanonindentation response of an electropolished surface, Acta Mater. 2009, 57, 503.

[5] D. Kiener, C. Motz, M. Rester, M. Jenko, G. Dehm, FIB damage of Cu and possible consequences for miniaturized mechanical tests, Mater. Sci. Eng., A 2007, 459, 262.

[6] S. Rubanov, P. R. Munroe, FIB-induced damage in silicon, Journal of Microscopy, 2004, 214, 213.

[7] G. Spoldi, S. Beuer, M. Rommel, V. Yanev, A. J. Bauer, H. Ryssel, Experimental observation of FIB induced lateral damage on silicon samples, Microelectronic Engineering, 2009, 86, 548.

[8] D. J. Larson, D. T. Foord, A. K. Petford-Long, H. Liew, M.G. Blamire, A. Cerezo, G. D. W. Smith, Field-ion specimen preparation using focused ion-beam milling, Ultramicroscopy 1999, 79, 287.

[9] J. Riedle, P. Gumbsch, H. F. Fischmeister, Cleavage anisotropy in tungsten single crystals, Phys. Rev. Lett. 1996, 76, 3594.

Publication E: Notched-Cantilever Testing on the Micrometer Scale – Effects of Constraints on Plasticity and Fracture Behaviour

Notched-Cantilever Testing on the Micrometer Scale – Effects of Constraints on Plasticity and Fracture Behaviour

S. Wurster[1)], C. Motz[1)], R. Pippan[1), 2)]

[1)] Erich Schmid Institute of Materials Science of the Austrian Academy of Sciences, Jahnstrasse 12, A-8700 Leoben, Austria

[2)] Christian Doppler Laboratory for Local Analysis of Deformation and Fracture, Jahnstrasse 12, A-8700 Leoben, Austria

Abstract

In this work, fracture experiments on micrometer-sized cantilevers, made of single crystalline tungsten, are described. The crystal is characterized by a preferred cleavage plane and crack propagation direction, showing the crystal's lowest fracture toughness. Micro-samples are produced using the recently developed Ion Slicing Technique prior to final FIB preparation of samples. In-situ experiments on notched cantilevers with varying misalignment of artificially made notch planes from the preferred cleavage plane are accomplished. This approach results in constraint acting on the crack front leading to higher apparent fracture toughness values.

Keywords

Tungsten, single crystal, micrometer-sized experiments, notched cantilever, cleavage plane, ion slicing, focused ion beam

1. Introduction

The brittle fracture and the brittle–to–ductile transition [1] of tungsten still lack a complete understanding. There are many material parameters, like crystal orientation [2, 3], grain boundaries [4, 5], impurities [5, 6], grain size [7], texture [8, 10], dispersions and alloying elements [11, 12] or strain rate [9], which affect the fracture behaviour of tungsten and tungsten alloys.

Thus, it is an evident approach to break down the whole problem to several minor ones leading to separate but identical investigations of these parameters– as far as this is possible at all. Making use of micrometer-sized specimen is reasonable when focussing on single parameters of the above-mentioned, as it is for example easy to prepare a variety of crystal orientations referring to the specimen's alignment – as will be discussed in this paper, or to prepare single grain boundaries within the samples [20].

With development and increasing application of Focused Ion Beam (FIB) workstations, the size of specimens for mechanical experiments shrank more and more. Beside compression [13], tensile [14] or bending [15] experiments, it is also possible to accomplish micro-fracture experiments of different types of brittle materials [16, 17] using micro-cantilever deflection technique. Interpretation and evaluation of small-scaled fracture tests, especially those of semi-brittle and ductile materials, are still not as developed as it would be necessary to determine e.g. valid fracture toughness values from experiments. Comparing the results from micro-mechanical experiments with values gained from standardized, macroscopic tests [18] is of great interest. There is the question, whether there is a size effect in terms of fracture toughness as the yield stress increases and hence the size of the plastic zone changes with decreasing sample size.

Nevertheless, it is possible to monitor the effects of the pointed-out parameters on the fracture behaviour of small specimens. Within this work, the effect of deviations of notch plane orientation and crystal's preferred cleavage plane on the fracture behaviour of tungsten single crystals are described.

2. Experiment

For production of micrometer-sized specimens, an ion sliced lamella acting as a preform, prior to FIB cutting is used. A detailed description of the ion slicing process is given in [19], but for the sake of completeness, a short summary is given here:

As starting geometry, a rectangular sample of 3 x 1 x 0.1 mm^3 is used. Low energy argon ions (~ 1 – 8 keV) impinge perpendicular to the surface measuring 3 x 0.1 mm^2 and remove material. What is left is a crescent-shaped and thinned-out area with a thickness of several micrometers

(Figure E.1, left side). When the settings are chosen correctly, the flanks on both sides are parallel and the length of the small bridge is about one millimetre. Starting with this thin lamella allows going an easy and quick way for succeeding cantilever production

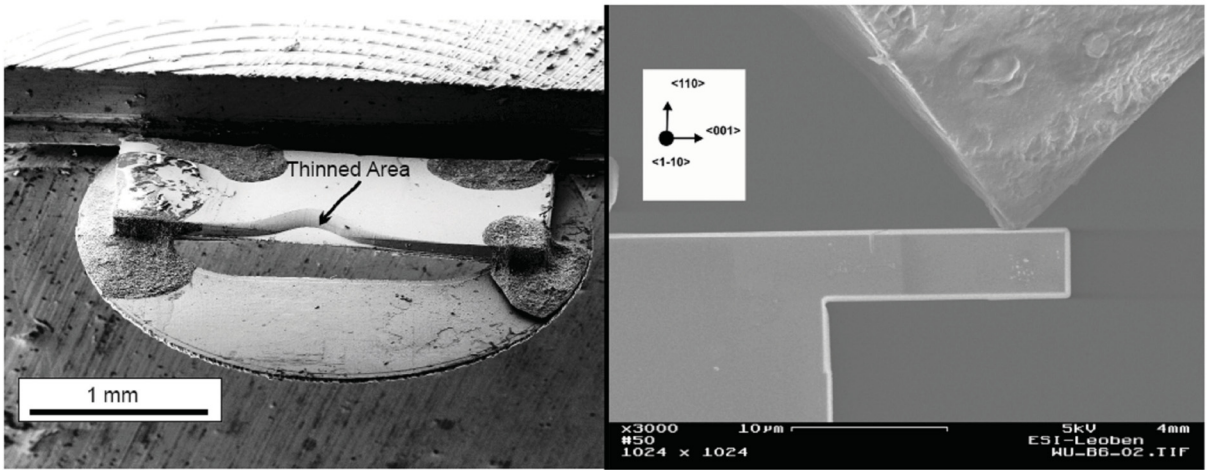

Figure E.1: left side: SEM micrograph of a single crystalline tungsten specimen after ion-slicing process. The samples is fixed on a copper support ring and mounted into a brass sample holder. Right side: SEM micrograph of a notched cantilever prior to loading by the cube corner indenter.

For a first investigation of the fracture behaviour of single crystalline tungsten, the {001}-<110> crack system is chosen. This system shows the lowest fracture toughness, 6.2 MPa $m^{1/2}$ ± 1.7 MPa $m^{1/2}$, of all investigated crack systems according to Riedle et al. [2]. Assuming an ideal configuration, the {001}-<110> system should be positioned, as it is depicted in Figure E.1, right side. Due to the large number of sequenced production steps, such as crystal growth, cutting, grinding, polishing, ion slicing, fixing the specimen on sample holders and mounting inside the vacuum chamber, there develop misalignment between specimen orientation and crystal orientation and the crack system is not located in an ideal position any more. Fortunately, the usage of a FIB makes it possible to rotate the position of the samples within the lamella or to cut the notch, needed for subsequent fracture experiments, at a certain angle – as we did it for the specimens described in the following. Another advantage when using this lamella-technique is that it is possible to place several specimens next to each other on one macroscopic specimen, assuring the same crystallography for all samples and making results' comparison easier.

Micro-cantilevers are cut using gallium ion currents of 5 nA – 2 nA for course milling and 500 pA for the final polishing of surfaces. Notches, which should somehow represent naturally grown cracks, are made with currents of 50 pA – 100 pA. These cuts last only seconds. For sure, the "blunt" crack tips of these FIB notches, typically having notch tip radii of about ten nanometers, do not agree with naturally grown cracks, which are much sharper. Three cantilevers are prepared with notch planes have different deviations ($\alpha_1 \sim 0°$, $\alpha_2 = 5°$, $\alpha_3 = 25°$) from the cleavage plane (see Table E.1 and Figure E.2). Crack propagation direction is held constant and is very close to <110>.

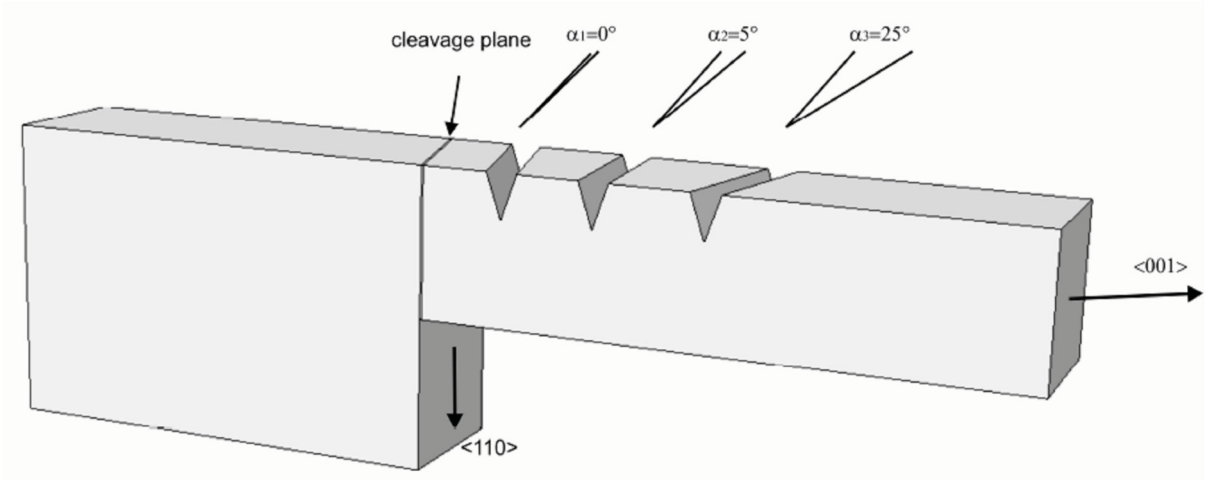

Figure E.2: Schematic compilation of all investigated notch planes. The {001} – cleavage plane is depicted at the cantilever's base.

All samples are tested in-situ in a scanning electron microscope (LEO 982), equipped with a micro-indenter (ASMEC, UNAT). Displacement-time curves are predefined and the loaddisplacement response is recorded. Several partial load releases, for crack propagation investigation, are made during the experiment. Due to the finite machine stiffness and specimen holder stiffness, it is necessary to correct the recorded displacement, which otherwise overestimates the cantilever bending. SEM micrographs, taken at distinctive loading points, enable the correlation of force and lamella translation. For each test, an individual spring constants *k* (see Table E.1) is the result, which corrects the displacement measurement.

3. Determination of stress intensity factors

For a first order evaluation of prevailing stress intensity *K* at the crack tip, before first crack propagation takes place, Equation (E.1), usually used for fracture toughness evaluation for three-point-bending (3PB) specimens according to ASTM E399 [18] is used.

$$K = 4 * \frac{F * L_L}{B * W^{3/2}} f(a/W) \tag{E.1}$$

with

$$f_{E399}(a/W) = \frac{3*(a/W)^{1/2} * [1.99 - (a/W)(1-a/W)(2.15 - 3.93*a/W + 2.7(a/W)^2]}{2(1+2a/W)(1-a/W)^{3/2}} \tag{E.2}$$

in which F is the force measured, B, W the width and thickness of the specimen, a the crack length and L_L is the distance of loading point to crack. Making following assessment: When replacing $F_{3PB}*S_{3PB}$, originally to be found in Equation (E.1), by $F*L_L$, whereas $F=F_{3PB}/2$ and $L_L=S_{3PB}/2$, it is necessary to include a factor of 4 in Equation (E.1) to finally end up with same stress intensities at the crack tip in case of cantilever testing.

To confirm this assessment, a more detailed analysis, using finite element methods (FEM) and ABAQUS code is performed, Two-dimensional, plane stress, 8-node bi-quadratic elements (CPS8) are used. An isotropic material having a Young's Modulus of E = 410G Pa and a Poisson's Ratio of v = 0.25 and shape of specimen similar to the experimental ones are used. In contrast to [18], where plane strain conditions are assumed, plane stress was chosen in this case, as the size of the sample is so small that surface effects and hence a plane stress field are supposed to prevail. The shape factor gained through simulation will be denominated $f_{Sim}(a/W)$ and is given in Equation (E.3). The difference between $4*f_{E399}(a/W)$ and $f_{Sim}(a/W)$ is well below 10% over the whole investigated ratio of crack length to specimen thickness (a/W).

$$f_{Sim}(a/W) = 4*\frac{3*(a/W)^{1/2}*(1,23-(a/W)*(1-a/W)(-6.09+13.96*(a/W)-14.05(a/W)^2))}{2*(1+2a/W)(1-a/W)^{3/2}} \qquad \text{(E.3)}$$

4. Results

With these equations, it is now possible to further process recorded load – displacement data. From the first unload sequence, where no crack propagation is supposed to have taken place, it is possible to estimate the crack length a by using Equation E.4, typically used for determining Young's moduli, where ligament W_{Lig} is equivalent to (W-a) and δ represents loading point displacement. The crack lengths determined with this method are summarized in Table E.1.

$$E = \frac{4*F*L_L^{\,3}}{\delta*B*W_{Lig}^{\,3}} \qquad \text{(E.4)}$$

Taking at hand the crack length gained from SEM micrographs, which seem to be more reliable, the stress intensity K at the crack tip can be calculated by using Equations (E.1) and (E.3). The result can be seen in Figure E.3. This evaluation does not take into account any crack extension or plastic deformation, respectively dislocation activity happening during the experiment. Figure E.3, right side, a SEM micrograph of cantilever #3, shows that the crack does not follow the predetermined crack path, but the crack path is inclined – it is most probably the {100} plane.

Table E.1: Summary of three samples with different deviations of the notch plane from the ideal crack plane

No. of cantilever	Deviation notch – crack plane	Spring constant of lamella [mN/µm]	L_L[10] / B / W [µm]	Crack length from Equ. (E.4) [µm]	Crack length from SEM micrographs
1	0°	12,82	8,6 / 7,2 / 3,6	1,6±0,6	1,5
2	5°	9,74	8,8 / 5,7 / 4,4	1,6±0,6	1,4
3	25°	Set to 11[11]	9,1 / 3,8 / 4,4	1,5	1,5

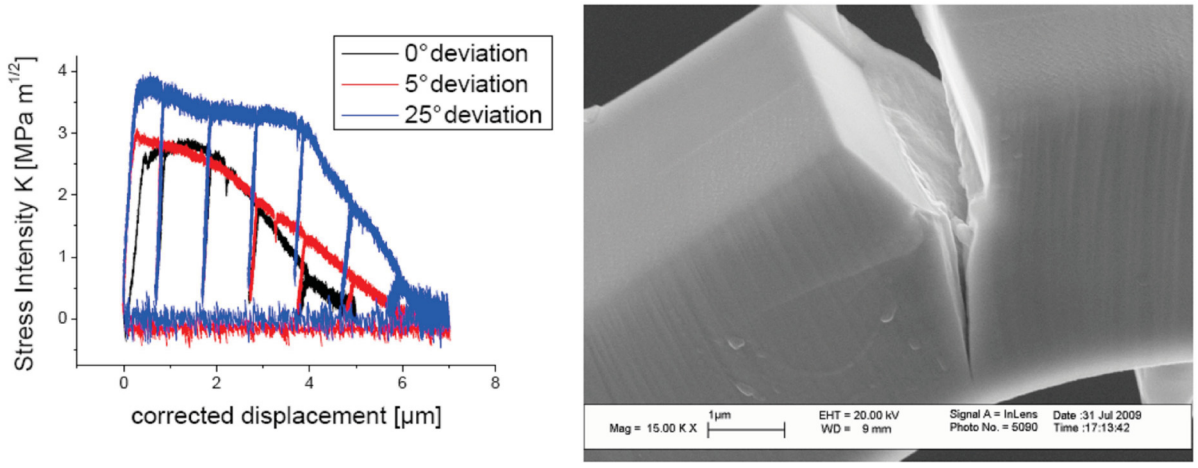

Figure E.3: Left side: Stress intensity vs. corrected load line displacement for all three different deviations of preferred crack system and notch plane. Right side: SEM micrograph of the notch region of the cantilever featuring a deviation of 25° between notch and cleavage plane

5. Summary & Conclusion

First experiments on FIB-notched cantilevers made of tungsten single crystal, oriented close to preferred cleavage orientation, were accomplished in order to investigate the influence of increasing angle between notch plane and preferred cleavage plane, having the lowest fracture toughness. The improvement of load-line displacement measurement by correlation of distinct point

[10] Due to inclined notches, a mean bending length, which is given here, is used for calculation of W_{Lig}. For calculation of K, the maximum L_L is used.

[11] Because of a lack of adequate SEM micrographs from the experiment, a reasonable spring constant – in relation to the other two received – was chosen.

in SEM micrographs at different load level is feasible, but not of very high accuracy. Hence, the crack lengths determined by SEM micrographs were used for further evaluations. K-values are too low in comparison to [3]. This is due to the fact that the size of the plastic zone ω, with

$$\omega \propto K^2 / \sigma_y^{\ 2} \tag{5}$$

where σ_y represents the yield stress of the material, is of the same size or larger as the specimen size, when choosing reasonable values such as 1 GPa for σ_y and 6 MPa*m$^{1/2}$ for K . Hence, linear elastic fracture mechanics underestimate the fracture toughness, when working in this size regime. Nevertheless, there is a clear trend of increasing maximum stress intensity with increasing deviation of preferred cleavage plane and artificial notch. An elasto-plastic analysis of the performed experiments will be presented in a forthcoming paper.

Acknowledgements

The authors thank Prof. Dr. Monika Jenko, head of the Institute of Metals and Technology, in Ljubljana, Slovenia for the opportunities to do the ion-slicing preparation and Peter Gumbsch from the Karlsruhe Institute of Technology / Fraunhofer IWM for providing the tungsten single crystal.

Disclaimer

This work, supported by the European Communities under the Contract of Association between EURATOM and the Austrian Academy of Sciences, was carried out within the framework of the European Fusion Development Agreement. The views and opinions expressed herein do not necessarily reflect those of the European Commission.

References for Publication E

[1] P. Gumbsch, Brittle fracture and the brittle-to-ductile transition of tungsten, J Nucl. Mater 323 (2003) 304-312

[2] J. Riedle, P. Gumbsch, H.F. Fischmeister, Cleavage anisotropy in tungsten single crystals, Phys. Rev. Lett. 76 (1996) 3594 – 3597

[3] J. Riedle, P. Gumbsch, H.F. Fischmeister, V.G. Glebovsky, V.N. Semenov, Fracture studies of tungsten single crystals, Materials Letters 20 (1994) 311-317

[4] J.M. Liu, B.W. Shen, Grain boundary fracture in tungsten bi-crystals, Acta Metall. 30 (1982) 1197-1202

[5] M. Grujicic, H. Zhao, G.L. Krasko, Atomistic Simulation of Σ3 (111) Grain Boundary Fracture in Tungsten Containing Various Impurities, Int. J of Ref. Met. Hard Mater. 15 (1997) 341-355

[6] Tran-Huu-Loi, J.P Morniroli, M. Gantois, M. Lahaye, Brittle fracture of polycrystalline tungsten, J of Mat. Sci. 20 (1985) 199-206

[7] M. Faleschini, H. Kreuzer, D. Kiener, R. Pippan, Fracture toughness investigations of tungsten alloys and SPD tungsten alloys, J Nucl. Mater. 367-370 (2007) 800-805

[8] D. Rupp, S.M. Weygand, Experimental investigation of the fracture toughness of polycrystalline tungsten in the brittle and semi-brittle regime, J Nucl. Mater. 386-388 (2009) 591-593

[9] A. Giannattasio, S.G. Roberts, Strain-rate dependence of the brittle-to-ductile transition temperature in tungsten, Phil. Mag. 87:17,2589-2598

[10] R.W. Margevicius, J. Riedle, P. Gumbsch, Fracture toughness of polycrystalline tungsten under mode I and mixed mode I/II loading, Mat. Sci. Eng. A 270 (1999) 197-209

[11] S. Wurster, B. Gludovatz, R. Pippan, High Temperature Fracture Experiments on Tungsten-Rhenium Alloys, Int. J of Ref. Met. Hard Mater. 28 (2010) 692-697

[12] Y. Mutoh, K. Ichikawa, K. Nagata, M. Takeuchi, Effect of rhenium addition on fracture toughness of tungsten at elevated temperatures, J Mat. Sci. 1995;30:770-775.

[13] M.D. Uchic, D.M. Dimiduk, J.N. Florando, W.D. Nix, Sample Dimensions Influence Strength and Crystal Plasticity, Science 305 (2004) 986-989

[14] D. Kiener, W. Grosinger, G. Dehm, R. Pippan, A further step towards understanding of size-dependent crystal plasticity: In situ tension experiments of minaturized single-crystal copper samples, Acta Materialia 56 (2008) 580-592

[15] C. Motz, T. Schöberl, R. Pippan, Mechanical properties of micro-sized copper bending beams machined by the focused ion beam technique, Acta Materialia 53 (2005) 4269-4279

[16] D. Di Maio, S.G. Roberts, Measuring fracture toughness of coatings using focused-ion-beam-machined microbeams, J Mat. Res. 20 (2005) 299-302

[17] K. Matoy, H. Schönherr., T. Detzel, T. Schöberl, R. Pippan, C. Motz, G. Dehm, A comparative micro-cantilever study of the mechanical behaviour of silicon based passivation films, Thin Solid Films 518 (2009) 247-256

[18] ASTM Standard E399-09, 2009, Standard Test Method for Linear-Elastic Plane-Strain Fracture Toughness KIC of Metallic Materials, ASTM International, West Conshohocken, PA, 2003, DOI: 10.1520/E0399-09, www.astm.org

[19] S. Wurster, C. Motz, M. Jenko, R. Pippan, Micrometer-Sized Specimen Preparation Based on Ion Slicing Technique, Adv. Eng. Mat. 12 (2010) 61-64

[20] D.E.J. Armstrong, M.E. Rogers, S.G. Roberts, Micromechanical testing of stress corrosion cracking of individual grain boundaries, Scripta Materialia, Vol. 61 (2009) 741-743

Publication F: Describing fracture on the micrometer scale employing single crystalline tungsten notched cantilevers

Describing fracture on the micrometer scale employing single crystalline tungsten notched cantilevers

Stefan Wurster [a], Christian Motz [a], Reinhard Pippan [a]

[a] Erich Schmid Institute of Materials Science of the Austrian Academy of Sciences, Jahnstraße 12, 8700 Leoben, Austria

Abstract

Fracture experiments using micrometer sized notched cantilevers were conducted to investigate the possibility of determining fracture mechanical parameters from the semi – brittle material tungsten. The second goal was to improve the understanding of semi – brittle fracture processes, for which single crystalline tungsten serves as a model material. The alignment of the starting notch plane with respect to the preferred {100} - cleavage plane, and consequently the crack front direction, were changed to retrieve the expected increase in toughness with increasing deviation. Due to the large plastic zone in relation to the small sample size, linear elastic fracture mechanics is inapplicable. Consequently, elastic-plastic fracture mechanics has to be introduced. Conditional fracture toughness values J_Q are calculated from corrected force vs. displacement diagrams; crack growth is accessible by direct observation of the in-situ experiments as well as with the help of unloading compliances. As a further tool, fracture toughness can be determined via crack tip opening displacement. Both methods result in higher toughness values compared to macro-sized single crystals found in literature.

Keywords
tungsten, single crystal, FIB, fracture, linear elastic fracture mechanics, elastic-plastic fracture mechanics, size effect, in-situ experiments, micro bending, crack tip opening displacement

1. Introduction

The microelectronic industry pushes the limits towards smaller components. Of course, the mechanical properties of materials in use are already explored in great depth on a macroscopic scale. However, the existence of mechanical size effects makes it important to quantify material properties at the same length scale of component sizes. This will be discussed later within this introduction. One of these properties is fracture. Fatigue and fracture determine the lifetime of components; as a consequence, it is appropriate to perform fracture experiments also on the microscopic scale.

Going one step back to the use of different small-scaled experiments such as compression, bending and tensile tests: These methods enable the determination of mechanical properties with high spatial resolution, furthermore being very material efficient – imagine the large number of samples which could be made out of one single macroscopic sample. Hence, micrometer sized experiments in general, and fracture experiments in particular, are the solutions for problems where one faces limited volumes of material. Beside the possibility of testing single microstructural constituents, like grains, grain boundaries [1] or especially aligned microstructures and multilayer systems [2, 3], it is by all means possible to receive parameters describing the fracture behavior of brittle materials [2-9] and also of semi-brittle materials, as this work will show.

The above-mentioned fact of a very limited testing volume is, for instance, beneficial for experiments on irradiated materials. The upcoming IFMIF-facility (International Fusion Materials Irradiation Facility) [10], which still needs to be constructed, is a fundamental part of the worldwide fusion research program aiming towards first generation fusion power plants. Gaining a comprehensive understanding of the interaction of a high flux of fast neutrons with matter is inevitably necessary. However, the volumes experiencing high neutron fluxes are very limited, the volume receiving the highest neutron fluxes (equivalent to more than 5 MW m^{-2}) contains about 100 cm^3 [10]. With this facility, it should be possible to achieve radiation damage levels of more than 100 displacements per atom [10]. Other measures to irradiate materials often result in a very surface-near irradiated volume – this can then be probed by using micrometer- and nanometer-sized samples (e.g. compression samples [11]). Of course, fracture experiments using large samples are well elaborated and look back on a long history [12], fracture experiments on the small scale are less elaborate. Nevertheless, it is possible, rather recommended, to use remnants of large-scaled fracture experiments as many more experiments can be made – hence, leading to a deeper knowledge. According to fracture, this can be done by micrometer-sized bending beams,

notched cantilevers or notched tensile samples as described in [13]. A feature of fracture experiments on the micrometer scale compared to other experiments (tensile, compression, pure bending) is the inherent appearance of a size effect. No other size effect such as the evident limitation of dislocation sources, starvation of dislocations due to the high ratio of surface to volume [14, 15], dislocation pile up in small samples [16, 17] or by introducing damage during production of samples [18], is necessary. Simply by changing the size of the samples from the mm- to the µm-size regime may alter the fracture behavior. For tensile experiments, downscaling is possible, in principle, to any size without changing the experiment. On the contrary, fracture experiments and the fracture process itself are governed by plastic deformation in front of the crack tip, which spread out for a certain length scale and the fracture behavior changes when the sample size is in the range, or smaller, compared to the plastic zone.

Fracture experiments using notched micro-cantilevers have already been performed using a variety of materials. Some of them are summarized in Table F.1, not claiming to be complete. It becomes evident that the Focused Ion Beam (FIB) workstation is the most important tool for fabricating small samples. The materials, which are described there, are not of outstanding toughness but sometimes of high strength. Fracture toughness evaluation of experiments outlined in this table use Linear Elastic Fracture Mechanics (LEFM) based on both analytical calculations and finite element simulations. Small scale yielding is a prerequisite for application of LEFM, hence the size of the plastic zone ω given as

$$\omega \propto {K_{IC}}^2 \Big/ {\sigma_y}^2 . \qquad \text{(F.1)}$$

has to be significantly smaller than the length of the crack and sample dimensions. K_{IC} is the critical stress intensity of the material for fracture in mode I and σ_y the material's yield strength; both have to be taken at the relevant test temperature. Formulating it in a more accurate way, ω has to be smaller than the K-dominated zone in front of the crack. A standard for measuring plane-strain fracture toughness values, ASTM E399 [19], sets the lower limit of crack length, a, and sample thickness, B, to $2.5*{K_{IC}}^2/{\sigma_y}^2$.

Matoy et al. [9] investigated the fracture behavior of chemical vapor deposited amorphous silicon-oxide, -oxynitride and –nitride using FIB-notched cantilevers. The most disadvantageous combination of fracture toughness and measured fracture stress σ_f appears for silicon nitride: K_{IC} = 1.73 MPa $m^{1/2}$, σ_f = 9.1 GPa. The fracture stress is taken as a lower limit for the yield strength; the samples do not show any plastic deformation. Thus, crack length and thickness have to be larger than 100 nm and it is easy to produce samples large enough to give meaningful results using LEFM.

In [4], fracture experiments using samples in the micrometer regime made of lamellar Ti-48Al are described. The authors report very low fracture toughness values (1.5 – 3.6 MPa $m^{1/2}$) for interlamellar crack orientation, i.e. the crack propagation direction is parallel to the lamellae. The lower bound is in accordance to energy calculations for cleavage fracture. For the translamellar crack orientation, where the crack propagation is perpendicular to the lamellae, the fracture toughness was found to be higher (5.0 – 8.1 MPa ^{½}) but lower in comparison to macroscopically large samples (~20 MPa $m^{1/2}$ [4]). The authors argued that extrinsic toughening mechanisms are not activated, nevertheless the small specimens' size in relation to this comparably high toughness might lead to a reduced value of $K_{IC.}$ So, is the method of using micrometer-sized fracture samples henceforth restricted to materials of limited fracture toughness and yield stress values?

In this study, the peculiarities of small-scaled fracture experiments will be discussed. Specimens that were made on the basis of the production route and experimental setup described in [13] will be used. The material chosen for this work was a tungsten single crystal, a material too tough or too soft at room temperature for successful application of LEFM on micrometer-sized samples. The single crystal used for these experiments was aligned in order to test the {100}-<011> crack system. Macro samples of this orientation having the lowest fracture toughness K_{IC} of (6.2 ± 1.7) MPa $m^{1/2}$ and energy release rate G of (82.5 ± 55) N/m at room temperature in comparison to all other systems (8.7 – 20.2) MPa $m^{1/2}$ were presented in [20, 21]. The denotation of the crack system, {hkl}-<uvw>, gives the crystallographic plane {hkl}, wherein the crack is introduced together with the direction of the crack front <uvw>. Setting the constant factor in Equation (F.1) to 1/π, the plastic zone ω for the tested crack system is about 29 µm, hence it is larger than the whole specimen. The yield strength σ_y was set to 650 MPa, according to [22], where tensile experiments – on a different length scale, however – of electron beam melted tungsten single crystal in [001] direction are described.

This leads to the point of transferability of certain mechanical properties from one range of sample sizes (mm and larger) to the other (tens of micrometers and below). What has to be kept in mind is that size effects are present, which was shown e.g. by Uchic et al. [23] for compression samples or by Fleck et al. [24] by comparing tensile and torsion experiments of thin wires, where they detected an increase in strength with decreasing size. On the one hand, an even more pronounced effect was found by Motz et al. [16] for small, FIB-made cantilevers. There is an increase in flow stress with decreasing cantilever thickness, which was explained by a combination of two processes: A decrease in available dislocation sources and dislocation pile-up at the neutral axis of the bending beam. On the other hand, Shim et al. [25] present a pronounced decrease in strength of FIB-made micro-pillars in comparison to as-grown micro-pillars. Therefore, one ends up with both a decrease in strength – seriously affecting the materials behavior via Equation (F.1) – which is due to introduction of defects by specimen production and with an increase in strength due to the small samples size. As a consequence, fracture experiments should be accompanied by tensile tests

using samples of the same size and which were subjected to the same production steps (i.e. ion beam milling).

Table F.1: Summarizing recent results investigating fracture behavior of various materials using micrometer-sized notched cantilevers,

Material	Ref.	Production & Size	Notches	Fracture Toughness K_{IC} K_Q, [MPa $m^{1/2}$]
Ti-48Al, two-phase single crystal lamellas	[4]	FIB-made from foils with a thickness of 20 µm, cantilevers of 10 x 20 x 50 µm³	FIB, interlamellar and translamellar, width: 0,5 µm, depth: 5 µm	Interlam.: K_Q = (1.5 – 3.6) MPa $m^{1/2}$; Translam.: K_Q = (5.0 – 8.1) MPa $m^{1/2}$
Monolithic Si, prepared to show (111) cleavage plane	[5]	FIB made cantilevers, from bulk material, specimens of pentagonal shape	FIB, line milling with 1 pA, notch width is expected to be in the order of 10 nm	4 samples, K_{IC} = (1.1 ± 0.016) MPa $m^{1/2}$
CVD-deposited WC coating on a bulk steel substrate	[5]	FIB made cantilevers, from bulk material, specimens of pentagonal shape	FIB, line milling with 1 pA, notch width is expected to be in the order of 10 nm	4 samples, K_{IC} = (3.2 ± 0.3) MPa $m^{1/2}$
Magnetron sputtered TiN film on single crystalline (100) Si	[6]	FIB, length of cantilevers: 60 µm – 77 µm, thickness: 10 µm – 10.8 µm, varying thickness of substrate	FIB, depth: 200 nm (50 pA), notch radius: 10 nm	4 samples, K_{IC} = (2.6 ± 0.3) MPa $m^{1/2}$
Ni – 11.5 wt% P amorphous alloy thin films	[7]	FIB, cantilevers: 10 x 12 x 50 µm³	FIB made notches of 6 µm (a/W = 0.5) in length. Fatigue pre-cracks by cyclic compressive loading.	K_Q = 5.4 MPa $m^{1/2}$, large scale yielding
Lamellar Ti-46Al-5Nb-1W (in at%, “Alloy 7”)	[8]	FIB, out of thin foils, cantilever measuring about 20 x 7 x 36 µm³	FIB, depth: less than 5 µm, width: 500 nm	12 samples, K_Q = 1.4 – 6.9 MPa $m^{1/2}$
Silicon oxide	[9]	FIB, cantilever, 1.69 (B) x 2.1 (W) x 5.1-5.2 (L) µm³	FIB, line milling (5 pA) , notch root radius ~ 10 nm	2 samples, K_{IC} = (0.63 – 0.72) MPa $m^{1/2}$
Silicon oxynitride	[9]	FIB, cantilevers, 1.65-1.67 (B) x 2.1 (W) x 5.2 (L) µm³	FIB, line milling (5 pA) , notch root radius ~ 10 nm	3 samples, K_{IC} = (0.91 – 1.00) MPa $m^{1/2}$
Silicion nitride	[9]	FIB, cantilever, 1.45-1.61 (B) x 2.1 (W) x 4.9 (L) µm³	FIB, line milling (5 pA) , notch root radius ~ 10 nm	4 samples, K_{IC} = (1.54 – 1.73) MPa $m^{1/2}$

However, an advantage of fracture experiments in relation to other experiments relying on defect free samples is that fracture samples do not use defect free materials per se. For both types, large samples and small-scaled samples, a crack has to be introduced or has to be present. This can be done by cyclic loading as it is demanded by standards [19, 26-29] and which is also possible on the small scale [7] but the majority of published scientific work relies on the introduction of a small notch with the FIB, e.g. using line milling with low currents in the pA regime. References [5, 6, 9] report on crack tip radii of about 10 nm, when using ion currents of 1 pA to 50 pA. For the investigations described here, currents of 50 pA to 100 pA were used. The question, whether a notch, which was made with the FIB, is equivalent to a natural crack still lacks a final answer and this publication will try to clarify this topic by comparing the fracture behavior of FIB-notched cantilever with fracture experiments on single crystalline tungsten specimens containing a natural crack.

2. Sample Preparation

The production of micrometer-sized specimens is outlined explicitly in [13], so just a short summary will be given here. An ion slicer (JEOL EM-09100IS) is used to remove large amounts of material, altering its actual purpose of transmission electron microscopy sample production. Low energy argon ions with a maximum energy of 6 keV are used. The result of the ion slicing process is a thin lamella with a few micrometers in thickness and up to about one millimeter in length. This lamella can now easily be used as a preform for further processing. This lamella features a decreased lateral stiffness in comparison to bulk material and an increased lateral stiffness in comparison to needle-shaped samples, respectively. Subsequently, any desirable sample shape (tensile, compression, bending) using a FIB workstation (LEO XB 1540) is producible. Several notched cantilevers were made; their dimensions and crack system are outlined in Table F.2.

Gallium ion currents for cutting the sample contours were 500 pA to 2 nA, ion currents of 50 pA to 100 pA were used for cutting the notches using the line milling mode. Acceleration voltage was 30 kV for all milling steps. For sample (S3), the fine notch was set into a rather blunt notch of triangular shape, which was cut from the specimen's side view. By changing the milling time, it is possible to adapt the notch depth. Using a milling time of 40 s/µm for an ion current of 50 pA or 20 s/µm (100 pA), both in line milling mode, resulted in a notch depth of approximately 1.5 µm for single crystalline tungsten. In addition to a series of small cantilevers cut from an ion sliced lamella, two cantilevers were cut out from half of a disk of single crystalline tungsten showing surface near cracks. These cracks were unintentionally introduced by cutting the crystal and serve as starting point for notched cantilever production – not from a thin lamella, but from the edge of the bulk material. FIB milling was again used to cut the specimens' shape. Notice that the crack front did not experience any gallium ion irradiation, except for the outermost surface of the side of the cantilever.

Table F.2: Dimensions and crack system of notched cantilevers. α is the adjusted angle between the normal vectors of notch plane and cleavage plane. L is the maximal bending length, B the sample thickness, W the sample width and a the crack length. $K_{Q,\ LEFM}$ is the fracture toughness determined in Section 3.1. Where not stated otherwise, all measurements are taken from SE micrographs. (S) stands for standard specimens

Specimen No.	Type of Crack System	α [°]	L [µm]	B [µm]	W [µm]	a [µm]	$K_{Q,LEFM}$ [MPa $m^{1/2}$]
(S1)	{15 1 0} - <1 15 17>	0	9,5	7,2	3,6	1,5	2,9
(S2)	{22 4 3} - <2 6 7>	5	9,4	5,7	4,4	1,4	3,1
(S3)	{29 7 6} - <9 19 22>	15	9	5,2	4,4	1,8[12]	3,7[13]
(S4)	{26 10 9} - <13 16 19>	25	9,6	3,8	4,4	1,5	3,5

The notches of cantilevers (S1) – (S4) were aligned with certain deviations in respect to the cleavage plane (Figure F.1). The crack system including the crack propagation direction was set up by cutting the preform for ion slicing from a tungsten single crystal of desired crystallography; furthermore, this systems was controlled by electron backscatter diffraction (EBSD) measurements on the as-received sample surface after ion slicing. Cantilever (S3) is equivalent to the specimen of "perfect" alignment, with the notch front being perpendicular to the lateral surfaces. To analyze the crack systems, especially those that are inclined at a certain angle to the perpendicularity of the sample's coordinate system, the software OIM – Orientation Imaging Microscopy v5.31 was used. Results on the crack systems are outlined in Table F.2. With increasing deviation of notch plane from cleavage plane there goes a change of crack front direction from <110> to <111>. The crack propagation direction was the same for all samples and was always very close to <1$\underline{1}$0>; according to EBSD analysis it was of <17 15 1> - type. What has to be mentioned when referring to EBSD measurements is that relative misorientations within a single specimen can be determined at rather high accuracy below 1°. However, absolute values incorporate higher inaccuracies, especially as the crystallography was measured by EBSD, the samples were then transferred to the FIB for cutting and mounted inside an scanning electron microscope (SEM) for in-situ testing. Consequently, a perfect alignment of loading direction towards the notch plane, which should then again be ideally positioned at a certain defined deviation from the cleavage plane is unlikely. Inaccuracies within a few degrees are expected. Henceforth, the four crack systems of the cantilevers (S1) to (S4) will be described by the deviations of the notch plane from the perpendicularity of the cantilevers and not from the EBSD-determined crystallography. The latter

[12] No according SE micrograph for determination of crack length, Crack length was determined from first unloading stiffness, Section 3.2.1.

[13] F_{max} instead of F_Q was used for determination of a critical stress intensity value, see Section 3.1.

case would result in deviations of 4°, 13°, 18° and 27° when compared to the crack systems listed in Table F.2.

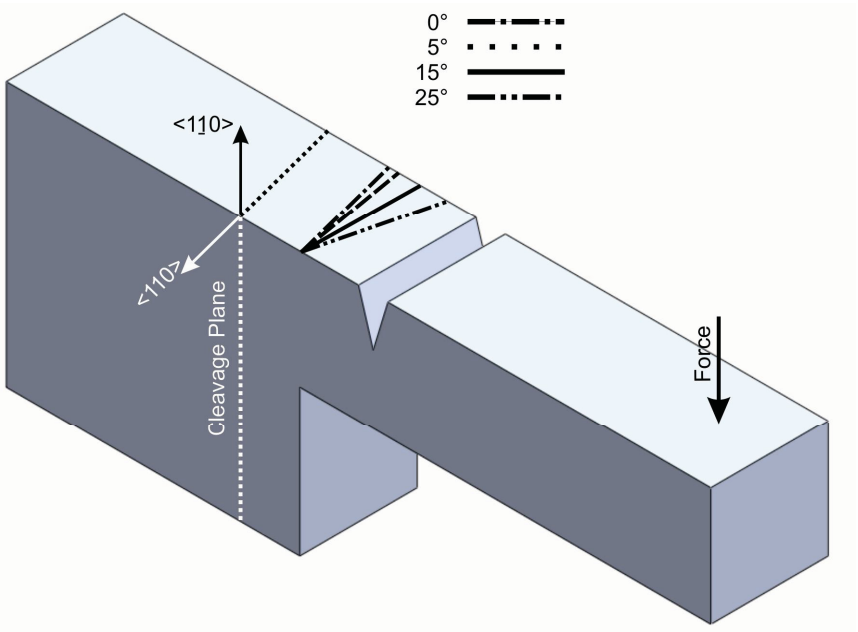

Figure F.1: Schematic representation of the notched cantilever of type (S3), showing the {100} – cleavage plane, the <1$\underline{1}$0> – direction being anti-parallel to crack propagation direction, the <110> – direction representing the crack front direction. Furthermore, the point of application of force and the four different notch systems (S1 = 0°, S2 = 5°, S3 = 15° and S4 = 25°) are indicated.

3. Results

3.1. Linear Elastic Fracture Mechanics Approach

No fatigue pre-cracking of cantilevers, such as it is described in [7] was conducted. Cantilevers were loaded in-situ in a SEM (LEO 982) using a micro indenter (ASMEC, UNAT) with a cube corner tip. Loading and unloading speed was set to 1 µm/min for all specimens, including the ones incorporating natural cracks ((NC1) and (NC2)). Stable crack extension was observed for all cantilevers and as a consequence J-Δa-curves can be drawn. This will be done in sections 3.2., describing the elastic-plastic approach. Force and indenter displacement are recorded and the results for specimens (S1) to (S4) are shown in Figure F.2,a. Several unloading steps during the experiment allow the observation of crack growth due to the decreasing cantilevers' compliance. The automatic recording of several thousands of SE micrographs for one single experiment results in detailed knowledge of the fracture progress.

The conditional critical stress intensity for notched cantilevers is derived according to equations (F.2) and (F.3).

$$K_Q = \frac{F_Q * L}{B * W^{3/2}} f(a/W) \tag{F.2}$$

$$f(a/W) = 4 * \frac{3 * (a/W)^{0,5} * (1,23 - (a/W) * (1 - (a/W)) * (-6,09 + 13,96 * (a/W) - 14,05(a/W)^2))}{2 * (1 + 2 * (a/W)) * (1 - (a/W))^{1,5}} \tag{F.3}$$

F_Q is the force determined according to ASTM E-399 [19], L the bending length, a the crack length, B the thickness of the specimen and W the width of the specimens. Determination of F_Q is done by intersecting a line with 95% of the slope of initial loading with the force vs. displacement curve and taking the highest value for F appearing before this point of intersection. F_Q and K_Q are presented together with specimens' dimensions in Table F.2. For specimen (S3), a change of slope in initial loading took place, this may be attributable to the breaking of a thin wall, being a remnant from FIB-notching. Consequently, for this sample the initial slope of loading cannot be used to determine K_Q, instead K_{max} was taken. For comparison, K_{max} is about 0.3 MPa $m^{1/2}$ larger than K_Q for (S1) and (S4), K_{max} is identic to K_Q for (S2). All six samples ((S1) to (S4) and (NC1) & (NC2)) do not fulfill all requirements that are given by standards determining the measurement of plane strain fracture toughness, thus, the results will be presented as conditional fracture toughness values, indicated with the subscript "Q".

A factor of 4 is added to Equation (F.3) to keep its form close to the shape factor of three-point-bending (3PB) tests given in ASTM E-399 [19]. Finite element simulations were conducted in order to determine the shape factor f(a/W) for this special sample shape, the result is presented in Equation (F.3) [30]. The parameters were fitted according to results of ABAQUS finite element simulations. There, J-values were determined for different values of a/W. Two-dimensional simulations were made using 8-node bi-quadratic elements (CPS8) [30]. Thus, f(a/W) from Equation (F.3) is just valid for cantilever of type (S3). No inclination of crack plane was taken into account. Thus, the FIB notch was made as it would be demanded for standard specimens. However, as the angles of inclination are small the same shape factor was considered for all other cantilevers. The results for the shape factor $f(a/W)$ differ from shape factors presented within ASTM E-399 [19] and Murakami's reference book [31] for 3PB-samples by less than 10% within the relevant regime of a/W. The specimens' dimensions were measured using SE microscopy and together with force F_Q and equations (F.2) and (F.3), a conditional critical fracture toughness value, K_Q, can be determined. This method does not take into account any crack propagation nor any plasticity, large scale yielding to be more precise. Both reasons lead to the fact that critical stress intensities do not represent valid values but only lower limits. The actual minimum limit for sample size according to [19] would be about 230 µm, this requirement is missed by about two orders of magnitude.

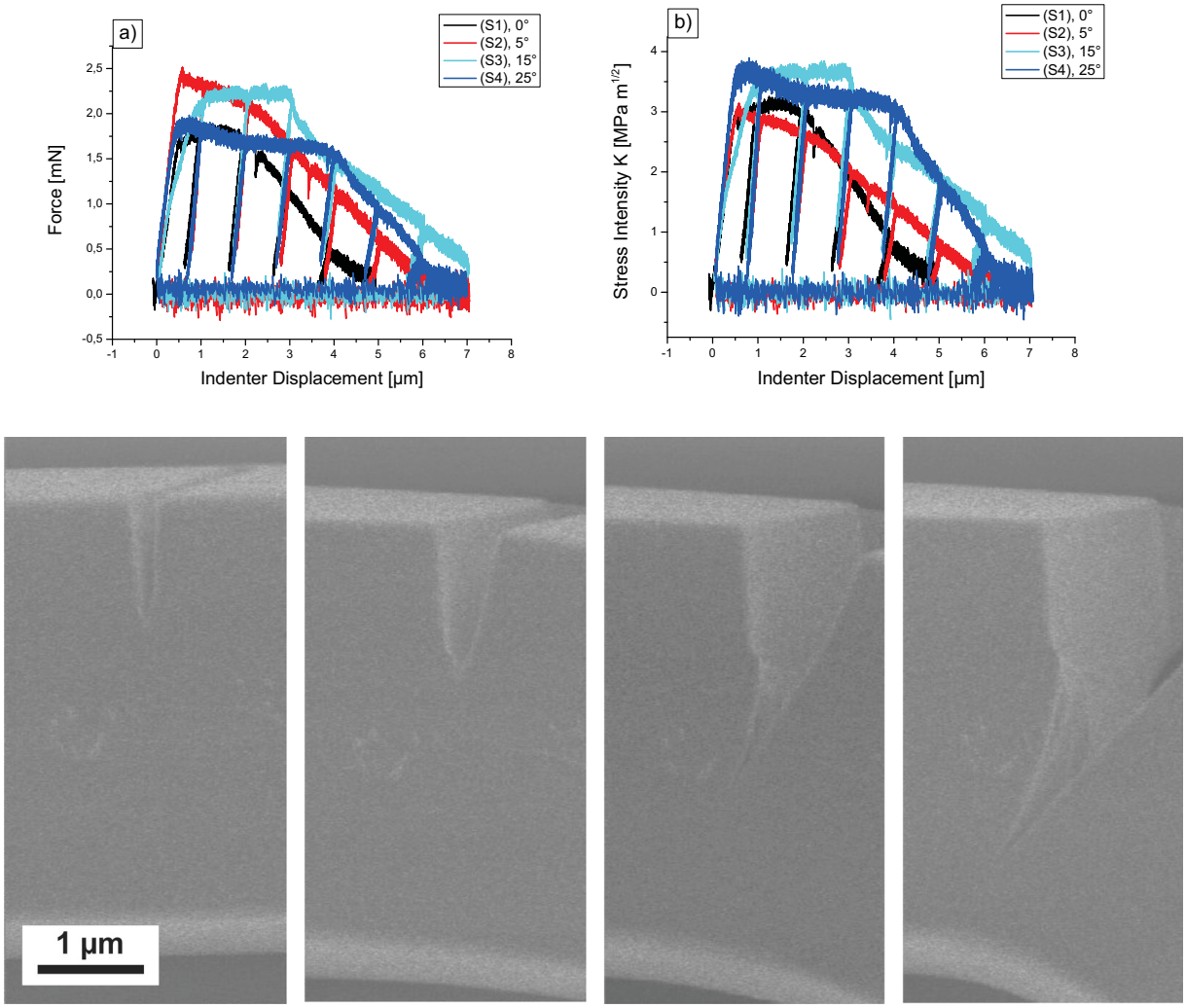

Figure F.2: a) Measured force vs. indenter displacement for (S1) to (S4), b) corresponding stress intensity factors at the crack tip based on LEFM and equations (F.2) and (F.3) without taking crack propagation into account. A sequence of SE micrographs of cantilever (S2) shown is included. They correspond to the starting point without any load applied and further on the moment before the 2nd, 4th and 6th unloading.

In fact, this procedure is sufficient for determination of mechanical properties for small components, as it results in a complete description of the reaction of a specimen to a load. In contrast, it is not sufficient when the goal is to derive valid fracture properties from small samples. For large scale yielding, other methods have been successfully applied for macroscopic samples. For large samples, fracture toughness can be determined using *J*-integrals, crack tip opening displacement (*CTOD*) or crack tip opening angle (*CTOA*). Stable crack growth is observable via the compliance method or potential drop method. Some of these approaches shall now be presented for the micrometer-sized fracture experiments.

3.2. Elastic – Plastic Fracture Mechanics Approach

3.2.1. J-Integral

Experiments were made to describe the fracture toughness using the *J*-Integral. Although ion slicing aids in reducing the time to manufacture these specimens, it is recommended to use the single specimen technique. This requires detailed knowledge of the crack propagation during the experiment, which can be achieved in two ways, first by the unloading compliances of the cantilevers and second by in-situ observation of the fracture process, crack growth respectively. Both methods are used for this work.

The measured load vs. displacement curves were corrected in respect to the compliance of the lamella – as already done in [30] and, furthermore, regarding indentation depth. In the ideal case, the cantilevers' support base should not show a translation due to the application of force, but this is not always the case. The in-situ experiments makes a large number of images and by fitting the displacement of the support at a certain force by a straight line it is possible to determine a quantity equivalent to the spring constant of the lamella. This was done for (S1) and (S2) resulting in 12.8 mN/µm for (S1), and 9.7 mN/µm for S2 [30]. In-situ observation of specimens (S3) and (S4) focused on the notched area, where the crack evolved, no spring constants could have been determined for these experiments. However, as the specimens are positioned next to each other on the same ion-sliced lamella, a reasonable corrective value of 11 mN/µm was chosen for (S3) and (S4).

Further, the recorded indenter displacement has to be corrected to take into account the generation of an indent. Four indentation-depth vs. load curves were recorded with the same indenter in bulk single crystalline tungsten and a quadratic fit of the initial part of the loading curve was used to correct for the generation of an indent. This leads, as for the lamella-related correction, to a decrease in the resulting cantilever displacement. Ideally, the combination of both corrections results in the force vs. displacement curves of a cantilever experiencing no indentation and sitting on an infinitely stiff support.

Several sample unloadings were made to determine crack growth for each sample, this can be seen in Figure F.2. The stiffness of the cantilever decreases when the crack grows. Hence, the ligament length (W-a_i) in the i-th step of unloading can be calculated according to the deflection of a cantilever:

$$W - a_i = \sqrt[3]{\frac{4kL^3}{BE}} \tag{F.4}$$

with k being the unloading compliance from the corrected load vs. displacement diagrams and E being the Young's Modulus, which was set to 400 GPa. Equation (F.4) is valid for a one-side fixed cantilever with a thickness of (W-a_i) and bending length L. The small distance from the notch to the cantilever's base, as well as the overall thickness W, was not taken into account. Using Equation (F.4) the other way round, with the notch length determined in the SEM for (S1), (S2) and (S4) (Table 2), the nearly isotropic Young's Modulus for tungsten single crystal is determined to be between 470 GPa and 550 GPa.

Equation (F.4) is a rather rough assumption; nevertheless, the results of calculations and direct observation agree as can be seen in Figure F.3. This figure shows that for small crack extensions, the crack lengths determined on the specimens' surfaces tend to be lower than the unloading stiffness indicates. This might be because of tunneling of the crack in the center of the specimen for short crack extensions and in a later stage, after the crack extension approached the surface, crack lengths from SE micrographs approach the ones derived from unloading stiffness. The largest difference in crack lengths appears for cantilever (S4) which might be related to a larger amount of crack tunneling in the sample's center. Comparing the starting crack lengths: The calculated crack lengths from the first unloading step, a_1, where hardly any or no crack propagation took place, do not differ by more than 300 nm from the length of the FIB-notches for (S1), (S2) and (S4). Initial crack lengths were measured post-mortem in the SEM as FIB-made notches are easily distinguishable from fracture surfaces.

The actual ASTM-standard for determination of the J-integral [27] relies on very detailed knowledge of the crack extension. Of course, it would be feasible to produce more unloading steps but one would rather end up with a low cycle fatigue experiment. Henceforth, J-values will be calculated using an old standard [29]. $J_{(i)}$ at the i-th point of unloading is given as the sum of elastic and plastic components:

$$J_{(i)} = \frac{(K_{(i)})^2(1-\nu^2)}{E} + \frac{\eta A_{Pl(i)}}{B(W-a_0)}. \qquad \text{(F.5)}$$

$K_{(i)}$ is determined by Equations (F.1) and (F.2), η is a constant factor set to 2, ν the Poisson's ratio and $A_{Pl(i)}$ the area beneath the load vs. displacement curve, excluding a triangle that is defined by the unloading line. Poisson's ratio was set to 0.28 for further evaluation. For each unloading step the according crack length and J-integral is determined; this results in Figure F.4 showing the curve J versus crack extension, the J-Δa-curve.

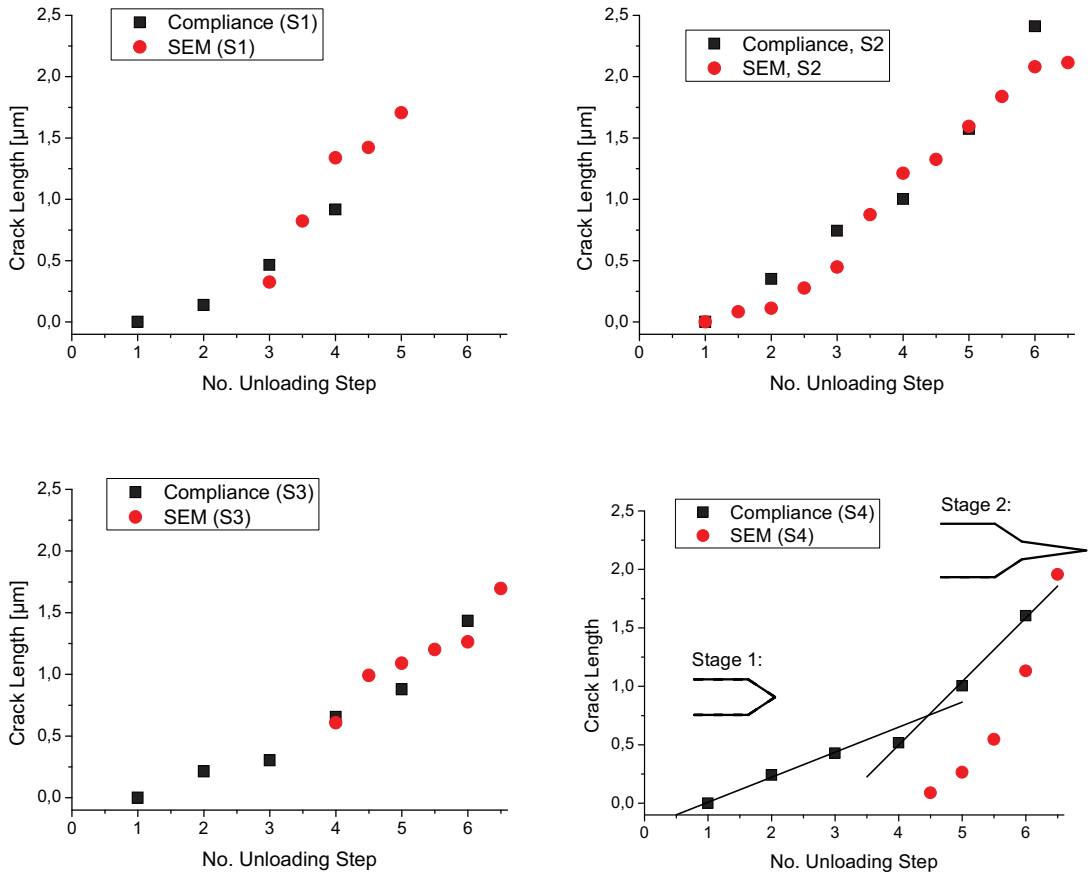

Figure F.3: Comparison of crack lengths for cantilevers (S1) to (S4), measured in SE micrographs corresponding to the beginning of the unloading procedure and in micrographs taken inbetween two unloading procedures (red points); black squares represent crack lengths determined by use of the compliance method, Equation (F.4). For cantilever (S4), the two different regimes of crack propagation, as they are discussed in the Section 4, are indicated.

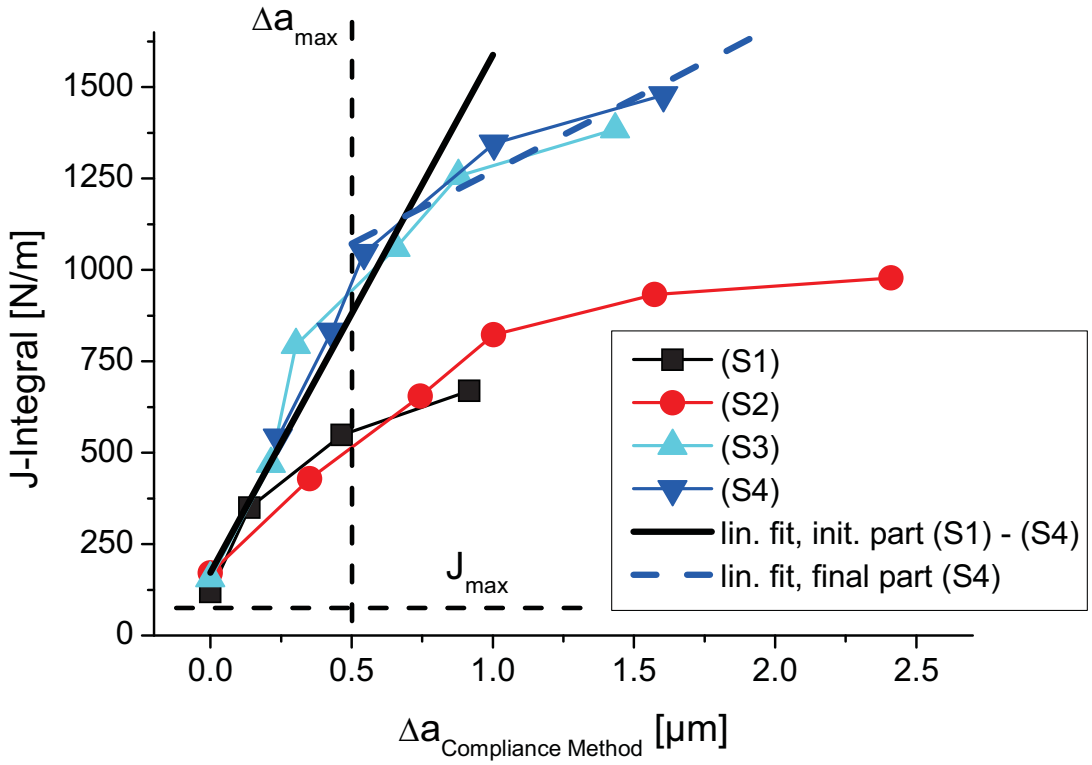

Figure F.4: *J*-integral vs. crack growth, *Δa,* (*J*-Δa-curves) for all notched cantilevers, showing limits for the maximum capability of *Δa* and *J* as it is described in the text.

All J-Δa curves show the typical shape also observed for macroscopic tests of ductile materials. This curve should then be fitted using a power law of the form [27]:

$$J(a) = C_1 \left(\frac{\Delta a}{k} \right)^{C_2} . \qquad \text{(F.6)}$$

k is a constant and C_1 and C_2 are determined by the fitting procedure. An intersection of this curve with a parallel line to the blunting line has to be made, whereas the blunting line is a straight line showing the initial slope of the *J*-Δa-curve. This parallel line to the blunting line should be drawn at an offset value for crack extension of 0.2 mm [27] – this is not possible to fulfill for experiments on this length scale.

A quantity that can be determined is the uppermost value of $J_{(i)}$ where crack extension already had to take place. For all specimens (S1) to (S4) this is before the second unloading step, because compliance is markedly increased at the second unloading compared to the first unloading. Of course, it is possible that crack propagation took place in advance of the first unloading step. Fracture toughness $K_{Q,J}$ can be calculated using:

$$K_{Q,J} = \sqrt{\frac{J\,E}{1-\nu^2}} \tag{F.7}$$

resulting in fracture toughness values of 12.5 MPa $m^{1/2}$, 13.8 MPa $m^{1/2}$, 14.4 MPa $m^{1/2}$ and 15.5 MPa $m^{1/2}$ for increasing misorientation from the cleavage plane.

Another possible fracture toughness determination method is to fit the set of data shown in Figure F.4 with two linear functions. The first one describes the blunting line, i.e. the summarized initial parts of all four *J*-Δa-curves, and the second the individual slopes of the final part of each *J*-Δa-curves. The slope of the initial linear fit (1417 MPa) is in very good agreement with the slope of the construction line that needs to be drawn according to standard ASTM 1820 [27]. This would then give a slope of 1300 MPa (= 2* σ_y); thus, being a hint for the applicability of the chosen value for the yield strength. For cantilever (S4), the linear fit of the final part is depicted in Figure F.3 and this method results in fracture toughness values of 12.8 MPa $m^{1/2}$, 18.4 MPa $m^{1/2}$, 20.9 MPa $m^{1/2}$ and 22.3 MPa $m^{1/2}$ for increasing deflection from the cleavage plane. Both results, presented in this paragraph are summarized together with results from LEFM and crack tip opening displacement in Figure F.7.

Standard [29] restricts the initial ligament size (W-a_0) and the thickness B to be greater than

$$(W - a_0), B > \frac{25 J_{IC}}{\sigma_Y} \tag{F.8}$$

with J_{IC} being the critical value describing the onset of stable crack extension. The smallest dimension of cantilever (S1) is 2.1 µm leading to a maximal acceptable J_{IC}-value of 55 N/m, again using 650 MPa for σ_y [22]. Actually, the *J*-value corresponding to the first unloading is 119 N/m. The smallest dimension of cantilever (S4) is 2.9 µm leading to a maximal J_{IC} value of 75 N/m, actually the *J*-value corresponding to the first unloading is 229 N/m. The requirements are not missed by two orders of magnitudes as for LEFM but just by a factor of two to three (see Figure F.4). The maximum crack extension for valid determination of *J*-values is – as for crack tip opening displacement, which will be outlined later – (W-a_0)/4. Taking the smallest value for (W-a_0) appearing in Table F.2, this would result in a conservative limit of about 500 nm; this limit is indicated in Figure F.4 with a parallel line to the y-axis.

3.2.2. Crack Opening Displacement

The determination of crack tip opening displacement is based on a hinge model, proposed e.g. in a British standard [28], which is adopted for notched cantilevers (see Figure F.5.). There, the fracture process of a 3PB bending sample is assumed to occur by a rotation. The center of rotation is at a depth of 0.45*(*W*-*a*) below the notch front. Determination of the bending angle *Θ* results from a combination of corrected indenter displacements at the beginning of unloadings in combination with the mean bending length. *CTOD* versus crack growth curves, also known as *CTOD*-Δa-curves, were evaluated; they are shown in Figure F.6. Crack extensions, shown in this figure, were determined via the unloading stiffness as it is described in Section 4.1.

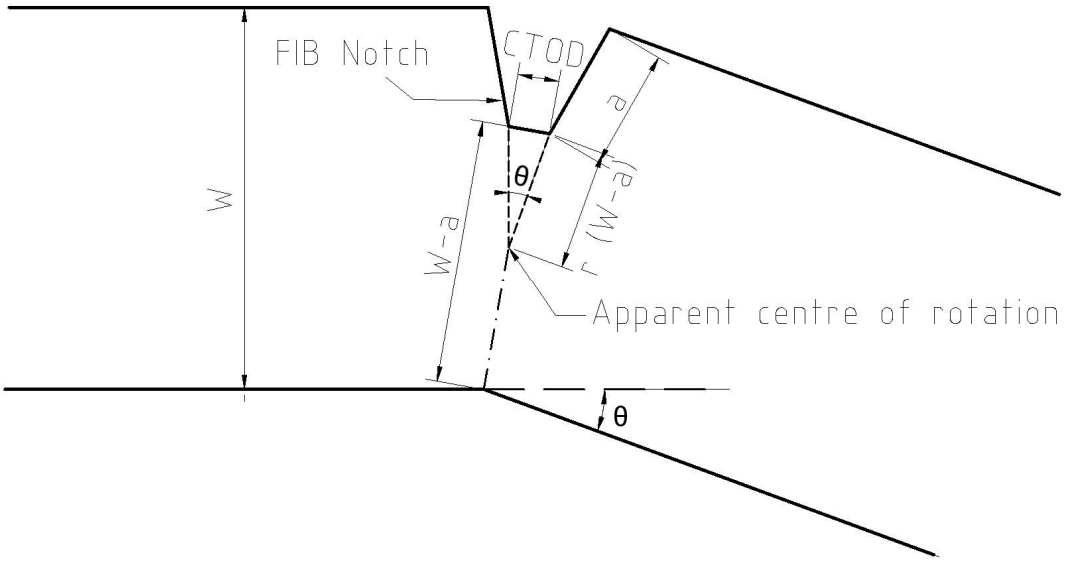

Figure F.5: Hinge model for micrometer sized notched cantilevers.

The maximum allowed value of CTOD is (W-a_0)/20 and (W-a_0)/4 is the maximum value for crack extension according to [27]. Conservative values for these limits are $CTOD_{max,conservative}$ = 100 nm and $\Delta a_{max,conservative}$ = 500 nm, respectively; they are included in Figure F.6 as parallel lines to the x- and y-axes. The final parts of the curves in Figure F.6 are not within the limit for Δa, the limitation in *CTOD* is even more restrictive. According to ASTM E1820 [27], the initial ligament length must be significantly larger, 35 times larger to be more precise, in order that $CTOD_{crit}$ is a size-independent value – this is also the case here. Nevertheless, the curves show an increase in CTOD with crack extension.

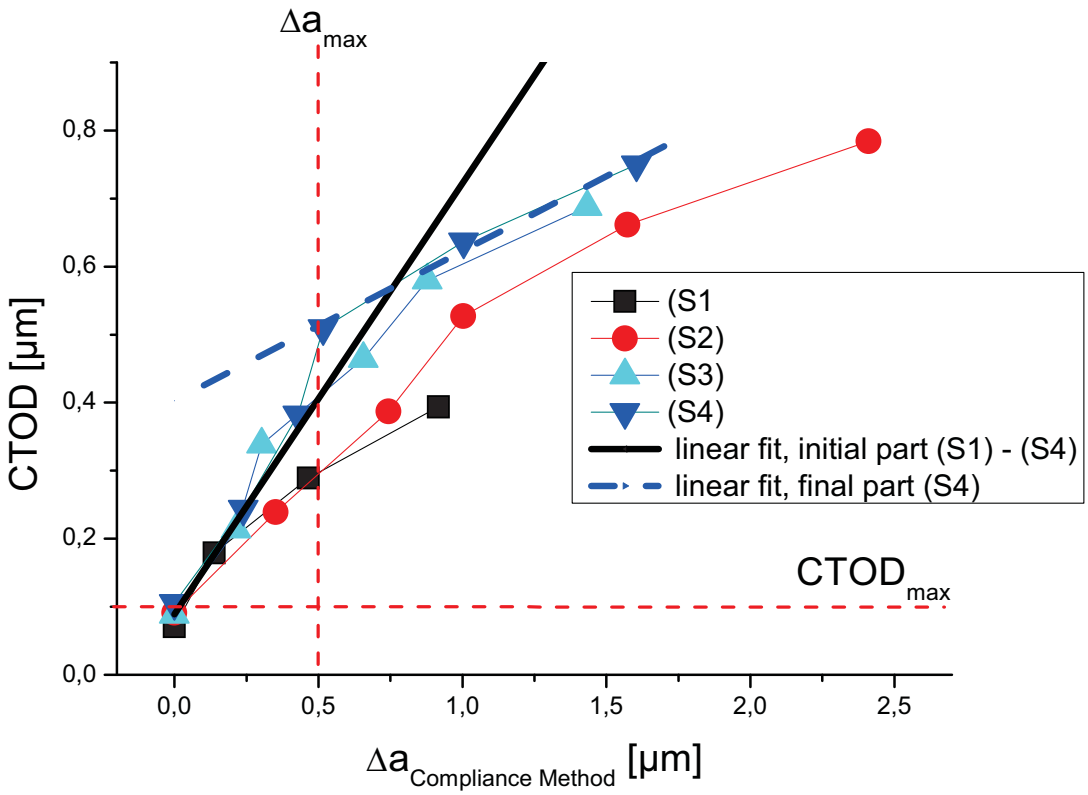

Figure F.6. *CTOD* versus crack growth *Δa* (*CTOD*-Δa-curves) for all FIB-notched cantilevers (S1) to (S4). *Δa* was determined from unloading stiffnesses. The maximum allowed values basing on smallest specimens' dimensions in Table F.2 for crack extension and *CTOD* are outlined in red, dashed lines. The blunting line, being a linear fit of the combination of all intital parts of the curves, is shown as a black line. The blue, dashed line is a linear fit of the final part of results of specimen (S4); the intersection of both lines leads to $CTOD_{crit}$ for (S4).

As it was proposed in the previous section for the *J*-Δa-curve, the *CTOD*-Δa-curve should be fitted according to a power law fit. The intersection with a parallel line to the blunting line, which should be drawn at a crack extension of 0.2 mm, gives a conditional critical crack tip opening $CTOD_Q$. Proposing another way of evaluation, one single line is drawn, derived by fitting the first two to three *CTOD*-values of all specimens – representing the blunting line. The slope of this line (0.63) is smaller by about a factor of two compared to the slope of the construcion line (1.4) proposed by ASTM 1820 [29], thus, indicating a different blunting behavior compared to ductile materials. The fitted line is intersected with individual fitted lines of the final parts of each *CTOD* vs. *Δa* curve. The point of intersection gives a result for conditional critical crack tip opening displacement $CTOD_Q$ and it is then possible to determine a critical stress intensity $K_{Q,CTOD}$ using equation (F.9) and

(F.10). No hardening is observed; therefore, assuming an elastic – perfectly plasitc material behavior, the relationship between J and CTOD is given by [32]

$$J = \sigma_y * CTOD \tag{F.9}$$

and subsequently

$$K_{Q,CTOD} = \sqrt{\sigma_y * E * CTOD_Q} \tag{F.10}$$

In case of evaluating work hardening materials, a coefficient mainly depending on the work hardening exponent has to be included [33]. Together with σ_y = 650 Mpa [22] and E = 400 GPa. Increasing critical crack tip opening displacement, $CTOD_C$, with increasing deviation of notch plane from cleavage plane was observed. $CTOD_Q$ were determined to be 230 nm, 470 nm, 480 nm and 570 nm for the sequence (S1) to (S4). The corresponding fracture toughnesses of 7.8 MPa $m^{1/2}$, 11.0 MPa $m^{1/2}$, 11.1 MPa $m^{1/2}$ and 12.2 MPa $m^{1/2}$ are depicted in Figure F.7. What has to be kept in mind categorically is the question of transferability of yield strength from one size regime to the other.

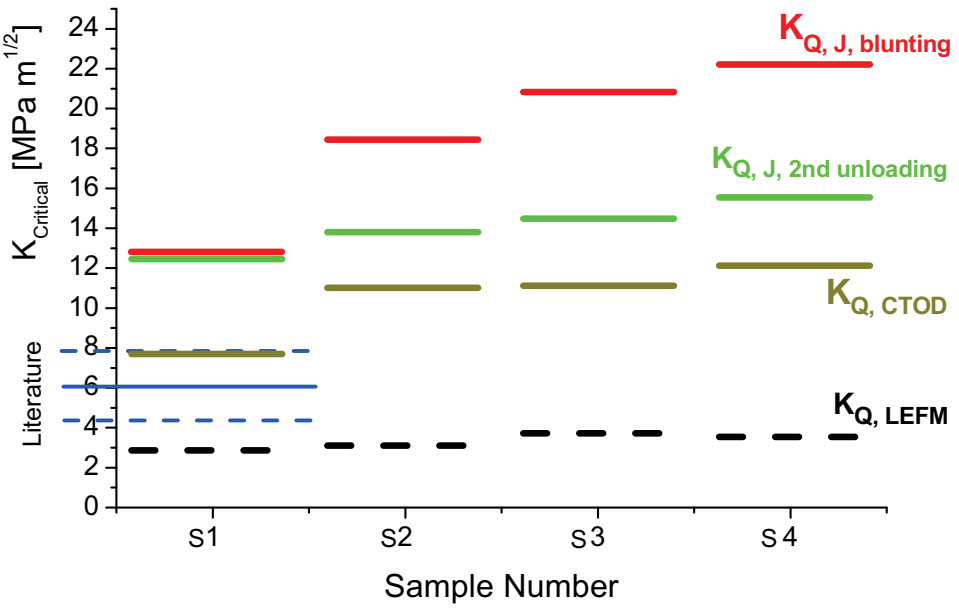

Figure F.7: Compilation of results of critical stress intensity factors for crack initiation, showing $K_{Q,\ LEFM}$ giving lower limits for fracture toughness together with results from elastic plastic evaluation ($K_{Q,J,blunting}$, $K_{Q,J,2nd\text{-}unloading}$ and $K_{Q,CTOD}$). The latter results overestimate the toughness according to LEFM – results from Riedle et al. [20, 21], which are also presented for the cleavage plane – notch direction configuration matching to cantilever (S1).

3.3. Naturally Cracked Cantilevers

To investigate whether a difference between in a FIB made notch and a natural crack exists, experiments using cantilevers incorporating such a natural crack were made. To perform this work, two specimens were produced out of a tungsten single crystal in bulk form. Due to heat produced during cutting of the single crystal, a large number of surface cracks evolved, showing the typical fish bone pattern. The cantilevers' top surface is of {111} – type and according results on experiments introducing cracks in tungsten single crystals by electrical discharge machining [34, 35] the crack planes are most likely of {100} – type. Without usage of the ion slicing process – as this would most likely eliminate the surface-near cracks – a thin lamella had to be produced with the FIB [16]. It is important to emphasize that the crack front did not experience any FIB-damage, except at the points where it penetrates the lateral surfaces. Figure F.3 shows that crack propagation starts in the center and ion damage of the lateral surfaces should be less an issue. The crack line at the cantilevers' top surface was perpendicular to the side surfaces; however, the natural crack did not propagate perpendicular to the surface but inclined at a certain angle (Figure F.8). To comprise evaluation of mode I fracture toughness values, the cantilever would have to be cut at a certain angle in respect to the single crystal's top surface. This would make production and testing more complicated.

Figure F.9,a depicts force vs. indenter displacement diagrams for the cantilever (NC2). Again, no catastrophic failure but stable crack growth was observed for (NC2); for (NC1). No significant decrease in cantilever stiffness was visible for (NC1). There is no qualitative difference in fracture behavior of differently produced notches / cracks according to load vs. displacement curves. It can be expected that FIB-notched samples deliver equivalent fracture toughness results as naturally cracked samples. The conditional fracture toughness value was determined to be 4.3 MPa $m^{1/2}$ for (NC2). The condition of $F_{max}/F_Q \leq 1.1$ stipulated in [19] is not fulfilled. What has to be taken into account is the inclined starting crack plane, as a consequence of pure mode I loading conditions not being fulfilled. Furthermore, the starting crack length is not constant over the specimens' thicknesses but it decreases for (NC1) and increases for (NC2) when starting from the front surfaces visible in Figure F.8. Equation F.10 [36]

$$\frac{k_I}{K_I} = \sin^2(\pi/2 - \alpha) \tag{F.11}$$

describes the effective stress intensity k_I at the crack tip of a crack that is kinked at an angle α with the kinked part having at least 50% of the length of the straight part. However, there is no straight part, experiencing pure mode I loading, for both natural cracks of (NC1) and (NC2). This equation could be used to derive quantitative results for mode I fracture toughness values; this was not carried out due to the changing crack length over the specimens' thickness. The apparent stress intensity factor K_I that is derived considering a crack of projected length is higher than the effective

stress intensity factor k_I at the crack tip. This change in crack length can explain the difference in K_Q – value of (NC1) compared to (S1) to (S4). Elastic-plastic evaluation of cantilever NC2 according to Section 3.2.1, including determination of crack growth via decrease in unloading stiffness results in Figure F.9,b. It shows the same trend as depicted in Figure F.4 for smaller FIB-notched cantilevers. However, the values of J are larger by about a factor of 2 to 4. A reason for this might be the disadvantageous geometry, crack deflection and the change in loading conditions to a mode mixity of modes I and II.

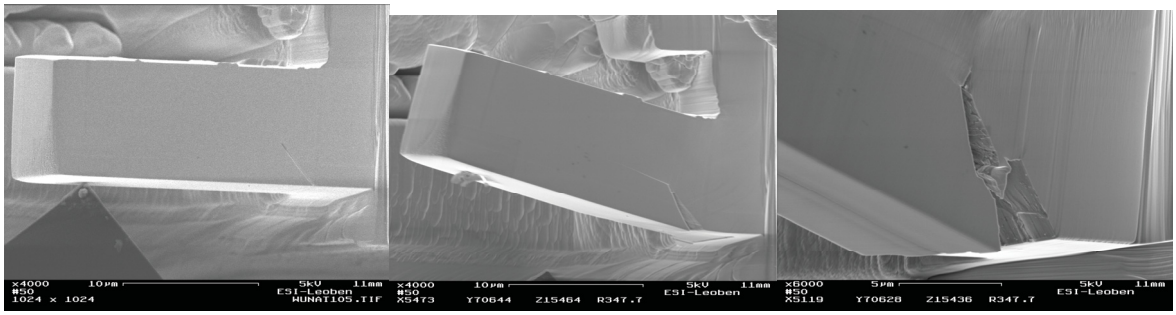

Figure F.8: Left: Experimental setup for testing naturally cracked cantilever (NC1) with a cube corner indenter. Center: Post-mortem SE micrograph that shows the indent and limited crack propagation. Right: Post-mortem SE micrograph of specimen (NC2) showing increased (~1 µm) crack propagation and crack deflection from the initial crack plane.

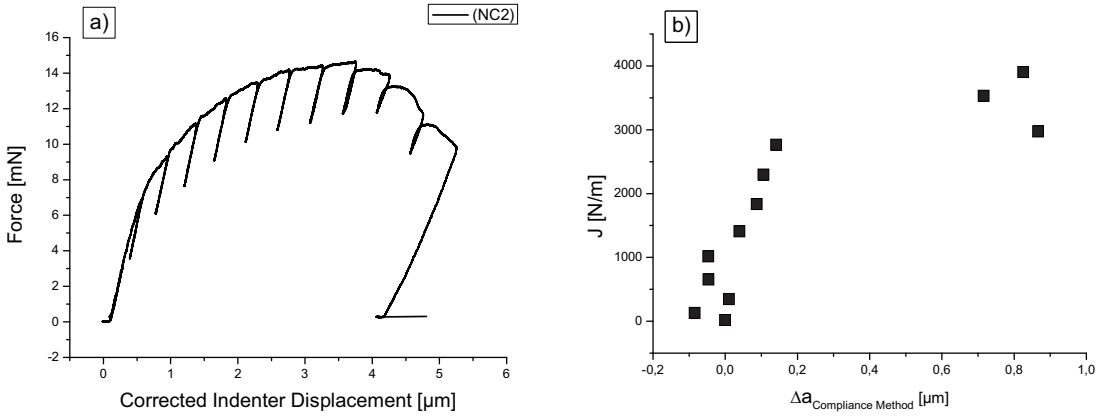

Figure F.9: a) Measured force vs. indenter displacement curve for cantilever (NC2) showing noticeable crack growth. Unloading step hysteresis in the lattter stage of the experiment might be related to crack closure events due to the rough fracture surface Figure F.8, right). b) J vs. Δa for (NC2) – the cantilever showing crack propagation – shows the same qualitative behavior as it was observed in Figure F.4.

4. Discussion

It is obvious when comparing figures F.2,a, F.3, F.4 and F.6 that two different stages of crack propagation are present in the experiments. This manifests as a marked load drop at different stages of the experiment, especially pronounced for cantilevers (S3) and (S4) and to a lesser extent for cantilevers (S1) and (S2). These load drops appear after the 2nd unloading for (S1) and (S2), after the 3rd for (S3) and after the 4th for (S4). Furthermore, in Figure F.3, the two different slopes of crack length versus equidistant unloading steps depict this effect. The change of slope in Figure F.6 is very informative concerning the shape of the crack front, the blunting behavior respectively. Although all four initial parts of the *CTOD*-Δa-curves were included to construct a common blunting line, it can be seen in Figure F.6 that the local Crack Tip Opening Angle ($CTOA_{local}$), defined as

$$CTOA_{local} = 2 * \tan^{-1}\left(\frac{\Delta CTOD/2}{\Delta(\Delta a)}\right), \tag{F.12}$$

for both cantilevers (S1) and (S2) is slightly below the mean value. Values for (S3) and (S4) are slightly above the mean value of 33°. This part can now be assigned to the first stage of the fracture process where blunting takes place with a low – but existent – amount of crack propagation in the range of hundreds of nanometers. Blunting is more pronounced for specimens with a higher misalignment towards the cleavage plane. It should be mentioned that this approach, using $CTOA_{local}$ gives a hint on the local, thus, time-dependent, shape of the crack tip, whereas the angle *Θ* that was introduced in Section 3.2.2., represents a mean *CTOA*. In the second stage of the fracture process, where the crack velocity is higher and, thus, noticeable stable crack propagation is present, $CTOA_{local}$ is smaller. The mean value seems to be independent of notch deviation. The transition from blunting to faster but stable crack propagation goes with the above – mentioned load drop. The proposed, resulting shape of the crack is depicted as inlays in Figure F.3.

The fracture process might be explained by a work from Hirsch et al. [37], where they propose a model for stable crack growth by micro-cleavage in semi brittle materials. The model is based on the emission of dislocations directly at the crack tip, on crystallographic planes that intersect the crack tip – in principle it should also be possible that dislocations are emitted on planes in advance of the crack tip in case of dislocation sources being present there. On this plane, regardless of being in front of the crack tip or intersecting the crack tip, shielding as well as anti-shielding dislocations are emitted. These anti-shielding dislocations force the crack to grow due to large crack opening stresses; shielding dislocations move away from the crack tip. Barely any hardening is observed (Figure F.2), hence, the process of dislocation emission is considered to be controlled by dislocation generation and not by the interaction of emitted dislocations with the crack tip, the

dislocation sources, respectively. Consequently, the above-mentioned two stages of crack growth are assumed also to take place in large samples.

What remains is the difference in crack velocity. In contrast to many fracture experiments on macroscopically large tungsten single crystals, the progress of fracture in the µm-regime is stable. Stable crack propagation, though, is not completely new for experiments on single crystalline tungsten. Hull et al. [34] performed fracture experiments using tensile specimens made of small sheets of arc-melted single crystalline tungsten. The tensile axis was [010] and micro-cracks were introduced on a (010) plane by the spark-machining technique. The samples had a rectangular cross section, 1.2 mm in width and 0.5 mm in thickness. For samples having all the same crack length of 0.08 mm, they found stable crack propagation for testing temperatures of 22 °C and above. After a certain amount of slow crack growth, whose extent increased with increasing testing temperature, the samples finally failed by catastrophic cleavage on planes of {100} – type. Further experiments shall focus on changing the energy release rate *G* versus crack resistance *R*. Even smaller samples shall be tested using a pico-indenter of high resolution in force and displacement. Larger samples – in the regime of tens of micrometers – will be produced using an improved method of argon ion polishing. By alteration of sample size, there goes a change of the amount of elastically stored energy and with an increase in volume one can expect a change from stable to unstable crack propagation as more energy is released upon a crack propagation *da.*

When summarizing the results from different evaluations presented in Section 3, it can be stated that – as expected – LEFM does not deliver correct but lower values for conditional critical stress intensities. This is attributable to the small sample size, which fails to fulfill the requirements, given by certain standards on fracture toughness measurements, by two orders of magnitude. However, together with critical *J*-values it is possible to define a range of toughness by using the linear elastic approach as a lower limit and a conservative upper value for critical crack initiation toughness determined from the second unloading step of each cantilever.

CTOD was evaluated by use of the hinge model presented in Figure F.5. Results from determination of a critical *CTOD* by linear interpolation of data in Figure F.6 for each cantilever show increasing toughness values with increasing deviation of notch plane from cleavage plane and from ideal crack front direction. The $K_{Q,CTOD}$ – value for (S1), 7.8 MPa $m^{1/2}$, is close to the upper bound given, defined by (6.2 ± 1.7) MPa $m^{1/2}$ [20]. Toughness values determined with this method depend on the yield strength of the material. As already mentioned, it is important to support the experiments with tensile tests using the material in the same condition. However, the matching slopes in the *J*-Δa-curves are an indicator that the yield strength of 650 MPa [22] is applicable.

Unloading steps for determination of crack extension are necessary for both, J-Δa- and CTOD-Δa-curves. A large number of SE micrographs could also serve for determination of crack length. However, at the initial stage of crack extension, tunneling of the crack in the center of the specimen seems to take place. Consequently, crack lengths from SE micrograph will underestimate the crack length, if crack growth is visible at all. As shown in Figure 4, crack lengths determined by both methods, unloading stiffness and SE measurements, coincide in the later stage of the experiments. Thus, a number of unloading steps is advisable and with a higher number of steps an increased accuracy in determination of the start of crack growth is expected. For a higher number of steps, there will probably be two unloading steps at the initial stage of the experiment indicating the same compliance of the cantilever. This in turn leads to a lower limit of *J*, where no crack propagation took place, i.e. there has been no change in compliance up to that point. Due to the lack of two unloading steps having the same slope, only an upper limit for toughness at crack initiation can be given. Conditional critical fracture toughness values for tungsten single crystal in its most brittle orientation ({100}-<011> crack system, [21]) were determined to be 12.5 MPa $m^{1/2}$ (second unloading step) and 12.8 MPa $m^{1/2}$ (linear fit of initial and final part of *J*-Δa-curve). By performing more unloading steps, it should be possible to determine the fracture toughness of tungsten single crystal of macroscopical samples having the same crack system more accurately.

Fracture experiments on naturally cracked cantilevers again show that LEFM gives lower limits for K_{IC}, thus, J-integral evaluation was conducted. Absolute quantities cannot / should not be given, due to the quite short bending length in relation to W; furthermore, the crack is not straight but kinked and experiences mixed mode loading conditions and the crack length over specimens' thickness is not constant. Nevertheless, values for fracture toughness and *J*-values are in the same range as it was found for smaller FIB-notched cantilevers. Concluding, both FIB-notches of adequate notch root radius and natural cracks lead to comparable results.

5. Conclusion

Fracture experiments using notched micrometer sized samples have been performed. One batch of samples was produced with the ion slicing technique. The batch of samples incorporating natural cracks was cut out of the bulk material using the FIB. Fracture never occurred by a single, catastrophic event but stable crack growth was observed. Two different stages of crack growth were observed for FIB-notched cantilevers. The first one comprises crack tip blunting together with a small amount of crack propagation. The local crack tip opening angle increases with increasing deviation of FIB-made notch from the dedicated cleavage plane. The observed stable fracture might be explained by the lack of large volumes accommodating elastically stored energy and, consequently, the energy release rate is lower. Due to the large plastic zone in front of the crack tip, leading to large scale yielding, linear elastic fracture mechanics – as it was applied for many other experiments of this kind using various different materials – does not lead to correct results.

However, LEFM gives a lower limit for critical fracture toughness values compared to results on the same crack system found in the literature. *J*-values give upper limits for fracture toughness. CTOD was determined basing on a hinge model and the resulting fracture toughness values are in good agreement with literature. Nevertheless, a higher number of unloading steps would result in a more accurate determination of initiation of crack propagation and would improve the accuracy of $K_{Q,CTOD}$ and especially of $K_{Q,J,\ blunting}$.

Disclaimer

This work, supported by the European Communities under the Contract of Association between EURATOM and the Austrian Academy of Sciences, was carried out within the framework of the European Fusion Development Agreement. The views and opinions expressed herein do not necessarily reflect those of the European Commission.

Acknowledgement

The authors thank Prof. Monika Jenko at the Institute of Metals and Technology (Ljubljana, Slovenia) for performing the ion slicing sample preparation.

References for Publication F

[1] D.E.J. Armstrong, M.E. Rogers, S.G. Roberts, Micromechanical testing of stress corrosion cracking of individual grain boundaries, Scripta Mater. 61 (2009) 741 – 743

[2] T.P. Halford, K. Takashima, Y. Higo, P. Bowen, Fracture tests of microsized TiAl specimens, Fatigue Fract. Engng. Mater. Struct. 28 (2005) 695 – 701

[3] K. Matoy, H. Schönherr, T. Detzel, D. Dehm, Micron-sized fracture experiments on amorphous SiOx films and SiOx/SiNx multilayers, Thin Solid Films 518 (2010) 5796 – 5801

[4] D. Miyaguchi, M. Otsu, K. Takashima, M. Takeyama, Microscale Fracture Toughness Testing of TiAl PST Crystals, Mater. Res. Soc. Symp. Proc. 1128 (2009) 197 – 202

[5] D. Di Maio, S.G. Roberts, Measuring fracture toughness of coatings using focused-ion-beam-machined microbeams, J. Mater. Res. 20 (2005) 299 – 302

[6] S. Massl, W. Thomma, J. Keckes, R. Pippan, Investigation of fracture properties of magnetron-sputtered TiN films by means of a FIB-based cantilever bending technique, Acta Mater. 57 (2009) 1768 – 1776

[7] K. Takashima, Y. Higo, Fatigue and fracture of a Ni-P amorphous alloy thin film on the micrometer scale, Fatigue Fract. Engng. Mater. Struct. 28 (2005) 703 – 710

[8] T.P. Halford, K. Takashima, Y. Higo, P. Bowen, Fracture tests of microsized TiAl specimens, Fatigue Fract. Engng. Mater. Struct. 28 (1005) 695 – 701

[9] K. Matoy, H. Schönherr, T. Detzel, T. Schöberl, R. Pippan, C. Motz, G. Dehm, A comparative micro-cantilever study on the mechanical behavior of silicon based passivation films, Thin Solid Film 518 (2009) 247-256

[10] T. Kondo, IFMIF, its facility concept and technology, J Nucl. Mater. 258 – 263 (1998) 47 – 55

[11] D. Kiener, P. Hosemann, S.A. Maloy, A.M. Minor, In situ nanocompression testing of irradiated copper, Nature Materials, in press, doi: 10.1038/nmat3055

[12] A.A. Griffith, The phenomena of rupture and flow in solids, Phil. Trans. Roy. Soc. A 221 (1920) 163 – 198

[13] S. Wurster, C. Motz, M. Jenko, R. Pippan, Micrometer-sized specimen preparation based on ion slicing technique, Adv. Eng. Mater. 12 (2010) 61-64

[14] J.R. Greer, W.D. Nix, Nanoscale gold pillars strengthened through dislocation starvation, Phys. Rev. B 73 (2006) 245410

[15] W.D. Nix, J.R. Greer, G. Feng, T. Lilleodden, Deformation at the nanometer and micrometer length scales: Effects of strain gradients and dislocation starvation, Thin Solid Films 515 (2007) 3152 – 3157

[16] C. Motz, T. Schöberl, R. Pippan, Mechanical properties of micro-sized copper bending beams machined by the focused ion beam technique, Acta Mater. 53 (2005) 4269 – 4279

[17] C. Motz, D. Weygand, J. Senger, P. Gumbsch, Micro-bending tests: A comparison between three-dimensional discrete dislocation dynamics simulations and experiments, Acta Mater. 56 (2008) 1942 – 1955

[18] D. Kiener, C. Motz, M. Rester, M. Jenko, G. Dehm, FIB damage of Cu and possible consequences for miniaturized mechanical tests, Mat. Sci. Eng. A 459 (2007) 262 – 272

[19] ASTM Standard E399-09, Standard Test Method for Linear-Elastic Plane-Strain Fracture Toughness KIC of Metallic Materials, ASTM International, West Conshohocken, PA, 2003, DOI: 10.1520/E0399-09, www.astm.org

[20] J. Riedle, P. Gumbsch, H.F. Fischmeister, Cleavage anisotropy in tungsten single crystals, Phys. Rev. Lett. 76 (1996) 3594 – 3597

[21] J. Riedle, Bruchwiderstand in Wolfram-Einkristallen: Einfluß der kristallographischen Orientierung, der Temperatur und der Lastrate (in German), PhD-thesis, University of Stuttgart

[22] R.H. Schnitzel, Deformation of tungsten single crystals from -77°C to 800°C, J. of Less-Common Met. 8 (1965) 81 – 89

[23] M.D. Uchic, D.M. Dimiduk, J.N. Florando, W.D. Nix, Sample Dimensions Influence Strength and Crystal Plasticity, Science 305 (2004) 986 – 989

[24] N.A. Fleck, G.M. Muller, M.F. Ashby, J.W. Hutchinson, Strain gradient plasticity: Theory and experiment, Acta metal. mater. 42 (1994) 475 – 487

[25] S. Shim, H. Bei, M.K. Miller, G.M. Phar,, E.P. George, Effects of focused ion beam milling on the compressive behavior of directionally solidified micropillars and the nanoindentation response of an electropolished surface, Acta Mater. 57 (2009) 503 – 510

[26] ESIS Recommendations for Determining the Fracture Resistance of Ductile Materials, ESIS P1-92, January 1992

[27] ASTM Standard E 1820-99a, Standard Test Method for Measurement of Fracture Toughness, ASTM International, West Conshohocken, PA, 2003

[28] Methods for Crack Opening Displacement (COD) Testing DD 19:1972, British Standards Institutions, London, 1972

[29] ASTM Standard E 813 – 89, Standard Test Method for J_{IC}, A Measure for Fracture Toughness, ASTM International, West Conshohocken, PA, 2003

[30] S. Wurster, C. Motz, R. Pippan, Notched-cantilever testing on the micrometer scale – effects of constraints on plasticity and fracture behaviour, Proceedings of the 18th European Conference on Fracture, Dresden, 2010

[31] Y. Murakami, Stress Intensity Factors Handbook, Volume 1, Pergamon Press, Oxford, New York, Beijing, Frankfurt, Sao Paulo, Sydney, Tokyo, Toronto, 1st edition, 1987

[32] J.R. Rice, A Path Independent Integral and the Approximate Analysis of Strain Concentration by Notches and Cracks, Trans ASME J. of Appl. Mech. 35 (1968) 379 – 386

[33] O. Kolednik, H.P. Stüwe, A proposal for estimating the slope of the blunting line, Int. J. of Fract. 33 (1987) R63 – R66

[34] D. Hull, P. Beardmore, A. Valintine, Crack Propagation in Single Crystals of Tungsten, Phil. Mag. 12 (1965) 1021 – 1041

[35] J.M. Liu, B.W. Shen, Crack nucleation in tungsten on crystallographic planes and on grain boundaries of twist misorientation, Scripta Metall. 17 (1983) 635 – 638

[36] S. Suresh, Fatigue of Materials, Cambridge Solid State Science Series, (E.A. Davis, I.M. Ward, Editors), pp 182, Cambridge, University press, Reprint 1994

[37] P.B. Hirsch, A.S. Booth, M. Ellis, S.G. Roberts, Dislocation-driven stable crack growth by microcleavage in semi-brittle crystals, Scripta Met. Et Mat. 27 (1992) 1723 – 1728

List of publications and conference contributions

Publications

Main author

[1] S. Wurster, R. Pippan, Nanostructured metals under irradiation, Scripta Mater. 60 (2009) 1083 – 1087

[2] S. Wurster, C. Motz, M. Jenko, R. Pippan, Micrometer-sized specimen preparation based on ion slicing technique, Adv. Eng. Mat. 12 (2010) 61 – 64

[3] S. Wurster, B. Gludovatz, R. Pippan, High temperature fracture experiments on tungsten – rhenium alloys, Int. J. Ref. Met. Hard Mater. 28 (2010) 692 – 697

[4] S. Wurster, B. Gludovatz, A. Hoffman, R. Pippan, Fracture behaviour of tungsten-vanadium and tungsten-tantalum alloys and composites, J. Nucl. Mater. 413 (2011) 166 – 176

[5] S. Wurster, C. Motz, R. Pippan, Describing fracture on the micrometer scale employing single crystalline tungsten notched cantilevers (in preparation)

Co-author

[6] B. Gludovatz, S. Wurster, A. Hoffmann, R. Pippan, Fracture toughness of tungsten alloys, Int. J. Ref. Met. Hard Mater. 28 (2010) 674 – 678

[7] J. Du, T. Höschen, M. Rasinski, S. Wurster, W. Grosinger, J-H. You, Feasibility study of a tungsten wire-reinforced tungsten matrix composite with ZrO_X interfacial coatings, Composites Science and Technology 70 (2010) 1482 – 1489

[8] M. Rieth, J.L. Boutard, S.L. Dudarev, T. Ahlgren, S. Antusch, N. Baluc, M.-F. Barthe, C.S. Becquart, L. Ciupinski, J.B. Correia, C. Domain, J. Fikar, E. Fortuna, C.-C. Fu, E. Gaganidze, T.L. Galán, C. Garcia-Rosales, B. Gludovatz, H. Greuner, K. Heinola, N. Holstein, N. Juslin, F. Koch, W. Krauss, K.J. Kurzydlowski, J. Linke, Ch. Linsmeier, N. Luzginova, H. Maier, M.S. Martinez, J.M. Missiaen, M. Muhammed, A. Munoz, M. Muzyk, K. Nordlund, D. Nguyen-Manh, P. Norajitra, J. Opschoor, G. Pintsuk, R. Pippan, G. Ritz, L. Romaner, D. Rupp, R. Schäublin, J. Schlosser, I. Uytdenhouwen, J.G. van der Laan, L. Ventelon, S. Wahlberg, F. Willaime, S. Wurster, M.A. Yar, Review of the EFDA programme on tungsten materials technology and science, J Nucl Mater, 2011 (in press), doi: 10.1016/j.jnucmat.2011.01.075

[9] T. Klünsner, S. Wurster, P. Supancic, R. Ebner, M. Jenko, J. Glätzle, A. Püschel, R. Pippan, Effect of specimen size on the tensile strength of WC-Co hard metal, Acta Mater. 59 (2011) 4244 – 4252

[10] B. Gludovatz, S. Wurster, T. Weingärtner, A. Hoffmann, R. Pippan, Influence of impurities on the fracture behaviour of tungsten, Philosophiocal Magazine 91 (2011) 3006 – 3020

[11] H. Li, S. Wurster, C. Motz, L. Romaner, C. Ambrosch-Draxl, R. Pippan, Dislocation core symmetry and slip planes in W alloys, in preparation

Conference Proceedings

Main author

[1] S. Wurster, B. Gludovatz, R. Pippan: "High Temperature Fracture Experiments on Tungsten – Rhenium Alloys", 17th Plansee Seminar – International Conference on High Performance P/M Materials – Proceedings Vol.1: P/M Metals, Plansee Group, 2009 (non peer-reviewed); also appearing as S. Wurster, B. Gludovatz, R. Pippan, High temperature fracture experiments on tungsten-rhenium alloys, Int. J. Ref. Met. Hard Mater. 28 (2010) 692 – 697

[2] S. Wurster, C. Motz, R. Pippan, Notched-cantilever testing on the micrometer scale – Effects of constraints on plasticity and fracture behaviour", Proceedings of the 18th European Conference on Fracture, Dresden, 2010 (non peer-reviewed)

Co-author

[3] B. Gludovatz, M. Faleschini, S. Wurster, A. Hoffmann, R. Pippan, Influence of microstructure on the fracture toughness of tungsten alloys, TMS 2008 Annual Meeting, 1 (2008) 449 – 454 (peer-reviewed)

[4] B. Gludovatz, S. Wurster, A. Hoffmann, R. Pippan, Fracture toughness of polycrystalline tungsten alloys" 17th Plansee Seminar – International Conference on High Performance P/M Materials – Proceedings Vol.1: P/M Metals, Plansee Group, 2009 (non peer-reviewed) also appearing as B. Gludovatz, S. Wurster, A. Hoffmann, R. Pippan, Fracture toughness of tungsten alloys, Int. J. Ref. Met. Hard Mater. 28 (2010) 674 – 678

[5] B. Gludovatz, S. Wurster, A. Hoffmann, R. Pippan, Fracture toughness of polycrystalline tungsten alloys, Conference Proceedings of the 12th International Conference on Fracture, Ottawa, 2009 (peer-reviewed)

[6] T. Klünsner, S. Wurster, R. Pippan, M. Jenko, R. Ebner, P. Supancic, J. Glätzle, A. Püschel, Comparison of bending strength of WC-Co hard metal in millimeter and micrometer sized specimens, Proceedings of the 18th European Conference on Fracture, Dresden, 2010 (non peer-reviewed)

Poster Presentations

[1] S. Wurster, B. Gludovatz, L. Romaner, R. Pippan, Influence of Microstructure on the Fracture Toughness of Tungsten Alloys, 1st International Conference on New Material for Extreme Environments, San Sebastian, July 2008

[2] S. Wurster, B. Gludovatz, A. Hoffmann, R. Pippan, High Temperature Fracture Experiments on different Tungsten – Rhenium Alloys, 15th International Conference on the Strength of Materials, Dresden, August 2009

[3] S. Wurster, B. Gludovatz, H. Li, L. Romaner, R. Pippan, G. Dehm, Wolfram für die Fusion, Fusion Expo, Vienna, March 2011

[4] S. Wurster, B. Gludovatz, R. Pippan, On the brittle fracture of tungsten and tungsten alloys and its impact on the material's usage for fusion applications, 13th International Workshop on Plasma-Facing Materials and Components for Fusion Applications / 1st International Conference on Fusion Energy Materials Science, Rosenheim, May 2011

Oral Presentations at Conferences and Workshops

[1] S. Wurster, S. Roberts, R. Pippan, Characterization of materials by instrumented micro-mechanical methods, First Workshop on Fusion Materials Science – FEMaS, Lisbon, January 2009

[2] S. Wurster, B. Gludovatz, R. Pippan, Fracture Behaviour of Tungsten and Tungsten Alloys, ESIS TC2 Meeting, Leoben, April 2009

[3] S. Wurster, B. Gludovatz, R. Pippan, High Temperature Fracture Experiments on Tungsten-Rhenium Alloys, 17th Plansee Seminar, Reutte, May 2009

[4] S. Wurster, C. Motz, R. Pippan, A new Micrometer-sized Specimen Preparation using Ion Slicing Technique and Focused Ion Beam, 15th International Conference on the Strength of Materials, Dresden, August 2009

[5] S. Wurster, C. Motz, R. Pippan, Micrometer-sized Tungsten Specimen Testing using Ion Slicing and Focused Ion Beam Techniques, 7th EUROMECH Solid Mechanics Conference, Lisbon, September 2009

[6] S. Wurster, J. Du, J.H. You, R. Pippan, Résumé on the International Summer School on Micro-Mechanical Experiments & 1st results on in-situ 3-point bending tests on W/W composites, 2nd Workshop on Fusion Energy Materials Science - FEMaS, Athens, January 2010

[7] S. Wurster, B. Gludovatz, H. Li, D. Luef, L. Romaner, C. Ambrosch-Draxl, R. Pippan, Intrinsic brittleness of tungsten & possible ductilization mechanisms, plasticity studies with focus on impurities & Re effects, MAT – W&WALLOYS Monitoring meeting, Garching bei München, February 2010

[8] S. Wurster, C. Motz, R. Pippan, Fracture Behaviour of Tungsten Based Materials on the µm-scale, 6th International Conference on Materials Structure & Micromechanics of Fracture, Brno, June 2010

[9] S. Wurster, C. Motz, R. Pippan, Notched Sample Testing on the Micrometer Scale – Effects of constraints on plasticity and fracture behaviour, 18th European Conference on Fracture, Dresden, September 2010

[10] S. Wurster, B. Gludovatz, C. Motz, R. Pippan: "Structural Material Development – Plasticity Fracture Mechanisms – Micro Plasticity W-Alloys", EFDA Monitoring Meeting, Garching bei München, February 2011

[11] S. Wurster, Th. Leitner, B. Gludovatz, P. Kutleša, R. Pippan, Fracture Behaviour of HPT-deformed W-materials, EFDA Monitoring Meeting, Frascati (Italy), June 2011

Co-Organiser of the 1st International Summer School on Micro-Mechanical Experiments, July 7th – July 10th 2009, Leoben